UNIVERSITÉ PIERRE ET MARIE CURIE

ÉCOLE DOCTORALE
Sciences Mécaniques, Acoustique, Electronique et Robotique de Paris
ED391

Analysis of Fluid-Structure Interaction in a Sodium Fast Reactor Core: Experimental, Theoretical and Numerical Evaluation of Damping and Frequencies

Thèse de doctorat de Mécanique des fluides
PAR Qing ZHOU

Dirigée par Hélène DUMONTET et Arnault MONAVON
Responsable CEA Jean-Paul MAGNAUD

Présentée et soutenue publiquement le 15 Décembre 2017 devant le jury composé de :

Directeur	Mme Hélène DUMONTET Professeur, UPMC
Rapporteur	Mme Élisabeth LACAZEDIEU LONGATTE Ingénieur Chercheur, EDF
Rapporteur	M. Olivier CADOT Professeur, The University of Liverpool
Examinateur	M. Daniel BROC Ingénieur Chercheur, CEA
Examinateur	M. Jean-Paul MAGNAUD Ingénieur Chercheur (superviseur), CEA
Examinateur	M. Arnault MONAVON MdC retraité (directeur), UPMC
Examinateur	M. Régis WUNENBURGER Professeur, UPMC
Invité	M. Laurent MARTIN Responsable RNR-Na (ASTRID), CEA

Université Pierre et Marie Curie

Abstract

Sciences Mécaniques, Acoustique, Electronique et Robotique de Paris

Doctor of Philosophy

Analysis of Fluid-Structure Interaction in a Sodium Fast Reactor Core: Experimental, Theoretical and Numerical Evaluation of Damping and Frequencies

by Qing ZHOU

In the scheme of French ASTRID (Advanced Sodium Technological Reactor for Industrial Demonstration) project, fluid-structure interaction phenomena involved in the dynamic behaviour of core flowering, which could happen during seismic events, are of high interest. Also core flowering behaviour is considered as the main initiating event for the four SCRAMs that happened in Phénix reactor during 1989 and 1990.

In objective to improve the knowledge of fluid-structure interaction phenomena of dynamic issues in a SFR core, especially focused on damping, this Ph.D. thesis have been conducted in experimental, numerical and analytical approaches based on free-vibration experiments on mono-assembly test facility PISE-1A and multi-assembly test facility PISE-2C.

Two series of free-vibration experiments have been performed on PISE-1A with different water heights and different mass fractions of water-glycerol mixtures to examine the dynamic behaviours with respect to different added mass, different densities and viscosities. Corresponding numerical interpretations have been conducted with $3D$ NAVIER-STOKES model in CAST3M code. Sources of uncertainties are discussed to explain the discrepancies between the numerical computation and experimental results. Edge effects are not found to have an important impact on the dynamic behaviours of the system.

On PISE-2C, free-vibration experiments with different modes of excitations have been conducted, including total flowering, partial flowering with internal crown excited and partial flowering with external crown excited. A reticulate model with homogenised linear hypothesis has been developed to interpret PISE-2C experiments. Good symmetries are found in PISE-2C suggesting that the deterministic tool is valid for the analysis.

Keywords: SFR, fluid-structure interaction, core flowering, vibrations

Université Pierre et Marie Curie

Résumé

Sciences Mécaniques, Acoustique, Electronique et Robotique de Paris

Doctorat

Analysis of Fluid-Structure Interaction in a Sodium Fast Reactor Core: Experimental, Theoretical and Numerical Evaluation of Damping and Frequencies

Qing ZHOU

Dans le cadre du projet ASTRID ((Advanced Sodium Technological Reactor for Industrial Demonstration), les interactions fluide-structure mettant en jeu la dynamique du coeur (gerbage), tels qu'elles peuvent survenir lors d'un séisme, sont d'un grand intérêt. Le gerbage du coeur est également reconnu comme l'événement le plus plausible pour expliquer les quatre AURN (Arrêt d'Urgence pour Radioactivité Négative) survenus dans le réacteur Phénix, durant les années 1989 et 1990.

L'objectif poursuivi est d'améliorer, pour leurs aspects dynamiques, la compréhension des interactions fluide-structure susceptibles de se produire dans un SFR (Sodium Fast Reactor). Le centre d'intérêt principal étant phénomène de dissipation visqueuse, cette thèse entreprend trois approches : expérimentale, numérique et analytique, en s'appuyant sur des expériences de vibrations libres menées sur deux installations, PISE1A, mono-assemblage et PISE2C, multi-assemblages.

Deux séries d'expériences de vibrations libres ont été menées sur PISE1A, en faisant varier la hauteur d'eau et en utilisant un mélange d'eau et de glycérol, dans des proportions variables. Le but est d'examiner l'influence des variations de masse ajoutée et de viscosité sur la dynamique des oscillations de l'assemblage. Les simulations numériques correspondantes, développées dans le code CAST3M, se sont appuyées sur la résolution des équations de Navier-Stokes 3D. Les écarts entre les résultats numériques et expérimentaux sont présentés et analysés. En particulier, les effets d'extrémité se sont révélés être d'une importance marginale.

Des expérience de vibrations libres ont également été effectuées sur PISE2C en sollicitant l'installation de trois façons différentes : mise en mouvement globale, mise en mouvement par la couronne externe puis par la couronne interne. Un modèle réticulé, fondé sur des hypothèses de symétrie et de linéarité a été développé parallèlement. Les résultats expérimentaux ont permis de confirmer les symétrie mais ont remis en cause les hypothèses de linéarité. Ce résultat encourage à persévérer dans la voie des modèles déterministes.

Mot-clès: RNR-Na, IFS, gerbage, vibrations

Acknowledgements

First and foremost, I would like to thank my supervisor Dr. Jean-Paul MAGNAUD, my advisor Prof. Arnault MONAVON and Prof. Hélène DUMONTET, for their continuous and generous support of my Ph.D. study and research, for their motivation and immense knowledge. Their guidance helped me in all the time of the research and writing of this thesis. I know I am not a very good student, sometimes even got myself into some bizarre troubles, but Arnault and Jean-Paul, they are always extremely patient with me. Without their help, I cannot go through all the difficulties I have met in these three years. It's impossible to imagine better advisors and mentors for my Ph.D. study other than them.

Besides, I want to thank the rest my thesis committee: Mme. Élisabeth LACAZEDIEU LONGATTE, Prof. Olivier CADOT, M. Daniel BROC and Prof. Régis WUNENBURGER, for their kind help.

Also, I want to thank my colleagues in Laboratoire des Applications en Thermohydraulique et Mécanique des fluides (LATF). My thanks goes to Mme. Danielle GALLO and Mme. Patricia SALVATORE for letting me taking part into this group and M. Laurent MARTIN for allowing me carry out this project.

Especially, I have to thank Dr. Benjamine CARRITEAU for his generous help during the experiments of PISE-1A and PISE-2C, and Dr. Lucia SARGENTINI for laying the base of this thesis and for her help at the beginning of my work.

I would like to thank all my friends for their accompany during these three happy years in Paris. As most of us are international students, we are going to leave here sooner or later. However, these memories with you will always be cherished.

Special thanks have to go to my dearest friends Ruimin, Yang and Daniel. Although we are separated in different countries on different continents, your support means even more to me than you have ever imagined.

Lastly, I would like to thank my family who are always in support of me no matter where I am and what I am doing. I know it's an extremely harsh year for everyone in the family especially for my parents and I. The shadows are hanging there and we can never predict what will happen in the future. But what we can do is to hold the present and do not let fear and sorrow immerse hope and happiness. This year didn't have a good beginning but it will end with a happy ending.

Contents

List of Figures

List of Tables

List of Abbreviations

ASTRID	**A**dvanced **S**odium **T**echnological **R**eactor for **I**ndustrial **D**emonstration
CEA	**C**ommissariat à l'**é**nergie **A**tomique
DAC	**D**issipositif **A**ssemblage **C**obalt
DOF	**D**egree **O**f **F**reedom
EDF	**É**lectricité de **F**rance
ERA	**E**igensystem **R**ealisation **A**lgorithm
FFT	**F**ast **F**ourier **T**ransform
FSI	**F**luid-**S**tructure **I**nteraction
MF	**M**ass **F**raction
SCRAM	**S**afety **C**ontrol **R**ods **A**ctivator **M**echanism
SFR	**S**odium **F**ast **R**eactor
WH	**W**ater **H**eight

List of Symbols

a_0	initial amplitude of vibration	m
b	width of channel	m
c_v	damping ratio	kg/s
e_k	kinetic energy	J
e_p	potential energy	J
e_t	total energy	J
f_{air}	frequency in air	Hz
f_{water}	frequency in water	Hz
f_n	natural frequency	Hz
F_0	fluid force scale	kg·m/s^2
F_f	fluid force	kg·m/s^2
k	stiffness	kg/s^2
m_0	mass in motion	kg
m_{hex}	hexagon mass	kg
m_{lam}	support blade mass	kg
m_{tot}	total mass	kg
m_{vis}	screws mass	kg
M_{water}	added mass by water	kg
M	mass of the structure	kg
$\mathbf{n}$	norm	
p	pressure	Pa
R^2	residual sum of squares	m^2
Re	REYNOLDS number	
St	STROUHAL number	
t	time	s
u	velocity	$\mathrm{m\,s^{-1}}$
U	velocity scale, x-direction	$\mathrm{m\,s^{-1}}$
V	velocity scale, y-direction	$\mathrm{m\,s^{-1}}$
w_1	under-relaxation factor	
x	displacement of structure	m
$\dot{x}$	velocity of structure	m/s
$\ddot{x}$	acceleration of structure	m/s^2
ϵ	amplitude parameter	
η	confinement parameter	
μ	dynamic viscosity	kg/(m·s)
ν	kinematic viscosity	m^2/s
ρ	density	kg/m^3
σ	STOKES number	
τ	time scale	s
ϕ	displacement potential	m^2

ξ	damping coefficient	
ω	angular fluid velocity	rad
ω_n	natural angular frequency	rad/s

Dedicated to my family

Chapter 1

Introduction

1.1 Background

In the frame of development for GEN IV reactor design concept, a major contribution to the development of Sodium Fast Reactor (SFR) has been paid in France [1]. ASTRID, in abbreviation of Advanced Sodium Technological Reactor for Industrial Demonstration, was proposed by Commissariat à l'Énergie Atomique (CEA). Companies and research institutes, such as Électricité de France (EDF), Areva and CEA are involved in the research and design project of ASTRID [2, 3, 4].

Here below, FIGURE 1.1 shows the scheme of ASTRID design.

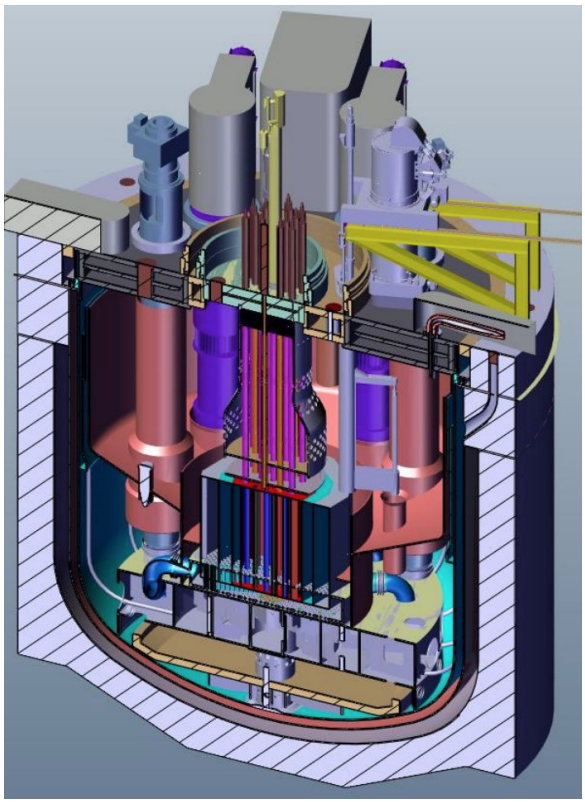

FIGURE 1.1: Scheme of ASTRID design

As one of the former French Sodium Fast Reactors, Phénix reactor was a small-scale pool-type SFR located at the Marcoule nuclear site. It was connected to the national electricity grid in 1974 and permanantly shut down in 2009 with an operating period of 34 years.

The scheme of Phénix reactor core is shown in FIGURE 1.2. There are six crowns of fissile assemblies located in the center, three crowns of fertile assemblies and two crowns of steel assemblies in Phénix reactor core [5, 6].

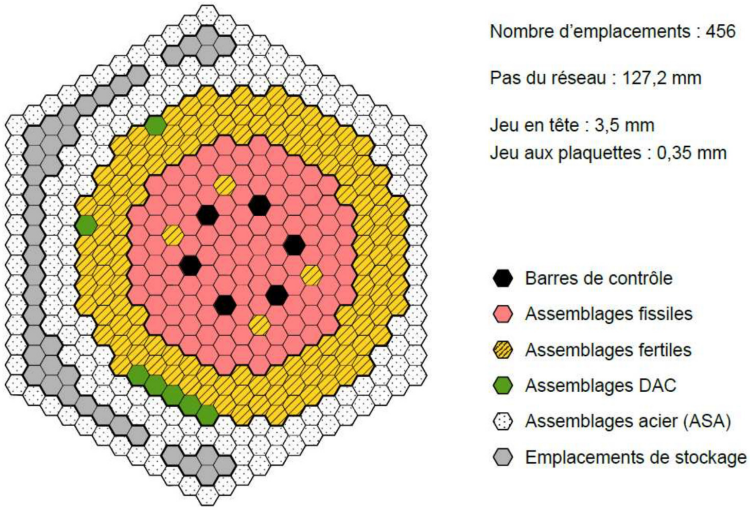

FIGURE 1.2: Scheme of Phénix reactor core

During its operation period, Phénix has experienced several periods of shutdown. Most of them are due to the leakage of the sodium and the consequent fires. However, during 1989 and 1990, Phénix had encountered four times of SCRAM (Safety Control Rods Activator Mechanism) due to negative reactivity. Until now, there is no accomplished explanation for these SCRAMs [7].

Power-vs-time curves for two out of the four SCRAMs is shown in FIGURE 1.3 [8]:

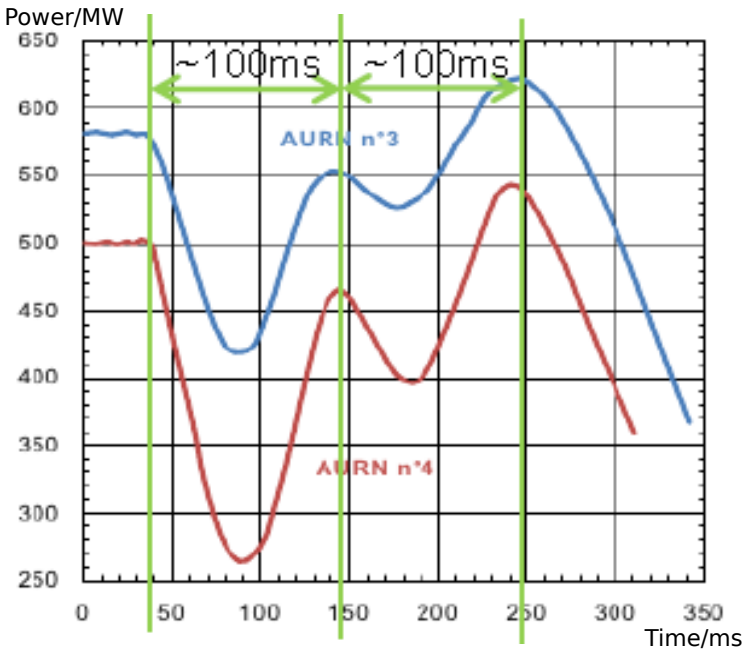

FIGURE 1.3: SCRAM time evolution in Phénix reactor

When comparing with the time scale of these SCRAMs, the only initiating event compatible with is core flowering. In order to approach the phenomena of core flowering, a lot of investigations have been paid. Several scenarios have been considered to be the cause of core flowering. Recently, a lot of interests have been focused on DAC scenario (Dispositif Assemblage Cobalt, see FIGURE 1.4) [9].

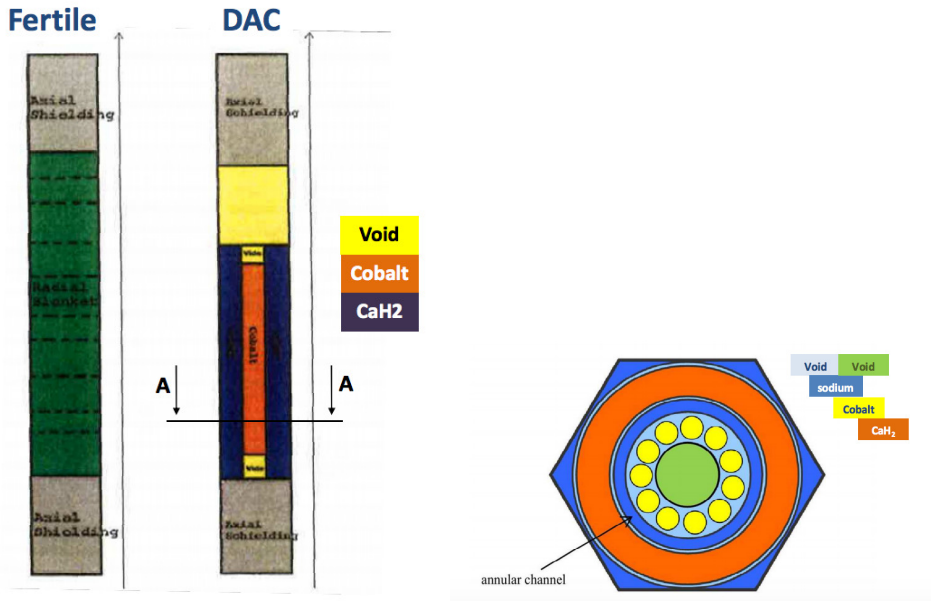

(a) Axial Cut (b) Transverse Cut

FIGURE 1.4: Sketch of DAC

DAC assemblies are the assemblies aimed at producing radioactive cobalt for medical use. As shown in FIGURE 1.4, they consist of capsules containing cobalt pellets and calcium hydride surroundings which are usually used as neutron moderator, locating near the fertile assemblies (see FIGURE 1.2). Therefore the fertile assemblies close to the DAC assemblies are partially exposed to moderated neutron flux and then generated extra thermal power. Especially, this side effect is even more probable for those with high burn-ups and rich fissile concentrations. Therefore, a perturbed temperature field in the vicinity of the DAC assemblies is to be formed [10, 11].

In the reason of incompletely accurate thermal-hydraulic design of the assemblies as suggested in recent report [12], the DAC assemblies may have experienced an unexpected high thermal power with possible blockage of the channel inside the DAC assemblies for sodium flowing. In this stagnant layer, due to high temperature, superheating state of the liquid sodium is possible to be reached. Vaporisation of the superheated liquid sodium can happen suddenly.

Two cases are possible depending on where the sudden vaporisation happens:

If it occurs at the outlet of the DAC assembly, in the hot collector, the expansion and then implosion of the bubble can cause a modification to the geometry of the core. This scenario was studied in 2010 by D. Broc, the mechanical constraints on the core was estimated by coupling the thermal-hydraulic model with the «CAST3M $up\phi$» model [13]. According to the Fluid-Structure Interaction (FSI) analysis, conditions of core flowering that is capable of causing SCRAM can hardly be attained if the sudden vaporisation of superheated sodium occurs in the hot collector.

If the sudden vaporisation happens within the DAC itself, a plug of high pressure sodium vapour (saturation pressure of the vapour at overheating temperature) will be formed. A quantity of liquid sodium in the inter-assembly gap will be expelled leading to geometric changes of the core. This scenario was studied in 2011 [14], but it was based on an underestimation of the recondensation of vapour in the expansion phase and the modelling was limited by a incomplete physical description of the interface between the vapour and liquid. To improve the modelling of the DAC scenario, thesis by E. Semeraro was taken in CEA to identify and quantify hydrodynamic instabilities [15].

During the seismic events, amplification of seismic waves in surficial geological layers, so-called seismic site effects, will happen [16]. The surface ground motion may be strongly amplified if the geological conditions are unfavourable. This effect shall be considered as the source of dynamic movement of as SFR core during seismic events. Inertia effect, deformations, horizontal and vertical shaking must be taken into account [17].

DAC scenario and seismic events are both in the scheme of dynamic behaviour of SFR core.

1.2 Objectives

This Ph.D. thesis will be in the framework of development of ASTRID project continuing the research on DAC scenario and the dynamic behaviour of SFR core during core flowering and seismic events.

As known, the presence of the liquid (liquid sodium and water) in place of air leads schematically to two types of effects, which occur in different ways depending on the type of excitation and the movement of the assemblies. These effects are very important for the core flowering behaviours with large relative movements between the fluid and assemblies. They are:

Inertia effects which cause a decrease in natural frequency of vibration by around 60% for a flowering movement, and 15% for an assembly at horizontal movement; The added mass by the presence of water can be deduced roughly by the classical expression [18]:

$$\frac{f_{air}}{f_{water}} = \sqrt{1 + \frac{M_{water}}{M}}.$$

where M_{water} is the added mass by water, M is the mass of the structure.

Dissipative effects which cause damping of the structure; it's impossible to have a simple equation for dissipation as added mass. Also, it is difficult to apprehend the dissipation since it's a second-order phenomenon. One way to roughly describe dissipative effects is dissipation ratio, which is ratio of period to the time when all the energies are dissipated. In a typical experiments in air, the dissipation ratio will be as small as 0.04.

Different components of the physical phenomena which occur, including inertial effect, dissipative effect and also kinetic energy transfer between the fluid and structure, are in need to be clearly identified.

Previous works mostly have focused on kinetic analysis and vibration frequency, little have been paid on dissipative effects. Most of the former research are in numerical field, not so many experimental approaches have been made, indeed, experimental facility like PISE-2C is quite new. This Ph.D. thesis will be mainly focused on the study of dissipative

effects to provide dissipative information of both structure and fluid for further numerical research with multiple numerical models, including $2D$ and $3D$ NAVIER-STOKES and $up\phi$ model, based on experiments on PISE-1A and PISE-2C. The damping information obtained during this Ph.D. project will help identify the input of Rayleigh damping for the $up\phi$ model implemented in BASILIQ code for complex computations of ASTRID project [19, 20]. Besides, verifications among different numerical models and codes have been planned, but not accomplished due to limit of time.

1.3 State of the Art

1.3.1 Existing methods

Linearised EULER model ($up\phi$) is based on linearised EULER equation. The fluid flow is considered to be non-viscous and incompressible. Instead of using only velocity u and pressure p to describe the flow field, a new variable as displacement potential ϕ, where $\mathbf{x_f} = \nabla\phi$, has been added to obtain a symmetrical matrix for solving the problem. With this definition, the flow field is supposed to be irrotational. Its advantage of light demand for computational power enables it to be applied to large-scale computations of flow field in SFR core. However, it has a major limitation that only inertial effects are considered, no dissipative effects are included in the model. To take into account the dissipative effects, so-called RAYLEIGH damping has been introduced [21, 22]. However, RAYLEIGH damping, as an supplementary input to $up\phi$ model, varies from scenario to scenario. Validation and verification works have to be accomplished by small-scale experiments and corresponding NAVIER-STOKES simulations.

Any codes applied to model the dynamic behaviours of a full-size reactor core shall be validated with experiments, especially with respect to dissipation phenomena.

1.3.2 Previous works

To improve the understanding of fluid-structure interaction in reactor core, the problems can be studied on three different scales with different numerical models:

- Micro-scale: mono-assembly test facility PISE-1A ($2D$ and $3D$ NAVIER-STOKES, $up\phi$);
- Meso-scale: multi-assembly test facility PISE-2C ($2D$ NAVIER-STOKES, MR, $up\phi$);
- Macro-scale: SFR core (MH, $up\phi$).

There are several important previous works on the three different scales that should be mentioned.

Homogenised model

Ph.D. thesis by Q. Desbonnets [23] is aimed at building an homogenised model, based on the Darcy velocity notion, for the vibration of tube bundles in fluid with regard to not only the inertial effects but viscous effects of the fluid and large structure displacement taken into account. Added mass and viscous related coefficients representing the inertial and dissipative effects without describing the local scale flow are used to facilitate the model.

During the the Ph.D. thesis of A. N. Gineau [24], a homogenised model with multi-scale approach has been developed to describe the fluid-structure interactions in a large-scale geometry with a big number of identical cylindrical tubes (assemblies) involved.

Fluid force was estimated from the micro-scale numerical solution of fluid-structure interaction over a small-size cylinder arrays which has representative mechanical properties of the whole system. Then this hydrodynamic force computed from micro-scale model was provided to the macro-scale model for computation of the complete geometry.

This multi-scale approach with homogenisation has been verified with a reference solution obtained by micro-scale simulation of equivalent system with arrays consisted by hundreds of cylindrical tubes. Good agreement was found indicating that it is valid for this large-scale geometry.

Also, simulation realised by coupling of NAVIER-STOKES equations and EULER-BERNOULLI equations with a rigid-body module implemented has been performed with Code_Saturn for simplified Phénix geometry [25].

Local model

The Ph.D. thesis of L. Sargentini [26] is focused on kinetic energy transfer between fluid and structure during core flowering and seismic events in order to improve the study on vibration phenomena of SFR core.

It is then conducted in three approaches: elaboration of analytical solution, development of numerical modelling and experiments.

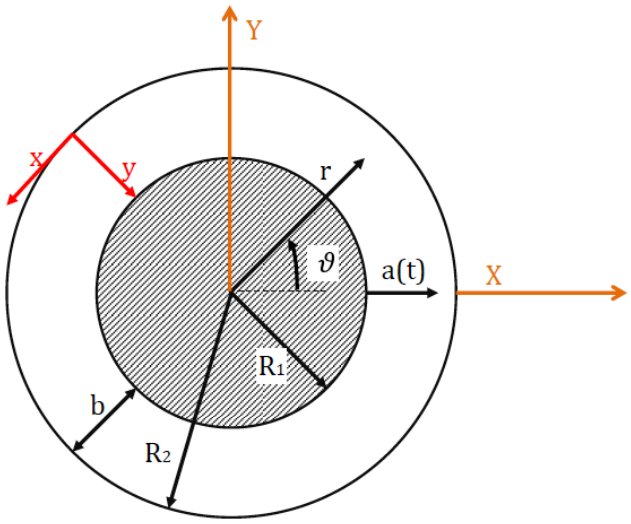

FIGURE 1.5: Cylindrical geometry

A flow regime map has been developed based on cylindrical geometry (see FIGURE 1.5) to identify flow regimes in the inter-assembly gaps at very short times scales (as SCRAMs) and longer time scales (as seismic events).

Several non-dimensional parameters have been introduced to describe the problem:

- Confinement parameter : $\eta = \frac{b}{R_2} \ll 1$;
- Amplitude parameter : $\epsilon = \frac{a_0}{b}$, where a_0 is the initial amplitude of the vibration, $0 \leq \epsilon \ll 1$;
- STROUHAL number : $\mathrm{St}_1 = \frac{R_1}{U/\omega}$, where U is the scale of velocity on x-direction, ω is the angular fluid velocity in the inter-assembly gap;

- REYNOLDS number : $\mathrm{Re} = \frac{Ub}{\nu}$;
- STOKES number : $\sigma = \frac{\omega b^2}{\nu} = \mathrm{ReSt}_1 \frac{\eta}{1-\eta}$, where ν is the dynamic viscosity ;
- Scale of pressure : $\frac{\delta p}{\rho U^2} = \sup\left\{\mathrm{St}_1, 1, \frac{1}{\sigma\epsilon}(= \frac{1}{\eta \mathrm{Re}})\right\}$.

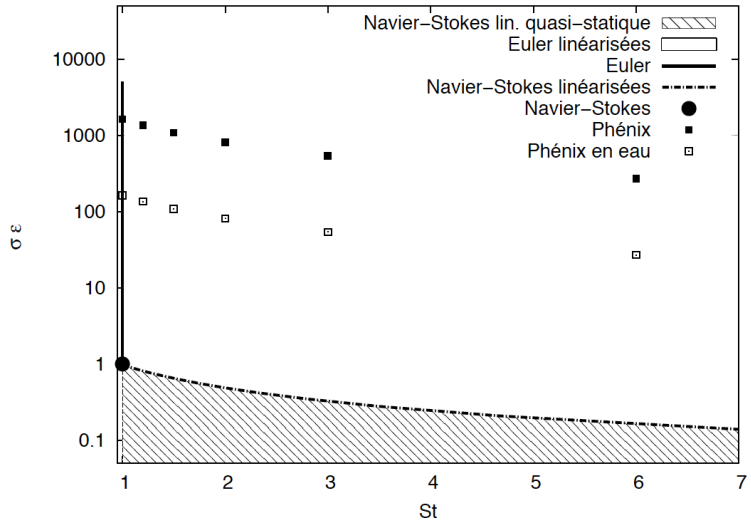

FIGURE 1.6: Flow map of incompressible viscous fluid around solid with strong confinement [26]

FIGURE 1.6 displays the flow map for incompressible viscous flow around a solid with strong confinement. The x-axis is STROUHAL number and the y-axis is $\sigma\epsilon$, which is inversely proportional to the viscous effects.

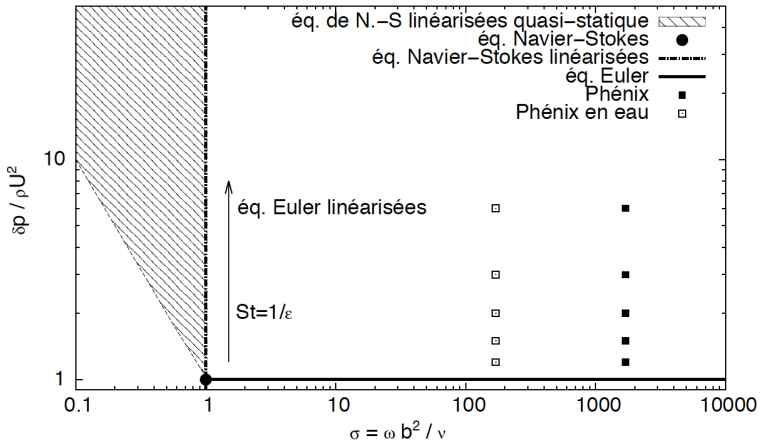

FIGURE 1.7: Pressure scales of incompressible viscous fluid around an oscillating solid with strong confinement

FIGURE 1.7 displays the flow map for incompressible viscous flow around an oscillating solid with strong confinement. The x-axis is STOKES number and the y-axis is $\delta p/\rho U^2$.

The flow map can be applied to choose the most suitable numerical model (NAVIER-STOKES, EULER, linearised EULER) for modelling of the fluid flow.

Besides, two small-scale experimental facilities, PISE-2C and PISE-1A, have been designed and constructed during her thesis. PISE-2C (see Chapter 3) is a multi-assembly test facility with 19 hexagonal assemblies distributed in 2 crowns. It has inter-assembly gaps at width = 3 mm, giving a representative horizontal scale of Phénix reactor core. PISE-1A (see Chapter 2) is a mono-assembly mock-up consisted of one hexagonal assembly and hexagonal outer container.

Free vibration tests on PISE-1A in water with different initial displacements varying from 0.5 mm to 2.5 mm have been performed to assess the effect of added mass and added damping. No results from PISE-2C has been obtained during L. Sargentini's thesis until the start of this Ph.D. thesis.

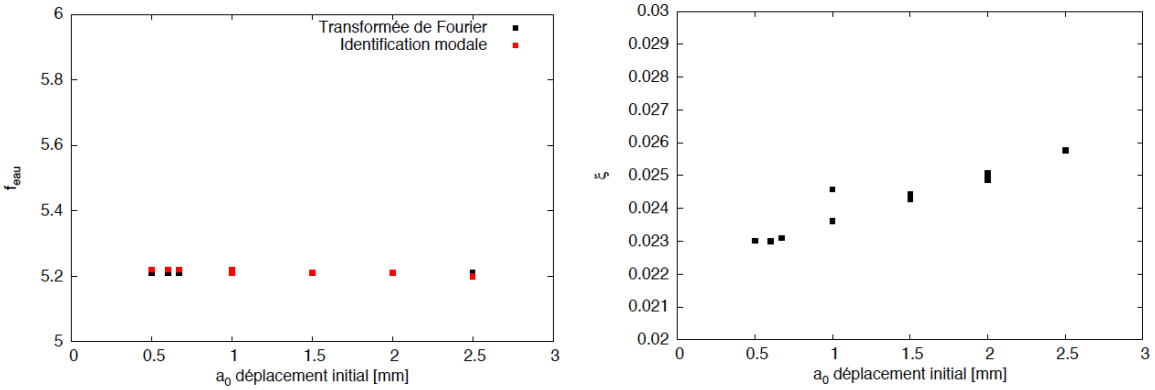

(a) Frequency (b) Damping coefficient

FIGURE 1.8: Frequency and damping coefficient with varying initial displacements [26]

2*D* NAVIER-STOKES model of incompressible viscous fluid has been implemented in CAST3M to simulate the free vibrations in both cylindrical and hexagonal geometry. The movement of the structure is described by a damped mass-spring system with one degree of freedom. The mechanical equation is then coupled with NAVIER-STOKES equation to represent the complete system. FIGURE 1.9 shows the comparison of experimental results with numerical results of CAST3M NAVIER-STOKES:

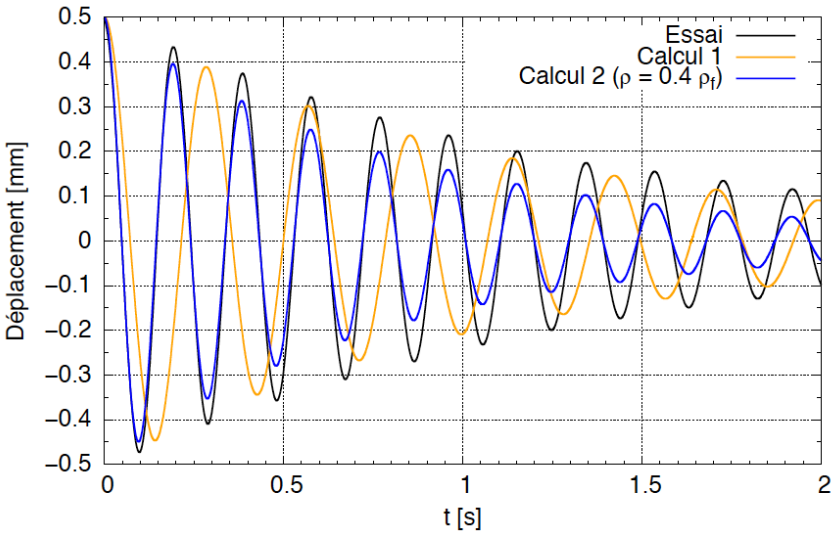

FIGURE 1.9: Comparison of numerical and experimental results [26]

Although the flow in PISE-1A is mainly $2D$, there are edge effects and $3D$ recirculation existing which are supposed to increase the frequencies. In $2D$ simulations, these effects are not taken into account. As shown in FIGURE 1.9 by the curve «Calcul 1», the numerical simulation gives a much lower frequency. Therefore, a decrease of fluid force by decreasing the fluid density has been applied (the curve «Calcul 2») to find a similar frequency as that in the experiments. This effect remained as an open question at the end of her thesis and needed to be validated by the experiments on PISE-1A with lower added mass, which can be realised by reducing the water height. Simulations with $3D$ $up\phi$ model have been conducted to look into the effects of added mass on vibration frequencies.

Also, master thesis by G. Artini [27] has paid efforts on evaluating the edge effects with $up\phi$ model in CAST3M based on PISE-1A geometry and visualisation of the recirculation in the inter-assembly gap with PIV technique. Fluid force is overestimated due to the fact that viscous effects is not considered in $up\phi$ model. The installation is shown in FIGURE 1.10. FIGURE 1.11 depicts the velocity filed captured from the PIV imaging after post-processing. Recirculation of flow can be clearly observed at the top and bottom of the hexagonal channel.

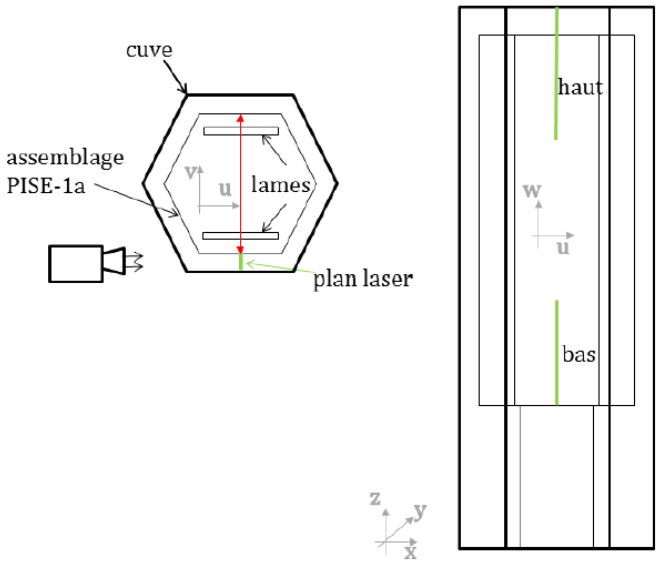

FIGURE 1.10: Installation of PIV [27]

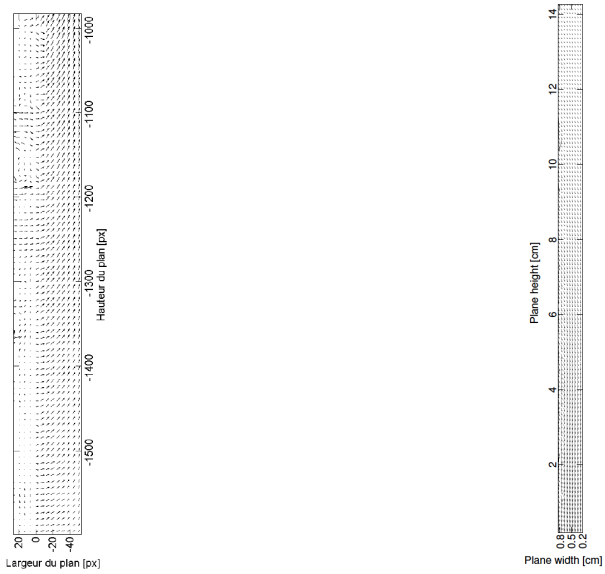

(a) Top (b) Bottom

FIGURE 1.11: Fluid velocity field visualised by PIV [27]

1.4 Scheme and Approaches

To progress in the knowledge of the fluid structure interaction phenomenon and better characterise the dissipation during dynamic behaviour of SFR core, it is necessary to develop analysis both numerically and experimentally.

The numerical approach applied so far in LATF is to try to approach the phenomena by local methods, developed at the micro-scale. These methods rely mainly on the NAVIER-STOKES EQUATIONS. The $up\phi$ model could not be tested during this thesis due to lack of time.

Two experimental facilities, mono-assembly test facility PISE-1A and multi-assembly test facility PISE-2C, were designed and implemented in CEA. Free-vibration experiments under different physical conditions and different modes of activation have been performed on these two test facilities.

For PISE-1A, to examine the dynamic behaviour of the mono-assembly mock-up with respect of varying added mass, a series of free-vibration experiments with the assembly released from a given position in different water heights has been performed. Besides, free-vibration experiments in water-glycerol mixture of varying mass fractions have been conducted to study the dynamic behaviour in liquids of different densities and viscosities. Also, injection experiments have been planned but have not be accomplished due to lack of time. Two parameters in ideal damper system, vibration frequency f and damping coefficient ξ, are introduced to describe the movements of the structure. Corresponding numerical simulations based on CAST3M code with $3D$ NAVIER-STOKES have been carried for both series of experiments. Both the experiments and the numerical approaches on PISE-1A will be discussed in Chapter 2. Moreover, coupling between the assembly and the container has been taken into account with a simplified cylindrical model as shown in Appendix B. Also the coupling between the assembly and base during free-vibrations in air is discussed with a mass-spring system of DOF (degree of freedom) at 2 in Appendix C.

For PISE-2C (see Chapter 3), as a multi-assembly mock-up with 2 crowns of assemblies (19 in total), free-vibration experiments modelling different modes of core flowering were performed, including total flowering, partial flowering (internal crown) and partial flowering (external crown). A reticulate model with reduced hypothesis has been developed in the effort of explaining the dynamic behaviour of PISE-2C during these experiments. Global parameters, for example, energies of the structure (potential, kinetic and total) and liquid volume contained in the mock-up, as long as symmetry indicators have been deducted from the displacement signal of the assemblies. These information will give us a clearer picture about the dynamic behaviour during the core flowering events.

The thesis will be organised in following structure:

- **Chapter 1 : Introduction**
  - Background
  - Objectives
  - State of the Art
  - Scheme and approaches
- **Chapter 2 : Experimental Approaches on PISE-1A and Corresponding Numerical Interpretation**
  - Introduction to PISE-1A
  - Free-vibration experiments on PISE-1A : in air, in water with varying water heights, in water-glycerol mixtures with varying mass fractions
  - Numerical simulations based PISE-1A experiments : numerical methodologies, data analysis methodologies, signal processing methodologies
  - Free-vibration experiments in air : for characterising structural parameters

  - Experiments with different water heights : frequency and damping coefficient (numerical results validated with experiments; velocity and energy
  - Experiments with water-glycerol mixture

- **Chapter 3 : Experimental and Analytical Approaches on PISE-2C**
  - Introduction to PISE-2C
  - Reticulate model : homogenised linear model for PISE-2C
  - Free-vibration experiments on PISE-2C : introduction to experiments including total flowering, partial flowering (internal crown), partial flowering (external crown)
  - Methodologies of analysis : displacement, velocity of assemblies, energies (single assembly, crown, whole mock-up), average outflow velocity, surface confined by assemblies' centres on external crown, indicators of symmetry
  - Total flowering : whole mock-up excited
  - Partial flowering (intern crown) : only internal crown excited
  - Partial flowering (external crown) : only external crown excited
- **Chapter 4 : Conclusions**
- **Appendix A : Analytical Analysis Based on Added Damping**
- **Appendix B : Oscillations of Two Cylinders Coupled by Fluid**
- **Appendix C : System of DOF at 2**
- **Appendix D : 3D effects : Recirculation Flow**
- **Appendix E : Analytical and Numerical Analysis on Two-dimensional Fluid Channel Model with Oscillating Wall and Continuous Injection**

Chapter 2

Experimental Approaches on PISE-1A and Corresponding Numerical Interpretation

To improve the study on fluid-structure interaction and flow behaviour during the vibration of assembly after initiating events, free-vibration experiments have been conducted on mono-assembly test facility PISE-1A under different physical conditions, including varying water heights, fluid densities and viscosities, allowing the code to reproduce the effect with these varying physical conditions. Corresponding numerical interpretations, with three dimensional Navier-Stokes model implemented in CAST3M code [28], have been performed for validation. However, the model implemented in CAST3M is not complete but with simplifications. Therefore, more analytical analysis should be made in supplementary to the numerical model.

Analytical model of spring-mass system with two degrees of freedom (Appendix C) has been taken into account to help explain the coupling movement of base and assembly during free-vibration experiment in air, which is not considered in numerical simulation. Moreover, coupling between container and assembly during free-vibration experiment in water has been treated with an analytical model in cylindrical geometry (Appendix B). This will help explain the discrepancies between the experiments and corresponding numerical simulations. Besides, analytical analysis on boundary condition transfer hasn't been examined.

In this chapter, we will look into both the experimental and numerical approaches.

2.1 Introduction to PISE-1A

PISE-1A (see FIGURE 2.1) is a mono-assembly test facility with an inter-gap of 7 mm width between the hexagonal assembly and the container. This gap width is higher than that of 3 mm in Phénix reactor core and multi-assembly test facility PISE-2C. But it still keeps a reasonably small magnitude to induce significant inertial effects while allows both easier visualisation of the fluid flow during oscillation and easier installation [29].

The PMMA made hexagonal assembly is connected to a horizontal metal plate by screws. Then it is welded to a twin-blade support which is fixed to a ground-fixed base by welding. An inlet nozzle is located at the middle height of the hexagonal assembly and six outlet nozzles are distributed radial-evenly allowing connection with a recirculation pump for planned injection experiments. The diameter of the inlet nozzle can be varied by using different inner orifice with diameter at 17.7 mm, 25 mm and 35 mm. The outer hexagonal container is fixed with the base by screws and connected with an upper water tank allowing total immerse of the assembly in liquid.

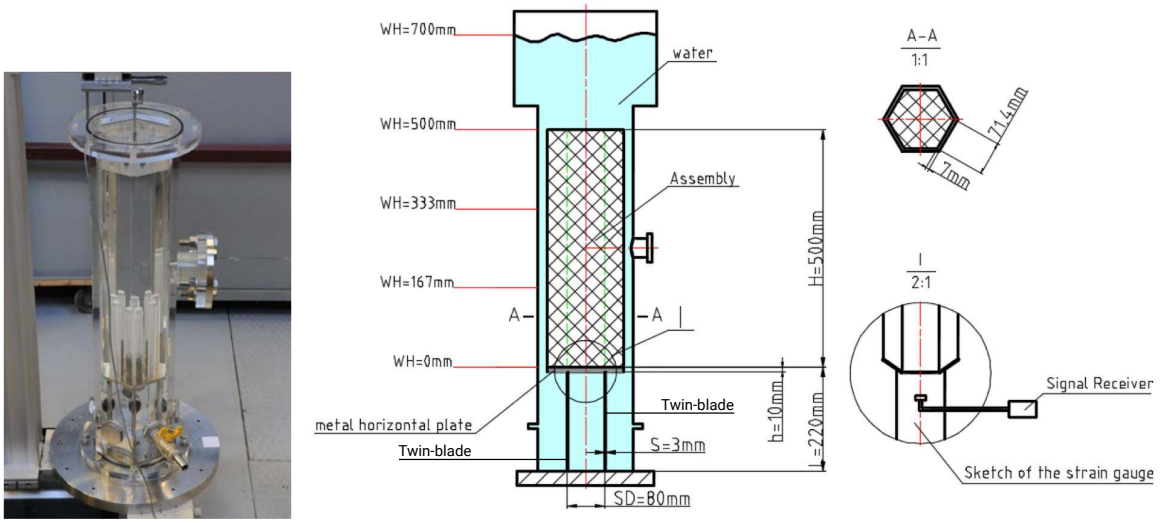

(a) PISE-1A (b) Scheme of PISE-1A

FIGURE 2.1: PISE-1A

During free-vibration tests, all the inlet and outlet nozzles will be shut to isolate the system.

To measure the displacement of the assembly during the experiments, a strain gauge is glued to the outer surface of the twin-blade support with an upward direction. As long as the deformation remains within the range of elasticity, the local deformation will be proportional to horizontal displacement of the plate of twin-blade support. The strain gauge implemented has a resistance of 120 Ω with a grid of 4.75$\times$4.57 mm. It is connected to a signal receiver then a PC to record the deformation signal. Calibration of the strain gauge was realised by verification with a laser displacement sensor. The laser sensor allows a measurement range of 20 mm at an average distance of 50 mm with a resolution at 0.025 μm. The assembly will be pulled to several given positions, both displacement measured by laser and deformation voltage measured by strain gauge would be recorded. The pulling force is not measured since the stress is not in interest. The calibration curve is shown in FIGURE 2.2. The displacement and deformation voltage are linearly correlated.

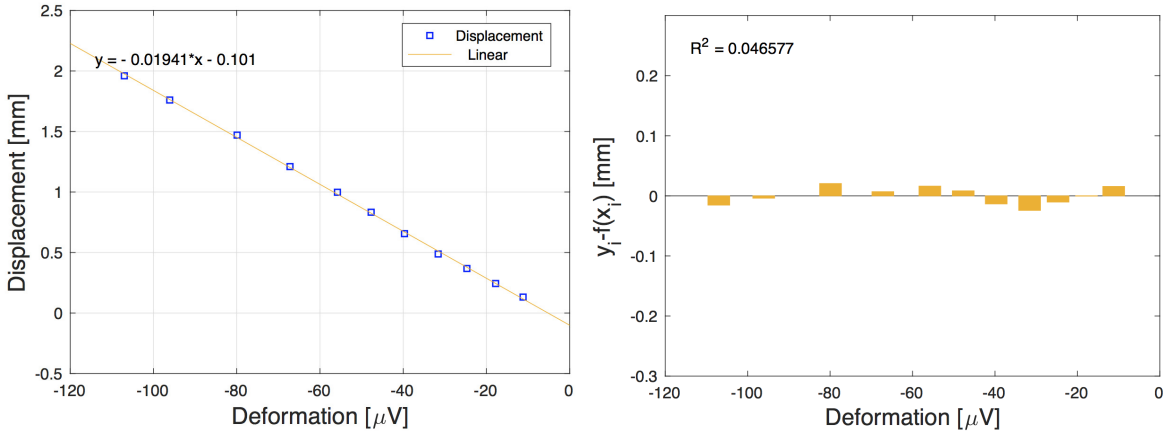

(a) Calibration curve (b) R^2

FIGURE 2.2: Calibration curve of strain gauge on PISE-1A

Therefore, the calibration factor will be -0.01941 mm/μV. $R^2 = \sum_{i=1}^{n}(y_i - f(x_i))^2$ is the residual sum of squares.

Here below TABLE 2.1 shows the weights of the PISE-1A's composites:

TABLE 2.1: Design weights of PISE-1A

m_{hex} [kg]	7.5	Hexagon mass
m_{lam} [kg]	2.4	Support blade mass
m_{vis} [kg]	0.5	Screws mass
m_{tot} [kg]	10.4	Total mass

Ratio of assembly's density to water density is different than that of assembly's density to sodium density in Phénix reactor core, meaning that the inertia of assembly in PISE-1A will be different from that of Phénix.

2.2 Free-vibration experiments on PISE-1A

Two series of free-vibration experiments have been performed to study the behaviour of flow and structure during free vibrations under different physical conditions. Also, to calibrate the structural parameters including stiffness and damping ratio, a series of free-vibration tests in air have been conducted .

The assembly will be pulled to a given initial position by a rope at the top of the assembly and then released to start the oscillation by cutting the rope suddenly. To determine the magnitude of initial displacement, several tests have been carried with initial displacement at around 1 mm and 3 mm respectively.

2.2.1 Free-vibration experiments in air

FIGURE 2.3 shows a typical test in air with an initial displacement of 3 mm.

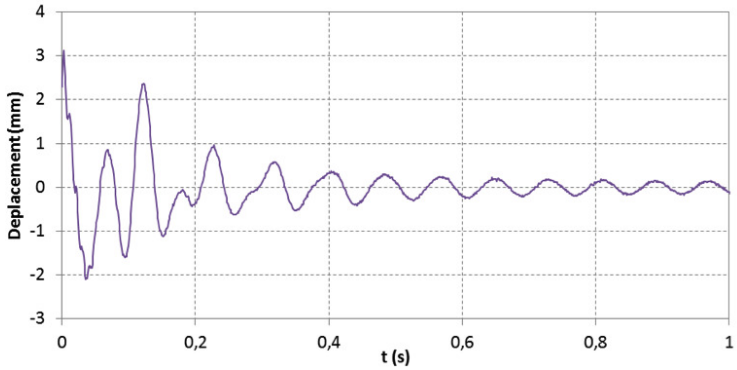

FIGURE 2.3: Time Evolution of Free Vibration Test in Air with Displacement around 3mm

At the beginning of the oscillation, irregular vibration signal coming from the shock of initiating cut has been recorded. This will affect the characterisation of both frequency and damping coefficient. Therefore, the experiments were preferred to be taken with smaller initial displacement to limit the influence from the initial cutting.

Five repeating tests in similar conditions were performed for repeatability. Due to difficulties in controling the initial displacement precisely, the initial displacements vary from 1 mm and 1.5 mm. FIGURE 2.4 shows the time evolution of the displacements. Noise from signal acquisition process exists. It will introduce uncertainties for calculation of structural parameters, especially damping coefficient.

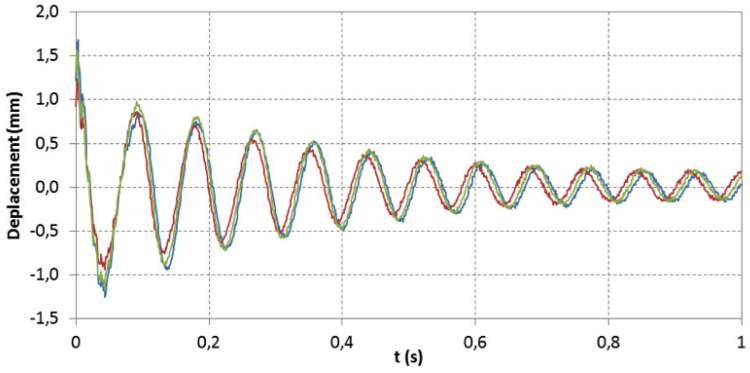

FIGURE 2.4: Time evolution of free vibration tests in air with displacement around 1mm

Since the air force acting on the assembly can be regarded as negligible when comparing to that in water and water-glycerol mixture, we can apply results from free vibration movement in air to obtain the best-approximate information of structural damping and stiffness.

2.2.2 Free-vibration experiments in water

To characterise the structural behaviour during free vibrations with increasing added mass by enhancing water heights, also in purpose of examining the edge effects, a series of free-vibration tests with different water heights was conducted on PISE-1A. Several different water levels have been chosen as:

- full water height with upper water tank filled

- full water height with empty water tank
- 2/3 of the assembly's height from the bottom of the assembly
- 1/3 of the assembly's height from the bottom of the assembly

If we take the reference plane at the bottom of the assembly, the four tests can be indexed as WH = 700 mm, 500 mm, 333 mm and 167 mm.

FIGURE 2.5 shows the experiments in water when WH = 167 mm.

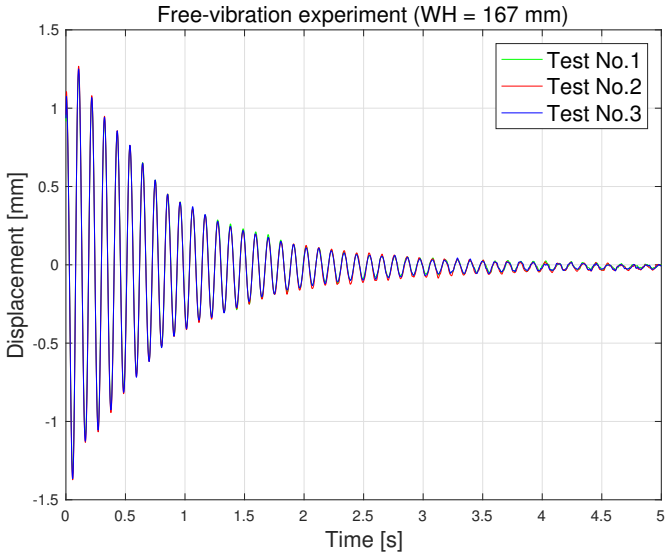

FIGURE 2.5: Time evolution of displacement (WH = 167 mm)

3 repeated tests has been performed with a duration of 5 s.

The repeatability in water is far more better than that in air as observed in the experiments.

2.2.3 Free-vibration experiments in water-glycerol mixtures

The second series is free-vibration experiments with different mass fractions of water-glycerol mixtures. With the mass fraction varies, both densities and kinetic viscosities vary. TABLE 2.2 shows the mass fractions of glycerol in the mixture and the corresponding densities and viscosities which were measured by a densimeter and viscosimeter respectively.

TABLE 2.2: Physical Properties of Water-glycerol Mixtures with Different Mass Fractions

Mass fraction (%)	ρ **(kg/m^3)**	**T (°C)**	ν **(m^2/s)**
0	1000	-	$1.01 \cdot 10^{-6}$
30	1070	25.8	$1.99 \cdot 10^{-6}$
40	1099	20.7	$3.38 \cdot 10^{-6}$
50	1126	20.9	$5.18 \cdot 10^{-6}$
60	1152	23	$8.66 \cdot 10^{-6}$
75	1194	22	$2.80 \cdot 10^{-5}$
81	1211	19.5	$5.64 \cdot 10^{-5}$
85	1220	21.4	$8.52 \cdot 10^{-5}$

FIGURE 2.6 displays the 6 repeated tests of the experiments with water-glycerol mixture of mass fraction at 30%.

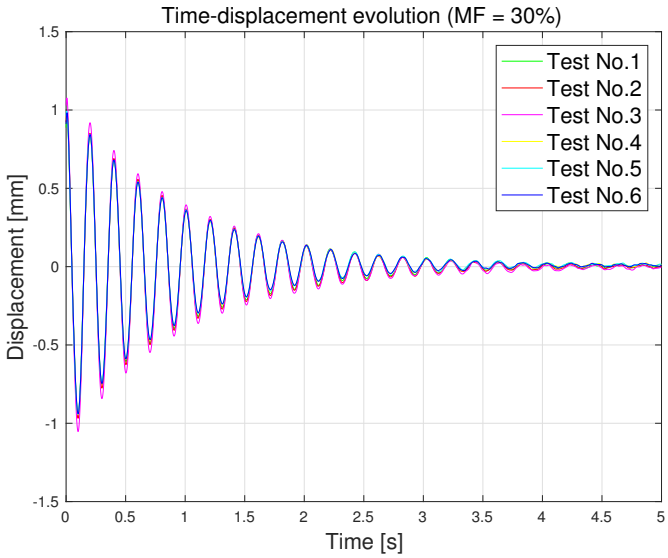

FIGURE 2.6: Time evolution of displacement (MF = 30%)

2.3 Numerical simulations based on PISE-1A experiments

Simulations corresponding to the experiments have been performed with 3-D Navier-Stokes model implemented in CAST3M code for interpretation and validation purpose. Numerical simulations does not take into account all the aspects of the experiments, for example, the coupling movement between assembly and base during free-vibration experiments in air and coupling between assembly and container during experiments in liquid.

2.3.1 Introduction to the numerical methodologies

2.3.1.1 Governing equations

Since the twin-blade support will limit the motion of the assembly to one single direction, we can apply a model of one-dimensional damped spring-mass system to describe the vibrating movement of the assembly. Therefore, in the case of free-vibration tests, there are two main equations involved: imcompressible 3-D Navier-Stokes equations for the description of fluid flow behaviour (Eq. 2.1) and mechanical equation for the motion of hexagonal assembly (Eq. 2.2). The two equations are coupled by the boundary fluid force acting on the assembly and boundary velocity of the hexagonal assembly.

- **Incompressible Navier-Stokes equations:**

$$\frac{\partial \mathbf{u}}{\partial t} + (\mathbf{u} \cdot \nabla)\mathbf{u} = -\frac{1}{\rho}\nabla p + \nu \Delta \mathbf{u}; \quad \nabla \cdot \mathbf{u} = 0; \tag{2.1}$$

- **1-D Mechanical equation:**

$$m_0 \ddot{x} + c_v \dot{x} + kx = F_f. \tag{2.2}$$

Here, m_0 is the mass in movement of the assembly.

FIGURE 2.7 shows the scheme of the blade when assembly is in movement. The blade can be divided into 8 equal layers (see FIGURE 2.7). The red schemes are the position when there is no deformation for the blade. The deformation of each layer is anti-symmetrical with respect to the vertical axis (black dash line) which passes the point of inflection. Layer 1 can be considered to be static. The deformation of layer 3&6, 4&5 have the same value but of different sign. Only the layer 2, 7 and 8 are involved in the movement with the assembly [26].

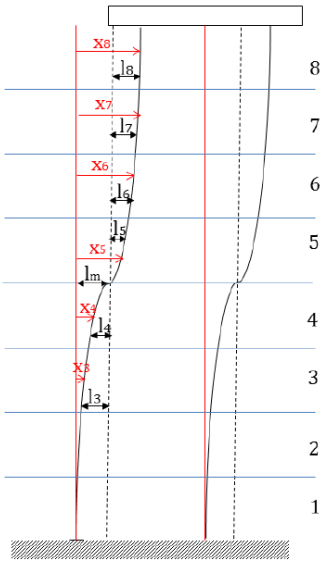

FIGURE 2.7: Scheme of the blade

Therefore, only 3/8 of the twin-blade support are considered to be involved in the vibration, $m_0 = m_{hexagon} + \frac{3}{8}m_{blade} + m_{supp} = 8.905$kg. m_{supp} is the sum mass of the additional parts including horizontal metal support and screws.

c_v is the structural damping ratio, k is the stiffness. They have been calibrated from the free vibration experiments in air.

F_f is the integral fluid force exerted on the assembly in x direction.

2.3.1.2 Boundary conditions

The outer vertical wall and the bottom of fluid domain is considered to be fixed with $\mathbf{u} = 0$. Non-slip condition has been applied.

The top surface of the fluid domain is set as free surface with a weak boundary condition $\oint p\mathrm{dA} = 0$ implied on momentum equation. Normal velocity on the free surface is supposed to be zero ($\mathbf{u} \cdot \mathbf{n} = 0$).

Velocity calculated from the mechanical equation Eq. 2.2 will be imposed on the fixed inner hexagonal mesh every time step simulating the movement of the assembly while the mesh was fixed.

2.3.1.3 Algorithms

First-order time scheme has been chosen to solve the Navier-Stokes equation meanwhile Newmark method with coefficient $\beta = 1/4$ and $\gamma = 1/2$ are used to deduct the displacement

from the mechanical equation Eq. 2.2. The Newmark method is at second order and is unconditionally stable in linear condition [30]. In our case, instead of resulting from the structural motion, the non-linearity mainly comes from the convective term of the fluid flow $(\mathbf{u}\cdot\nabla)\mathbf{u}$ in Eq. 2.1. Therefore, to avoid the instabilities, the Newmark scheme implemented in CAST3M have been modified from the original Newmark scheme to treat the non-linearity [31]. It can be expressed as:

$$\begin{cases} m_0\ddot{x}^n + c_v\dot{x}^n + kx^n = F_f^n \\ \tilde{k} = k + \frac{4m_0}{\Delta t^2} + \frac{2c_v}{\Delta t} \\ dx = \left(F_f^n + F_f^{n+1} - 2kx^n + \frac{4m_0}{\Delta t}\dot{x}^n\right)/\tilde{k} \\ x^{n+1} = x^n + dx \\ \dot{x}^{n+1} = \frac{2}{\Delta t}(x^{n+1} - x^n) - \dot{x}^n \\ \ddot{x}^{n+1} = \frac{1}{m_0}(F_f^{n+1} - kx^{n+1}) \\ F_f^{n+1} = \mathbf{e}_x \cdot \int_{\partial C}(-p\mathrm{I} + 2\mu\mathbf{D}) \cdot n d\mathrm{A} \end{cases} \tag{2.3}$$

Additionally, methods including implicit computation with under-relaxation of fluid force were taken to constrain further instabilities introduced by the coupling between the governing equations. We will discuss it in later section.

2.3.1.4 Mesh

As shown in FIGURE 2.1, the geometry of the fluid domain in the experiments can be viewed as three parts: the upper water tank, hexagonal channel and the lower water tank.

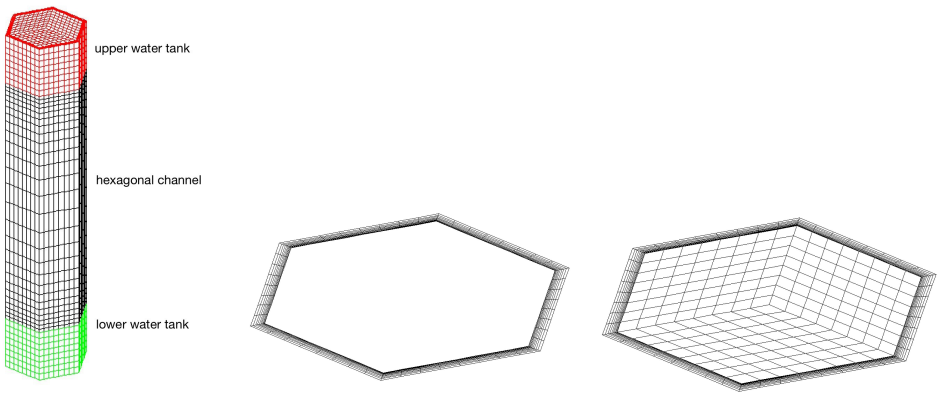

(a) Complete geometry (b) Horizontal hexagonal channel (c) Top free surface

FIGURE 2.8: 3-D mesh of PISE-1A

A 3-D mesh of PISE-1A of complete geometry is shown in FIGURE 2.8.

The inner hexagon represents the hexagonal assembly while the outer one represents the container of PISE-1A. Twin-blades support is not included in the geometry for the reason of simplification, however, as discussed above, 3/8 of the upper part's mass are considered in the total mass of assembly for the calculation of mechanical equation.

For better capture of the flow behaviour in the vicinity of the assembly, finer mesh was placed towards the inner hexagon horizontally in the hexagonal channel. Edge effects are

expected to happen on the top and bottom of the hexagonal channel, therefore element number is increased at these positions.

For the cases with lower water heights below the upper water tank, the geometry will only be composed of hexagonal channel and lower water tank. FIGURE 2.9 shows the mesh when water heights at WH = 167 mm.

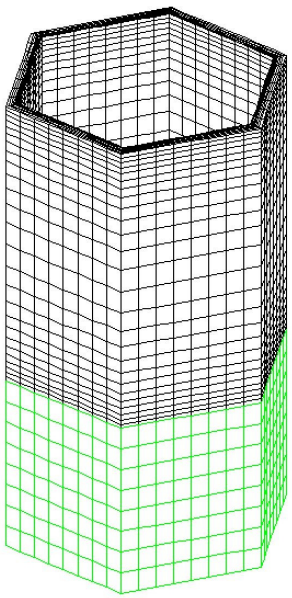

FIGURE 2.9: 3-D mesh of PISE-1A with WH = 167 mm

The geometry was meshed with hexahedron elements. Total element number involved for cases with different heights are shown in the following table:

TABLE 2.3: Mesh size of cases with different water heights

H [mm]	**700**	**500**	**333**	**167**
Number of Elements	2.2×10^4	1.8×10^4	1.8×10^4	1.8×10^4

With the geometry moved from full height with upper water tank filled to lower water heights, the free surface moves from the top free surface to top surface of the hexagonal channel. The total number of elements reduces due to removal of the upper water tank.

2.3.1.5 Stability

After solving the NAVIER-STOKES equations, the fluid force calculated will be input to the mechanical equation of current time step, structural velocity computed from the mechanical equation will be imposed to the inner hexagon as boundary condition for NAVIER-STOKES equation at next time step.

Therefore, for ith time step, the mechanical equation solved in the computation will be:

$$m_0\ddot{x}^i + c_v\dot{x}^i + kx^i = F_f^i.$$

However, the boundary condition of assembly's velocity imposed for the NAVIER-STOKES equation at ith time step has the value of $\dot{x}^{i-1}$ which is from the computation of $i-1$ time step.

This one time-step non-continuity between the Navier-Stokes equation and mechanical equation is the source of instability.

To limit this instability coming from the coupling between NAVIER-STOKES equation and mechanical equation without compromising much in the computation of mechanical equation, implicit method with under-relaxation of the fluid force has been implemented.

For ith time step, to limit the instability, a portion of fluid force at $(i-1)$th time step has been taken into account, controlled by a so-called under-relaxation factor w_1, $0 \leq w_1 \leq 1$:

$$F_f^i \mapsto w_1 F_f^i + (1 - w_1) F_f^{i-1}, \tag{2.4}$$

With w_1 decreases, the level of under-relaxation increases, more portion of fluid force from last time step $(i-1)$ will be taken into account in the calculation of current time step (i). With w_1 increases, the fluid force input to computation will be closer to fluid force at current step, thus the mechanical equation solved numerically will be closer to real mechanical equation. When $w_1 = 1$, there is no under-relaxation (real problem), while, when $w_1 = 0$, it is in full under-relaxation.

Implicit method has been implemented to reach the convergence $(x_{i+1} - x_i)/x_i$ of 10^{-6} for fluid force in the purpose to get a fluid force as close as the current value F_f^i. FIGURE 2.10 shows the convergence curve for the implicit method. After 20 iterations, it has already reached the margin of convergence.

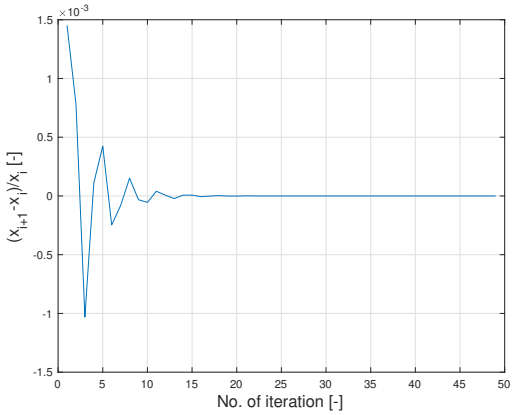

FIGURE 2.10: Convergence of implicit method

The instabilities will increase with increasing fluid force which is proportional to water heights, fluid densities and viscosities. Therefore, as water height increases, or the mass fraction increases, the under-relaxation level has to be increased (w_1 should be decreased). For water height at the lowest level (WH $= 167$mm), the calculation will be stable without under-relaxation. For WH=333 mm, it would be stable for $w_1 \leq 0.5$, while for full water height (WH=500mm or 700 mm), it would only be stable when $w_1 \leq 0.1$. For the cases with water-glycerol mixture, only $w_1 \leq 0.1$ will make the calculation stable. Also with the instabilities increases, the rate of convergence will decrease therefore the iterations need for converging will increases.

2.3.1.6 Comments

The numerical model is based on a simplified geometry comparing to that of the real geometry of PISE-1A. The structure of twin-blade support is neglected with the $3/8$ of the mass

added to the mass in motion m_0. From the observation of vibration frequency and damping coefficient in free-vibration experiments with and without the upper water tank filled, no obvious difference has been found. We can suppose that the shape of upper tank does not affect the movement of the assembly and the flow behaviour much. Therefore, for simplification reason, the edges of the upper water tank has been simplified to the same dimension as the hexagonal container.

As stated in boundary condition, velocity of assembly is imposed on a fixed mesh, in other words, effects of boundary transfer is not taken into account in the numerical model. Since the initial amplitude is as big as $1/7$ of the width of channel, boundary transfer may affect the dynamic behaviour. Analytical model shall be developed to improve understanding of this phenomena.

In the numerical simulations, the coupling of the assembly with base during movement in air has not been considered (Appendix C). Also the coupling of the assembly with outer container during vibration in liquid is not taken into account (Appendix B). The former will introduce uncertainties when characterising structural parameters while the latter will affect the damping coefficient and frequency of free-vibration experiments in liquids.

2.3.2 Introduction to data analysis methodologies for frequency and damping coefficient

Take the scaling as defined following in Eq. 2.5:

$$t = \tau\bar{t}, \quad x = x_0\bar{x}, \quad F_f = F_0\bar{F}. \tag{2.5}$$

Here, τ, x_0, F_0 are scaling parameters for time, displacement and fluid force respectively. $F_0 \geq |F(t)| \geq 0, \;\; x_0 \geq |x(t)| \geq 0$.

Therefore, Eq. 2.2 can be translated into:

$$\frac{m_0}{k\tau^2}\ddot{\bar{x}} + \frac{c_v}{k\tau}\dot{\bar{x}} + \bar{x} = \frac{F_0}{kx_0}\bar{F}. \tag{2.6}$$

As the displacement of the assembly will be the driving source of all the movement:

$$\sup\left\{\frac{m_0}{k\tau^2}, \frac{c_v}{k\tau}, \frac{F_0}{kx_0}\right\} \sim 1.$$

When the fluid force is 0, the free vibration will mainly be driven by inertial force and convective force. These two terms will be determined by two time scales according to Eq. 2.6:

$$\tau_m = \sqrt{m/k}, \;\; \tau_c = c_v/k; \tag{2.7}$$

Fluid force should be at the same order with the resilience force, therefore, it can be suggested that $F_0 = kx_0$. We can introduce a characteristic stiffness defined as:

$$k_0 = F_0/x_0. \tag{2.8}$$

The equation will then be transformed as:

$$\frac{\tau_m^2}{\tau^2}\ddot{\bar{x}} + \frac{\tau_c}{\tau}\dot{\bar{x}} + \bar{x} = \frac{k_0}{k}\bar{F}. \tag{2.9}$$

Vibration frequency and damping coefficient can be expressed as:

$$f_n = \frac{1}{2\pi}\sqrt{\frac{k}{m}} = \frac{1}{2\pi\tau_m}, \quad \omega_n = 2\pi f_n, \quad \xi = \frac{c_v}{2\sqrt{km}} = \frac{\tau_c}{2\tau_m}. \tag{2.10}$$

Therefore, the structural stiffness and damping ratio can be calculated as:

$$k = 4\pi^2 m f_n^2 = m\omega_n^2, \; c_v = 2\xi\sqrt{km}. \tag{2.11}$$

To carry out optimised analysis on both experimental and numerical results, three different methodologies for data analysis have been tested with repeated tests of free-vibration experiments in air.

Two parameters, namely damping coefficient ξ and vibration frequency f, will be introduced to characterise the oscillating behaviour as weakly damped oscillator in ideal damper frame [32]. In fact, the reality is much more complex, instead of being constant, the two parameters are functions of time (see FIGURE 2.20). Therefore, the damping coefficient ξ and vibration frequency f shall be taken as just indicators of dissipation effects in the system.

The three different methodologies are regression method, ERA method and FFT method respectively.

2.3.2.1 Regression method

For homogenous equation in ideal damper frame,

$$\ddot{x} + 2\xi\omega_n\dot{x} + \omega_n^2 x = 0, \tag{2.12}$$

when $c_v > 2\omega_n m_0$, the oscillation is under-damped, therefore the solution can be written as:

$$x(t) = Ae^{-\xi\omega_n t}\sin(\omega_d t - \phi). \tag{2.13}$$

The frequency of vibration can be expressed as $f = \frac{\omega_d}{2\pi} = \frac{\sqrt{1-\xi^2}\omega_n}{2\pi}$, characteristic damping time $\tau = 1/(\xi\omega_n) = 2m_0/c_v$.

Therefore, when analysing the displacement of assembly during free vibration tests, a function as the same form of Eq. 2.13 was used for regression purpose. Damping ratio ξ and vibration frequency f can be obtained from this procedure.

However, the experimental signal is not exactly a harmonic solution as stated in the homogeneous problem. Moreover, with the unavoidable introduction of noises, the regression method will introduce a large amount of uncertainties since it will be highly sensitive to the choice of peaks.

2.3.2.2 ERA method

ERA is in abbreviation of Eigensystem Realisation Algorithm. It can be used as a modal analysis technique and generates a system realisation using a time domain response. It is used for modal parameter identification and model reduction for dynamical systems from test data. The algorithms consists of two major parts, namely, basic formulation of the minimum-order realisation and modal parameter identification [33].

In the section of the basic formulation, state-variable equations has been defined for a finite dimensional, discrete-time, linear, time-invariant dynamical system as:

$$x(k+1) = Ax(k) + Bu(k). \tag{2.14}$$

$$y(k) = Cx(k). \tag{2.15}$$

A finite dimensional, discrete-time, linear, time-invariant dynamical system has the state-variable equations:

$$x(k+1) = Ax(k) + Bu(k). \tag{2.16}$$

$$y(k) = Cx(k). \tag{2.17}$$

Where x is an n-dimensional state vector, u an m-dimensional control input and y a p-dimensional output or measurement vector. The integer k is the sample indicator. The transition matrix A characterises the dynamics of the system.It is a representation of mass, stiffness and damping properties.

Moreover, the uncertainty coming from the presence of almost unavoidable noise and structural nonlinearity will be treated with modal parameter identification and modal reduction. Two indicators, modal amplitude coherence γ and modal phase collinearity μ, have been introduced to quantify the system and noise modes. Then the reduced system model will be determined based on the accuracy indicators. After reconstructing the function and comparing with the measurement data, it will give the right minimum-order realisation with respect to the affect of noise from which we can extract the vibration frequency f and damping coefficient ξ.

2.3.2.3 FFT method

To process the data, the full data sets were expanded to a length of 10000 data points (10s in sampling time considering sampling frequency as 1000 Hz) by zero-padding.

Fast Fourier Transform method with Hanning filter to remove the influence of noise was used as for analysis of frequency and damping coefficient.

Take an underdamped oscillator as example,

$$a(t) = e^{-\gamma t}\cos(\omega_0 t + \phi)\theta(t), \tag{2.18}$$

where the unit step function is defined by

$$\theta(t) = \begin{cases} 1, & t > 0 \\ 0, & t \leq 0 \end{cases} \tag{2.19}$$

After Fourier transform,

$$\overline{A}(\omega) = \frac{1}{2\pi i}\frac{\omega - i\gamma}{(\omega - i\gamma)^2 - \omega_0^2} \tag{2.20}$$

Therefore, with the vibration frequency found at $f_{max} = \omega_{max}/2\pi$, damping coefficient can be calculated $\xi = \Delta f/(2f_n)$ where $\Delta f = f_{right} - f_{left}$, $f_n = f_{max}$ is the full width at half height (FWHH) as shown in FIGURE 2.11 [34].

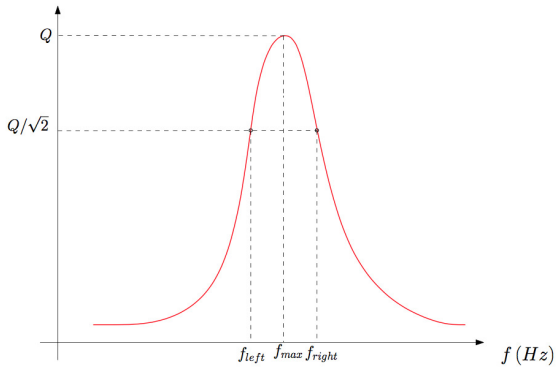

FIGURE 2.11: FFT method for analysis of frequency and damping coefficient

2.3.3 Methodologies of signal processing

Before starting analysing, the raw signal data collected from the experiments have to be processed in order to remove unwanted noise and deduct the velocity information from the time-displacement curve.

Several digital filters have been implemented and tested in Matlab scripts to process with the raw experimental signal.

2.3.3.1 Butterworth filter

The Butterworth filter is a type of signal processing filter designed to have as flat a frequency response as possible in the passband [35].

The gain $G(\omega)$ of an n-order Butterworth low pass filter is given in terms of the reader function $H(j\omega)$ as:

$$G_n^2(\omega) = |H(j\omega)|^2 = \frac{G_0^2}{1 + (\frac{j\omega}{j\omega_c})^{2n}}, \tag{2.21}$$

Where, n is the order of filter, ω_c is the cutoff frequency, G_0 is the DC gain (gain at zero frequency).

Here in our case, a 2nd-order low-pass Butterworth filter with a cut-off frequency at 50 Hz was implemented. Since the acquisition frequency is 1000 Hz, the Nyquist frequency at 1000/2 = 500 hz, the normalised cut-off frequency will be $\pi * 50/(1000/2) = 0.1\pi$ rad/s. FIGURE 2.12 shows the magnitude response of this low-pass Butterworth filter.

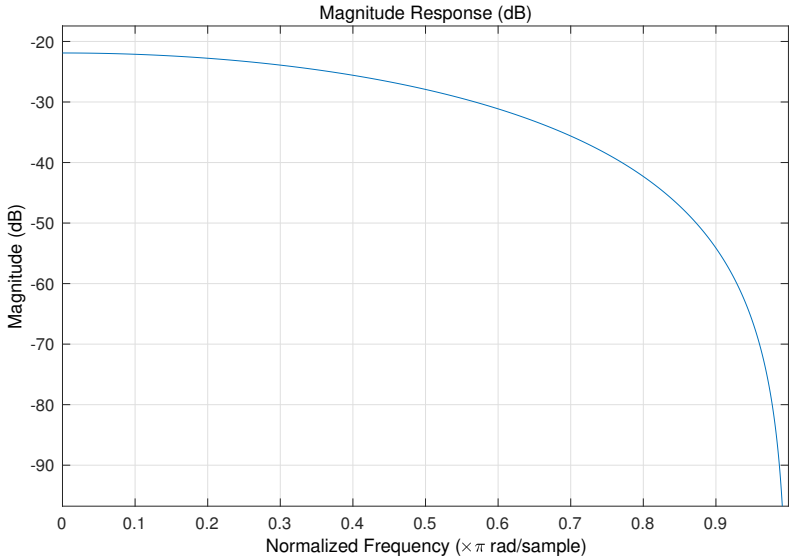

FIGURE 2.12: Magnitude response of low-pass Butterworth filter

Zero-phase filtering with 2nd-order low-pass Butterworth filter has been implemented. It is realised by processing the input data in both forward and reverse directions. This will help to preserve the features in the filtered signal at the exact time where they occur in the original signal helping us to deduct the velocity from the time-displacement signal [36, 37]. FIGURE 2.13 displays the comparison of original input data, zero-phase filtered data with low-pass Butterworth filter and non zero-phase filtered data with the same filter. Here, the original input data used is free-vibration experiments of PISE-1A in air.

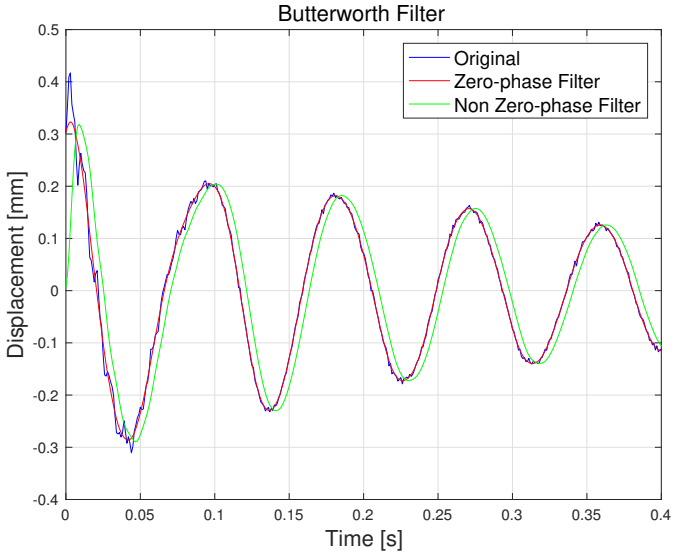

FIGURE 2.13: Comparison of zero-phase filtering and non-zero filtering

A phase lag from the original input data to that with non-zero phase filter can be seen while the signal filtered with zero-phase filter is perfectly in phase with the original input signal with the high-frequency noise removed. When applying Fourier transform to the

original data and that filtered with zero-phase low-pass Butterworth filter, the frequency responses are shown in FIGURE 2.16.

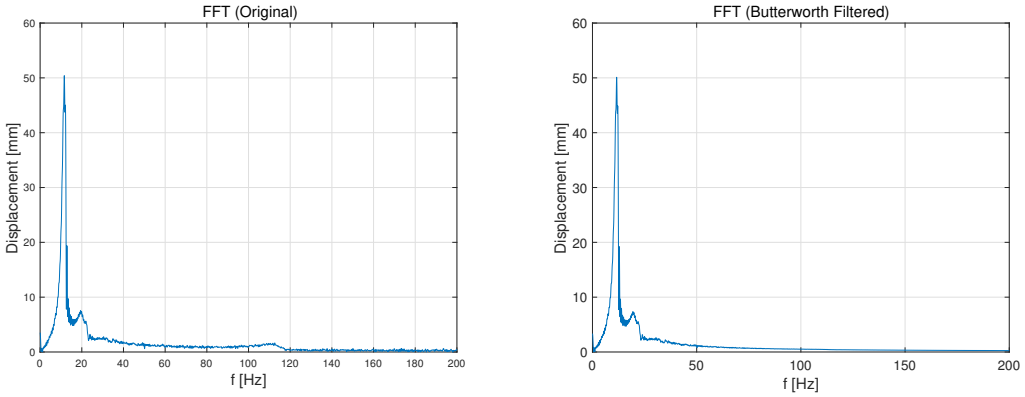

(a) Original (b) Butterworth filtered

FIGURE 2.14: Fourier transform of original data and Butterworth filtered data

In this case, vibration signal in our interest concentrated around the highest frequency at 11.6 Hz. Comparing original signal and Butterworth filtered signal, little difference can be found in the range from 0 to 20 Hz. Only unwanted high-frequency noises are eliminated from the signal. Therefore, it can be concluded that this zero-phase low-pass Butterworth filter is effective.

2.3.3.2 Hanning filtering

A Hanning filter [38] has been implemented in the frequency domain for more accurate filtering. Here is the function of this Hanning filter shown below:

$$\begin{cases} \mathrm{M} = 1, & 0 \leq f \leq 45 \\ \mathrm{M} = \cos(pi * (f - 45)/40)/2 + 0.5, & 45 \leq f \leq 85 \\ \mathrm{M} = 0, & 85 \leq f \sim \infty \end{cases} \tag{2.22}$$

The cut-off frequency is at 50 Hz. From 0 to 45 Hz, the magnitude amplifier is at 1 to assure all the signals in this passband will be preserved. For frequency higher than 55 Hz, the magnitude amplifier is set at 0 to form the stop band. Since this filter is applied directly on frequency domain, it is zero-phase shift filter. FIGURE 2.15 displays this Hanning filter in frequency domain.

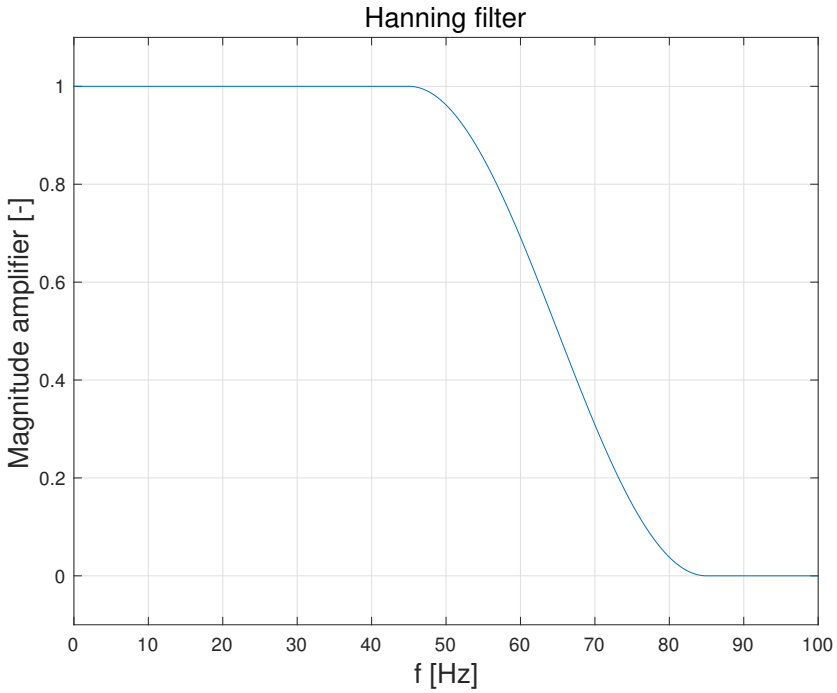

FIGURE 2.15: Hanning filter in frequency domain

With this filter, the frequency responses of the original data and the filtered data are displayed in FIGURE below:

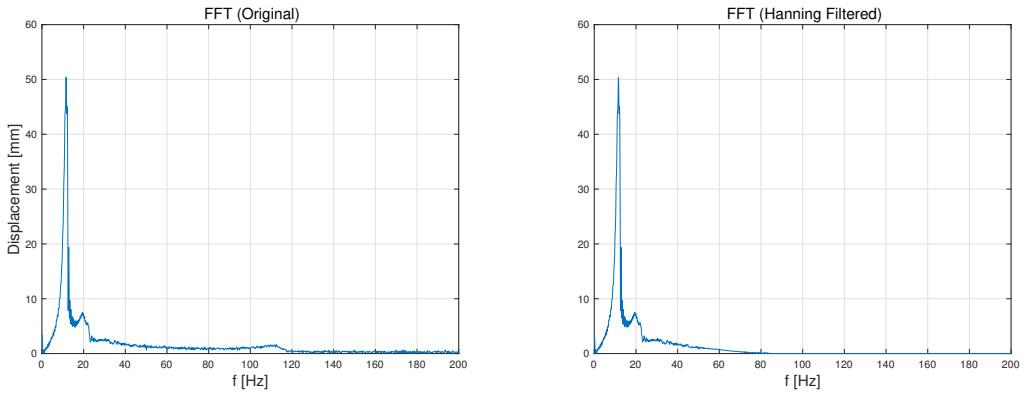

(a) Original (b) Hanning filtered

FIGURE 2.16: Frequency response of original data and Hanning filtered data

Little difference occurred between the original signal and the filtered data before the cut-off frequency at 50 Hz. All the noise with frequency higher than 85 Hz has been removed. Therefore, we can conclude that this filter is efficient in preserving the important information in interest while removes completely the high-frequency noise.

After filtering and inverse Fourier transform, the filtered signal will be:

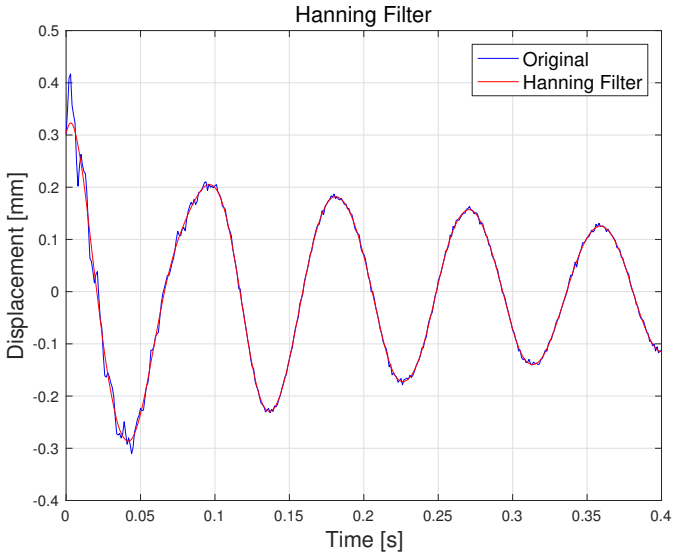

FIGURE 2.17: Hanning filtered displacement

Both of the two filters are efficient in filtering the noise and preserving the signal in interest. Also these two kinds of filters are almost equivalent in applications.

2.4 Methodologies of analysis on velocity and energy of PISE-1A

As discussed in above section, filtering for original signals enables us to obtain smoother filtered time-displacement for further processing to deduct information of velocity and energy.

2.4.1 Velocity

Velocity was deducted from the time evolution of displacement with 2nd-order time scheme [39].

$$\dot{x}_n = \frac{3x_{n+1} - 4x_n + x_{n-1}}{2\Delta t} \tag{2.23}$$

Where $\dot{x}_n$ and x_n are the velocity and displacement at t (nth step) respectively.

2.4.2 Energy

Time evolution of kinetic, potential and total energy can be calculated with displacement and velocity as:

$$e_k(t) = \frac{1}{2} m_0 \dot{x}(t)^2; \quad e_p(t) = \frac{1}{2} k x^2(t); \quad e_t(t) = e_k(t) + e_p(t); \tag{2.24}$$

Here, $e_k(t)$, $e_p(t)$ and $e_t(t)$ are kinetic energy, potential energy and total energy at time instant t respectively.

2.5 Free-vibration experiments in air

As introduced above, four repeated tests of free-vibration experiments in air have been conducted to calibrate the structural stiffness and damping ratio with a duration of 5 s and initial displacement at around 1 mm.

2.5.1 Frequency and damping coefficient

To get a more accurate prediction of the physical structural parameters, for free vibration tests in air, all three data analysis methodologies have been applied to calculate the vibration frequency and damping coefficient for all four repeated tests. The range of the data for the same group of tests are shown in FIGURE 2.18.

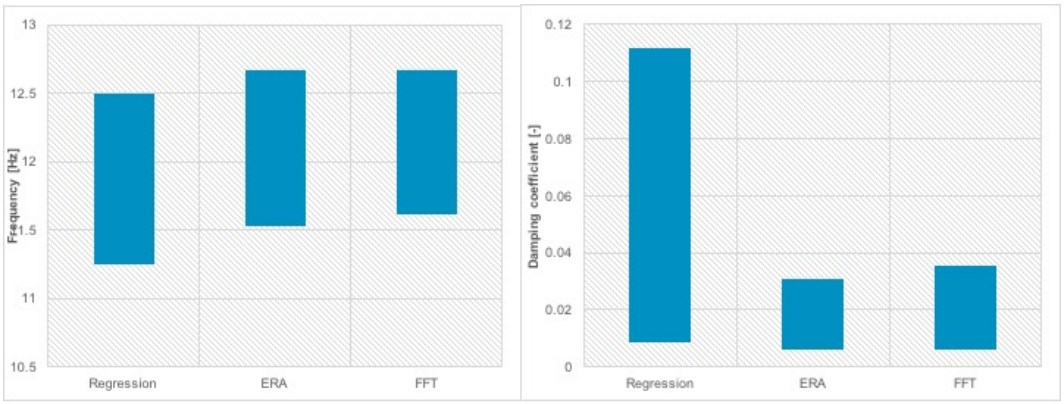

(a) Range of vibration frequency (b) Range of damping coefficient

FIGURE 2.18: Comparison of data analysis methodologies with results of free vibration tests in air

For frequency, all three methods have similar performances. While for damping coefficient, the results of the three different methodologies show big discrepancies. Comparing to ERA method and FFT method, regression method has a much larger range of damping coefficient. This may due to the high dependancy of regression method on choices of the peak points. ERA method slightly outperforms FFT method when comparing the range of damping coefficient. The spectrum of experimental data after fast Fourier transform is not as smooth as shown in FIGURE 2.11 but with several lower peaks distributed (see FIGURE 2.19) . This may be the factor that compromises the performance of FFT methods when calculating the damping coefficient. Therefore, when choosing the reference value for calculating the structural parameters, results from ERA method were considered.

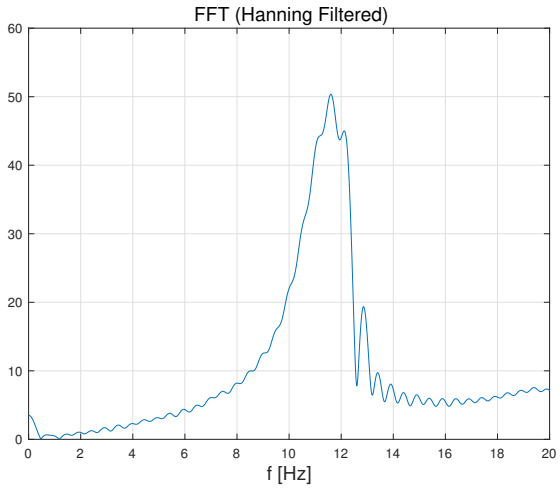

FIGURE 2.19: Spectrum of one experiment in air (Hanning filtered)

Therefore, results of frequencies and damping coefficients calculated with ERA method were chosen to be the reference result for calibrating the structural parameters.

There is a tendency of increasing frequency and decreasing damping coefficient with time evolution during the whole test period.

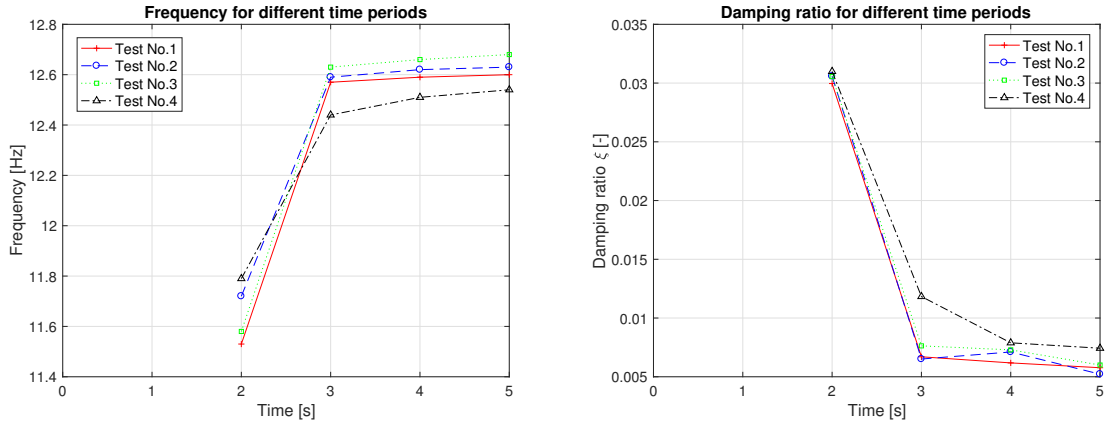

(a) Frequency

(b) Damping coefficient

FIGURE 2.20: Comparison of frequency and damping coefficients for different periods

FIGURE 2.20 shows the frequency and damping coefficient calculated with ERA method for different time periods during the four repeated tests in air. For each time point, the results were obtained using the signal during the previous 1s. The value of frequency and damping coefficient are clearly varying with time which is in contrast with the assumption of ideal damper system. For all four tests, frequency results are increasing with time evoluted while damping coefficient is decreasing with time goes by. Although the initial displacement has an amplitude as small as 1 mm but considering the displacement to channel width ratio ($\sim 1/7$), it's relatively big. This may affect the oscillation after releasing. The first results have the most discrepancies with the ones after. This may due to the reduction

of non-linearities occurring at the start of the tests with time which results from the convective force that is proportional to the displacement. Therefore, it is more reasonable to use the frequency and damping coefficient from the later period to represent the real structural vibration. Considering the effect of noise, the reference period was chosen between 3s to 4s.

Therefore, the input structural stiffness $k = 56019$ N/m and damping ratio $c_v = 7.378$ kg/s. The mechanical equation (Eq. 2.2) input can be written as:

$$8.905 * \ddot{x} + 7.378 * \dot{x} + 56019 * x = F_f. \tag{2.25}$$

The results of numerical simulations are highly dependant on the structural physical parameters input in the mechanical equation. The uncertainty from calibrating the structural vibration frequency and damping coefficient will lead to uncertainty of structural damping and stiffness, eventually lead to uncertainty of the numerical results.

To conclude, considering the time-varying frequencies and damping coefficients calculated from one single experiments, as well as discrepancies among repeating tests, also taking into account the fact that the numerical simulation is highly dependant on the input structural parameters derived from the free-vibration experiments in air, the value of the frequency and damping coefficients may not be as interesting as the varying trend.

2.5.2 Velocity and energy

Time evolution of the assembly's velocity from beginning of the vibration to 1 s for all four repeated tests is shown in FIGURE 2.21.

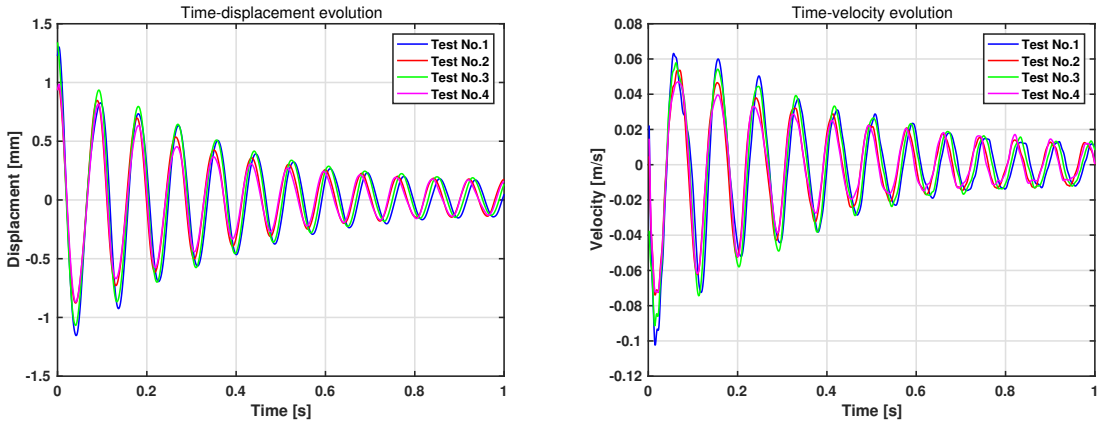

(a) Time-displacement evolution

(b) Time-velocity evolution

FIGURE 2.21: Time evolution of displacement and velocity (free vibration in air)

Displacement signals has been cut to a certain time instant to remove the first part of signals which are significantly affected by initial cut. Therefore, the displacements don't start exactly from the initial amplitude, the initial velocities are not exactly at 0.

Difference of maximum magnitudes comes from variation of initial displacement. Slight discrepancies in phase results from the varying vibrating frequencies.

With the velocity and displacement, we can calculate the potential energy and kinetic energy according to Eq. 2.24. Here below, FIGURE 2.22 shows the time evolution of kinetic energy, potential energy and total energy for the four repeated tests.

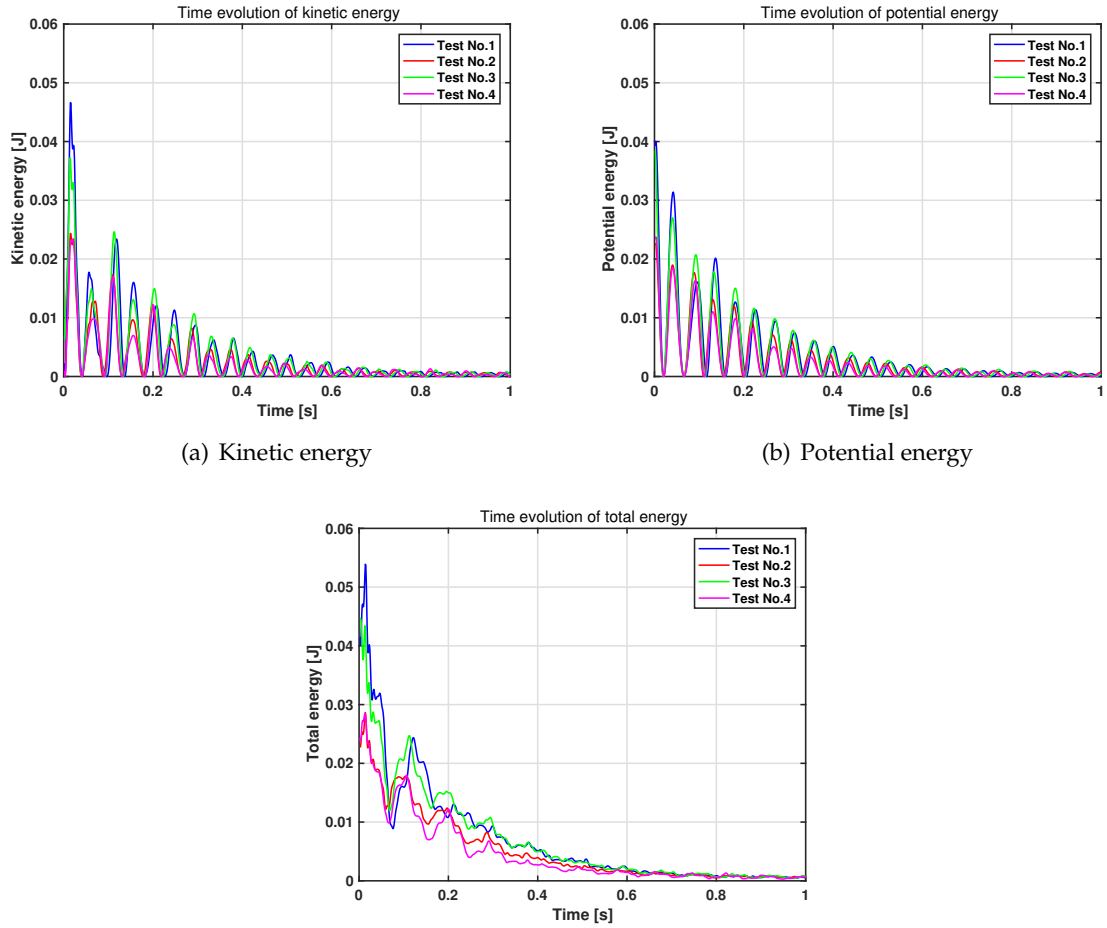

(a) Kinetic energy

(b) Potential energy

(c) Total energy

FIGURE 2.22: Time evolution of energy (free vibration in air)

As introduced above, the signals don't start exactly from the beginning of the movement, therefore, there are increase of total mechanical energy at the beginning of the signal.

At the beginning of the vibration, almost all the energies are contained as potential energy inasmuch that the starting velocities are close to 0. In the first quarter of period from 0 s to 0.02 s, kinetic energy of the assembly continued to increase to the maximum while the potential energy fell to 0. For a system when there is no coupling between the assembly and the base, the total energy of the assembly should be dissipated continuously as presented in the homogenous problem in the following section.

To understand this variations, for the free-vibration experiments in air, it is possible to simplify the coupling problem of assembly and base into a mass-spring system with 2 degrees of freedom (see Appendix C). This simplified problem will give time evolution of energies as shown in FIGURE 2.23:

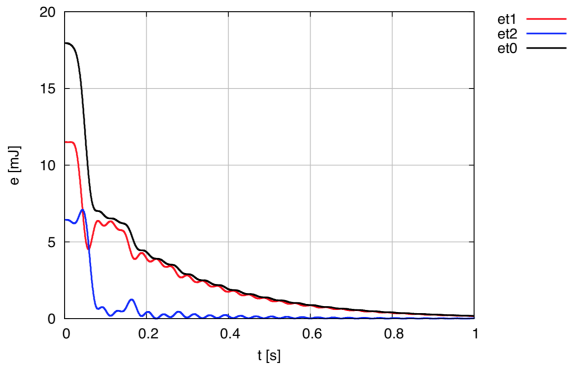

FIGURE 2.23: Energy evolution (analytical solution)

Here, e_{t1} is the total energy of the assembly. Oscillations of total energy can be observed at the beginning of the movement. However, it diminishes after several periods of vibrations. This is compatible with what displayed by the experiments. Therefore, we can conclude that the oscillation in total mechanical energy of the assembly during the first several periods results from the coupling of the assembly and base.

For all four repeated tests, most portions of total energy got dissipated after 0.6 s (around 7 periods of vibrations).

There are discrepancies between the four repeated tests. Variation of initial energy results from varying initial displacement.

2.5.3 Homogeneous problem

With the structural damping ratio and stiffness calculated for Eq. 2.2, supposing the assembly is vibrating in vacuum, we will be reaching a homogeneous problem Eq. 2.12. The solution to this equation is Eq. 2.13.

Therefore, we can plot the displacement and velocity evolution as following FIGURE 2.24:

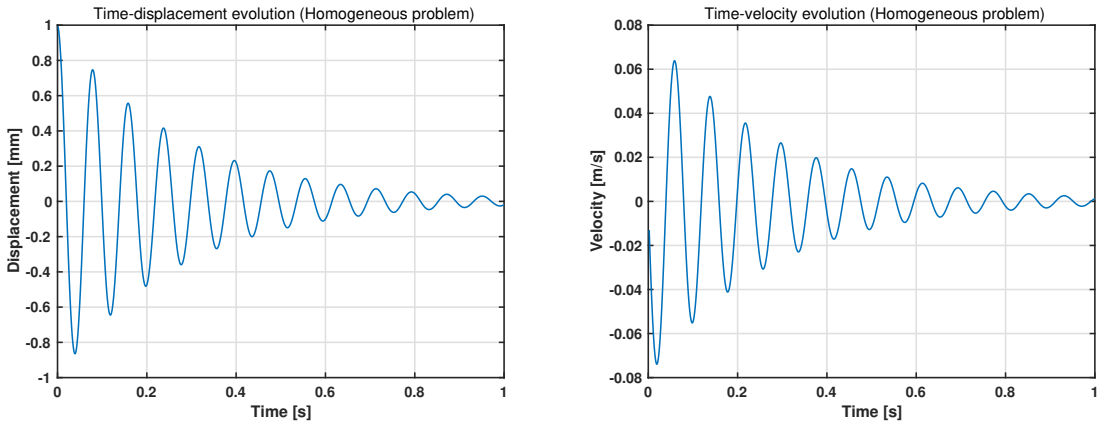

(a) Displacement (b) Velocity

FIGURE 2.24: Time evolution of displacement and velocity (homogeneous problem)

Evolutions of kinetic, potential and total energy are displayed in FIGURE 2.25:

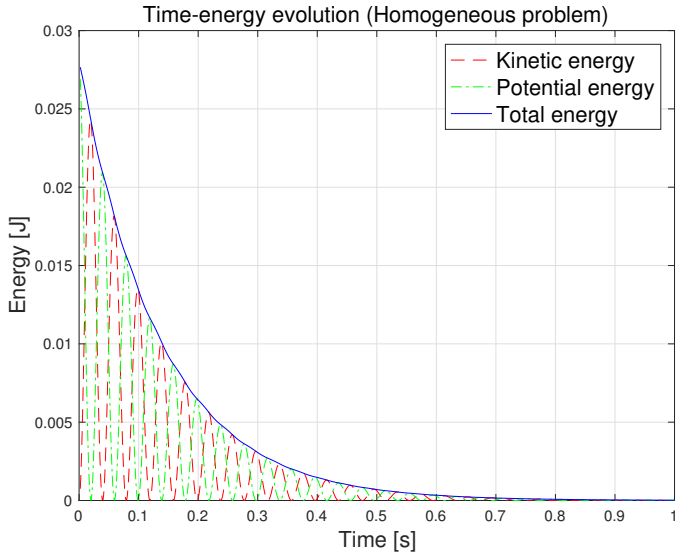

FIGURE 2.25: Time evolution of energy (homogeneous problem)

Maximum kinetic energy is at similar magnitude as potential energy. Total mechanical energy of the assembly can no longer transfer into mechanical energy of the surrounded air flow, therefore, it dissipated with time gradually and continuously. Almost whole portion of energy diminished after around 0.6 s (around 7 periods of vibration).

2.6 Experiments with different water heights

Simulations with structural damping and stiffness given by the tests in air have been performed to interpret the experiments in water with different heights. Note that reducing the water height is equivalent to augmentation of the assembly's mass and reducing the added mass.

2.6.1 Flow behaviour

Take one simulation with implicit method at WH = 167 mm as an example (see FIGURE 2.9). In this case, the recirculation region at the top and bottom will superimpose over each other. The simulation gives good prediction of the velocity and pressure field in this case.

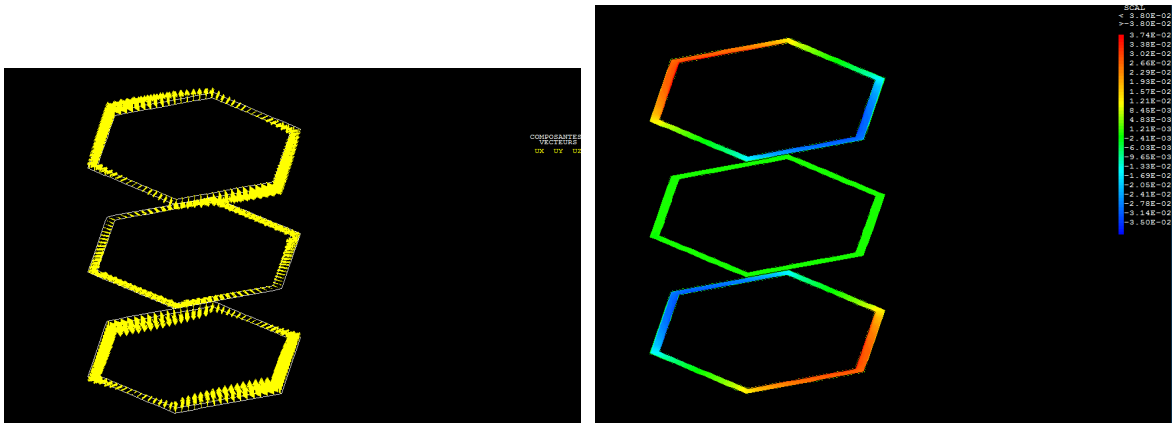

(a) Velocity vector (b) Vertical velocity

FIGURE 2.26: Velocity field

FIGURE 2.26 shows the cuts of velocity fields at three different levels, on the top, in the middle and at the bottom of the assembly. It is at a time instant $t = 5$ s when the assembly is moving to the left and the amplitude of oscillation is already at a low level.

FIURE 2.26(a) displays the velocity vector, while FIGURE 2.26(b) shows the vertical velocity. There is outflow on the left side of the hexagonal channel and inflow on the right side. On the plane at mid-height, almost zero vertical velocity is observed meaning that the fluid flow in the vicinity of mid-height is approximately $2D$ flow. The recirculation at the edges is not affecting the $2D$ flow in the middle.

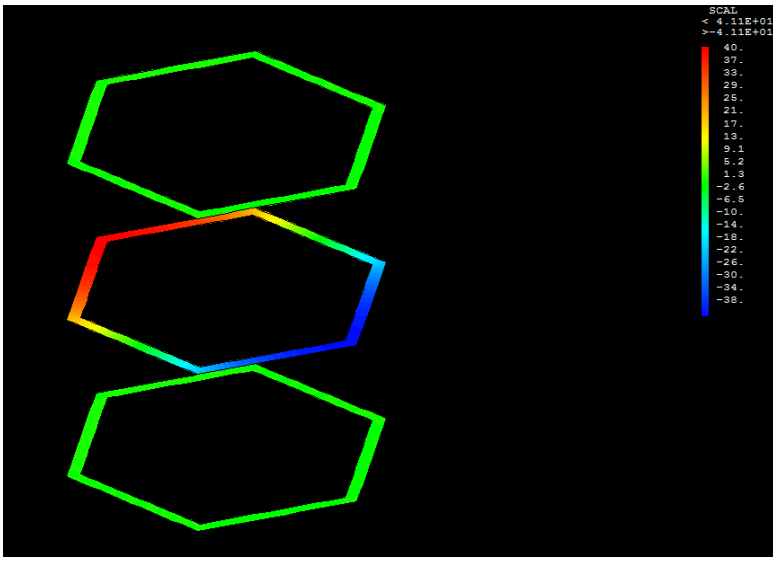

FIGURE 2.27: Pressure field

FIGURE 2.27 is the cuts pressure field at the three different levels corresponding to the velocity field shown in FIGURE 2.26. Zero pressure occurs on the top and bottom of the hexagonal channel. Positive pressure on the left side of the mid-plane and negative pressure on the right part of the hexagonal channel. This is consistent with the boundary condition and the velocity field.

2.6.2 Frequency and damping coefficient

FIGURE 2.28 shows the vibration frequency and damping coefficient evolution with different water heights.

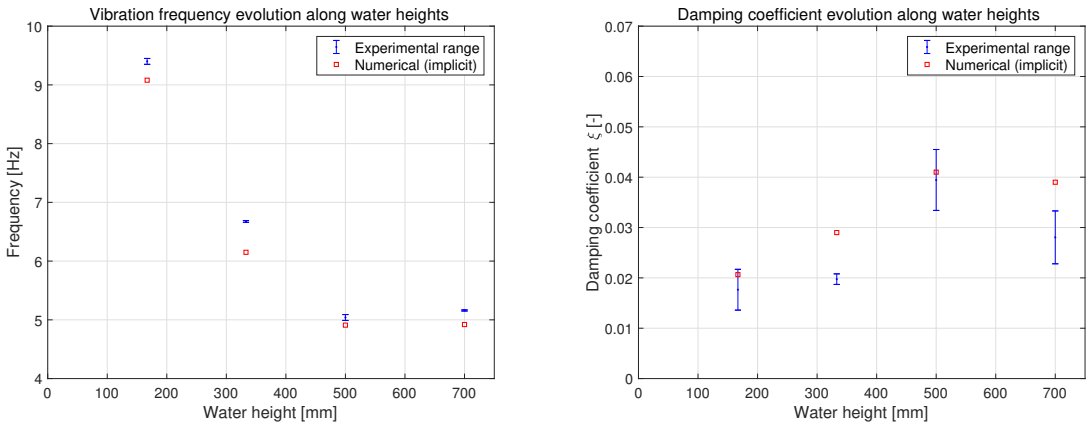

(a) Frequency

(b) Damping coefficient

FIGURE 2.28: Frequency and damping coefficient for tests with different water heights

In FIGURE 2.28, vibration frequency and damping coefficient of both experiments and numerical simulations are plotted. Range of experimental results from repeated tests has been plotted as well as numerical results with implicit method.

As water height increases, vibration frequency decreases and damping coefficient increases due to increase of fluid force acting on the assembly which is proportional to water height. Comparing the case when water height at the top of the assembly with a thin foil cover (WH=500mm) and that when at full water height with upper water tank filled (WH=700mm) , edge effect of the recirculation from the top shows little influence on damping coefficient and vibrating frequency. There is a trend of decreasing frequency and increasing damping coefficient from WH=167mm to WH=500mm, both in numerical results and experiments. This is due to the increasing added mass with the increase of water height. However, when WH=333mm, the damping coefficient of experiments doesn't increase comparing with that when WH=167mm, which is different from both the expected behaviour and the numerical simulation. Therefore, it is supposed that some errors may involved in this experiment when WH=333mm.

During experiments, the outer container is supposed to be fixed, however, in reality, it may be affected by the vibration of the hexagonal assembly. Coupling of the movement of outer container and the movement of the assembly will affect each other mutually.

A simplified model with coupled $2D$ cylindrical model has been elaborated in AppendixB. FIUGRE B.2 shows the spectra for the vibration of coupled cylindrical assembly and cylindrical outer container.

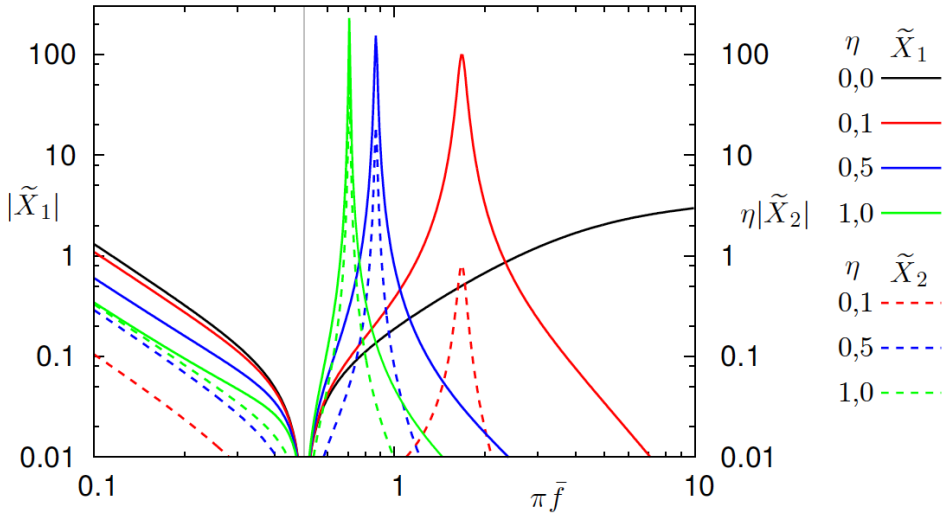

FIGURE 2.29: Spectra

Here, index 1 is for the assembly while index 2 for the container. With η increases, the peak is moving towards the left side and the half width decrease. This indicates that considering the coupling, there is a tendency of decrease in both frequency and damping coefficient.This may be the reason that all numerical computations tend to give higher damping coefficients when comparing to experimental results. This model used here doesn't take into account the mass and damping of the container, that is why the frequency is identical to the assembly.

2.6.3 Velocity and energy

Here below, FIGURE 2.30 shows the time series of velocity and energy in the case when water height at 700 mm (full water height with upper water tank filled) and water height at 167 mm (1/3 of the whole assembly height).

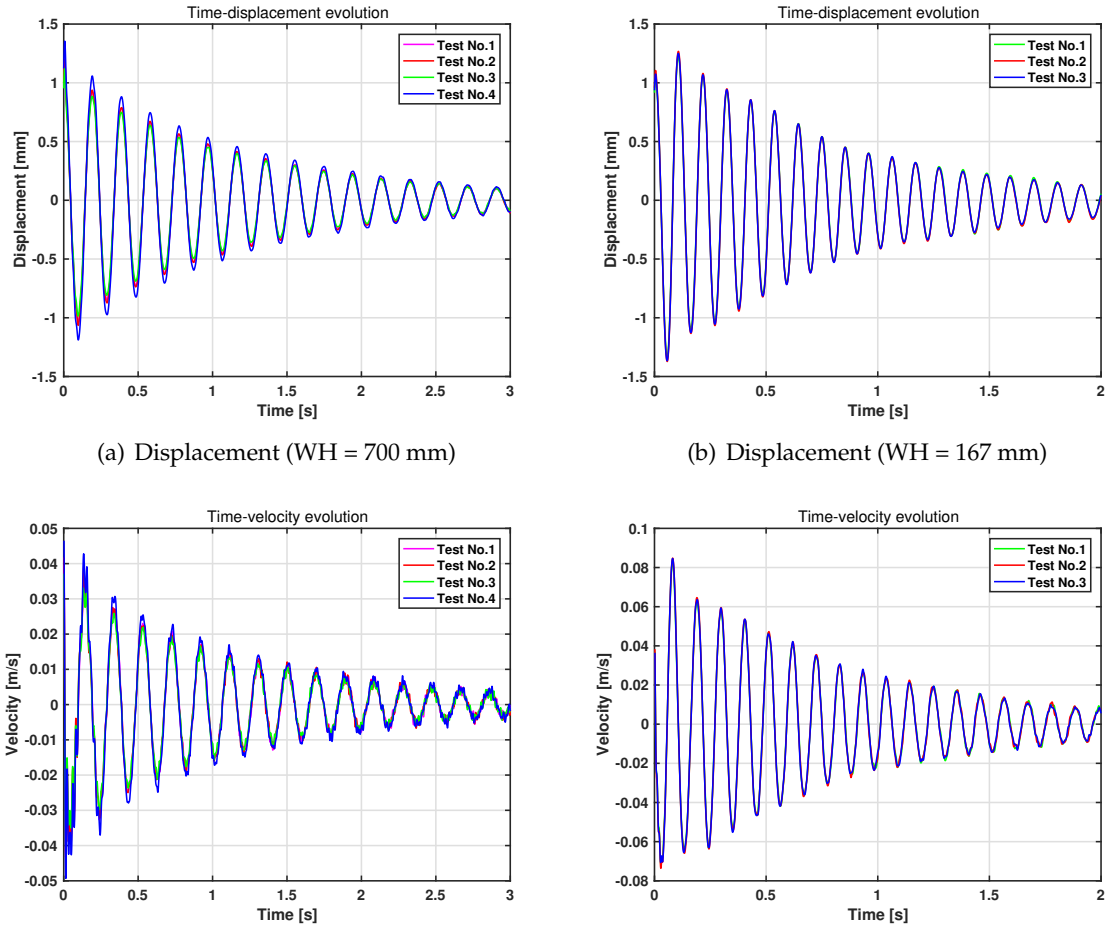

(a) Displacement (WH = 700 mm)

(b) Displacement (WH = 167 mm)

(c) Velocity (WH = 700 mm)

(d) Velocity (WH = 167 mm)

FIGURE 2.30: Time evolution of displacement and velocity (free vibration in water at WH = 700 mm and 167 mm)

Four and three repeated tests have been conducted for the case when water height is at 700 mm and 167 mm respectively. Smaller discrepancies exist among the repeated tests than that of free-vibration experiments in air.

FIGURE 2.31 displays the time evolution of kinetic, potential and total mechanical energy for the two cases with different water heights.

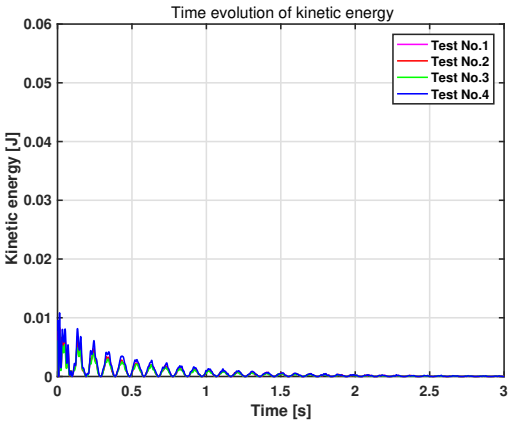

(a) Kinetic energy (WH = 700 mm)

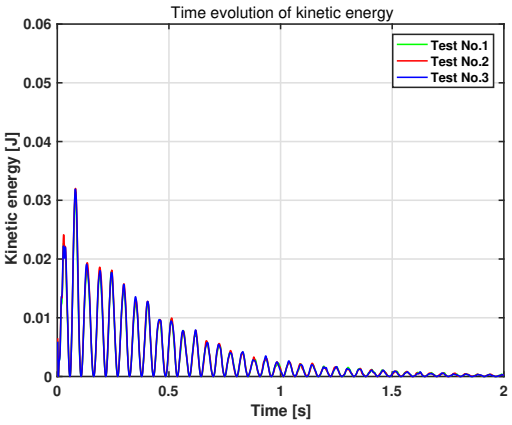

(b) Kinetic energy (WH = 167 mm)

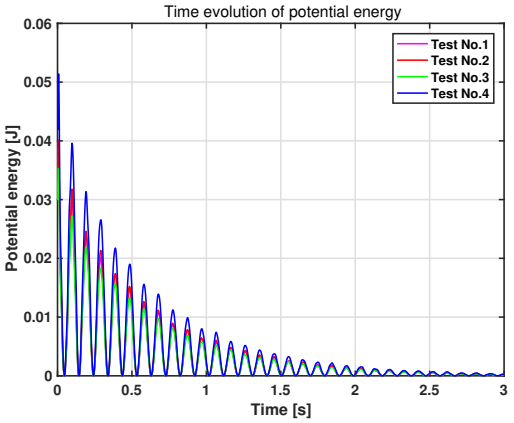

(c) Potential energy (WH = 700 mm)

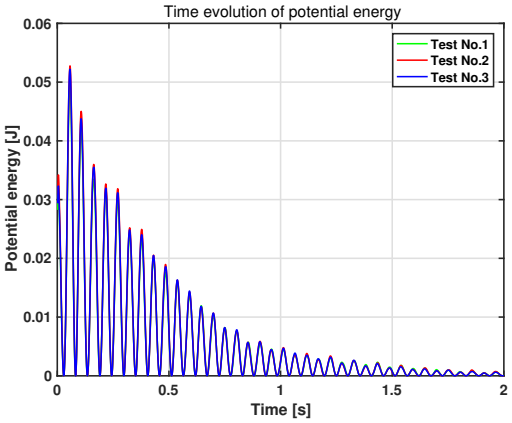

(d) Potential energy (WH = 167 mm)

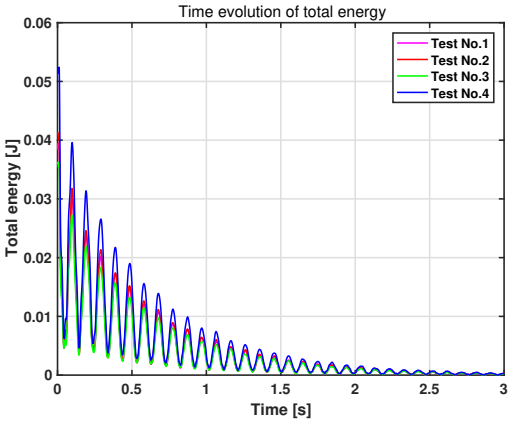

(e) Total energy (WH = 700 mm)

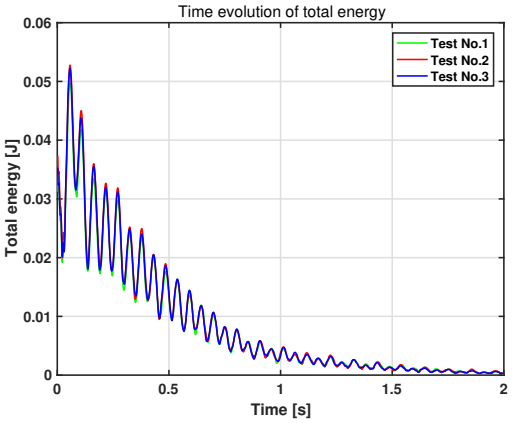

(f) Total energy (WH = 167 mm)

FIGURE 2.31: Time evolution of energy (free vibration in water at WH = 700 mm and 167 mm)

When water height at 167 mm, the dissipation ratio is at 0.028 while it's at 0.033 when water height at 700 mm.

More than 25% of the total mechanical energy of the assembly comes from kinetic energy

when water height at 167 mm while only less than 10% when at 700 mm. Portion of kinetic energy in total mechanical energy of the assembly is larger when it's at lower water height due to less confinement of motion by the fluid. Transfer and dissipation of kinetic energy during the interaction of the structure and surround flow (air or fluid) plays more important role in the whole regime of energy transfer when the water height decreases.

Almost whole portion of mechanical energy got dissipated after 2 s (around 10 periods of vibrations) during the case when water height at 700 mm while 1.5 s (around 14 periods) during the case when water height at 167 mm.

2.7 Experiments with water-glycerol mixture

Second series of experiments was conducted with water-glycerol mixture of different mass fractions. Interpretations of these tests will be shown in this section.

2.7.1 Frequency and damping coefficient

FIGURE 2.32 shows the vibration frequency and damping coefficient evolution with different mass fractions.

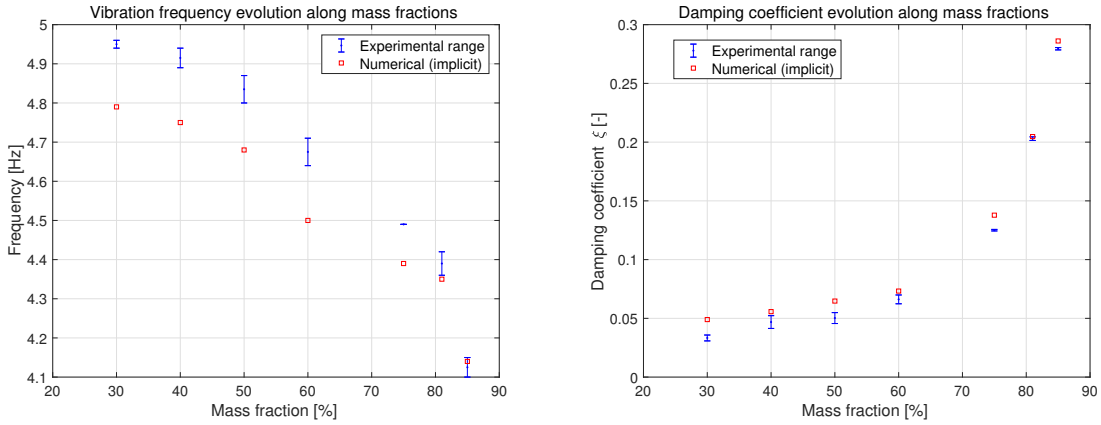

(a) Frequency (b) Damping coefficient

FIGURE 2.32: Frequency and damping coefficient for tests with water-glycerol mixtures

As mass fraction increases, density and viscosity also increase. Fluid force acting on the assembly, hence added mass, would increase. This may be the main reason of the decreasing tendency of vibration frequency and increase of damping coefficient with the increase of mass fraction. Also with the increase of fluid force, numerical instabilities increase. The under-relaxation level is obliged to be as high as $w_1 = 0.1$ to constrain the instablities.

Discrepancy between numerical simulations and experiments decreases with mass fraction increases. This may due to reduction of non-linearities with increase of viscosity.

2.7.2 Velocity and energy

FIGURE 2.33 shows the time evolution of velocity and energy for the cases when mass fraction is at 30% and 85%.

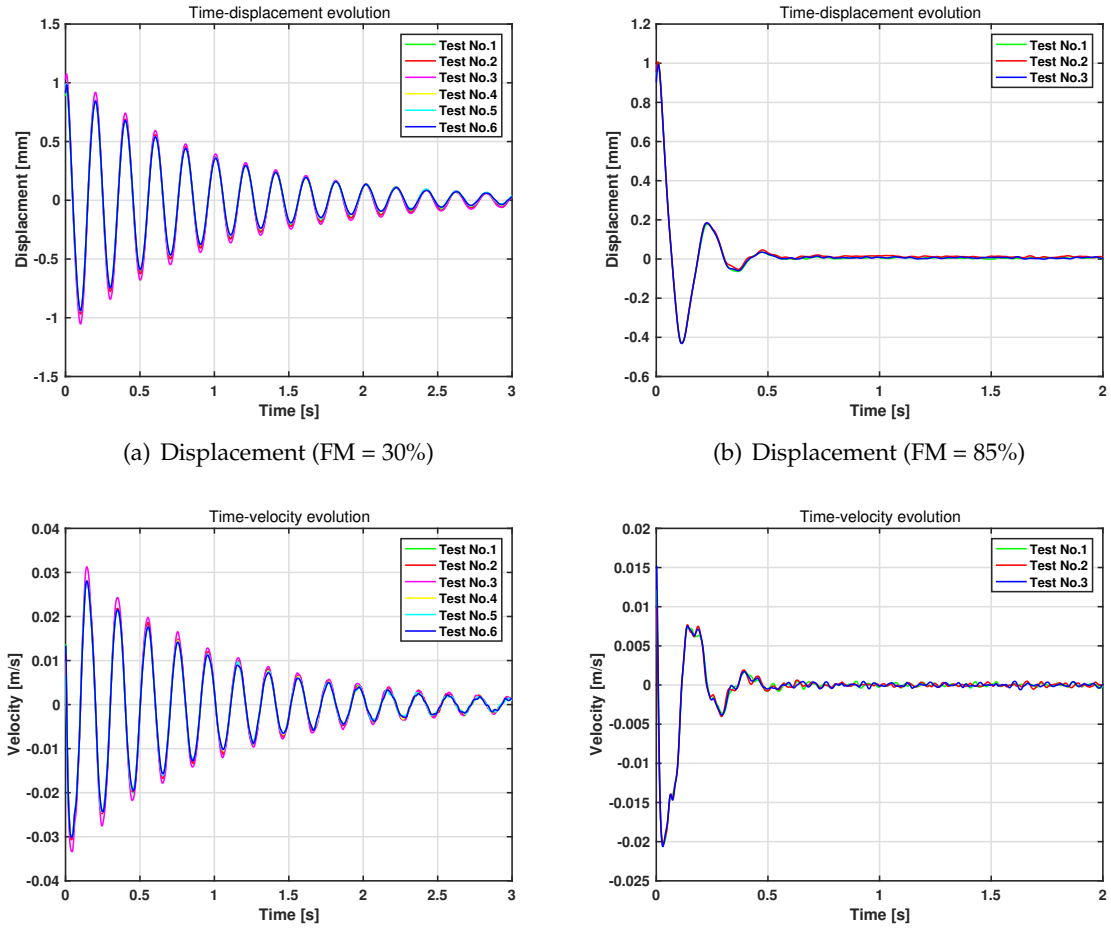

(a) Displacement (FM = 30%)

(b) Displacement (FM = 85%)

(c) Velocity (FM = 30%)

(d) Velocity (FM = 85%)

FIGURE 2.33: Time evolution of displacement and velocity (free vibration in water at FM = 30% and 85%)

With the damping coefficient increases with the increasing mass fraction, the displacement when mass fraction at 85% is very quickly damped to 0.

FIGURE 2.34 displays the time series of kinetic, potential and total mechanical energy of the assembly in the cases when mass fraction is at 30% and 85%.

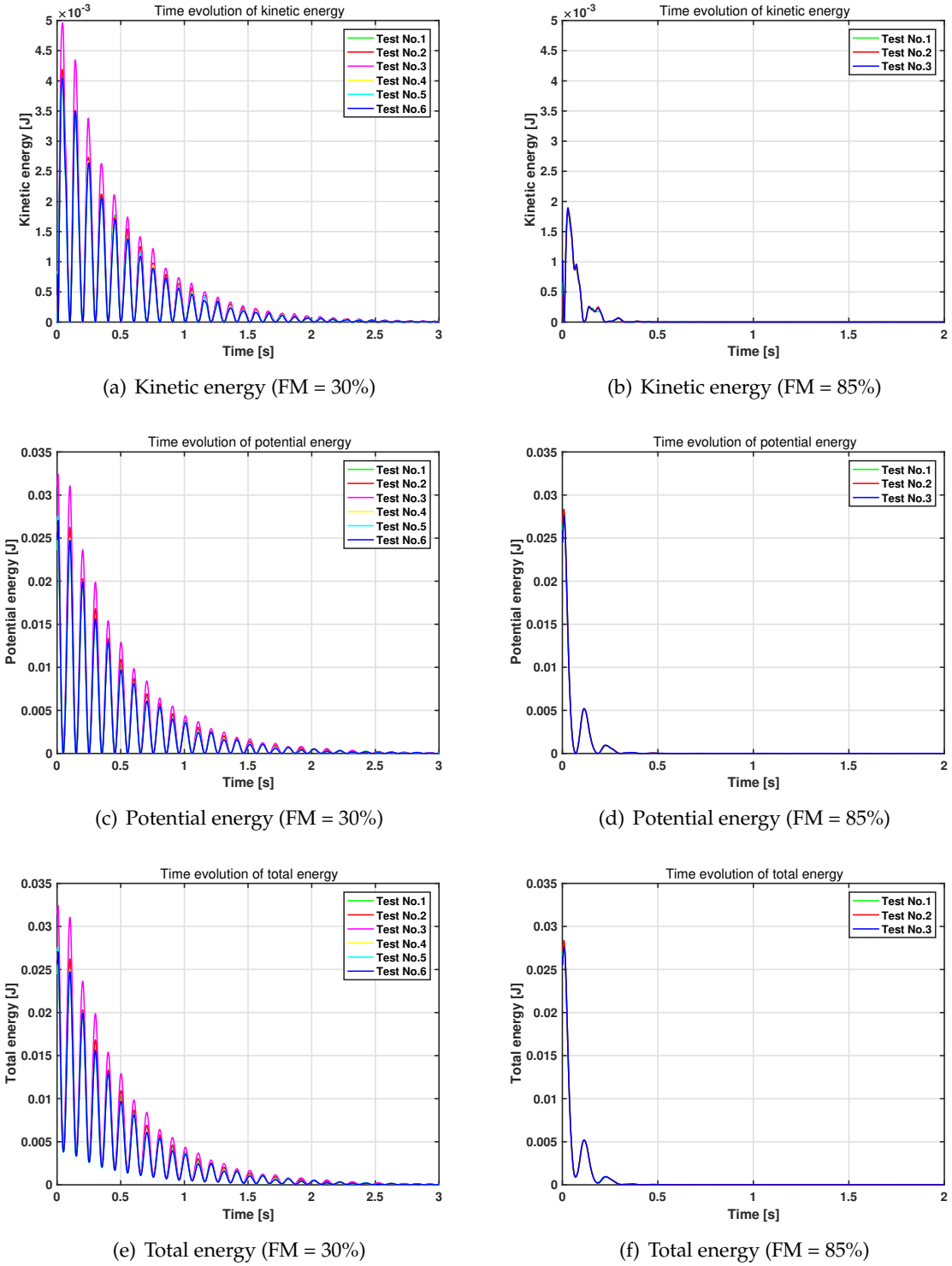

(a) Kinetic energy (FM = 30%)

(b) Kinetic energy (FM = 85%)

(c) Potential energy (FM = 30%)

(d) Potential energy (FM = 85%)

(e) Total energy (FM = 30%)

(f) Total energy (FM = 85%)

FIGURE 2.34: Time evolution of energy (free vibration in water at FM = 30% and 85%)

When mass fraction is at 30%, the dissipation ratio is around 0.037; when mass fraction is at 85%, the dissipation ratio is 0.224.

The total energy, when mass fraction at 85%, was very quickly dissipated away while whole portion of mechanical energy diminished after around 2 s in the case of 30%.

2.8 Conclusions

In this chapter, experimental analysis based on displacement of the assembly during free-vibration experiments under different physical conditions has been presented. Corresponding numerical interpretation with 3D Navier-Stokes model implemented in Cast3M code have been conducted.

Uncertainties coming from non-linearities and initial shock results in uncertainties when determining damping and frequency. This will not only affect the numerical simulation inasmuch that it is highly sensitive to structural parameters calculated from free-vibration experiments in air, but also affect the accuracy when characterising damping coefficients and frequencies calibrated from the experiments. Also, coupling of the assembly with the base during movements in air will also affect the characterising of structural parameter (see Appendix C).

As introduced parameters based on ideal damper system to describe the movement of the assembly, frequency and damping coefficient are supposed to be constant all along the vibrating duration which is not the case in reality (see FIGURE 2.20). Therefore, the assumption of weakly damped oscillator is not met in the experiments, the value of the damping coefficients and frequencies will not be as meaningful as its varying trends, indeed they can be taken as indicators of the dissipative effects in the system.

In numerical simulation, as discussed in Appendix B, coupling of the assembly with the container during experiments in liquids have not been taken into account. This effect will explain the lower damping coefficients of the experiments comparing the numerical simulations. However, lower frequencies resulted from numerical computations are not expected by this simplified model. More elaborated model shall be need for better understanding.

Boundary transfer is not considered in the numerical simulation. Since the initial displacement is as big as 1/7 of the channel width, it may have influences on the dynamic behaviour during the movements. Corresponding analytical analysis shall be helpful to understand this phenomena better.

For the first series of experiments with varying water height, damping coefficient increases with increasing added mass as the water height increases.

For the experiments with different mass fractions of glycerol in the water-glycerol mixture, damping coefficient increases and energy dissipation accelerates with increasing mass fractions due to increasing fluid force.

Chapter 3

Experimental and Analytical Approaches on PISE-2C

As a small-scale experimental facility with 19 assemblies, PISE-2C is designed and implemented in the purpose of proving first evaluation of collective effects that occur when several assemblies are vibrating in the vicinity of each other. Free-vibration experiments in different scenarios, including total flowering, partial flowering (internal crown) and partial flowering (external crown), have been performed on PISE-2C. A reticulate model with hypothesis of homogenisation and small differential displacement has been developed and reduces the whole geometry to only 3 assemblies. Corresponding computation with the reticulate model will be compared with the experimental results including the comparison of displacement curves, energies and volume variations. Disorders among assemblies have been observed in the experiments. Longer dissipation time is computed from analytical model than in experiments.

3.1 Introduction to PISE-2C

PISE-2C is a small-scale test facility designed to model the dynamic behaviour of Phénix reactor core during core flowering. It is composed by 19 assemblies distributed in two crowns with 3 mm inter-gap width, the same as in Phénix, giving a representative horizontal scale of Phénix core while the height of the assemblies has been reduced to 50 cm which is about 10 times lower than the real assembly height of Phénix. As shown by PISE-1A, edge effects don't significantly affect the dynamic behaviour of the assemblies.

A fixed central assembly is set in the center of the two crowns with injection nozzle located at the middle height of the assembly to connect with a pump in purpose of injection test which will be realised in recent future. The surrounding assemblies are placed in order to simulate the radial expansion happening during a core flowering event.

All the PMMA-made assemblies are manufactured with stainless steel twin-blade support at the bottom fixed with the ground-fixed base. It will constrain the movements of the assemblies in the perpendicular direction to the support plate plane simulating the reactor core flowering behaviour in horizontal plane.

Like PISE-1A, strain-gauges have been glued to the outer surface of the twin-blade supports with upward direction. They will be used to measure the displacement of each assembly. Further instalment of pressure sensor is undergoing.

Design parameters of PISE-2C assembly and twin-blades support will be listed in TABLE 3.1 below:

TABLE 3.1: Design Parameters PISE-2c

Design Parameters for the Assemblies (PISE-2c)					
b [mm]	3	Gap width	R_{int} [mm]	64.94	Equivalent internal ray
l [mm]	71.4	Side of the hexagon	R_{ext} [mm]	67.94	Equivalent external ray
ρ [kg · m^{-3}]	1190	PMMA density	m_s [kg · m^{-1}]	15.76	Hexagon linear mass
A_s [mm^2]	13251.7	Hexagon surface	H_{hex} [mm]	500	Hexagon height
Design Parameters for twin support blades					
h [mm]	10	Thickness horizontal plate	L [mm]	220	Height support blade
s [mm]	3	Thickness support blade	SD [mm]	84	Distance twin blade

The eighteen assemblies beside the fixed central assembly are indexed as Assembly No. 1 to 18, here below, FIGURE 3.1 shows the localisation of all the eighteen movable assemblies.

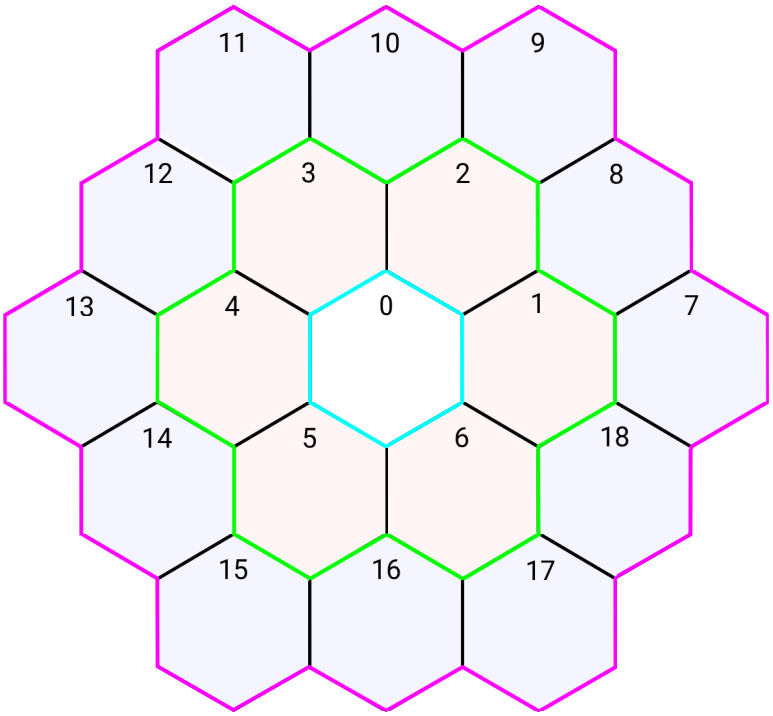

FIGURE 3.1: Distribution of Movable Assemblies with Number Index

To facilitate the experiments in liquid, a container was implemented to PISE-2C with a size of 1000 mm×1000 mm×1160 mm as shown in FIGURE 3.2. Also, a crab has been installed above the facility to control the initial displacement and the release of assemblies.

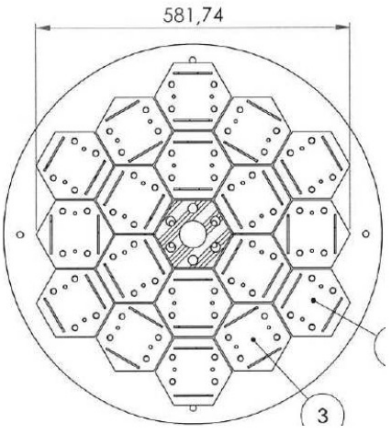

(a) Horizontal scheme

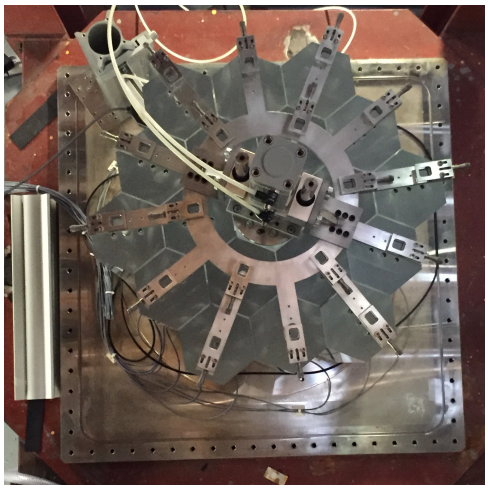

(b) Above view

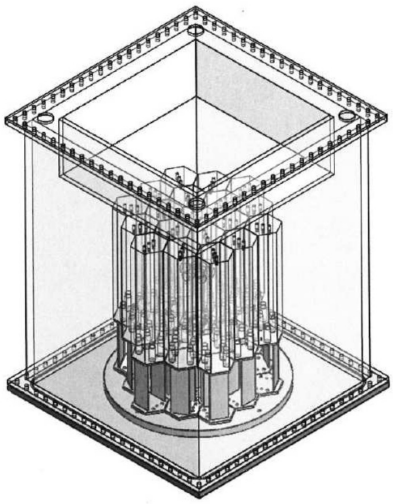

(c) Scheme of whole mock-up

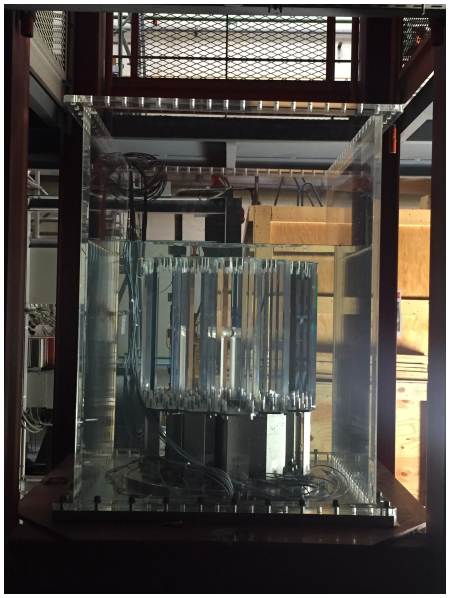

(d) Mock-up with container

(e) Mock-up without container

FIGURE 3.2: PISE-2C

Similar to the calibration of strain gauge for PISE-1A, each assembly except the fixed central assembly in PISE-2C was set on a base with strain gauge and laser installed ensembly. The assembly was then pulled by a rope to several given positions. Displacement measured by laser and deformation voltage obtained by strain gauge was recorded. After several tests with changing positions, a linear correlation can be found between the displacement and deformation voltage. Take the calibration curve of Assembly No. 4 as an example:

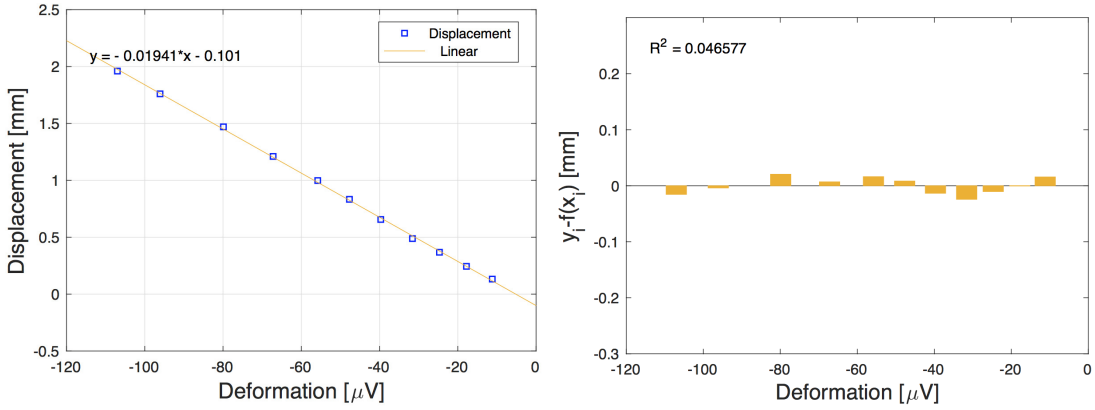

(a) Calibration Curve (b) R

FIGURE 3.3: Calibration Curve of Assembly No.2

FIGURE 3.3 shows the calibration curve of Assembly No.4. Here, calibration factor $\epsilon = -0.004713$ mm/μV. $R^2 = \sum_{i=1}^{n}(y_i - f(x_i))^2$ is the residual sum of squares. Different assemblies will have different calibration factors. FIGURE 3.4 displays the distribution of calibration factors for all the assemblies in PISE-2C. Assembly No. 12 has the lowest value of calibration factor among all the assemblies while Assembly No. 3 has the highest. From the lowest to the highest, there is a difference around 10%.

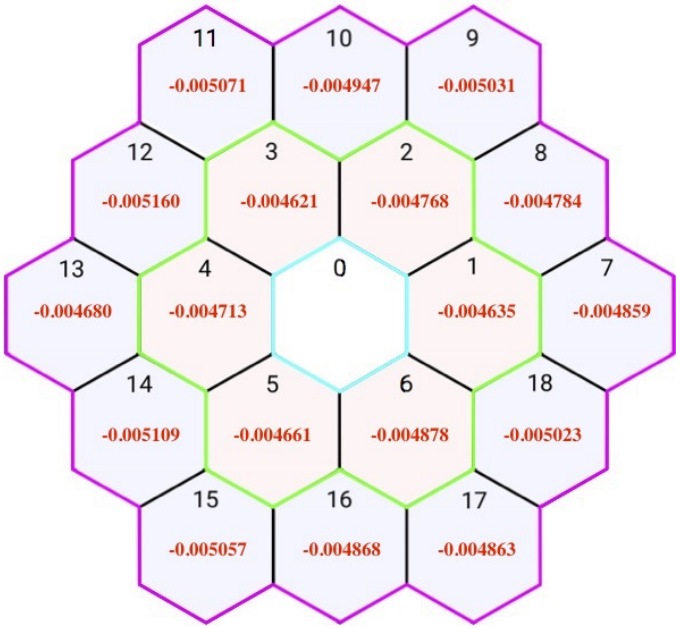

FIGURE 3.4: Calibration Factors for All the Assemblies in PISE-2C

TABLE 3.2 includes the information of variations for the calibration factors.

TABLE 3.2: Variations of Calibration Factors for PISE-2C

Average Value [mm/μV]	**Standard Deviation** [$\mathrm{mm}^2/\mu V^2$]	**Standard Error [%]**
-0.0004874	0.0001734	3.56

Structural parameters including structural stiffness and damping have to be calibrated for each assembly with vibration frequency and damping coefficient from free-vibration experiments in air of each assembly.

Same as the methodology used for determining calibration factors, the assembly will be placed on ground-fixed base. To start the free vibration in air, it was pulled to a given position around 1 mm by rope and then released. Time evolution of the displacement during the vibration process was recorded. As introduced in Chapter 3, ERA method was implemented to deduct the vibration frequency and damping coefficient. Therefore, the structural stiffness k and structural damping ratio c_v can be calculated as indicated in Eq. 2.11.

FIGURE 3.5(a) shows the distribution of calculated frequency f in orange digits and damping coefficient ξ in blue digits. FIGURE 3.5 displays the calculated structural stiffness k and damping ratio c_v in orange and blue digits respectively.

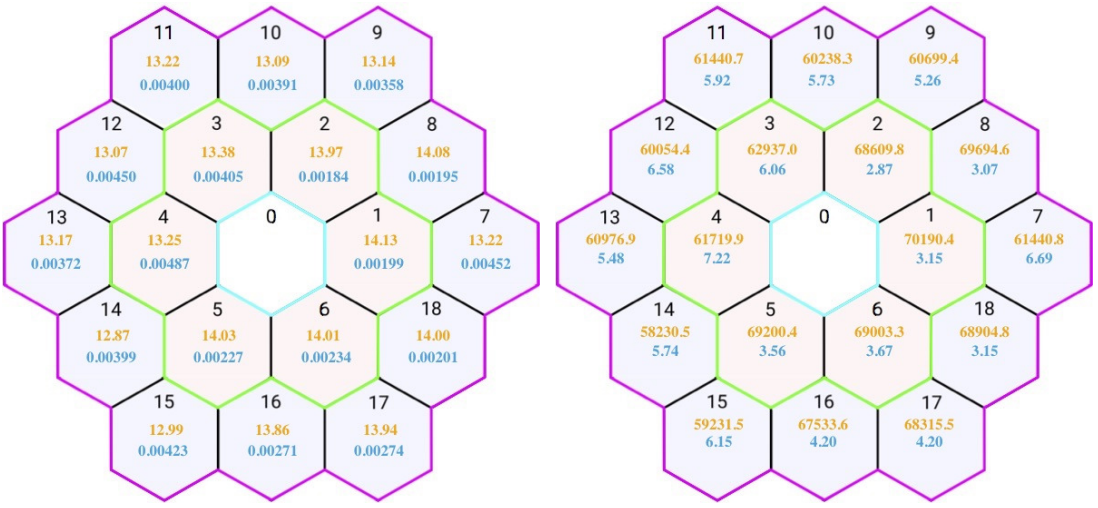

(a) Frequency and ξ (b) k and c_v

FIGURE 3.5: Structural Parameters of PISE-2C

Variations of structural parameters exist among assemblies. Here below TABLE 3.3 includes variation information of k and c_v.

TABLE 3.3: Variations of Structural Parameters in PISE-2C

	Average Value	**Standard Deviation**	**Standard Error (%)**
k **[N/m]**	64361.8	4347.0	6.75
c_v **[kg/s]**	4.93	1.43	29.07

The distributions of structural stiffness k are relatively more concentrated with less variations while the variations of structural damping ratio c_v is as high as 29.07%.

3.2 Reticulate model

The aim of this section is to study the dynamics of assemblies by reducing the flow in each channel to its $1D$ approximation. This approach has already been explored by Shimogo & Shinohara [40] as well as by Jacquelin et al. [41, 42]. However, unlike these authors, the objective is not to homogenise the plan because of the simplicity of the PISE-2C mock-up. This is an exploratory study that can be supplemented by more complete calculations developed with CAST3M. The results from this reticulate model aren't in good agreement with that of experiments. Therefore, more efforts are needed to improve this model.

This approach is based on several simplifying assumptions which are listed below and therefore have a reduced scope:

- rigid assemblies ;
- translation movements for the assemblies ;
- $2D$ flow and movements of assemblies;
- elastic restoring force ;
- thin channels ;
- incompressible viscous fluid ;
- flow treated in average on the widths of channels ;
- negligible edge effects.

The study comes in 5 steps:

1 - Analysis and schematisation of the flow.

2 - Coupling between the simplified flow and the movement of walls.

3 - Resolution for PISE-2C.

4 - Energetic balances.

5 - Time evolutions.

The study presented here takes as an applicative method to analyse the experimental mock-up PISE-2C.

Due to the complexity and multiple degrees of freedom, one should not expect close agreement between theory and experiments, especially at a local level. On the other hand, certain global parameters such as the total mechanical energy or the volume of fluid present at an instant could be restored correctly, as the errors being absorbed by integration.

The simplifications for a linear theory make it possible to progress far enough in the description of the phenomena and highlight the different behaviours at the origin of the movement of the assemblies.

At the end of this analysis, the unknown scales are determined (frequencies, dissipations, speeds, pressures). The evolutions of several quantities are detailed in the conservative case and in the dissipative case:

- displacements of the assemblies ;

- volume of fluid included in the installation ;
- perimeters of the crowns ;
- potential energies and kinetic energies by crown ;
- flow velocity in certain channels ;
- nodal pressures.

Several modes have been examined:

- total flowering : at initial instant, both the two crowns are displaced;
- partial flowering : at initial instant, only one crown is displaced, the other is left to oscillate freely.

3.2.1 Position of problem

The problem studied is a transient initiated from a periodic oscillating regime. It may originate from the irruption of sodium vapour bubble or from seismic wave (the latter will not be covered).The canonical problem envisaged here is that of a release with zero initial velocity. In addition to the mechanical properties of assemblies and fluid, the length scale of the initial displacement is also given.

3.2.1.1 General hypothesis

The dispositive study is limited by the hypothesis following:

- plane movement, both for fluid and the assemblies ;
- rigid assemblies, in translation;
- incompressible viscous fluid.

This schematisation differs from reality mainly because the fluid can not flow longitudinally (perpendicular to the plane of the figure), which leads to an overestimation of the pressure forces and hinders the movement of the assemblies. In addition, the $1D$ approximation ignores the recirculation effect.

Moreover, this model does not take into account the rotation, the flexion of the assemblies or the deformation of the assemblies' surfaces. Since the pressure distribution in the channels is substantially linear, the resultant of the pressure forces exerted on one face does not necessarily pass the center of the assembly and could thus be at the origin of a torque.

m is the linear mass of an assembly. It is associated with an inertial force:

$$\boldsymbol{f}_m = -m\,\ddot{\boldsymbol{r}}, \tag{3.1}$$

Where $\boldsymbol{r}$ describes the instant displacement of an assembly's center. In order to account for the stiffness of the assembly, there is an elastic force which recalls each assembly towards its equilibrium position:

$$\boldsymbol{f}_K = -K\,\boldsymbol{r}, \tag{3.2}$$

Where K is the stiffness. In addition, the structure is also affected by dissipative phenomena, modelled here as the action of a damper:

$$\boldsymbol{f}_D = -D\,\dot{\boldsymbol{r}}, \tag{3.3}$$

Where D is damping. This structural dissipation should not be confused with the dissipation in the fluid.

The mechanical parameters K and D are assumed to be the same for all the assemblies. *Dimensions* : $\dim[K] = \mathrm{kg}/(\mathrm{m}\cdot\mathrm{s}^2)$ and $\dim[D] = \mathrm{kg}/(\mathrm{m}\cdot\mathrm{s})$.

3.2.1.2 Dimensions

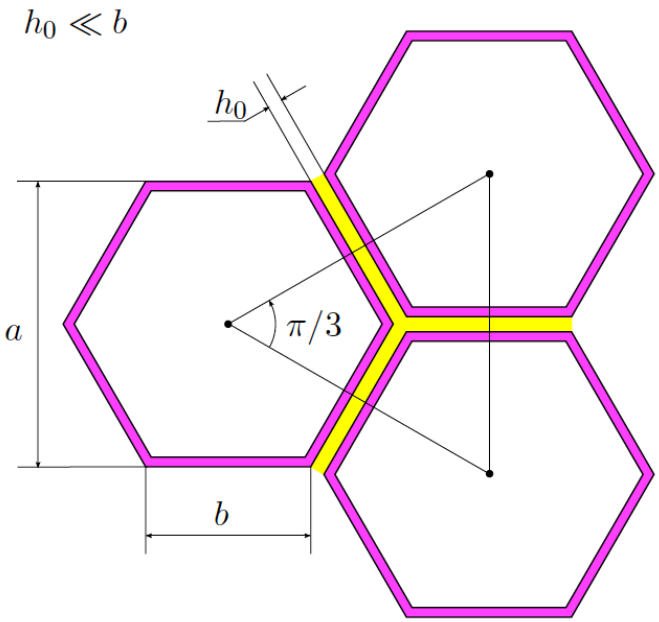

FIGURE 3.6: Inter-assembly space

The geometry of a hexagonal assembly is defined by the following parameters (FIGURE 3.6):

a : distance between two opposite faces;
$b = a/\sqrt{3}$: length of a face;
$h_0 \ll a \sim b$: width of an inter-assembly channel at rest.

The linearised volume of a channel at rest is $bh_0 + (\sqrt{3}/2)\, h_0^2$ $[\mathrm{m}^3/\mathrm{m}]$.

3.2.1.3 Fluid

The fluid is incompressible and viscous with density ρ and dynamic viscosity $\mu = \rho\nu$ (water or sodium).

3.2.1.3.1 Equations

The fluid circulates in a channel of uniform width, the walls of which moves in space and time, due to the movement of assemblies.

To take into account this double effect, one must place oneself in a relative coordinate system whose axes are aligned with the instantaneous plane of the channel's symmetry and the inlet section (FIGURE 3.7).

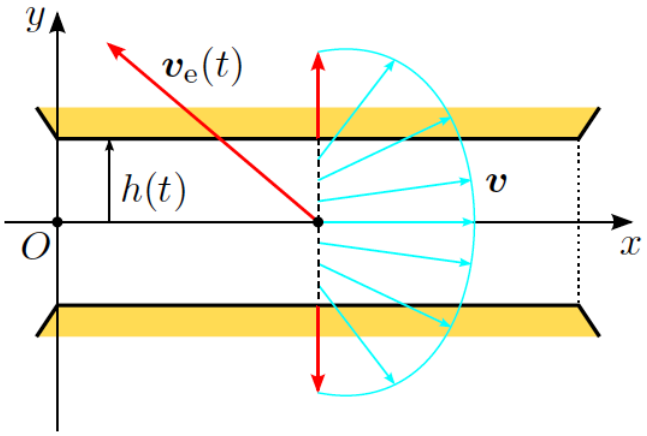

FIGURE 3.7: Channel in movement

Take $\boldsymbol{v}_e(t)$ as the entrainment velocity (the velocity of the moving frame relative to the inertial reference frame). Since the phenomena of seismic forces are excluded, this velocity can only come from the movement of the assemblies, not from that of the base. Simultaneously, the width of the channel is also varying over time. Let $h(t)$ be its half width.

The equations of the motion are written in relative coordinates and in the absence of rotation:

$$\begin{cases} \operatorname{div} \boldsymbol{v} = 0, \\ \rho\Big(\dfrac{\partial \boldsymbol{v}}{\partial t} + \boldsymbol{\nabla v}\cdot\boldsymbol{v}\Big) = -\rho\,\dfrac{\mathrm{d}\boldsymbol{v}_e}{\mathrm{d}t} - \boldsymbol{\nabla} p + \mu\Delta\boldsymbol{v}, \end{cases} \tag{3.4}$$

And the non-penetration condition will be:

$$\frac{\mathrm{d}}{\mathrm{d}t}\big[y \mp h(t)\big] = \mp\frac{\mathrm{d}h}{\mathrm{d}t} + v = 0. \tag{3.5}$$

This statement is incomplete because it lacks the pressure and velocity conditions on the walls and ends of the channel. Due to the small-displacement approximation, entrainment terms are negligible in all the discussion following.

3.2.1.3.2 Scales

Here below are the scales:

$$\begin{array}{lll} t = \tau\,\bar{t}, & x = b\,\bar{x}, & y = h_0\,\bar{y} = \varepsilon b\,\bar{y} \quad \text{with} \quad \varepsilon \ll 1, \\ u = U\,\bar{u}, & v = V\,\bar{v}, & p = p_0 + (\delta p)\,\tilde{p}, \qquad \mathsf{Re} = Uh_0/\nu, \quad \mathsf{St} = b/(U\tau), \\ u_e = U_e\,\bar{u}_e, & v_e = U_e\,\bar{v}_e, & h = h_0\,\bar{h} = h_0 + (\delta h)\,\tilde{h} = h_0(1+\eta\,\tilde{h}). \end{array}$$

Here, $\varepsilon \ll 1$ and $\eta \leq 1$ are named as confinement parameter and amplitude parameter respectively. With the overall displacement of the assemblies being concomitant with the variation in width of the channels, a single time scale is sufficient. The change of linear variable on the components of the velocity and the reference value of the pressure ($p_0 = p(0)$) is reasonable because of the initial conditions (at rest). Finally, since the entrainment movement has no priori at privileged direction, it is useless to differentiate the scales of its velocity.

In reason of mass conservation, it's clear that $V = \varepsilon\, U$, allowing elimination of V from the problem.

By definition of the change of scale for the pressure, we must retain the scale provided by the longitudinal momentum equation (according to x):

$$\frac{(\delta p)}{\rho U^2} = \sup\Big\{\mathsf{St},\ 1,\ \frac{1}{\varepsilon \mathsf{Re}}\Big\}, \tag{3.6}$$

and this results in the classical degeneracy of the transverse momentum equation by:

$$\partial\tilde{p}/\partial\bar{y} = 0 \quad \Longrightarrow \quad \tilde{p} = \tilde{p}(\bar{x}, \bar{t}).$$

Therefore, the problem will become:

• *Equations :*

$$\begin{cases} \dfrac{\partial \bar{u}}{\partial \bar{x}} + \dfrac{\partial \bar{v}}{\partial \bar{y}} = 0. \\ \mathsf{St}\,\dfrac{\partial \bar{u}}{\partial \bar{t}} + \dfrac{\partial \bar{u}^2}{\partial \bar{x}} + \dfrac{\partial}{\partial \bar{y}}(\bar{u}\bar{v}) = -\dfrac{(\delta p)}{\rho U^2}\,\dfrac{\partial \tilde{p}}{\partial \bar{x}} + \dfrac{1}{\varepsilon \mathsf{Re}}\,\dfrac{\partial^2 \bar{u}}{\partial \bar{y}^2}, \\ 0 = -\dfrac{\partial \tilde{p}}{\partial \bar{y}}, \end{cases}$$

• *Boundary conditions:*

$$\bar{y} = \pm(1 + \eta\,\tilde{h}) \ : \quad \bar{u} = 0, \quad \bar{v} = \pm\eta \mathsf{St}\,\frac{\mathrm{d}\tilde{h}}{\mathrm{d}\bar{t}}.$$

3.2.1.3.3 Parietal stress

The stress exerted by the fluid on a surface $\mathcal{S}$ is an objective quantity (independent of the change of reference), written as:

$$\boldsymbol{f} = -\int_{\mathcal{S}} \boldsymbol{\sigma}\cdot\boldsymbol{n}\,\mathrm{d}A = -\int_{\mathcal{S}} (-p\,\mathbf{I} + \boldsymbol{\tau})\cdot\boldsymbol{n}\,\mathrm{d}A,$$

where $\boldsymbol{n}$ is the external norm of fluid. To determine the first approximation of parietal stress, taking into account thin-layer approximation, we will have the following expression in non dimensional form:

$$\boldsymbol{\sigma}\cdot\boldsymbol{n} = \begin{pmatrix} 0 \\ \mp p_0 \end{pmatrix} \pm \rho U^2 \begin{pmatrix} \dfrac{1}{\mathsf{Re}}\Big(\dfrac{\partial \bar{u}}{\partial \bar{y}} + \varepsilon^2 \dfrac{\partial \bar{v}}{\partial \bar{x}}\Big) \\ -\dfrac{(\delta p)}{\rho U^2}\,\tilde{p} + \dfrac{2\varepsilon}{\mathsf{Re}}\,\dfrac{\partial \bar{v}}{\partial \bar{y}} \end{pmatrix} \simeq \begin{pmatrix} 0 \\ \mp p_0 \end{pmatrix} \pm \rho U^2 \begin{pmatrix} \dfrac{1}{\mathsf{Re}}\,\dfrac{\partial \bar{u}}{\partial \bar{y}} \\ -\dfrac{(\delta p)}{\rho U^2}\,\tilde{p} \end{pmatrix},$$

The tangential component consists of the first approximation of the parietal friction and the normal component reduces to the pressure. It is a conventional result of thin-layer approximation.

3.2.1.3.4 Average on a section

To put the integration of momentum equation into $1D$ approximation, it is supposed that $\bar{u}$ is independent of $\bar{y}$ and the flow remains laminar. The friction can be described by:

$$\bar{\tau}_{\mathrm{p}|\pm} = \mp C_{\mathrm{f}}\,\bar{u} \quad \text{where} \quad C_{\mathrm{f}} = \text{constant} \sim 1 > 0.$$

Therefore, the momentum equation can be simplified to:

$$\mathsf{St}\,\frac{\partial}{\partial\bar{t}}\bar{u} + \frac{\partial\bar{u}^2}{\partial\bar{x}} = -\frac{(\delta p)}{\rho U^2}\,\frac{\partial\tilde{p}}{\partial\bar{x}} - \frac{C_{\mathrm{f}}}{\varepsilon\mathsf{Re}}\,\frac{\bar{u}}{\bar{h}}, \tag{3.7}$$

The $1D$ approximation also allows the integration of mass conservation:

$$\begin{aligned}
&\bar{v} = -(\bar{y}+\bar{h})\frac{\partial\bar{u}}{\partial\bar{x}} - \eta\mathsf{St}\,\frac{\mathrm{d}\tilde{h}}{\mathrm{d}\bar{t}} \quad\Longrightarrow\quad \frac{\partial\bar{u}}{\partial\bar{x}} = -\eta\mathsf{St}\,\frac{1}{\bar{h}}\frac{\mathrm{d}\tilde{h}}{\mathrm{d}\bar{t}}\\
\Longrightarrow\quad &\bar{u} = \bar{u}_{|0} - \eta\mathsf{St}\,\frac{\mathrm{d}\tilde{h}}{\mathrm{d}\bar{t}}\,\frac{\bar{x}}{\bar{h}} \quad\text{and}\quad \bar{v} = \eta\mathsf{St}\,\frac{\mathrm{d}\tilde{h}}{\mathrm{d}\bar{t}}\,\frac{\bar{y}}{\bar{h}},
\end{aligned}$$

$$\eta\mathsf{St}\,\frac{1}{\bar{h}}\frac{\mathrm{d}\tilde{h}}{\mathrm{d}\bar{t}} = \bar{u}_{|0} - \bar{u}_{|1} \quad\Longleftrightarrow\quad \begin{cases} \bar{u} &= \bar{u}_{|0} + (\bar{u}_{|1} - \bar{u}_{|0})\,\bar{x},\\ \bar{v} &= -(\bar{u}_{|1} - \bar{u}_{|0})\,\bar{y}, \end{cases} \tag{3.8}$$

The pressure is determined by integration, when $\bar{x} = 1$:

$$\mathsf{St}\,\frac{\mathrm{d}}{\mathrm{d}\bar{t}}\Big[\tfrac{1}{2}(\bar{u}_{|1} + \bar{u}_{|0})\Big] + \bar{u}_{|1}^2 - \bar{u}_{|0}^2 = -\frac{(\delta p)}{\rho U^2}\,(\tilde{p}_{|1} - \tilde{p}_{|0}) - \frac{C_{\mathrm{f}}}{\varepsilon\mathsf{Re}}\,\tfrac{1}{2}(\bar{u}_{|1} + \bar{u}_{|0})\frac{1}{\bar{h}}. \tag{3.9}$$

This expression essentially links the average velocity and the difference of pressure at the ends. The difference in velocity matters only when the non-linear terms are not negligible.

3.2.1.3.5 Integration of pressure force

From above equation, integrating pressure force, we will get:

$$\begin{aligned}
\frac{(\delta p)}{\rho U^2}\int_0^1 \tilde{p}\,\mathrm{d}\bar{x} = \quad & \frac{1}{2}\frac{(\delta p)}{\rho U^2}\,(\tilde{p}_{|1} + \tilde{p}_{|0})\\
&+ \frac{1}{12}\mathsf{St}\,\frac{\mathrm{d}}{\mathrm{d}\bar{t}}(\bar{u}_{|1} - \bar{u}_{|0}) + \frac{1}{6}(\bar{u}_{|1} - \bar{u}_{|0})^2 + \frac{1}{12}\frac{C_{\mathrm{f}}}{\varepsilon\mathsf{Re}}\,\frac{1}{\bar{h}}(\bar{u}_{|1} - \bar{u}_{|0}).
\end{aligned} \tag{3.10}$$

This appears as the sum of the integral of the mean pressure in the channel plus a variation due to the dynamic effects and the friction of the flow. The latter expression has the advantage of involving only nodal values. Note that when linearisation is possible, this resultant is a linear function of these nodal values.

3.2.1.3.6 Mean values and variations

Impose:

$$\begin{aligned}
\tfrac{1}{2}(\bar{u}_{|1} + \bar{u}_{|0}) = \bar{u}_{\mathrm{m}} \qquad &\text{and} \quad \bar{u}_{|1} - \bar{u}_{|0} = \Delta\bar{u},\\
\tfrac{1}{2}(\tilde{p}_{|1} + \tilde{p}_{|0}) = \tilde{p}_{\mathrm{m}} \qquad &\text{and} \quad \tilde{p}_{|1} - \tilde{p}_{|0} = \Delta\tilde{p}.
\end{aligned}$$

The momentum equation and pressure force can be written as:

$$\mathsf{St}\,\frac{\mathrm{d}\bar{u}_\mathrm{m}}{\mathrm{d}\bar{t}} + 2\bar{u}_\mathrm{m}\,\Delta\bar{u} = -\frac{(\delta p)}{\rho U^2}\,\Delta\tilde{p} - \frac{C_\mathrm{f}}{\varepsilon\mathsf{Re}}\,\frac{\bar{u}_\mathrm{m}}{\bar{h}}. \tag{3.11a}$$

$$\frac{(\delta p)}{\rho U^2}\int_0^1 \tilde{p}\,\mathrm{d}\bar{x} = \frac{(\delta p)}{\rho U^2}\,\tilde{p}_\mathrm{m} + \frac{1}{12}\left[\mathsf{St}\,\frac{\mathrm{d}}{\mathrm{d}\bar{t}}(\Delta\bar{u}) + 2(\Delta\bar{u})^2\right] + \frac{1}{6}\,\frac{C_\mathrm{f}}{\varepsilon\mathsf{Re}}\,\frac{\Delta\bar{u}}{\bar{h}}. \tag{3.11b}$$

Mass conservation will be:

$$\Delta\bar{u} = -\eta\mathsf{St}\,\frac{1}{\bar{h}}\frac{\mathrm{d}\tilde{h}}{\mathrm{d}\bar{t}}. \tag{3.12}$$

It is through this last relation that the coupling between the dynamics of the assemblies and that of the fluid takes place; it is therefore fundamental.

3.2.1.4 Solid

3.2.1.4.1 Reference coordinates and external forces

The movement of assemblies is studied in reference frame (see FIGURE 3.8)

- ▷ Absolute reference coordinates (center) : $\{O;\,X,Y\}$;
- ▷ Initial position of assembly's center : C_0 ;
- ▷ Actual position of assembly's center : $C(t)$.

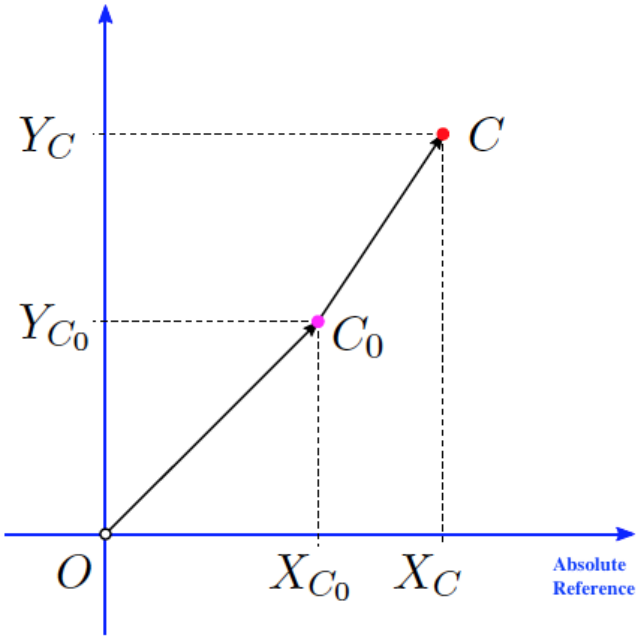

FIGURE 3.8: Reference coordinates

Whatever the nature of the external forces, each assembly is supposed to be driven by a translation without rotation, so that the faces of two adjacent assemblies always remain parallel. It is subject (at most) to three types of external forces (FIGURE 3.9):

- the force exerted by fluid on each face;

- the restoring force acting at its center of inertia (see Eq. 3.2);
- the frictional force intrinsic to the structure (see Eq. 3.3).

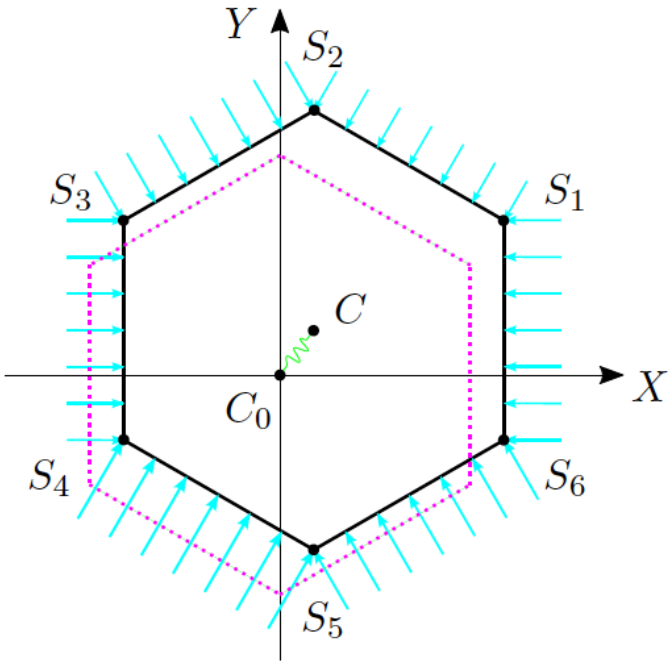

FIGURE 3.9: External forces

3.2.1.4.2 Equations

$X_C(t)$ and $Y_C(t)$ are the coordinates of the assembly's center of inertia C in the reference coordinates and its non-perturbed position C_0. $p_n(x,t)$ is the pressure exerted on the surface S_nS_{n+1}, where $n = 1, \cdots, 6$. x is the the abscissa defined locally in the channel. Therefore, in reference coordinates:

$$\begin{aligned} m\frac{\mathrm{d}^2X_C}{\mathrm{d}t^2} &= -K\left(X_C - X_{C_0}\right) - D\frac{\mathrm{d}X_C}{\mathrm{d}t} + \frac{1}{2}\int_0^b \left(-p_1 + p_2 + 2p_3 + p_4 - p_5 - 2p_6\right)\mathrm{d}x, \\ m\frac{\mathrm{d}^2Y_C}{\mathrm{d}t^2} &= -K\left(Y_C - Y_{C_0}\right) - D\frac{\mathrm{d}Y_C}{\mathrm{d}t} + \frac{\sqrt{3}}{2}\int_0^b \left(-p_1 - p_2 + p_4 + p_5\right)\mathrm{d}x. \end{aligned} \tag{3.13}$$

Strictly speaking, these equations should take account of friction, but the result established in section 3.2.1.3.3 shows that its contribution is negligible in comparison with that of pressure. Given the scope envisaged, the dissipation which occurs in the structure could also be neglected.

3.2.1.4.3 Scales

The movement of the assemblies is limited by the value of the inter-assembly space $2h_0$ and it therefore needs to make an affine change of variables on the coordinates at the assembly's center:

$$\begin{cases} X_C &= X_{C_0} + \eta h_0 \widetilde{X}_C \\ Y_C &= Y_{C_0} + \eta h_0 \widetilde{Y}_C \end{cases} \quad \text{with} \quad \eta \leq 1. \tag{3.14}$$

η measures the amplitude of the walls' oscillations with respect to the initial width of the channel.

A situation such that the amplitude of the overall movement of the assemblies is much greater than the amplitude of the variations in the width of the channels is excluded for the purpose of simplicity. This hypothesis is based on the fact that the movements envisaged are of the «flowering» type and present a central symmetry.

As the movements of the assemblies are a priori arbitrary, there is no reason to differentiate between the pressure scales of each channel. On the other hand, it is clear that we can neglect the initial pressure and retain only variations. It becomes:

$$\frac{m}{K\tau^2}\frac{\mathrm{d}^2\widetilde{X}_C}{\mathrm{d}\bar{t}^2} = -\widetilde{X}_C - \frac{D}{K\tau}\frac{\mathrm{d}\widetilde{X}_C}{\mathrm{d}\bar{t}} + \frac{1}{2}\frac{(\delta p)}{\varepsilon\eta K}\int_0^1 \left(-\tilde{p}_1 + \tilde{p}_2 + 2\tilde{p}_3 + \tilde{p}_4 - \tilde{p}_5 - 2\tilde{p}_6\right)\mathrm{d}\bar{x}, \quad (3.15a)$$

$$\frac{m}{K\tau^2}\frac{\mathrm{d}^2\widetilde{Y}_C}{\mathrm{d}t^2} = -\widetilde{Y}_C - \frac{D}{K\tau}\frac{\mathrm{d}\widetilde{Y}_C}{\mathrm{d}\bar{t}} + \frac{\sqrt{3}}{2}\frac{(\delta p)}{\varepsilon\eta K}\int_0^1 \left(-\tilde{p}_1 - \tilde{p}_2 + \tilde{p}_4 + \tilde{p}_5\right)\mathrm{d}\bar{x}. \quad (3.15b)$$

The presentation of Eq. 3.15 implicitly assumes that, starting from a deformed state at rest, the restoring force is the driving force of the assemblies' movement.

3.2.2 Coupling

In precedent section, the dynamic equations of the assemblies and fluid are established independently. In this section, coupling between the structure and fluid will be introduced.

3.2.2.1 Kinematic coupling

3.2.2.1.1 Definitions

It involves linking the entrainment velocity and the displacements of the walls as defined in a local coordinate (channel) to their definition in the absolute coordinate system, leading to the definition of the numbering for vertices of an assembly.

All assemblies are oriented in the same way and can be deducted from the central assembly by translation $\overrightarrow{OC(t)}$ where $C(t)$ is the position of the assembly's center at time instant t. It is therefore sufficient to relate the definitions to the generic assembly.

$$\begin{aligned}
&\overrightarrow{OM} = \overrightarrow{OC_0} + \overrightarrow{C_0C} + \overrightarrow{CS} + \overrightarrow{SM},\\
&\overrightarrow{OC_0} = X_{C_0}\,\boldsymbol{e}_X + Y_{C_0}\,\boldsymbol{e}_Y,\\
&\overrightarrow{C_0C} = \left(X_C - X_{C_0}\right)\boldsymbol{e}_X + \left(Y_C - Y_{C_0}\right)\boldsymbol{e}_Y,\\
&\overrightarrow{CS} = b\,\boldsymbol{i}, \quad \overrightarrow{SM} = x\,\boldsymbol{e}.
\end{aligned}$$

3.2.2.1.2 Width-displacement relations

The width $2h(t)$ of a channel is determined by the relative position of the assemblies' surfaces which delimit it. The objective of this section is to establish the expression of h as a function of the adjacent assemblies' coordinates.

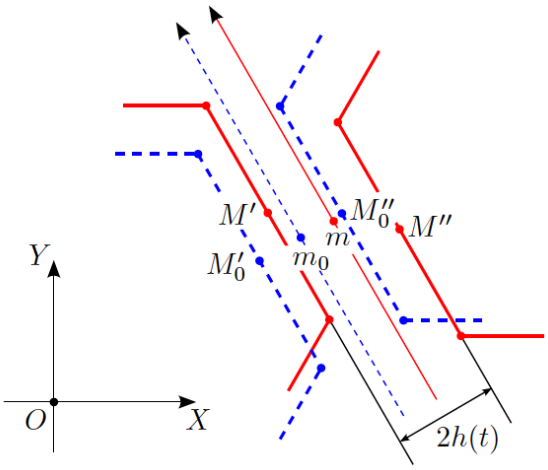

FIGURE 3.10: Displacement of an assembly

For two adjacent assemblies, with $C'(t)$ and $C''(t)$ as the centers, $M'(t)$ and $M''(t)$ the middle point of the two faces, $\boldsymbol{n}'$ and $\boldsymbol{n}'' = -\boldsymbol{n}'$ the external normal vectors at each faces, the half width of a channel will be (see FIGURE 3.10):

$$h = \tfrac{1}{2}\overrightarrow{M'M''} \cdot \boldsymbol{n}' \quad \text{where} \quad \boldsymbol{n}' = \overrightarrow{C_0'C_0''}/C_0'C_0'',$$

$$\begin{aligned}\overrightarrow{M'M''} &= \overrightarrow{OC''} + \overrightarrow{C''M''} - \left(\overrightarrow{OC'} + \overrightarrow{C'M'}\right) \\ &= \left(X_{C''} - X_{C'}\right)\boldsymbol{e}_X + \left(Y_{C''} - Y_{C'}\right)\boldsymbol{e}_Y + \overrightarrow{C''M''} - \overrightarrow{C'M'}.\end{aligned}$$

Therefore,

$$\begin{aligned}h &= \tfrac{1}{2}\left[\left(X_{C''} - X_{C'}\right)\left(\boldsymbol{e}_X \cdot \boldsymbol{n}'\right) + \left(Y_{C''} - Y_{C'}\right)\left(\boldsymbol{e}_Y \cdot \boldsymbol{n}'\right) - a\right], \\ \frac{\mathrm{d}h}{\mathrm{d}t} &= \tfrac{1}{2}\left[\frac{\mathrm{d}}{\mathrm{d}t}\left(X_{C''} - X_{C'}\right)\left(\boldsymbol{e}_X \cdot \boldsymbol{n}'\right) + \frac{\mathrm{d}}{\mathrm{d}t}\left(Y_{C''} - Y_{C'}\right)\left(\boldsymbol{e}_Y \cdot \boldsymbol{n}'\right)\right].\end{aligned} \tag{3.16}$$

3.2.2.1.3 Nondimensionalisation

$$\begin{aligned}h_0\,\bar{h} &= \tfrac{1}{2}\big(\big\{\left[\left(X_{C''} - X_{C_0''}\right) - \left(X_{C'} - X_{C_0'}\right) + \left(X_{C_0''} - X_{C_0'}\right)\right]\boldsymbol{e}_X \\ &\qquad + \left[\left(Y_{C''} - Y_{C_0''}\right) - \left(Y_{C'} - Y_{C_0'}\right) + \left(Y_{C_0''} - Y_{C_0'}\right)\right]\boldsymbol{e}_Y\big\} \cdot \boldsymbol{n}' - a\big) \\ &= h_0 + \tfrac{1}{2}\big(\big\{\left[\left(X_{C''} - X_{C_0''}\right) - \left(X_{C'} - X_{C_0'}\right)\right]\boldsymbol{e}_X + \left[\left(Y_{C''} - Y_{C_0''}\right) - \left(Y_{C'} - Y_{C_0'}\right)\right]\boldsymbol{e}_Y\big\} \cdot \boldsymbol{n}'\big) \\ &= h_0 + (\delta h)\,\tilde{h} = h_0\Big\{1 + \tfrac{1}{2}\eta\big[\left(\widetilde{X}_{C''} - \widetilde{X}_{C'}\right)\boldsymbol{e}_X + \left(\widetilde{Y}_{C''} - \widetilde{Y}_{C'}\right)\boldsymbol{e}_Y\big] \cdot \boldsymbol{n}'\Big\}.\end{aligned} \tag{3.17}$$

In the case where $\eta \ll 1$, it becomes possible to flatten the boundary conditions. This results in the rate of change in channel width as:

$$\begin{aligned}\frac{(\delta h)}{\tau}\frac{\mathrm{d}\tilde{h}}{\mathrm{d}\bar{t}} = \tfrac{1}{2}\frac{\eta h_0}{\tau}\frac{\mathrm{d}}{\mathrm{d}\bar{t}}\big[&\left(\widetilde{X}_{C''} - \widetilde{X}_{C'}\right)\boldsymbol{e}_X \\ &+ \left(\widetilde{Y}_{C''} - \widetilde{Y}_{C'}\right)\boldsymbol{e}_Y\big] \cdot \boldsymbol{n}'.\end{aligned} \tag{3.18}$$

3.2.2.2 Dynamic coupling

The coordinates of assembly's center:

$$\frac{m}{K\tau^2}\frac{\mathrm{d}^2\widetilde{X}_C}{\mathrm{d}\bar{t}^2} = -\widetilde{X}_C - \frac{D}{K\tau}\frac{\mathrm{d}\widetilde{X}_C}{\mathrm{d}\bar{t}} + \frac{(\delta p)}{\varepsilon\eta K}\,\boldsymbol{F}.\boldsymbol{e}_X \tag{3.19a}$$

$$\frac{m}{K\tau^2}\frac{\mathrm{d}^2\widetilde{Y}_C}{\mathrm{d}\bar{t}^2} = -\widetilde{Y}_C - \frac{D}{K\tau}\frac{\mathrm{d}\widetilde{Y}_C}{\mathrm{d}\bar{t}} + \frac{(\delta p)}{\varepsilon\eta K}\,\boldsymbol{F}.\boldsymbol{e}_Y. \tag{3.19b}$$

One face of the assembly is subjected to a pressure force given by the expression Eq. 3.11b:

$$\frac{(\delta p)}{\rho U^2}\int_0^1 \tilde{p}\,\mathrm{d}\bar{x} = \frac{(\delta p)}{\rho U^2}\,\tilde{p}_\mathrm{m} + \tfrac{1}{12}\left[\mathsf{St}\,\frac{\mathrm{d}}{\mathrm{d}\bar{t}}(\Delta\bar{u}) + 2(\Delta\bar{u})^2\right] + \tfrac{1}{6}\frac{C_\mathrm{f}}{\varepsilon\mathsf{Re}}\,\frac{\Delta\bar{u}}{\bar{h}}, \tag{3.20}$$

The components are determined by Eq. 3.11a and 3.12:

$$\begin{aligned}
&\mathsf{St}\,\frac{\mathrm{d}\bar{u}_\mathrm{m}}{\mathrm{d}\bar{t}} + 2\bar{u}_\mathrm{m}\,\Delta\bar{u} = -\frac{(\delta p)}{\rho U^2}\,\Delta\tilde{p} - \frac{C_\mathrm{f}}{\varepsilon\mathsf{Re}}\,\frac{\bar{u}_\mathrm{m}}{\bar{h}},\\
&\Delta\bar{u} = -\eta\mathsf{St}\,\frac{1}{\bar{h}}\,\frac{\mathrm{d}\tilde{h}}{\mathrm{d}\bar{t}}.
\end{aligned} \tag{3.21}$$

Given the number of equations and in the absence of boundary conditions, this system is clearly incomplete, we will continue on the phenomenological analysis of the physical problem.

3.2.2.3 Phenomenological analysis

3.2.2.3.1 Generality

Assemblies The assemblies are moved by an initial displacement and returned to their initial position by the elastic force. This initial displacement determines the mechanical energy stored in the system. The movement is limited by the inertial forces, the dissipation of the structure and the pressure forces.

The fluid flow is mainly driven by the variation in the width of the channels, which results in a pressure difference at the ends which constitutes the effective driving force. These forces are balanced by the forces of local inertia and by the convective forces of inertia, if the amplitude of the movement of the walls is sufficient.

Applied on momentum balance of assemblies, we will get:

$$1 = \sup\left\{\frac{m}{K\tau^2}, \frac{D}{K\tau}, \frac{(\delta p)}{\varepsilon\eta K}\right\},$$

The scale $\tau_K = \sqrt{m/K}$ is characterised of spring-mass system; it is often presented as a frequency $2\pi f_\mathrm{n} = \sqrt{K/m}$. Generally, the dissipations specific to the structure are small and the following inequality is verified: $D/(K\tau) \ll 1$. Whatever the case, this grouping makes it possible to define a characteristic time of dissipations: $\tau_D = D/K$ and $D^2 \ll Km$, $\tau_D \ll \tau_K$.

The above relationship highlights three physically permissible situations where the dissipations in the structure are definitely negligible.

▷ *Complete problem* :

$$1 \sim m/(K\tau^2) \sim (\delta p)/(\varepsilon\eta K) \quad\Longrightarrow\quad \tau \sim \tau_K \quad \text{and} \quad (\delta p) \sim \varepsilon\eta K;$$

The three efforts are of the same order.

▷ *Free movement* :

$$1 = m/(K\tau^2) \gg (\delta p)/(\varepsilon\eta K) \quad \Longrightarrow \quad \tau = \tau_K \quad \text{and} \quad (\delta p) \ll \varepsilon\eta K.$$

The influence of fluid on the movement of assemblies is negligible. This is what happens when the fluid is gaseous (air).

▷ *Quasi-static movement* :

$$1 = (\delta p)/(\varepsilon\eta K) \gg m/(K\tau^2) \quad \Longrightarrow \quad (\delta p) = \varepsilon\eta K \gg \eta m/\tau^2 \quad \text{and} \quad \tau \gg \tau_K.$$

The influence of the assemblies' inertia is negligible and the movement is aperiodic because tthe assemblies will not go beyond their position of equilibrium.

Fluid For the fluid, we have:

$$\frac{(\delta p)}{\rho U^2} = \sup\left\{\mathsf{St},\, 1,\, \frac{C_\mathrm{f}}{\varepsilon \mathsf{Re}}\right\} \quad \text{where} \quad \mathsf{St} = \frac{b}{U\tau} \quad \text{and} \quad \mathsf{Re} = \frac{Uh_0}{\nu} \quad \text{with} \quad h_0 = \varepsilon b.$$

$$(\delta h) = \eta h_0 \quad \Longrightarrow \quad U_\mathrm{e} = \eta h_0/\tau \quad \Longrightarrow \quad U_\mathrm{e}/U = \varepsilon\eta\,\mathsf{St}.$$

And:

$$\eta\,\mathsf{St} = 1. \tag{3.22}$$

Indeed, given the non-penetration condition, a value different from ηSt would either lead to $\bar{v}_{|\bar{h}} = 0$ or $\mathrm{d}\bar{h}/\mathrm{d}\bar{t} = 0$, both results are invalid. Consequently, $U_\mathrm{e}/U = \varepsilon \ll 1$, the entrainment forces of inertia are always negligible with regard to the convective forces and are therefore always neglected in the case following.

3.2.2.3.2 Complete problem

$$\tau = \tau_K = \sqrt{m/K}, \quad U = \eta b/\tau_K \quad \text{and} \quad (\delta p) = \varepsilon\eta K.$$

These relations are constrained by the two parameters: $\varepsilon \ll 1$ (confinement parameter) and $\eta \leq 1$ (amplitude parameter). The scales of flow are solutions of the equations at the following order:

$$\frac{\varepsilon\eta K}{\rho U^2} = \sup\left\{\mathsf{St},\, 1,\, \frac{C_\mathrm{f}}{\varepsilon \mathsf{Re}}\right\} \quad \text{where} \quad \mathsf{St} = 1/\eta \geq 1, \tag{3.23}$$

This will have several solutions depending on the value of STROUHAL number:

Low STROUHAL number $\mathsf{St} \ll 1$. This case is excluded.

STROUHAL number at order 1 $\mathsf{St} \sim 1$. We will have:

$$\eta \sim 1, \quad \varepsilon \sim \eta\,\gamma \quad \text{and} \quad C_\mathrm{f} \sim \eta\, h_0^2/(\nu\tau_K) \quad \text{where} \quad \gamma = \rho b^2/m.$$

High STROUHAL number $\mathsf{St} = 1/\eta \gg 1$. The convective force are negligible and the equation are linearised. The boundary conditions can be flattened.

▷ *Complete problem :* pressure ∼ local inertia ∼ friction.

$$\frac{\varepsilon\eta K}{\rho U^2} \sim \mathsf{St} \sim \frac{C_\mathrm{f}}{\varepsilon \mathsf{Re}}.$$

$$\varepsilon = \gamma \ll 1 \quad \text{and} \quad C_\mathrm{f} = h_0^2/(\nu\tau_K).$$

Therefore, the pressure scale: $(\delta p) = \eta\gamma K$. In the case where the first approximation is not satisfied ($\epsilon > \gamma$), the 1D approximation of fluid flow will no longer be valid.

▷ *Perfect-fluid approximation :* pressure ∼ inertia ≫ friction ; this configuration is in contradiction with the hypothesis of viscous fluid.

$$\frac{\varepsilon\eta K}{\rho U^2} = \mathsf{St} \gg \frac{C_\mathrm{f}}{\varepsilon \mathsf{Re}}.$$

$$\varepsilon = \gamma \ll 1 \quad \text{and} \quad C_\mathrm{f} \ll h_0^2/(\nu\tau_K).$$

$(\delta p) = \eta\gamma K$.

▷ STOKES *approximation:* pressure ∼ friction ≫ inertia.

$$\frac{\varepsilon\eta K}{\rho U^2} = \frac{C_\mathrm{f}}{\varepsilon \mathsf{Re}} \gg \mathsf{St}.$$

The movement of the assembly is aperiodic.

$$C_\mathrm{f}\gamma = \varepsilon h_0^2/(\nu\tau_K) \quad \text{and} \quad C_\mathrm{f} \gg h_0^2/(\nu\tau_K).$$

The scale of pressure: $(\delta p) = \varepsilon\eta K$.

3.2.2.3.3 Other movements

Free movement The movement of the assembly is not affected by the presence of the fluid, in first approximation. The only coupling between the motion of the assembly and the fluid flow is imposed by the non-penetration condition which is always written as $\eta\mathsf{St} = 1$. On the other hand, the relation $(\delta p) = \varepsilon\eta K$ is no longer applicable.

Quasi-static movements In first approximation, the inertia of the assembly is negligible and the problem is quasi-static, there is a succession of equilibrium between the restoring force and the pressure forces. The pressure scale is given by this equilibrium $(\delta p) = \varepsilon\eta K$, the time scale is imposed as $\tau \gg \tau_K$.

3.2.2.3.4 Comments

By limiting itself to the case of the complete problem for the dynamics of assemblies where three scales are determined:

$$\tau = \tau_K, \quad U = \eta b/\tau_K \quad \text{and} \quad (\delta p) = \varepsilon\eta K,$$

the fluid flow is controlled by two basic parameters:

$$\mathsf{St} = 1/\eta \geq 1 \quad \text{and} \quad \Pi = C_\mathrm{f}\,\nu\tau_K/h_0^2 > 0.$$

3.2.2.4 Mesh

To describe the geometry properly, a system of numbering has to be introduced (see FIGURE 3.11).

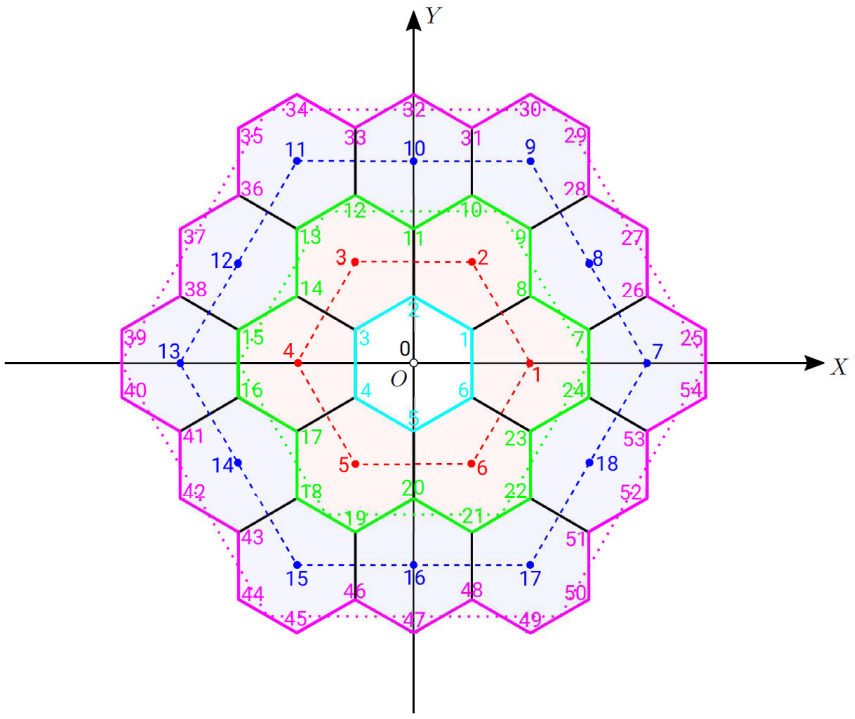

FIGURE 3.11: Geometry of PISE-2C

3.2.2.4.1 Terminology

PISE-2C can be broken down into several families of similar objects: nodes, channels, assemblies and crowns.

Channels The channels, represented by segments, are the regions between the two facing surfaces of two adjacent assemblies. Referring to FIGURE 3.11, the radial channels (black) and the circumferential channels (cyan and green) are distinguished. Conventionally, the radial channels are oriented from the center to the outside of the mock-up while the circumferential channels are oriented in the trigonometric direction (FIGURE 3.12). These channels can be grouped into crowns (dotted line). The outer faces, coloured in magenta (FIGURE 3.11), are, so to speak, characterised with half-channels. They comply with the same convention of orientation.

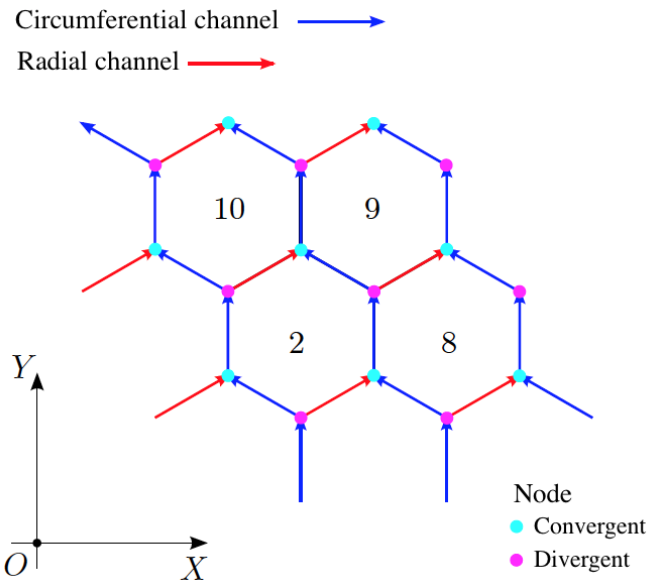

FIGURE 3.12: Orientations of channels

Nodes The nodes are the point representation of the region where three channels meet. Depending on their location, and taking into account the convention of channel orientation, it is necessary to distinguish the convergent nodes from the divergent nodes (FIGURE 3.12). A convergent node is characterised with two channels that merge into one. Conversely, a divergent node is where one single channel divides into two. The nodes can be associated by crown. More simply, the nature of a node is determined by the radial channel: converge if the radial channel injects into the node, diverge if the radial channel ejects from the node.

Of course, an exception must be made for nodes which are associated with only one channel and are named outlets.

Assemblies Channels and nodes are associated with two or three assemblies. These assemblies are grouped by crowns: inner crown (one assembly, white), median crown (6 assemblies, light rose) and outer crown (12 assemblies, light blue) (FIGURE 3.11).

The centres of the assemblies on the same crown are distributed on a hexagon (dashed line). Each assembly has 6 vertices. A node is therefore the union of three or two vertices.

3.2.2.4.2 Numbering

Nodes The principal numbering system is that of the nodes. To avoid ambiguity, each node receives an unique number. This numbering develops from the center O (see FIGURE 3.11), following a centrifugal spiral. For example, crowns consist of the following nodes:

- ▷ internal crown (cyan) : $\mathbb{N}_{\mathrm{i}} = \{1, 2, \cdots, 6\}$, $\mathrm{Card}(\mathbb{N}_{\mathrm{i}}) = 6$;
- ▷ median crown (green) : $\mathbb{N}_{\mathrm{m}} = \{7, 8, \cdots, 24\}$, $\mathrm{Card}(\mathbb{N}_{\mathrm{m}}) = 18$;
- ▷ external crown (magenta) : $\mathbb{N}_{\mathrm{e}} = \{25, 26, \cdots, 54\}$, $\mathrm{Card}(\mathbb{N}_{\mathrm{e}}) = 30$.

To distinguish the convergent nodes (cyan, FIGURE 3.12) and divergent nodes (magenta, FIGURE 3.12):

▷ internal crown (cyan) :

- convergent nodes : $\mathbb{N}_{\mathrm{i}}^{\mathrm{c}} = \emptyset$, $\mathrm{Card}(\mathbb{N}_{\mathrm{i}}^{\mathrm{c}}) = 0$;
- divergent nodes : $\mathbb{N}_{\mathrm{i}}^{\mathrm{d}} = \{1, 2, \cdots, 6\}$, $\mathrm{Card}(\mathbb{N}_{\mathrm{i}}^{\mathrm{d}}) = 6$;

▷ median crown (green) :

- convergent nodes : $\mathbb{N}_{\mathrm{m}}^{\mathrm{c}} = \{8, 11, 14, 17, 20, 23\}$, $\mathrm{Card}(\mathbb{N}_{\mathrm{m}}^{\mathrm{c}}) = 6$;
- divergent nodes : $\mathbb{N}_{\mathrm{m}}^{\mathrm{d}} = 7, 9, 10, 12, 13, 15, 16, 18, 19, 21, 22, 24\}$, $\mathrm{Card}(\mathbb{N}_{\mathrm{m}}^{\mathrm{d}}) = 12$;

▷ external crown (magenta) :

- outlets : $\mathbb{N}_{\mathrm{e}}^{\mathrm{e}} = \{26, 28, 31, 33, 36, 38, 41, 43, 46, 48, 51, 53\}$, $\mathrm{Card}(\mathbb{N}_{\mathrm{e}}^{\mathrm{e}}) = 12$;
- summits : $\mathbb{N}_{\mathrm{e}}^{\mathrm{s}} = \{25, 27, 29, 30, 32, 34, 35, 37, 39, 40, 42, 44, 45, 47, 49, 50, 52, 54\}$, $\mathrm{Card}(\mathbb{N}_{\mathrm{e}}^{\mathrm{s}}) = 18$.

Assemblies The numbering of the assemblies is also unique and develops like that of the nodes, from the center, to the outside, according to each crown.

▷ central assembly (white) : $\mathbb{K}_{\mathrm{c}} = \{0\}$, $\mathrm{Card}(\mathbb{K}_{\mathrm{i}}) = 1$;

▷ internal crown (light rose) : $\mathbb{K}_{\mathrm{i}} = \{1, 2, 3, 4, 5, 6\}$, $\mathrm{Card}(\mathbb{K}_{\mathrm{m}}) = 6$;

▷ external crown (light blue) : $\mathbb{K}_{\mathrm{e}} = \{7, 8, 9, 10, 11, 12, 13, 14, 15, 16, 17, 18\}$, $\mathrm{Card}(\mathbb{K}_{\mathrm{e}}) = 12$.

- summits : $\mathbb{K}_{\mathrm{e}}^{\mathrm{s}} = \{7, 9, 11, 13, 15, 17\}$,
- medians : $\mathbb{K}_{\mathrm{e}}^{\mathrm{m}} = \{8, 10, 12, 14, 16, 18\}$.

Channels The numbering of the channels is more intricate because it is necessary to distinguish the radial channels, the circumferential channels and the external faces. The solution chosen consists in identifying a channel by its nodes in accordance with the convention (see FIGURE 3.12). This is a rather cumbersome solution but without ambiguity:

▷ Radial channel :

- internal crown : $\mathbb{R}_{\mathrm{i}} = \{1-8, 2-11, 3-14, \cdots, 6-23\}$, $\mathrm{Card}(\mathbb{R}_{\mathrm{i}}) = 6$;
- external crown : $\mathbb{R}_{\mathrm{e}} = \{7-26, 9-28, 10-31, \cdots, 24-53\}$, $\mathrm{Card}(\mathbb{R}_{\mathrm{e}}) = 12$;

▷ Circumferential channel :

- internal crown : $\mathbb{C}_{\mathrm{i}} = \{1-2, 2-3, 3-4, \cdots, 6-1\}$, $\mathrm{Card}(\mathbb{C}_{\mathrm{i}}) = 6$;
- external crown : $\mathbb{C}_{\mathrm{e}} = \{7-8, 8-9, 9-10, \cdots, 24-7\}$, $\mathrm{Card}(\mathbb{C}_{\mathrm{e}}) = 18$;
- external faces : $\mathbb{F}_{\mathrm{e}} = \{25-26, 26-27, 28-29, \cdots, 54-25\}$, $\mathrm{Card}(\mathbb{F}_{\mathrm{e}}) = 30$.

3.2.2.5 Countings

3.2.2.5.1 Unknowns

In this $1D$ model, in addition to the coordinates at the centres of the assemblies, the unknowns come from the fluid flow and are essentially associated with the ends of the channels. There are four variables: two velocities and two pressures, altogether with the coordinates, making 6 unknowns per internal or external node. However, the outlets are associated with only two unknowns (one velocity and one pressure). The pressures on the external faces must also be taken into account.
• *Counts* :

▷ 2 coordinates by the assembly's center :
$$2 \times [\mathrm{card}\,(\mathbb{K}_{\mathrm{i}}) + \mathrm{card}\,(\mathbb{K}_{\mathrm{e}})] = 36\ ;$$

▷ 3 pressures and 3 velocities for nodes on internal and median crown :
$$6 \times [\mathrm{card}\,(\mathbb{N}_{\mathrm{i}}) + \mathrm{card}\,(\mathbb{N}_{\mathrm{m}})] = 144\ ;$$

▷ 1 pressure and 1 velocity for nodes on external crown :
$$2 \times \mathrm{card}\,(\mathbb{N}_{\mathrm{e}}^{\mathrm{e}}) = 24\ ;$$

▷ 1 pressure on external face :
$$\mathrm{card}\,(\mathbb{F}_{\mathrm{e}}) = 30.$$

In total, the problem comports 234 unknowns.

3.2.2.5.2 Equations

Conditions at nodes In all cases, for all nodes, we should have mass conservation and the equality of pressures (subject to adaptation to the nature of the node, convergent or divergent). In all cases, a node combines two circumferential channels (numbered c_1 and c_2) and a radial channel denoted by r_0 (see FIGURE 3.12):

▷ convergent node ($r_0 \cup c_1 \longrightarrow c_2$) :
$$\bar{u}_{r_0|1} + \bar{u}_{c_1|1} = \bar{u}_{c_2|0} \quad \text{and} \quad \tilde{p}_{r_0|1} = \tilde{p}_{c_1|1} = \tilde{p}_{c_2|0}, \tag{3.24}$$
Where the index 0 or 1 indicates the origin or the ends of the channel.

▷ divergent node ($c_1 \longrightarrow c_2 \cup r_0$) :
$$\bar{u}_{c_1|1} = \bar{u}_{c_2|0} + \bar{u}_{r_0|0} \quad \text{and} \quad \tilde{p}_{r_0|0} = \tilde{p}_{c_1|1} = \tilde{p}_{c_2|0}. \tag{3.25}$$

These conditions can be reformulated in terms of averages and variations:

$$\begin{aligned}
&\bar{u}_{\mathrm{m},c_1} - \bar{u}_{\mathrm{m},c_2} + \bar{u}_{\mathrm{m},r_0} + \tfrac{1}{2}\big(\Delta\bar{u}_{c_1} + \Delta\bar{u}_{c_2} + \Delta\bar{u}_{r_0}\big) = 0 \qquad &&\text{: convergent node ;}\\
&\bar{u}_{\mathrm{m},c_1} - \bar{u}_{\mathrm{m},c_2} - \bar{u}_{\mathrm{m},r_0} + \tfrac{1}{2}\big(\Delta\bar{u}_{c_1} + \Delta\bar{u}_{c_2} + \Delta\bar{u}_{r_0}\big) = 0 \qquad &&\text{: divergent node .}
\end{aligned}$$

The state of each node is specified by a condition on the velocities (mass conservation) and two conditions on the pressures (equality). There are no conditions on velocities of outlets but the pressure is known.

Conditions on external faces As has just been mentioned, the pressure exerted on the external faces is known.

Counting of equations The problem statement consists of a set of differential equations and algebraic equations.

- ▷ Eq. 3.19 of assembly's movement (2 coordinates) :
  $2 \times [\mathrm{Card}(\mathbb{K}_\mathrm{i}) + \mathrm{Card}(\mathbb{K}_\mathrm{e})] = 36$;
- ▷ Eq. 3.21 of fluid movement in the channels (mass and momentum) :
  $2 \times [\mathrm{Card}(\mathbb{R}_\mathrm{i}) + \mathrm{Card}(\mathbb{R}_\mathrm{e}) + \mathrm{Card}(\mathbb{C}_\mathrm{i}) + \mathrm{Card}(\mathbb{C}_\mathrm{e})] = 84$;
- ▷ Eq. 3.24 and 3.25 at nodes (mass conservation and 2 legalities of pressure) :
  $3 \times [\mathrm{Card}(\mathbb{N}_\mathrm{i}) + \mathrm{Card}(\mathbb{N}_\mathrm{m})] = 72$;
- ▷ conditions at outlets (pressure) :
  $\mathrm{Card}(\mathbb{N}_\mathrm{e}^\mathrm{e}) = 12$;
- ▷ conditions on external faces (pressure) :
  $\mathrm{Card}(\mathbb{F}_\mathrm{e}) = 30$.

The number of equations are as much as 234 to close the system.

3.2.3 Resolution

The resolution of an algebra-differential system from 234 equations to 234 unknowns is out of reach and it is necessary to start with simplifying the statement by taking advantage of the symmetries to reduce the dimension of the problem. This deductive approach gives a complete picture of the symmetries of the mock-up and the resulting simplifications. However, it is not the one adopted during the equation for which an inductive approach is preferred, based on an apriori and intuitive scheme.

3.2.3.1 Notations

The following notations are introduced for formulation:

$$m^* = \frac{m}{K\tau^2}, \quad D^* = \frac{D}{K\tau}, \quad \mathsf{Eu} = \frac{(\delta p)}{\rho U^2} \quad \text{and} \quad C_\mathrm{f}^* = \frac{C_\mathrm{f}}{\varepsilon \mathsf{Re}}.$$

3.2.3.2 Trivial simplifications

Efforts on faces The pressures on the external faces are all equal to each other and have the value of the initial pressure p_0:

$$\forall\, n \in \mathbb{F}_\mathrm{e} \ : \quad \overline{\boldsymbol{F}}_n = 0.$$

Therefore, we can eliminate $\mathrm{card}\,(\mathbb{F}_\mathrm{e}) = 30$ unknowns and 30 equations.

Pressure at outlets For the same reason, the pressures at the outlets are also equal to the external pressure:

$$\forall\, n \in \mathbb{N}_\mathrm{e}^\mathrm{e} \ : \quad \tilde{p}_n = 0,$$

This will reduce the dimension of system by $\mathrm{card}\,(\mathbb{N}_\mathrm{e}^\mathrm{e}) = 12$ unknowns and equations.

Pressure at nodes Since there is equal pressure on nodes, there is no need to keep three values, it is enough to retain only one value and to assign to it the number of the node. It can reduce the system by $2 \times [\mathrm{card}\,(\mathbb{N}_\mathrm{i}) + \mathrm{card}\,(\mathbb{N}_\mathrm{m})] = 48$ unknowns.

3.2.3.3 Kinematic constraints

By construction, the center of the assemblies are constrained to move on the radial direction. Therefore, its position is determined by a single coordinate Z: $Z = X/\alpha = Y/\beta$, $\alpha = \cos\theta$ and $\beta = \sin\theta$ (see FIGURE 3.13).

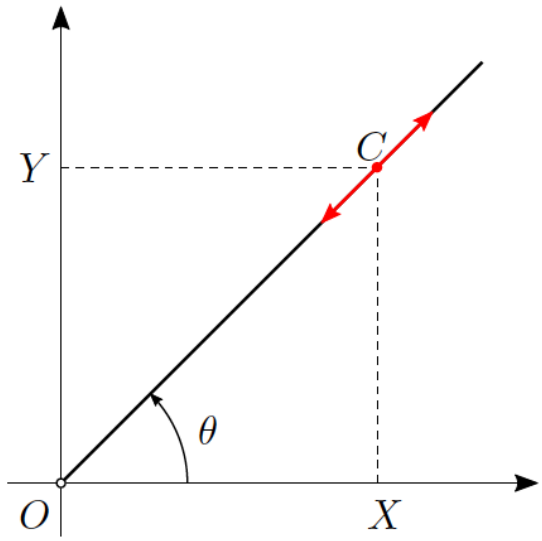

FIGURE 3.13: Kinematic constraints

$$Z = Z_0 + \eta h_0\,\widetilde{Z} \quad \text{where} \quad \begin{cases} Z_0 & = X_0/\alpha = Y_0/\beta, \\ \widetilde{Z} & = \widetilde{X}/\alpha = \widetilde{Y}/\beta. \end{cases} \tag{3.26}$$

In these terms, Eq. 3.19 of assembly's movement can be written as:

$$m^* \frac{\mathrm{d}^2\widetilde{Z}}{\mathrm{d}\bar{t}^2} = -\widetilde{Z} - D^* \frac{\mathrm{d}\widetilde{Z}}{\mathrm{d}\bar{t}} + \frac{(\delta p)}{\varepsilon\eta K}\,\overline{F}, \tag{3.27}$$

This imposes the condition:

$$\overline{F} = (\overline{\boldsymbol{F}}.\boldsymbol{e}_X)/\alpha = (\overline{\boldsymbol{F}}.\boldsymbol{e}_Y)/\beta \quad \Longleftrightarrow \quad (\beta\,\boldsymbol{e}_X - \alpha\,\boldsymbol{e}_Y)\cdot\overline{\boldsymbol{F}} = 0,$$

which replaces 18 integral conditions on the pressure field with 18 differential equations.

3.2.3.4 Symmetries

The objective of this section is to show the symmetries which allows to limit the study on only one sixth of the whole mock-up (see FIGURE 3.14):

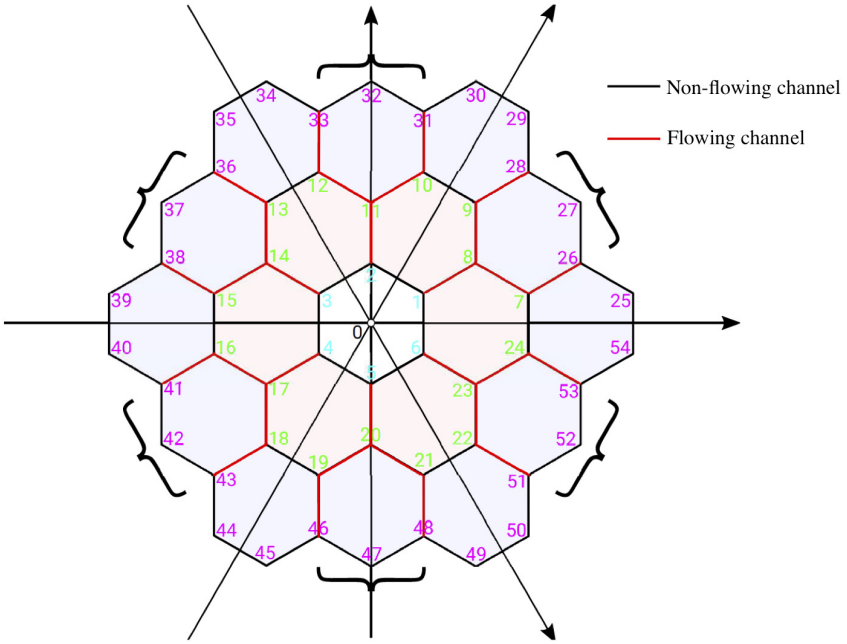

FIGURE 3.14: Privileged path

3.2.3.4.1 Assemblies

Due to the kinematic constraints and the uniformity of the external pressure, it is intuitive to assume that the movements of two assemblies occupying symmetrical positions with respect to the center O of the core are symmetrical; they are grouped in the table below:

Central symmetry						
Crown $\mathbb{K}_i$	1-4		2-5		3-6	
Crown $\mathbb{K}_e$	7-13	8-14	9-15	10-16	11-17	12-18

Another property to be observed is the invariance of the figure by rotations of $\pi/6$. Since the kinematic constraints and the initial conditions are given with the same symmetry, it follows that the movements of the assemblies are identified by radial vectors grouped in the table below:

Invariance by rotation		
Angle	Summits	Medians
0	7-1-0-4-13	8-0-14
$\pi/6$	9-2-0-5-15	10-0-16
$\pi/3$	11-3-0-6-17	12-0-18

Moreover, it is sufficient to examine a half radial vector because of the central symmetry.

3.2.3.4.2 Channels

Similar properties of the flow characteristics can be deduced from the symmetry of the channels. The table below shows the radial channels regrouped with the assemblies.

Crown	$\mathbb{K}_i$		$\mathbb{K}_e$			
Assembly	1	2	7	8	9	10
Radial channel	6-23 1-8	1-8 2-11	24-53 7-26	7-26 9-28	9-28 10-31	10-31 12-33

In the table above, the assemblies are identified by the numbers of the centres while the radial channels which associate with them are marked by the numbers of their ends.

It thus appears, by transitivity, that the dynamic conditions (velocities, pressures) which prevail in a crown of radial channels are identical. For example, since channels 7-26 and 24-53 ,also 7-26 and 9-28 are identified by symmetry, it results that channels 24-53 and 9-28 are also identified.

However, there is no reason for these conditions to be identical for the two radial channel rings $\mathbb{R}_i$ and $\mathbb{R}_e$ which imposes certain properties on the flows of the circumferential channels $\mathbb{C}_i$ and $\mathbb{C}_e$. In the first place, we must distinguish those that are connected to two radial channels belonging to the same crown (this is the case for all the channels of $\mathbb{C}_i$).

$\mathbb{C}_i^n$	1-2	2-3	3-4	4-5	5-6	6-1

They have the peculiarity of being subjected to the same pressure at each of their ends. Consequently, the mean velocity is zero or what amounts to the same, the velocities at the ends are equal and opposite. For this reason they are assigned the exponent «n» indicating that they are non-flowing; however, the volume of fluid contained varies as a function of the distance of the facing faces.

The other circumferential channels interconnect the two crowns $\mathbb{R}_i$ and $\mathbb{R}_e$: these are the channels through which the fluid aspirated or discharged by the core. More precisely, as a consequence of the orientation conventions, the average velocity are equal and opposite. These considerations lead us to distinguish two families in the $\mathbb{C}_e$ crown: the non-flowing channels $\mathbb{C}_e^n$ and the flowing channels $\mathbb{C}_e^d$:

$\mathbb{C}_e^n$	24-7	9-10	12-13	15-16	18-19	21-22
$\mathbb{C}_e^d$	7-8-9	10-11-12	13-14-15	16-17-18	19-20-21	22-23-24

There are thus 6 independent privileged paths (see FIGURE 3.14), with identical characteristics:

$$1 \to 8 \to \begin{cases} 7 \to 26 \\ 9 \to 28 \end{cases} \qquad 2 \to 11 \to \begin{cases} 10 \to 31 \\ 12 \to 33 \end{cases} \qquad 3 \to 14 \to \begin{cases} 13 \to 36 \\ 15 \to 38 \end{cases}$$

$$4 \to 17 \to \begin{cases} 16 \to 41 \\ 18 \to 43 \end{cases} \qquad 5 \to 20 \to \begin{cases} 19 \to 46 \\ 21 \to 48 \end{cases} \qquad 6 \to 23 \to \begin{cases} 22 \to 51 \\ 24 \to 53 \end{cases}$$

More precisely, given a non-flowing channel identified by its order number «c», the flow that runs through is subject to the condition:

$$\bar{u}_{m,c} = 0 \quad \Longleftrightarrow \quad \bar{u}_{c|0} + \bar{u}_{c|1} = 0, \tag{3.28}$$

where the indices «0» and «1» designate respectively the origin and the end of the channel, in accordance with the orientation conventions. Also the distribution channels are associated by pairs of order numbers «c» and «$c+1$», on the same crown of circumferential channels,

the symmetry of the flows is expressed by:

$$\bar{u}_{\mathrm{m},c} + \bar{u}_{\mathrm{m},c+1} = 0 \quad \Longleftrightarrow \quad \begin{cases} \bar{u}_{c|1} + \bar{u}_{c+1|0} & = 0, \\ \bar{u}_{c|0} + \bar{u}_{c+1|1} & = 0. \end{cases} \tag{3.29}$$

3.2.3.5 Counting

3.2.3.5.1 Assemblies

The central symmetry and the rotational invariance make it possible to eliminate all assemblies of the internal crown $\mathbb{K}_{\mathrm{i}}$ except one, and to keep only one summit and one median for the outer crown $\mathbb{K}_{\mathrm{e}}$, :

- ▷ $a \in \mathbb{K}_{\mathrm{i}}$: $\widetilde{Z}_a = \widetilde{Z}_{\mathrm{i}}$;
- ▷ $a \in \mathbb{K}_{\mathrm{e}}^{\mathrm{s}}$: $\widetilde{Z}_a = \widetilde{Z}_{\mathrm{e}}^{\mathrm{s}}$, summits ;
- ▷ $a \in \mathbb{K}_{\mathrm{e}}^{\mathrm{m}}$: $\widetilde{Z}_a = \widetilde{Z}_{\mathrm{e}}^{\mathrm{m}}$, midians.

It therefore remains three coordinates: $\widetilde{Z}_{\mathrm{i}}$, $\widetilde{Z}_{\mathrm{e}}^{\mathrm{s}}$ and $\widetilde{Z}_{\mathrm{e}}^{\mathrm{m}}$; in other words, 15 unknowns and 15 equations are thus eliminated on 18 assemblies. More precisely, by limiting itself to the first scheme: $\widetilde{Z}_{\mathrm{i}} = \widetilde{Z}_1$, $\widetilde{Z}_{\mathrm{e}}^{\mathrm{s}} = \widetilde{Z}_7$ and $\widetilde{Z}_{\mathrm{e}}^{\mathrm{m}} = \widetilde{Z}_8$ (see FIGURE 3.15).

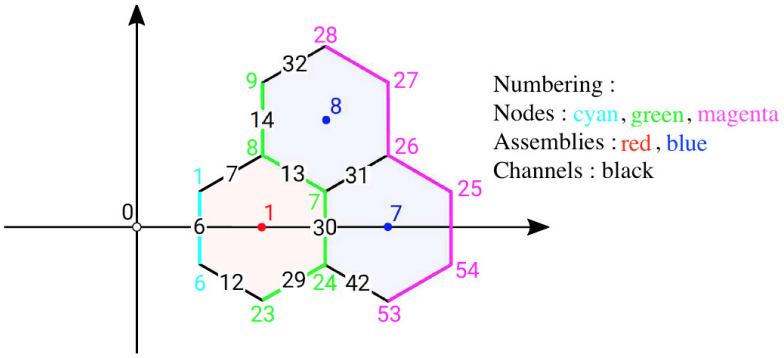

FIGURE 3.15: Minimised version

3.2.3.5.2 Pressure

These are pressures at the nodes. Due to the properties of the radial channel crowns, the pressures are uniform on the crowns $\mathbb{N}_{\mathrm{i}}$, $\mathbb{N}_{\mathrm{m}}^{\mathrm{c}}$ and $\mathbb{N}_{\mathrm{m}}^{\mathrm{d}}$:

- ▷ $n \in \mathbb{N}_{\mathrm{i}}$: $\tilde{p}_n = \tilde{p}_{\mathrm{i}}$;
- ▷ $n \in \mathbb{N}_{\mathrm{m}}^{\mathrm{c}}$: $\tilde{p}_n = \tilde{p}_{\mathrm{m}}^{\mathrm{c}}$, convergent nodes ;
- ▷ $n \in \mathbb{N}_{\mathrm{m}}^{\mathrm{d}}$: $\tilde{p}_n = \tilde{p}_{\mathrm{m}}^{\mathrm{d}}$, divergent nodes.

Like for the coordinates, there remains three unknown pressures: $\tilde{p}_{\mathrm{i}}$, $\tilde{p}_{\mathrm{m}}^{\mathrm{c}}$ and $\tilde{p}_{\mathrm{m}}^{\mathrm{d}}$, which amounts to eliminating 21 out of 24 unknowns. Moreover, these pressures are subject to 3 integral conditions:

$$\tilde{p}_1 = \tilde{p}_2 = \tilde{p}_3 = \tilde{p}_4 = \tilde{p}_5 = \tilde{p}_6 = \tilde{p}_{\mathrm{i}},$$
$$\tilde{p}_8 = \tilde{p}_{11} = \tilde{p}_{14} = \tilde{p}_{17} = \tilde{p}_{20} = \tilde{p}_{23} = \tilde{p}_{\mathrm{m}}^{\mathrm{c}},$$
$$\tilde{p}_9 = \tilde{p}_{10} = \tilde{p}_{12} = \tilde{p}_{13} = \tilde{p}_{15} = \tilde{p}_{16} = \tilde{p}_{18} = \tilde{p}_{19} = \tilde{p}_{21} = \tilde{p}_{22} = \tilde{p}_{24} = \tilde{p}_7 = \tilde{p}_{\mathrm{m}}^{\mathrm{d}}.$$

3.2.3.5.3 Reduction of problem

The reduction of the problem's dimension results from the apparent symmetries in FIGURE 3.15 (see also FIGURE 3.16) and the observations made in sections 3.2.3.5.1 and 3.2.3.5.2. The core can be divided into 6 sectors whose characteristics are deduced by rotations of $\pi/6$. The problem can therefore be reduced to that shown schematically in FIGURE 3.15.

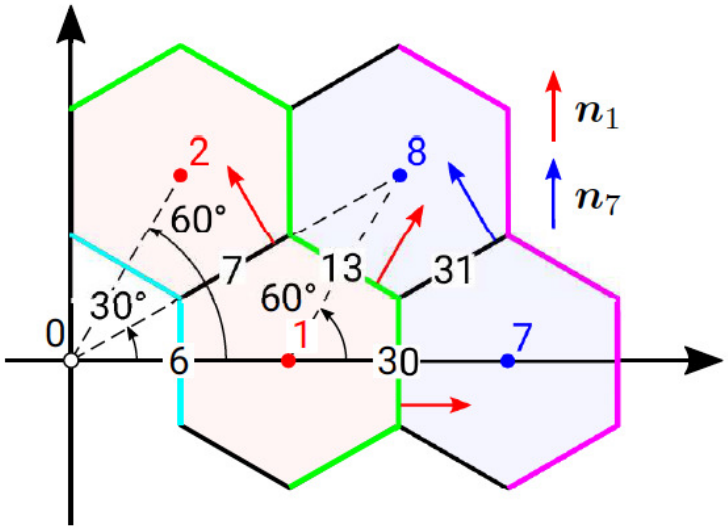

FIGURE 3.16: PISE-2C, angles

Rather than proceeding by successive reductions, the chosen approach is inductive and consists in display, from FIGURE 3.15, that the problem has a solution and only one solution. The elements to consider are:

- Assemblies (3) : 1, 7 and 8.
- Channels (10) : 6, 7, 12, 13, 14, 29, 30, 31, 32 and 42.
- Nodes (10) : 1, 6, 7, 8, 9, 23, 24, 26, 28 and 53.

Assemblies Each assembly is determined by its position over time and a differential equation for the unknown $\widetilde{Z}(\bar{t})$ (see section 3.2.3.3).

Channels The flow in each channel is governed by two differential equations (see Section 3.2.2.2). The circumferential channels 6 and 30 are non-flowing while the channels 13, 14 and 29 are flowing; the channels 13 and 14 are symmetrical. The radial channels 7 and 12 on the one hand, the channels 31, 32 and 42 on the other hand are respectively situated on the same crown and are therefore identical. After eliminating the channels whose characteristics can be deduced from those of another, there are 10 representatives: 6, 30 (non-flowing), 13 (flowing) 7 and 31 (radial), or 20 differential equations.

Nodes Each node is characterised by one pressure and three velocities.

Pressure

Due to the invariance by rotation of the radial channels, the pressures are uniform on each

crown, namely 1, 6, then 8, 23, then 7, 9, 24 and finally 26, 28 and 53. Note that the last three are null. There are therefore only 3 representatives: 1, 7 and 8.

Velocities

The velocities are connected by the mass balance of each node but also by relations resulting from the symmetries. Each channel having two ends, it is necessary to start by distinguishing 20 different values. By locating a velocity by the channel number «c» and the node number «n», it is denoted $\bar{u}_{c|n}$. In the following table, the nodes are displayed in accordance with the orientation convention, which means that the first of the two velocities of one pair is the one at the origin of the channel and the other of that at the end:

$\bar{u}_{6\|6} \to \bar{u}_{6\|1}$	$\bar{u}_{7\|1} \to \bar{u}_{7\|8}$	$\bar{u}_{12\|6} \to \bar{u}_{12\|23}$	$\bar{u}_{13\|7} \to \bar{u}_{13\|8}$	$\bar{u}_{14\|8} \to \bar{u}_{14\|9}$
$\bar{u}_{29\|23} \to \bar{u}_{29\|24}$	$\bar{u}_{30\|24} \to \bar{u}_{30\|7}$	$\bar{u}_{31\|7} \to \bar{u}_{31\|26}$	$\bar{u}_{32\|9} \to \bar{u}_{32\|28}$	$\bar{u}_{42\|24} \to \bar{u}_{42\|53}$

These velocities intervene firstly in the mass balance at each node:

$$\begin{aligned}
\bar{u}_{6|1} &= \bar{u}_{1|1} + \bar{u}_{7|1} && \text{: node 1, divergent ;}\\
\bar{u}_{5|6} &= \bar{u}_{6|6} + \bar{u}_{12|6} && \text{: node 6, divergent ;}\\
\bar{u}_{30|7} &= \bar{u}_{13|7} + \bar{u}_{31|7} && \text{: node 7, divergent ;}\\
\bar{u}_{7|8} &= \bar{u}_{14|8} - \bar{u}_{13|8} && \text{: node 8, convergent ;}\\
\bar{u}_{14|9} &= \bar{u}_{15|9} + \bar{u}_{32|9} && \text{: node 9, divergent ;}\\
\bar{u}_{12|23} &= \bar{u}_{29|23} - \bar{u}_{41|23} && \text{: node 23, convergent ;}\\
\bar{u}_{29|24} &= \bar{u}_{30|24} + \bar{u}_{42|24} && \text{: node 24, divergent.}
\end{aligned}$$

The relations of symmetries:

$$\begin{aligned}
&\bar{u}_{1|1} = -\bar{u}_{6|1}, \quad \bar{u}_{5|6} = -\bar{u}_{6|6}, \quad \bar{u}_{6|1} = -\bar{u}_{6|6}, \quad \bar{u}_{7|1} = \bar{u}_{12|6}, \quad \bar{u}_{7|8} = \bar{u}_{12|23},\\
&\bar{u}_{13|7} = -\bar{u}_{14|9}, \quad \bar{u}_{13|7} = -\bar{u}_{29|24}, \quad \bar{u}_{13|8} = -\bar{u}_{14|8}, \quad \bar{u}_{13|8} = -\bar{u}_{29|23}, \quad \bar{u}_{15|9} = -\bar{u}_{30|7},\\
&\bar{u}_{30|7} = -\bar{u}_{30|24}, \quad \bar{u}_{31|7} = \bar{u}_{32|9}, \quad \bar{u}_{31|7} = \bar{u}_{42|24}, \quad \bar{u}_{31|26} = \bar{u}_{32|28}, \quad \bar{u}_{31|26} = \bar{u}_{42|53}.
\end{aligned}$$

After eliminating the velocities by means of these latter relations and starting with the nodes with the highest index, the table becomes:

~~$\bar{u}_{6\|6}$~~ $\to \bar{u}_{6\|1}$	$\bar{u}_{7\|1} \to \bar{u}_{7\|8}$	~~$\bar{u}_{12\|6}$~~ $\to$ ~~$\bar{u}_{12\|23}$~~	$\bar{u}_{13\|7} \to \bar{u}_{13\|8}$	~~$\bar{u}_{14\|8}$~~ $\to$ ~~$\bar{u}_{14\|9}$~~
~~$\bar{u}_{29\|23}$~~ $\to$ ~~$\bar{u}_{29\|24}$~~	~~$\bar{u}_{30\|24}$~~ $\to \bar{u}_{30\|7}$	$\bar{u}_{31\|7} \to \bar{u}_{31\|26}$	~~$\bar{u}_{32\|9}$~~ $\to$ ~~$\bar{u}_{32\|28}$~~	~~$\bar{u}_{42\|24}$~~ $\to$ ~~$\bar{u}_{42\|53}$~~

It remains to apply mass balances to eliminate $\bar{u}_{7|1} = 2\bar{u}_{6|1}$, $\bar{u}_{31|7} = \bar{u}_{30|7} - \bar{u}_{13|7}$ and $\bar{u}_{13|8} = -\frac{1}{2}\bar{u}_{7|8}$, so that the list of unknown velocities can be summarised as:

$$\bar{u}_{6|1}, \quad \bar{u}_{7|8}, \quad \bar{u}_{13|7}, \quad \bar{u}_{30|7} \quad \text{and} \quad \bar{u}_{31|26}.$$

Therefore,

$$\begin{aligned}
&\text{channel 6 :} && \bar{u}_{\mathrm{m},6} = 0, && \Delta\bar{u}_6 = 2\bar{u}_{6|1},\\
&\text{channel 7 :} && \bar{u}_{\mathrm{m},7} = \tfrac{1}{2}(\bar{u}_{7|8} + 2\bar{u}_{6|1}), && \Delta\bar{u}_7 = \bar{u}_{7|8} - 2\bar{u}_{6|1},\\
&\text{channel 13 :} && \bar{u}_{\mathrm{m},13} = \tfrac{1}{2}(-\tfrac{1}{2}\bar{u}_{7|8} + \bar{u}_{13|7}), && \Delta\bar{u}_{13} = -\tfrac{1}{2}\bar{u}_{7|8} - \bar{u}_{13|7},\\
&\text{channel 30 :} && \bar{u}_{\mathrm{m},30} = 0, && \Delta\bar{u}_{30} = 2\bar{u}_{30|7},\\
&\text{channel 31 :} && \bar{u}_{\mathrm{m},31} = \tfrac{1}{2}(\bar{u}_{31|26} + \bar{u}_{30|7} - \bar{u}_{13|7}), && \Delta\bar{u}_{31} = \bar{u}_{31|26} - \bar{u}_{30|7} + \bar{u}_{13|7}.
\end{aligned} \tag{3.30}$$

Thus, the nodal velocities are replaced by mean values and variations, according to the above definitions:

$$\bar{u}_{\mathrm{m},7}, \quad \bar{u}_{\mathrm{m},13}, \quad \bar{u}_{\mathrm{m},31}, \quad \Delta\bar{u}_6, \quad \Delta\bar{u}_7, \quad \Delta\bar{u}_{13}, \quad \Delta\bar{u}_{30}, \quad \Delta\bar{u}_{31}\,;$$

Although the numbers of unknowns in each representation are not equal, it is easy to verify that it is possible to go back to the nodal values starting from averages and variations because these relationships are not linearly independent.

3.2.3.6 States

The results obtained in the precedent sections are sufficient to give an explicit formulation of the equations and coupling conditions supposed to solve the problem presented in FIGURE 3.15.

3.2.3.6.1 Dynamics of assemblies

Pressure force By exceptionally numbering the pressures by the channel number, it becomes:

$$\begin{aligned}
\overline{F}_{1,X} &= \tfrac{1}{2}\int_0^1 -\tilde{p}_{13}\,\mathrm{d}\bar{x} - \tfrac{1}{2}\int_0^1 -\tilde{p}_{7}\,\mathrm{d}\bar{x} - \int_0^1 -\tilde{p}_{6}\,\mathrm{d}\bar{x} - \tfrac{1}{2}\int_0^1 -\tilde{p}_{12}\,\mathrm{d}\bar{x} + \tfrac{1}{2}\int_0^1 -\tilde{p}_{29}\,\mathrm{d}\bar{x} + \int_0^1 -\tilde{p}_{30}\,\mathrm{d}\bar{x} \\
&= \int_0^1 \tilde{p}_6\,\mathrm{d}\bar{x} + \int_0^1 \tilde{p}_7\,\mathrm{d}\bar{x} - \int_0^1 \tilde{p}_{13}\,\mathrm{d}\bar{x} - \int_0^1 \tilde{p}_{30}\,\mathrm{d}\bar{x},
\end{aligned} \tag{3.31}$$

$$\overline{F}_{7,X} = -\tfrac{1}{2}\int_0^1 -\tilde{p}_{31}\,\mathrm{d}\bar{x} - \int_0^1 -\tilde{p}_{30}\,\mathrm{d}\bar{x} - \tfrac{1}{2}\int_0^1 -\tilde{p}_{42}\,\mathrm{d}\bar{x} = \int_0^1 \tilde{p}_{30}\,\mathrm{d}\bar{x} + \int_0^1 \tilde{p}_{31}\,\mathrm{d}\bar{x}. \tag{3.32}$$

$$\begin{aligned}
\overline{F}_{8,X} &= -\tfrac{1}{2}\int_0^1 -\tilde{p}_{32}\,\mathrm{d}\bar{x} - \int_0^1 -\tilde{p}_{14}\,\mathrm{d}\bar{x} - \tfrac{1}{2}\int_0^1 -\tilde{p}_{13}\,\mathrm{d}\bar{x} + \tfrac{1}{2}\int_0^1 -\tilde{p}_{31}\,\mathrm{d}\bar{x} \\
&= \tfrac{1}{2}\int_0^1 \tilde{p}_{13}\,\mathrm{d}\bar{x} + \int_0^1 \tilde{p}_{14}\,\mathrm{d}\bar{x},
\end{aligned} \tag{3.33}$$

$$\overline{F}_{8,Y} = \tfrac{\sqrt{3}}{2}\int_0^1 -\tilde{p}_{32}\,\mathrm{d}\bar{x} - \tfrac{\sqrt{3}}{2}\int_0^1 -\tilde{p}_{13}\,\mathrm{d}\bar{x} - \tfrac{\sqrt{3}}{2}\int_0^1 -\tilde{p}_{31}\,\mathrm{d}\bar{x} = \tfrac{\sqrt{3}}{2}\int_0^1 \tilde{p}_{13}\,\mathrm{d}\bar{x}.$$

By symmetries, $\overline{\boldsymbol{F}}_1$ and $\overline{\boldsymbol{F}}_7$ don't have component on $\boldsymbol{e}_Y$.

It remains therefore to explicit the integrals of $\tilde{p}_6$, $\tilde{p}_7$, $\tilde{p}_{13}$, $\tilde{p}_{14}$ and $\tilde{p}_{30}$ according to Eq. 3.20:

$$\begin{aligned}
\mathsf{Eu}\int_0^1 \tilde{p}_6\,\mathrm{d}\bar{x} &= \mathsf{Eu}\,\tilde{p}_1 + \tfrac{1}{12}\Big[\mathsf{St}\frac{\mathrm{d}}{\mathrm{d}\bar{t}}(\Delta\bar{u}_6) + 2(\Delta\bar{u}_6)^2\Big], \\
\mathsf{Eu}\int_0^1 \tilde{p}_7\,\mathrm{d}\bar{x} &= \tfrac{1}{2}\mathsf{Eu}\,(\tilde{p}_1+\tilde{p}_8) + \tfrac{1}{12}\Big[\mathsf{St}\frac{\mathrm{d}}{\mathrm{d}\bar{t}}(\Delta\bar{u}_7) + 2(\Delta\bar{u}_7)^2 + C_{\mathrm{f}}^*\,\frac{\Delta\bar{u}_7}{\bar{h}_7}\Big], \\
\mathsf{Eu}\int_0^1 \tilde{p}_{13}\,\mathrm{d}\bar{x} &= \tfrac{1}{2}\mathsf{Eu}\,(\tilde{p}_7+\tilde{p}_8) + \tfrac{1}{12}\Big[\mathsf{St}\frac{\mathrm{d}}{\mathrm{d}\bar{t}}(\Delta\bar{u}_{13}) + 2(\Delta\bar{u}_{13})^2 + C_{\mathrm{f}}^*\,\frac{\Delta\bar{u}_{13}}{\bar{h}_{13}}\Big], \\
\mathsf{Eu}\int_0^1 \tilde{p}_{30}\,\mathrm{d}\bar{x} &= \mathsf{Eu}\,\tilde{p}_7 + \tfrac{1}{12}\Big[\mathsf{St}\frac{\mathrm{d}}{\mathrm{d}\bar{t}}(\Delta\bar{u}_{30}) + 2(\Delta\bar{u}_{30})^2\Big], \\
\mathsf{Eu}\int_0^1 \tilde{p}_{31}\,\mathrm{d}\bar{x} &= \tfrac{1}{2}\mathsf{Eu}\,\tilde{p}_7 + \tfrac{1}{12}\Big[\mathsf{St}\frac{\mathrm{d}}{\mathrm{d}\bar{t}}(\Delta\bar{u}_{31}) + 2(\Delta\bar{u}_{31})^2 + C_{\mathrm{f}}^*\,\frac{\Delta\bar{u}_{31}}{\bar{h}_{31}}\Big].
\end{aligned} \tag{3.34}$$

From the combination of these relations, it results in the forces applied to the assemblies. These expressions make explicitly the terms in phase or in quadrature with the movement. Note that the motion of all assemblies is not necessarily affected by the friction and that the quadratic terms are the origin of terms with frequency double of the natural frequency. Finally, it should be observed that in the case where $\mathsf{St} \gg 1$ and $\eta \ll 1$, the quadratic terms disappear and the widths are substantially equal to one, thus restoring the linearity.

Equations These equations are formulated according to the definitions given in section 3.2.3.3. The three equations for the assemblies will be:

$$\begin{aligned}
m^* \frac{\mathrm{d}^2 \widetilde{Z}_1}{\mathrm{d}\bar{t}^2} &= -\widetilde{Z}_1 - D^* \frac{\mathrm{d}\widetilde{Z}_1}{\mathrm{d}\bar{t}} + \frac{(\delta p)}{\varepsilon \eta K} \overline{F}_{1,X}, \\
m^* \frac{\mathrm{d}^2 \widetilde{Z}_7}{\mathrm{d}\bar{t}^2} &= -\widetilde{Z}_7 - D^* \frac{\mathrm{d}\widetilde{Z}_7}{\mathrm{d}\bar{t}} + \frac{(\delta p)}{\varepsilon \eta K} \overline{F}_{7,X}, \\
m^* \frac{\mathrm{d}^2 \widetilde{Z}_8}{\mathrm{d}\bar{t}^2} &= -\widetilde{Z}_8 - D^* \frac{\mathrm{d}\widetilde{Z}_8}{\mathrm{d}\bar{t}} + \frac{2\sqrt{3}}{3} \frac{(\delta p)}{\varepsilon \eta K} \overline{F}_{8,X}.
\end{aligned} \tag{3.35}$$

The transposition of the equations for $\widetilde{Z}_1$ is $\widetilde{Z}_7$ is immediate since these two centres are on one axis; only $\widetilde{Z}_8$ requires a correction.

3.2.3.6.2 Dynamics of fluid

For channel 6, 7, 13, 30 and 31:

$$\begin{aligned}
\Delta \bar{u}_6 &= -\eta \mathsf{St} \frac{1}{\bar{h}_6} \frac{\mathrm{d}\tilde{h}_6}{\mathrm{d}\bar{t}}, \qquad \Delta \bar{u}_7 = -\eta \mathsf{St} \frac{1}{\bar{h}_7} \frac{\mathrm{d}\tilde{h}_7}{\mathrm{d}\bar{t}}, \qquad \Delta \bar{u}_{13} = -\eta \mathsf{St} \frac{1}{\bar{h}_{13}} \frac{\mathrm{d}\tilde{h}_{13}}{\mathrm{d}\bar{t}}, \\
\Delta \bar{u}_{30} &= -\eta \mathsf{St} \frac{1}{\bar{h}_{30}} \frac{\mathrm{d}\tilde{h}_{30}}{\mathrm{d}\bar{t}}, \qquad \Delta \bar{u}_{31} = -\eta \mathsf{St} \frac{1}{\bar{h}_{31}} \frac{\mathrm{d}\tilde{h}_{31}}{\mathrm{d}\bar{t}}, \\
\mathsf{St} \frac{\mathrm{d}\bar{u}_{\mathrm{m},7}}{\mathrm{d}\bar{t}} + 2\bar{u}_{\mathrm{m},7} \Delta \bar{u}_7 &= -\mathsf{Eu} \left(\tilde{p}_8 - \tilde{p}_1\right) - C_{\mathrm{f}}^* \frac{\bar{u}_{\mathrm{m},7}}{\bar{h}_7}, \\
\mathsf{St} \frac{\mathrm{d}\bar{u}_{\mathrm{m},13}}{\mathrm{d}\bar{t}} + 2\bar{u}_{\mathrm{m},13} \Delta \bar{u}_{13} &= -\mathsf{Eu} \left(\tilde{p}_8 - \tilde{p}_7\right) - C_{\mathrm{f}}^* \frac{\bar{u}_{\mathrm{m},13}}{\bar{h}_{13}}, \\
\mathsf{St} \frac{\mathrm{d}\bar{u}_{\mathrm{m},31}}{\mathrm{d}\bar{t}} + 2\bar{u}_{\mathrm{m},31} \Delta \bar{u}_{31} &= \mathsf{Eu}\, \tilde{p}_7 - C_{\mathrm{f}}^* \frac{\bar{u}_{\mathrm{m},31}}{\bar{h}_{31}}.
\end{aligned} \tag{3.36}$$

Note that the momentum balances of channels 6 and 30 are automatically verified due to symmetry. This system can be reversed with respect to pressures and provide the values of $\tilde{p}_1$, $\tilde{p}_7$ and $\tilde{p}_8$ as:

$$\begin{aligned}
\mathsf{Eu}\, \tilde{p}_7 &= \mathsf{St} \frac{\mathrm{d}\bar{u}_{\mathrm{m},31}}{\mathrm{d}\bar{t}} + 2\bar{u}_{\mathrm{m},31} \Delta \bar{u}_{31} + C_{\mathrm{f}}^* \frac{\bar{u}_{\mathrm{m},31}}{\bar{h}_{31}}, \\
\mathsf{Eu}\, \tilde{p}_8 &= \mathsf{St} \frac{\mathrm{d}}{\mathrm{d}\bar{t}} \left(\bar{u}_{\mathrm{m},31} - \bar{u}_{\mathrm{m},13}\right) + 2\left(\bar{u}_{\mathrm{m},31} \Delta \bar{u}_{31} - \bar{u}_{\mathrm{m},13} \Delta \bar{u}_{13}\right) + C_{\mathrm{f}}^* \left(\frac{\bar{u}_{\mathrm{m},31}}{\bar{h}_{31}} - \frac{\bar{u}_{\mathrm{m},13}}{\bar{h}_{13}}\right), \\
\mathsf{Eu}\, \tilde{p}_1 &= \mathsf{St} \frac{\mathrm{d}}{\mathrm{d}\bar{t}} \left(\bar{u}_{\mathrm{m},7} + \bar{u}_{\mathrm{m},31} - \bar{u}_{\mathrm{m},13}\right) + 2\left(\bar{u}_{\mathrm{m},7} \Delta \bar{u}_7 + \bar{u}_{\mathrm{m},31} \Delta \bar{u}_{31} - \bar{u}_{\mathrm{m},13} \Delta \bar{u}_{13}\right) \\
&\qquad + C_{\mathrm{f}}^* \left(\frac{\bar{u}_{\mathrm{m},7}}{\bar{h}_7} + \frac{\bar{u}_{\mathrm{m},31}}{\bar{h}_{31}} - \frac{\bar{u}_{\mathrm{m},13}}{\bar{h}_{13}}\right).
\end{aligned} \tag{3.37}$$

For the mass balance:

$$\begin{aligned} &\bar{u}_{6|1} = \tfrac{1}{2}\Delta\bar{u}_6, \quad \bar{u}_{7|8} = \Delta\bar{u}_6 + \Delta\bar{u}_7, \quad \bar{u}_{13|7} = -\tfrac{1}{2}\Delta\bar{u}_6 - \tfrac{1}{2}\Delta\bar{u}_7 - \Delta\bar{u}_{13}, \\ &\bar{u}_{30|7} = \tfrac{1}{2}\Delta\bar{u}_{30}, \quad \bar{u}_{31|26} = \tfrac{1}{2}\Delta\bar{u}_6 + \tfrac{1}{2}\Delta\bar{u}_7 + \Delta\bar{u}_{13} + \tfrac{1}{2}\Delta\bar{u}_{30} + \Delta\bar{u}_{31}. \end{aligned} \tag{3.38}$$

Therefore, the average velocity:

$$\begin{aligned} &\bar{u}_{\mathrm{m},6} = 0, \quad \bar{u}_{\mathrm{m},7} = \Delta\bar{u}_6 + \tfrac{1}{2}\Delta\bar{u}_7, \quad \bar{u}_{\mathrm{m},13} = -\tfrac{1}{2}\big(\Delta\bar{u}_6 + \Delta\bar{u}_7 + \Delta\bar{u}_{13}\big), \\ &\bar{u}_{\mathrm{m},30} = 0, \quad \bar{u}_{\mathrm{m},31} = \tfrac{1}{2}\big(\Delta\bar{u}_6 + \Delta\bar{u}_7 + 2\Delta\bar{u}_{13} + \Delta\bar{u}_{30} + \Delta\bar{u}_{31}\big), \end{aligned} \tag{3.39}$$

which are therefore also calculated on the basis of variations in width. This is not surprising because the flow results from these variations. This finding would not be consistent in the case of fluid injection.

It is interesting to observe, as can be foreseen, that variations in width accumulate from the center, contrary to the pressures that accumulate towards the center.

3.2.3.6.3 Coupling

The widths concerned are those of the channels which separate the retained assemblies or, the channels numbered as:$\tilde{h}_6$, $\tilde{h}_7$, $\tilde{h}_{13}$, $\tilde{h}_{30}$ and $\tilde{h}_{31}$. It is then possible to express the mass balance Eq. 3.21_2 only as a function of the coordinates of the assemblies' centres and the variations of velocities:

$$\bar{h} = 1 + \tfrac{1}{2}\eta\big[(\alpha''\widetilde{Z}_{C''} - \alpha'\widetilde{Z}_{C'})(\boldsymbol{e}_X \cdot \boldsymbol{n}') + (\beta''\widetilde{Z}_{C''} - \beta'\widetilde{Z}_{C'})(\boldsymbol{e}_Y \cdot \boldsymbol{n}')\big],$$

where $\alpha = \cos\theta$ and $\beta = \sin\theta$. The values are shown in the following table:

Channel	Assemblies	α'	β'	α''	β''	$\boldsymbol{e}_X \cdot \boldsymbol{n}'$	$\boldsymbol{e}_Y \cdot \boldsymbol{n}'$
6	$0-1$	1	0	1	0	1	0
7	$1-2$	1	0	$1/2$	$\sqrt{3}/2$	$-1/2$	$\sqrt{3}/2$
13	$1-8$	1	0	$\sqrt{3}/2$	$1/2$	$1/2$	$\sqrt{3}/2$
30	$1-7$	1	0	1	0	1	0
31	$7-8$	1	0	$\sqrt{3}/2$	$1/2$	$-1/2$	$\sqrt{3}/2$

Therefore,

$$\begin{aligned} \bar{h}_6 &= 1 + \tfrac{1}{2}\eta\,\widetilde{Z}_1, \\ \bar{h}_7 &= 1 + \tfrac{1}{4}\eta\,(\widetilde{Z}_1 + \widetilde{Z}_2) = 1 + \tfrac{1}{2}\eta\,\widetilde{Z}_1, \\ \bar{h}_{13} &= 1 + \tfrac{1}{4}\eta(\sqrt{3}\,\widetilde{Z}_8 - \widetilde{Z}_1), \\ \bar{h}_{30} &= 1 + \tfrac{1}{2}\eta(\widetilde{Z}_7 - \widetilde{Z}_1), \\ \bar{h}_{31} &= 1 + \tfrac{1}{4}\eta\,\widetilde{Z}_7. \end{aligned} \tag{3.40}$$

There are several remarks on these expressions:

- by symmetry, $\bar{h}_7$ is expressed only as a function of the motion of the assembly 1 ;
- the variations of $\bar{h}_6$ result only from the movement of the assembly 1 because the assembly 0 (to its left) is motionless ;
- the assembly 8 does not contribute to $\bar{h}_{31}$ because it moves parallel to the face 31.

3.2.3.7 Equations

3.2.3.7.1 Preliminaries

The equation of this problem leads, in the general case, to excessively complex expressions. The following assumptions are made for simplification:

- ▷ complet dynamic problem ;
- ▷ high STROUHAL number : $\mathsf{St} \gg 1$;
- ▷ small amplitude parameter : $\eta = 1/\mathsf{St} \ll 1$.

It will results in the scales following:

$$\tau = \tau_K = \sqrt{m/K}, \quad U = \eta b/\tau_K, \quad (\delta p) = \varepsilon\eta K \quad \text{and} \quad \mathsf{Eu} = \frac{\varepsilon\eta K}{\rho U^2} \sim \mathsf{St} \sim C_\mathrm{f}^* \gg 1,$$

Under these conditions:

$$\varepsilon = \gamma \quad \text{et} \quad C_\mathrm{f} = h_0^2/(\nu\tau_K) \quad \text{where} \quad \gamma = \rho b^2/m.$$

Consequently, the quadratic terms are negligible and the boundary conditions can be flattened.

3.2.3.7.2 Applied force

$$\begin{aligned}
\mathsf{Eu}\overline{F}_{1,X} &= \frac{3}{2}\mathsf{St}\frac{\mathrm{d}}{\mathrm{d}\bar{t}}\big(\bar{u}_{\mathrm{m},7} - \bar{u}_{\mathrm{m},13}\big) + \frac{\mathsf{St}}{12}\frac{\mathrm{d}}{\mathrm{d}\bar{t}}\big(\Delta\bar{u}_6 + \Delta\bar{u}_7 - \Delta\bar{u}_{13} - \Delta\bar{u}_{30}\big) + \frac{5}{3}C_\mathrm{f}^*\big(\bar{u}_{\mathrm{m},7} - \bar{u}_{\mathrm{m},13}\big),\\
\mathsf{Eu}\overline{F}_{7,X} &= \frac{3}{2}\mathsf{St}\frac{\mathrm{d}\bar{u}_{\mathrm{m},31}}{\mathrm{d}\bar{t}} + \frac{\mathsf{St}}{12}\frac{\mathrm{d}}{\mathrm{d}\bar{t}}\big(\Delta\bar{u}_{30} + \Delta\bar{u}_{31}\big) + \frac{5}{3}C_\mathrm{f}^*\,\bar{u}_{\mathrm{m},31},\\
\mathsf{Eu}\overline{F}_{8,X} &= \frac{3}{4}\mathsf{St}\frac{\mathrm{d}}{\mathrm{d}\bar{t}}\big(2\bar{u}_{\mathrm{m},31} - \bar{u}_{\mathrm{m},13}\big) + \frac{\mathsf{St}}{8}\frac{\mathrm{d}}{\mathrm{d}\bar{t}}\big(\Delta\bar{u}_{13}\big) + \frac{C_\mathrm{f}^*}{2}\big(3\bar{u}_{\mathrm{m},31} - \bar{u}_{\mathrm{m},13}\big).
\end{aligned}$$

3.2.3.7.3 Velocities

It is necessary to begin by explaining the variations from mass balances Eq. 3.36, taking into account Eq. 3.22:

$$\begin{aligned}
\Delta\bar{u}_6 &= -\frac{1}{2}\frac{\mathrm{d}\widetilde{Z}_1}{\mathrm{d}\bar{t}}, & \Delta\bar{u}_7 &= -\frac{1}{2}\frac{\mathrm{d}\widetilde{Z}_1}{\mathrm{d}\bar{t}}, & \Delta\bar{u}_{13} &= -\frac{1}{4}\Big(\sqrt{3}\,\frac{\mathrm{d}\widetilde{Z}_8}{\mathrm{d}\bar{t}} - \frac{\mathrm{d}\widetilde{Z}_1}{\mathrm{d}\bar{t}}\Big),\\
\Delta\bar{u}_{30} &= -\frac{1}{2}\Big(\frac{\mathrm{d}\widetilde{Z}_7}{\mathrm{d}\bar{t}} - \frac{\mathrm{d}\widetilde{Z}_1}{\mathrm{d}\bar{t}}\Big), & \Delta\bar{u}_{31} &= -\frac{1}{4}\frac{\mathrm{d}\widetilde{Z}_7}{\mathrm{d}\bar{t}},
\end{aligned}$$

From which we can deduct the expression of average velocities (Eq. 3.39):

$$\bar{u}_{\mathrm{m},7} = -\frac{3}{4}\frac{\mathrm{d}\widetilde{Z}_1}{\mathrm{d}\bar{t}}, \quad \bar{u}_{\mathrm{m},13} = \frac{3}{8}\frac{\mathrm{d}\widetilde{Z}_1}{\mathrm{d}\bar{t}} + \frac{\sqrt{3}}{8}\frac{\mathrm{d}\widetilde{Z}_8}{\mathrm{d}\bar{t}}, \quad \bar{u}_{\mathrm{m},31} = -\frac{3}{8}\frac{\mathrm{d}\widetilde{Z}_7}{\mathrm{d}\bar{t}} - \frac{\sqrt{3}}{4}\frac{\mathrm{d}\widetilde{Z}_8}{\mathrm{d}\bar{t}}.$$

It remains to defer these expressions to those of the forces in order to obtain them as a sum of derivatives of the coordinates at the assemblies' centres:

$$\begin{aligned}
\mathsf{Eu}\overline{F}_{1,X} &= \frac{\mathsf{St}}{24}\frac{\mathrm{d}^2}{\mathrm{d}\bar{t}^2}\big(-44\,\widetilde{Z}_1+\widetilde{Z}_7-4\sqrt{3}\,\widetilde{Z}_8\big)-\frac{C_\mathrm{f}^*}{12}\frac{\mathrm{d}}{\mathrm{d}\bar{t}}\big(21\,\widetilde{Z}_1+2\sqrt{3}\,\widetilde{Z}_8\big),\\
\mathsf{Eu}\overline{F}_{7,X} &= \frac{\mathsf{St}}{24}\frac{\mathrm{d}^2}{\mathrm{d}\bar{t}^2}\big(\widetilde{Z}_1-15\,\widetilde{Z}_7-9\sqrt{3}\,\widetilde{Z}_8\big)-\frac{C_\mathrm{f}^*}{12}\frac{\mathrm{d}}{\mathrm{d}\bar{t}}\big(7\,\widetilde{Z}_7+\tfrac{9}{2}\sqrt{3}\,\widetilde{Z}_8\big),\\
\mathsf{Eu}\overline{F}_{8,X} &= -\frac{\mathsf{St}}{24}\frac{\mathrm{d}^2}{\mathrm{d}\bar{t}^2}\big(6\,\widetilde{Z}_1+\frac{27}{2}\,\widetilde{Z}_7+12\sqrt{3}\,\widetilde{Z}_8\big)-\frac{C_\mathrm{f}^*}{12}\frac{\mathrm{d}}{\mathrm{d}\bar{t}}\big(3\,\widetilde{Z}_1+\tfrac{27}{4}\widetilde{Z}_7+6\sqrt{3}\,\widetilde{Z}_8\big).
\end{aligned}\tag{3.41}$$

At this point, the modifications to be made to the inertia of the assembly and its damping appear clearly. It must also be observed that the fluid reacts instantaneously when the assemblies move because of the accelerations.

3.2.3.7.4 System of equations

In matrix form , the equations are:

$$\begin{pmatrix} M_{11} & M_{17} & M_{18}\\ M_{71} & M_{77} & M_{78}\\ M_{81} & M_{87} & M_{88}\end{pmatrix}\cdot\frac{\mathrm{d}^2}{\mathrm{d}\bar{t}^2}\begin{pmatrix}\widetilde{Z}_1\\ \widetilde{Z}_7\\ \widetilde{Z}_8\end{pmatrix}+\begin{pmatrix} D_{11} & D_{17} & D_{18}\\ D_{71} & D_{77} & D_{78}\\ D_{81} & D_{87} & D_{88}\end{pmatrix}\cdot\frac{\mathrm{d}}{\mathrm{d}\bar{t}}\begin{pmatrix}\widetilde{Z}_1\\ \widetilde{Z}_7\\ \widetilde{Z}_8\end{pmatrix}+\begin{pmatrix}\widetilde{Z}_1\\ \widetilde{Z}_7\\ \widetilde{Z}_8\end{pmatrix}=0,$$

$$\text{where :}\quad\begin{cases} M_{11}=m^*+\dfrac{11}{6}\,\mathsf{St}^*, & M_{17}=-\dfrac{1}{24}\,\mathsf{St}^*, & M_{18}=\dfrac{\sqrt{3}}{6}\,\mathsf{St}^*\\ M_{71}=-\dfrac{1}{24}\,\mathsf{St}^*, & M_{77}=m^*+\dfrac{5}{8}\,\mathsf{St}^*, & M_{78}=\dfrac{3\sqrt{3}}{8}\,\mathsf{St}^*,\\ M_{81}=\dfrac{\sqrt{3}}{6}\,\mathsf{St}^*, & M_{87}=\dfrac{3\sqrt{3}}{8}\,\mathsf{St}^*, & M_{88}=m^*+\mathsf{St}^*,\end{cases}$$

$$\text{et :}\quad\begin{cases} D_{11}=D^*+\dfrac{7}{4}\,C_\mathrm{f}^\star, & D_{17}=0, & D_{18}=\dfrac{\sqrt{3}}{6}\,C_\mathrm{f}^\star,\\ D_{71}=0, & D_{77}=D^*+\dfrac{7}{12}\,C_\mathrm{f}^\star, & D_{78}=\dfrac{3\sqrt{3}}{8}\,C_\mathrm{f}^\star,\\ D_{81}=\dfrac{\sqrt{3}}{6}\,C_\mathrm{f}^\star, & D_{87}=\dfrac{3\sqrt{3}}{8}\,C_\mathrm{f}^\star, & D_{88}=D^*+\dfrac{7}{8}\,C_\mathrm{f}^\star.\end{cases}$$

In accordance with what is expected, the system of equations is indeed homogeneous and coupled:

$$\mathsf{M}\cdot\frac{\mathrm{d}^2\widetilde{\boldsymbol{Z}}}{\mathrm{d}\bar{t}^2}+\mathsf{D}\cdot\frac{\mathrm{d}\widetilde{\boldsymbol{Z}}}{\mathrm{d}\bar{t}}+\widetilde{\boldsymbol{Z}}=0.$$

Due to the linearity of the equations, the action of the fluid on an assembly effectively decomposes into a component in phase with the movement of this assembly and a quadrature component. This simplicity would disappear if non-linearities that has been neglected become significant.

More simply, the matrices M and D can be decomposed into two parts of contributions:

$$\mathsf{M}=m^*\,\mathsf{I}+\mathsf{St}^*\,\mathsf{M}_\mathrm{f}\quad\text{and}\quad\mathsf{D}=D^*\,\mathsf{I}+C_\mathrm{f}^*\,\mathsf{D}_\mathrm{f},$$

Where,

$$\mathsf{M}_\mathrm{f} = \frac{1}{24}\begin{pmatrix} 44 & -1 & 4\sqrt{3} \\ -1 & 15 & 9\sqrt{3} \\ 4\sqrt{3} & 9\sqrt{3} & 24 \end{pmatrix} \quad \text{and} \quad \mathsf{D}_\mathrm{f} = \frac{1}{24}\begin{pmatrix} 42 & 0 & 4\sqrt{3} \\ 0 & 14 & 9\sqrt{3} \\ 4\sqrt{3} & 9\sqrt{3} & 24 \end{pmatrix}.$$

From a physical point of view, the phenomena are simply distributed: the inertia of each assembly is modified by terms proportional to STROUHAL number, while the damping is supplemented by terms which depend only on viscous friction. These contributions have a sign that comes from the orientation of the channels. Note that the matrix of inertias is symmetric, which was expected since it is the only one that remains in the absence of dissipation, in the case where the device is conservative.

From the view of terminology, the notions of «added mass» and «added damping», taking into account their matrix character, appear as language facilities and do not have much physical meaning.

3.2.3.8 Integrations

3.2.3.8.1 Preliminaries

The first step consists in inverting the matrix M so as to isolate the second derivatives of the unknowns. By way of indication, the analytical expression of the inverse of the matrix M is given below:

$$\begin{aligned}
M_{11}^{-1} &= (234\,\mathsf{St}^{\star 2} + 1872\,m^{*}\mathsf{St}^{\star} + 1152\,m^{*2})/\Delta_1, \\
M_{12}^{-1} &= (264\,\mathsf{St}^{\star 2} + 48\,m^{*}\mathsf{St}^{\star})/\Delta_1, \\
M_{13}^{-1} &= -(414\,\mathsf{St}^{\star 2} + 576\,m^{*}\mathsf{St}^{\star})/\Delta_2, \\
M_{22}^{-1} &= (2016\,\mathsf{St}^{\star 2} + 3264\,m^{*}\mathsf{St}^{\star} + 1152\,m^{*2})/\Delta_1, \\
M_{23}^{-1} &= -(2400\,\mathsf{St}^{\star 2} + 1296\,m^{*}\mathsf{St}^{\star})/\Delta_2, \\
M_{33}^{-1} &= (1318\,\mathsf{St}^{\star 2} + 2832\,m^{*}\mathsf{St}^{\star} + 1152\,m^{*2})/\Delta_1,
\end{aligned}$$

Where,

$$\Delta_1 = 349\,\mathsf{St}^{\star 3} + 3568\,m^{*}\mathsf{St}^{\star 2} + 3984\,m^{*2}\mathsf{St}^{\star} + 1152\,m^{*3} \quad \text{et} \quad \Delta_2 = \sqrt{3}\,\Delta_1.$$

The mathematical complexity of these expressions obscures the physical interpretation and discourages from continuing in this direction; it is therefore necessary to go directly to the numerical resolution.

3.2.3.8.2 Numerical integration

The approach followed in this section consists in giving an initial state compatible with the hypotheses and in calculating the time evolution of the structure. Formally, the system can be written as:

$$\frac{\mathrm{d}^2\widetilde{\boldsymbol{Z}}}{\mathrm{d}\bar{t}^2} + \mathsf{C}\cdot\frac{\mathrm{d}\widetilde{\boldsymbol{Z}}}{\mathrm{d}\bar{t}} + \mathsf{K}\cdot\widetilde{\boldsymbol{Z}} = 0 \quad \text{where} \quad \mathsf{C} = \mathsf{M}^{-1}\cdot\mathsf{D} \quad \text{and} \quad \mathsf{K} = \mathsf{M}^{-1}. \tag{3.42}$$

The method is very classical and involves solving a system of six equations of the first order to six unknowns, subject to introducing the auxiliary unknown $\widetilde{\boldsymbol{V}} = \mathrm{d}\widetilde{\boldsymbol{Z}}/\mathrm{d}\bar{t}$:

$$\frac{\mathrm{d}\widetilde{\boldsymbol{V}}}{\mathrm{d}\bar{t}} + \mathsf{C}\cdot\widetilde{\boldsymbol{V}} + \mathsf{K}\cdot\widetilde{\boldsymbol{Z}} = 0, \qquad \frac{\mathrm{d}\widetilde{\boldsymbol{Z}}}{\mathrm{d}\bar{t}} = \widetilde{\boldsymbol{V}}, \qquad \widetilde{\boldsymbol{Z}}(0) = \widetilde{\boldsymbol{Z}}_0 \quad \text{and} \quad \widetilde{\boldsymbol{V}}(0) = 0.$$

This is a problem with initial values, integrable with a standard method.

3.2.3.8.3 Energies

The results of the integration are the displacements $\widetilde{\boldsymbol{Z}}$ and the velocity $\widetilde{\boldsymbol{V}}$ of the assemblies' centres. After multiplication of Eq. 3.27 by $\mathrm{d}\widetilde{Z}/\mathrm{d}\bar{t}$, it becomes:

$$\tfrac{1}{2}m^*\frac{\mathrm{d}}{\mathrm{d}\bar{t}}\Big(\frac{\mathrm{d}\widetilde{Z}}{\mathrm{d}\bar{t}}\Big)^2 + D^*\Big(\frac{\mathrm{d}\widetilde{Z}}{\mathrm{d}\bar{t}}\Big)^2 + \tfrac{1}{2}\frac{\mathrm{d}\widetilde{Z}^2}{\mathrm{d}\bar{t}} = \mathsf{St}^\star\frac{\mathrm{d}\widetilde{Z}}{\mathrm{d}\bar{t}}\overline{F},$$

where the first and third terms of the left side can be respectively derived from the kinetic energy and the potential energy of an assembly. Summed on the set of crowns, it allows to follow the energy transfers between the structure and the fluid. These transfers are not conservative because of the second term and the right side whose contribution is indirectly affected by the dissipation associated with the movement of the fluid.

3.2.3.8.4 Volumes

Due to the movements of the assemblies, the volume of fluid contained in the inter-assembly channels is variable and its variations can be interpreted in a pictorial way as a «respiration».

The volume sought consists of channels of different types, listed in TABLE 3.4. There are several types of channels to be distinguished: internal or external. Each channel of volume $2hb$ is associated with a confluence of approximate volume $\sqrt{3}\,h^2$ (equilateral triangle, see FIGURE 3.17). Except for the frontier channels, each channel divides its junctions with four other channels; a junction is thus divided into three. The type of channel refers to its number as it intervenes in Eq. 3.40.

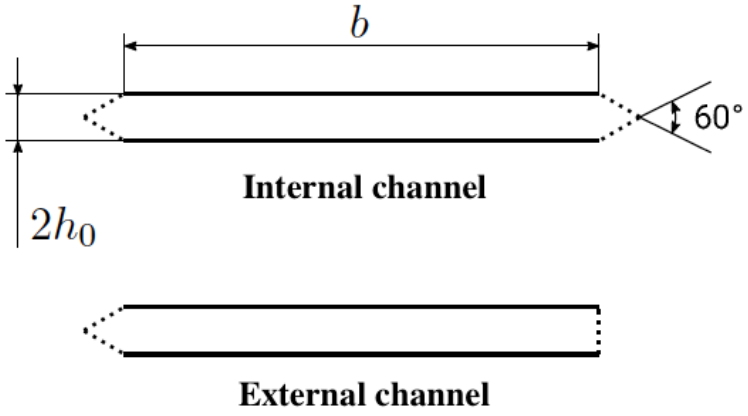

FIGURE 3.17: Volume of channels

TABLE 3.4: Constitutive channel of volume

Channel	Localisation	Volume	Type of width	Number
radial	internal	$2h_0b\big(1+\frac{\sqrt{3}}{3}\varepsilon\bar{h}\big)\bar{h}$	7	6
radial	external	$2h_0b\big(1+\frac{\sqrt{3}}{6}\varepsilon\bar{h}\big)\bar{h}$	31	12
circumferential	flowing	$2h_0b\big(1+\frac{\sqrt{3}}{3}\varepsilon\bar{h}\big)\bar{h}$	13	12
circumferential	non-flowing	$2h_0b\big(1+\frac{\sqrt{3}}{3}\varepsilon\bar{h}\big)\bar{h}$	30	12

The volume V therefore contains terms of order ε, η, $\varepsilon\eta$ and $\varepsilon\eta^2$. Such precision is not necessary and only orders ε and η are retained. With all calculations made, the volume of fluid is written as:

$$V = 12h_0b\Big\{7+2\sqrt{3}\,\varepsilon+\eta\Big[\Big(1+\frac{\sqrt{3}}{3}\,\varepsilon\Big)\Big(\frac{\sqrt{3}}{2}\,\widetilde{Z}_8-\widetilde{Z}_1\Big)+\Big(\frac{3}{2}+\frac{5\sqrt{3}}{12}\,\varepsilon\Big)\widetilde{Z}_7\Big]\Big\}.$$

As $V_{\rm r} = 12h_0b\big(7+2\sqrt{3}\,\varepsilon\big)$, the variation of V is:

$$\frac{V(t)-V_{\rm r}}{\eta V_{\rm r}} = \frac{\Big(1+\frac{\sqrt{3}}{3}\,\varepsilon\Big)\Big(\frac{\sqrt{3}}{2}\,\widetilde{Z}_8-\widetilde{Z}_1\Big)+\Big(\frac{3}{2}+\frac{5\sqrt{3}}{12}\,\varepsilon\Big)\widetilde{Z}_7}{7+2\sqrt{3}\,\varepsilon}. \tag{3.43}$$

3.2.3.8.5 Perimeters

Another parameter capable of giving an overall picture of the evolution of the installation is the perimeter of each crown:

$$\begin{aligned}\Pi_{\rm i} &= C_1C_2+C_2C_3+\cdots+C_6C_1 && \text{: internal crown ;}\\ \Pi_{\rm e} &= C_7C_8+C_8C_9+\cdots+C_{18}C_7, && \text{: external crown.}\end{aligned}$$

the length of each segment $C'C''$ is calculated from the coordinates of the centres:

$$C'C'' = \|\overrightarrow{C'C''}\| = \big[\big(X_{C''}-X_{C'}\big)^2+\big(Y_{C''}-Y_{C'}\big)^2\big]^{1/2},$$

Where,

$$X_{C''}-X_{C'} = \alpha''Z_{C''}-\alpha'Z_{C'} \quad\text{and}\quad Y_{C''}-Y_{C'} = \beta''Z_{C''}-\beta'Z_{C'}.$$

Since the α and β are the trigonometric lines of the same angle, it follows:

$$\big(C'C''\big)^2(t) = Z_{C'}^2+Z_{C''}^2-2(\alpha'\alpha''+\beta'\beta'')Z_{C'}Z_{C''}.$$

It remains to develop:

$$\begin{aligned}\big(C'C''\big)^2(t) = {}& \big(Z_{C_0'}+\eta h_0\,\widetilde{Z}_{C'}\big)^2+\big(Z_{C_0''}+\eta h_0\,\widetilde{Z}_{C''}\big)^2\\ &-2(\alpha'\alpha''+\beta'\beta'')\big(Z_{C_0'}+\eta h_0\,\widetilde{Z}_{C'}\big)\big(Z_{C_0''}+\eta h_0\,\widetilde{Z}_{C''}\big).\end{aligned}$$

It would be possible to develop this expression for $\eta\to 0$, but this approximation is not indispensable to numerical computation.

The coordinates (X, Y) of the centers are reduced to the unique variable Z by the expressions:

$$\begin{aligned} C_1C_2 &: \quad \alpha_1 = 1, \quad \beta_1 = 0, \quad \alpha_2 = 1/2, \quad \beta_2 = \sqrt{3}/2, \\ C_7C_8 &: \quad \alpha_7 = 1, \quad \beta_7 = 0, \quad \alpha_8 = \sqrt{3}/2, \quad \beta_8 = 1/2. \end{aligned}$$

$$\begin{aligned} Z_1 = X_1, \quad Z_2 &= 2X_2 = 2\sqrt{3}\,Y_2/3, \\ Z_7 = X_7, \quad Z_8 &= 2\sqrt{3}\,X_8/3 = 2Y_8. \end{aligned}$$

Examining the FIGURE 3.16 shows that:

$$\begin{aligned} Z_{C_1}(0) &= Z_{C_2}(0) = C_1C_2(0), \\ Z_{C_7}(0) &= 2\sqrt{3}\,Z_{C_8}(0)/3 = 2C_7C_8(0). \end{aligned}$$

Due to the symmetries, the case of C_1C_2 is very simple since $Z_{C_1} = Z_{C_2}$ and the triangle $C_0C_1C_2$ is equilateral:

$$C_1C_2(t) = Z_{C_1}(0) + \eta h_0\,\widetilde{Z}_{C_1}(\bar{t}) = C_1C_2(0) + \eta h_0\,\widetilde{Z}_{C_1}(\bar{t}) = a + 2h_0 + \eta h_0\,\widetilde{Z}_{C_1}(\bar{t}).$$

Otherwise,

$$C_1C_2 = a + 2h_7(t) \quad \Longrightarrow \quad \bar{h}_7(\bar{t}) = 1 + \tfrac{1}{2}\eta\,\widetilde{Z}_{C_1}.$$

The case of C_7C_8 is a a little more complicated:

$$\big(C_7C_8\big)^2 = Z_{C_7}^2 + Z_{C_8}^2 - \sqrt{3}\,Z_{C_7}Z_{C_8} = \tfrac{1}{4}Z_{C_7}^2,$$

By following,

$$C_7C_8 = a + 2h_0 + \tfrac{1}{2}\eta\,\widetilde{Z}_{C_7} = a + 2h_{31} \quad \Longrightarrow \quad \bar{h}_{31}(t) = 1 + \tfrac{1}{4}\eta\,\tilde{h}_{31}(\bar{t}).$$

Depending on symmetry, the expression of perimeters can be considerably simplified and evaluated:

$$\begin{aligned} \Pi_{\mathrm{i}} &= 6\,C_1C_2 = 6\big\{a + 2h_0\big[1 + \tfrac{1}{2}\eta\widetilde{Z}_{C_1}(\bar{t})\big]\big\}, \\ \Pi_{\mathrm{e}} &= 12\,C_7C_8 = 12\big\{a + 2h_0\big[1 + \tfrac{1}{4}\eta\widetilde{Z}_{C_7}(\bar{t})\big]\big\}. \end{aligned}$$

The parameters are calculated following:

$$\begin{aligned} \widetilde{\Pi}_{\mathrm{i}}(\bar{t}) &= \frac{\Pi_{\mathrm{i}}(t) - \Pi_{\mathrm{i}}(0)}{\varepsilon\eta\,\Pi_{\mathrm{i}}(0)} = \frac{\widetilde{Z}_1}{\sqrt{3} + 2\varepsilon} && \text{: internal crown,} \\ \widetilde{\Pi}_{\mathrm{e}}(\bar{t}) &= \frac{\Pi_{\mathrm{e}}(t) - \Pi_{\mathrm{e}}(0)}{\varepsilon\eta\,\Pi_{\mathrm{e}}(0)} = \frac{1}{2}\frac{\widetilde{Z}_7}{\sqrt{3} + 2\varepsilon}. && \text{: external crown.} \end{aligned}$$

and it is therefore sufficient to examine the displacements $\widetilde{Z}_1$ and $\widetilde{Z}_7$.

3.2.3.9 Characteristics of flow

The three functions $\widetilde{Z}_1(\bar{t})$, $\widetilde{Z}_7(\bar{t})$ and $\widetilde{Z}_8(\bar{t})$ is known, it is possible to go back to the speeds and pressures of the flow.

The expressions of mean velocities as a function of displacements are given in previous section:

$$\bar{u}_{\mathrm{m},7} = -\frac{3}{4}\frac{\mathrm{d}\widetilde{Z}_1}{\mathrm{d}\bar{t}}, \quad \bar{u}_{\mathrm{m},13} = \frac{1}{8}\frac{\mathrm{d}}{\mathrm{d}\bar{t}}\big(3\widetilde{Z}_1 + \sqrt{3}\widetilde{Z}_8\big) \quad \text{and} \quad \bar{u}_{\mathrm{m},31} = -\frac{1}{8}\frac{\mathrm{d}}{\mathrm{d}\bar{t}}\big(3\widetilde{Z}_7 + 2\sqrt{3}\widetilde{Z}_8\big).$$

$$\tilde{p}_1 = -\frac{3}{8}\Big(\mathsf{St}^\star \frac{\mathrm{d}^2}{\mathrm{d}\bar{t}^2} + C_\mathrm{f}^\star \frac{\mathrm{d}}{\mathrm{d}\bar{t}}\Big)\Big(3\widetilde{Z}_1 + \widetilde{Z}_7 + \sqrt{3}\widetilde{Z}_8\Big),$$
$$\tilde{p}_7 = -\frac{1}{8}\Big(\mathsf{St}^\star \frac{\mathrm{d}^2}{\mathrm{d}\bar{t}^2} + C_\mathrm{f}^\star \frac{\mathrm{d}}{\mathrm{d}\bar{t}}\Big)\Big(3\widetilde{Z}_7 + 2\sqrt{3}\widetilde{Z}_8\Big),$$
$$\tilde{p}_8 = -\frac{3}{8}\Big(\mathsf{St}^\star \frac{\mathrm{d}^2}{\mathrm{d}\bar{t}^2} + C_\mathrm{f}^\star \frac{\mathrm{d}}{\mathrm{d}\bar{t}}\Big)\Big(\widetilde{Z}_1 + \widetilde{Z}_7 + \sqrt{3}\widetilde{Z}_8\Big).$$

3.2.4 Energetic balance

The objective of the PISE-2C experiment is to approach as close as possible to a realistic assessment of dissipation. This section is devoted to the energy balances of the fluid and the structure. The total energy balance is established, monitored and its balance can be seen as a measure of the consistency of the model.

3.2.4.1 Initial formulation

3.2.4.1.1 Energy of fluid

Since the fluid is incompressible, the thermal effects are negligible and the volume forces are inactive, the appropriate balance is that of the kinetic energy. For any volume, we can write:

$$\frac{\mathrm{d}}{\mathrm{d}t}\int_{\mathcal{V}} \tfrac{1}{2}\rho \boldsymbol{v}^2 \,\mathrm{d}V = \int_{\mathcal{V}} \boldsymbol{f}\cdot\boldsymbol{v}\,\mathrm{d}V - \int_{\mathcal{V}} \mathbf{D}:\boldsymbol{\tau}\,\mathrm{d}V - \int_{\partial\mathcal{V}} \big[\tfrac{1}{2}\rho\boldsymbol{v}^2(\boldsymbol{v}-\boldsymbol{w}) - \boldsymbol{v}\cdot\boldsymbol{\sigma}\big]\cdot\boldsymbol{n}\,\mathrm{d}A. \tag{3.44}$$

The main technical difficulty is to have a correct definition of $\mathcal{V}$ as well as the motion of its boundary $\partial\mathcal{V}$.

3.2.4.1.2 Energy of the structure

It is equal to the sum of the assemblies' energies. $\mathcal{S}$ is an assembly with surface $\partial\mathcal{S}$, homogeneous linear density ρ_s and centered at C. It is displacing with a velocity of $\dot{\boldsymbol{Z}} = \dot{Z}(t)\boldsymbol{e}$ where $\boldsymbol{e}$ is a constant unit vector, depending only on the assembly. There is point external force $\boldsymbol{F}(t)$ and contact force $\boldsymbol{\sigma}\cdot\boldsymbol{n}_\mathrm{s}$ acting on the assembly, where $\boldsymbol{\sigma}$ is the constrain tensor of fluid. $\boldsymbol{n}_\mathrm{s} = -\boldsymbol{n}$ is the external norm of the assembly, then:

$$\frac{\mathrm{d}}{\mathrm{d}t}\int_{\mathcal{S}} \tfrac{1}{2}\rho_\mathrm{s}\dot{Z}^2 \,\mathrm{d}V = \boldsymbol{F}\cdot\dot{Z}\boldsymbol{e} - \int_{\partial\mathcal{S}} \big[\tfrac{1}{2}\rho_\mathrm{s}\dot{Z}^2(\dot{Z}\boldsymbol{e}-\boldsymbol{w}) - \dot{Z}\boldsymbol{e}\cdot\boldsymbol{\sigma}\big]\cdot\boldsymbol{n}_\mathrm{s}\,\mathrm{d}A.$$

The volume of an assembly is: $V_\mathrm{s} = \mathrm{vol}(\mathcal{S})$, after having observed that the normal velocity of surface displacement is necessarily identical to that of the solid, the above expression is simplified as:

$$\frac{\mathrm{d}}{\mathrm{d}t}\big(\tfrac{1}{2}m\dot{Z}^2\big) = \boldsymbol{F}\cdot\dot{Z}\boldsymbol{e} + \int_{\partial\mathcal{S}} \dot{Z}\boldsymbol{e}\cdot\boldsymbol{\sigma}\cdot\boldsymbol{n}_\mathrm{s}\,\mathrm{d}A.$$

where $m = \rho_\mathrm{s}V_\mathrm{s}$ is the linear mass of the assembly. $\boldsymbol{F} = -K(Z - Z_{|0})\boldsymbol{e} - D\dot{Z}\boldsymbol{e}$. The energy balance of the assembly can be written as:

$$\frac{\mathrm{d}}{\mathrm{d}t}\big(\tfrac{1}{2}m\dot{Z}^2\big) + \tfrac{1}{2}K\frac{\mathrm{d}}{\mathrm{d}t}(Z - Z_{|0})^2 = -D\,\dot{Z}^2 - \dot{Z}\boldsymbol{e}\cdot\int_{\partial\mathcal{S}}\boldsymbol{\sigma}\cdot\boldsymbol{n}\,\mathrm{d}A. \tag{3.45}$$

3.2.4.1.3 Combination of balance

This combination consists of eliminating the internal forces of the system consisted of the assemblies and the fluid. It is necessary to start by using the fact that on $\partial\mathcal{V}$, except the outlets, the velocity of the fluid is equal to that of the assemblies' wall due to the non-slip condition. The surface of the fluid volume $\mathcal{V}$ must therefore be divided into two parts: the first, $\mathcal{A}_\mathrm{s}$, in contact with the assemblies; the second, $\mathcal{A}_\mathrm{e}$, in the fluid at the outlets; $\partial\mathcal{V} = \mathcal{A}_\mathrm{s} \cup \mathcal{A}_\mathrm{e}$. The non-slip conditionon $\partial\mathcal{V}_\mathrm{s}$ is written as: $\boldsymbol{v} = \boldsymbol{w} = \dot{Z}\boldsymbol{e}$. With these notations, the energy balance of the fluid becomes:

$$\frac{\mathrm{d}}{\mathrm{d}t}\int_\mathcal{V} \tfrac{1}{2}\rho\boldsymbol{v}^2\,\mathrm{d}V = -\int_\mathcal{V} \mathbf{D} : \boldsymbol{\tau}\,\mathrm{d}V + \int_{\mathcal{A}_\mathrm{s}} \dot{Z}\boldsymbol{e}\cdot\boldsymbol{\sigma}\cdot\boldsymbol{n}\,\mathrm{d}A - \int_{\mathcal{A}_\mathrm{e}} \left[\tfrac{1}{2}\rho\boldsymbol{v}^2(\boldsymbol{v}-\boldsymbol{w}) - \boldsymbol{v}\cdot\boldsymbol{\sigma}\right]\cdot\boldsymbol{n}\,\mathrm{d}A.$$

The assemblies are numbered from 0 to J, the energy of structure are the sum of all the assemblies' contribution:

$$\sum_{j=0}^{J}\frac{\mathrm{d}}{\mathrm{d}t}\left[\tfrac{1}{2}m\dot{Z}_j^2 + \tfrac{1}{2}K(Z_j - Z_{j|0})^2\right] = -\sum_{j=0}^{J} D\,\dot{Z}_j^2 - \sum_{j=0}^{J}\dot{Z}_j\boldsymbol{e}_j\cdot\int_{\partial\mathcal{S}_j}\boldsymbol{\sigma}\cdot\boldsymbol{n}\,\mathrm{d}A,$$

where it is assumed that the m, K and D characteristics are the same for all assemblies as a simplification. Note also that the surfaces of the assemblies on the external crown are incomplete because their external faces must be excluded.

By definition $\bigcup_{j=0}^{J}\partial\mathcal{S}_j = \mathcal{A}_\mathrm{s}$, after summing the two balance equations together, the contact force will be eliminated:

$$\begin{aligned}
\frac{\mathrm{d}}{\mathrm{d}t}\left\{\sum_{j=1}^{J}\left[\tfrac{1}{2}m\dot{Z}_j^2 + \tfrac{1}{2}K(Z_j - Z_{j|0})^2\right] + \int_\mathcal{V}\tfrac{1}{2}\rho\boldsymbol{v}^2\,\mathrm{d}V\right\} &\quad \text{: energies,}\\
= -2\mu\int_\mathcal{V}\mathbf{D}:\mathbf{D} - \sum_{j=1}^{J} D\,\dot{Z}_j^2 &\quad \text{: dissipations,}\\
-\int_{\mathcal{A}_\mathrm{e}}\left[\tfrac{1}{2}\rho\boldsymbol{v}^2(\boldsymbol{v}-\boldsymbol{w}) + \cancel{p\boldsymbol{v}} - \cancel{2\mu\boldsymbol{v}\cdot\mathbf{D}}\right]\cdot\boldsymbol{n}\,\mathrm{d}A. &\quad \text{: flux,}
\end{aligned} \tag{3.46}$$

where the sum starts from $j = 1$. Moreover, the stress tensor is newtonian: $\boldsymbol{\sigma} = -p\,\mathbf{I} + \boldsymbol{\tau} = -p\,\mathbf{I} + 2\mu\mathbf{D}$, where the pressure is p_0 on $\mathcal{A}_e$ (it can be taken as reference since the fluid is incompressible). Moreover, the pressure of the viscous stress acting on the outlets is considered to be negligible.

No matter whatever the sign is of the flux, the two dissipative terms are strictly negative and the origin of the reduction of global energy. The flow term corresponds to what has been referred above as «respiration» (see section 3.2.3.8.4). Note that the fluid pressure does not participate in the definition of the energy of the system; it acts indirectly on the velocity of fluid and assemblies.

3.2.4.2 Geometrical elements

3.2.4.2.1 Volume $\mathcal{V}$

The fluid domain is constituted by 42 channels and 24 junctions. At rest, the unit volumes of these two constitutes have values of $2h_0b$ and $\sqrt{3}\,h_0^2$ respectively (see section 3.2.3.8.4):

$$\mathrm{vol}(\mathcal{V}_\mathrm{r}) = 84h_0b[1 + (2\sqrt{3}/7)\,\varepsilon].$$

The constituent channels are distributed as shown in TABLE 3.5, while the assemblies must be divided into two categories:

- internal assemblies : $1, \cdots, 6$;
- external assemblies : $7, \cdots, 18$;
  - summits : $7, 9, 11, 13, 15, 17$;
  - medians : $8, 10, 12, 14, 16, 18$.

The assemblies at summits have 3 faces in contact with external fluid domain while the ones at median positions have only 2 faces. However, this difference does not entail any consequences since the pressure is not integrated on the faces of the assemblies.

The volume $\mathcal{V}$ is time-varying: $\mathrm{vol}(\mathcal{V}) = V(t)$ because of the assemblies' displacements and the outlets. However, due to the flattening of boundary conditions, these volumes can be considered in their undeformed state.

TABLE 3.5: Constitutive channels

Channel	Localisation	Flow	No.	Total number
circumferential	internal	no	1, 2, 3, 4, 5, 6	6
radial	internal	yes	7, 8, 9, 10, 11, 12	6
circumferential	external	yes	13, 14, 16, 17, 19, 20, 22, 23, 25, 26, 28, 29	12
circumferential	external	no	15, 18, 21, 24, 27, 30	6
radial	external	yes	31, 32, 33, 34, 35, 36, 37, 38, 39, 40, 41, 42	12

3.2.4.2.2 Surface $\partial\mathcal{V}$

Only surface of outlets at nodes $26, 28, 31, 33, 36, 38, 41, 43, 46, 48, 51, 53$ are concerned with the balance.

TABLE 3.6: Outlets-channels-assemblies correspondance

Outlet	26	28	31	33	36	38	41	43	46	48	51	53
Channel	31	32	33	34	35	36	37	38	39	40	41	42
Assemblies	7-8	8-9	9-10	10-11	11-12	12-13	13-14	14-15	15-16	16-17	17-18	18-7

These surfaces are deformed over time but only the consequent extensions of the variation in width of the associated channel as well as the translation due to the displacement of the adjacent assemblies are retained (see TABLE 3.6); the velocity (collinear to the axis of the channel) is therefore supposed to remain orthogonal to the outlet. The shifting of two adjacent assemblies would introduce an inclination of the outlet relative to the axis of the channel whose small angle would intervene by its cosine.

3.2.4.3 Evaluation of balance

Some additional hypothesis are needed to simplify the terms of balance.

3.2.4.3.1 Flux

1D approximation makes it possible to specify the fluid velocity definition: $\boldsymbol{v} = u\,\boldsymbol{n}$ where $\boldsymbol{n}$ is the unit vector aligned with the channel axis leading to the outlet and pointing to the outside of the mock-up.

The normal displacement velocity of the surface $\boldsymbol{w}\cdot\boldsymbol{n}$ is composited of the lateral extension of the outlet (no effect) and its translation, whose velocity is evaluated as the average of the velocities of the adjacent assemblies:

$$\boldsymbol{w}_i\cdot\boldsymbol{n}_i = \tfrac{1}{2}(\dot{Z}_j\boldsymbol{e}_j + \dot{Z}_{j+1}\boldsymbol{e}_{j+1})\cdot\boldsymbol{n}_i \simeq \tfrac{1}{2}(\dot{Z}_j + \dot{Z}_{j+1}),$$

where «i» is the the number of the outlet (node) while «j» and «$j+1$» are the numbers of the adjacent assemblies.

Neglecting arbitrarily the contribution of viscous constrains, the energy flux transversing the outlet can be written as:

$$\int_{\mathcal{A}_{\mathrm{e},i}} \tfrac{1}{2}\rho\boldsymbol{v}^2(\boldsymbol{v}-\boldsymbol{w})\cdot\boldsymbol{n}\,\mathrm{d}A = 2h_k\big\{\tfrac{1}{2}\rho u_i^2[u_i - \tfrac{1}{2}(\dot{Z}_j+\dot{Z}_{j+1})]\big\}, \tag{3.47}$$

where, «k» is the number of the channel; the indices «i», «j» and «k» are not independent. (See TABLE 3.6).

3.2.4.3.2 Dissipation

From the definition of dissipation and calculation has already been presented in previous sections, the result will lead to:

$$\int_0^b \mathrm{d}x\int_{-h}^{h}\mu\Big(\frac{\partial u}{\partial y}\Big)^2\mathrm{d}y = \tfrac{2}{9}\mu U^2\,\frac{C_\mathrm{f}^2}{\varepsilon}\,\bar{h}\big(\bar{u}_{|0}^2+\bar{u}_{|1}^2+\bar{u}_{|0}\bar{u}_{|1}\big) = \tfrac{2}{3}\mu U^2\,\frac{C_\mathrm{f}^2}{\varepsilon}\,\bar{h}\big[\bar{u}_\mathrm{m}^2+\tfrac{1}{12}(\Delta\bar{u})^2\big]. \tag{3.48}$$

This last result shows that it is the mean velocity that contributes mostly to dissipation, except in the non-flowing channels where $\bar{u}_\mathrm{m}=0$. Moreover, due to the hypothesis of small displacements of the solid walls, $\bar{h}\simeq 1$.

3.2.4.3.3 Kinetic energy of fluid

Kinetic energy contained in a channel is:

$$\begin{aligned}\int_0^b \mathrm{d}x\int_{-h}^{h}\tfrac{1}{2}\rho\boldsymbol{v}^2\,\mathrm{d}y &= \tfrac{1}{2}\rho U^2 bh_0\int_0^1\mathrm{d}\bar{x}\int_{-\bar{h}}^{\bar{h}}\bar{u}^2\,\mathrm{d}\bar{y} = \rho U^2 bh_0\,\bar{h}\int_0^1\bar{u}^2\,\mathrm{d}\bar{x}\\ &= \tfrac{1}{3}\rho U^2 bh_0\,\bar{h}\big(\bar{u}_{|0}^2+\bar{u}_{|1}^2+\bar{u}_{|0}\bar{u}_{|1}\big) = \rho U^2 bh_0\,\bar{h}\big[\bar{u}_\mathrm{m}^2+\tfrac{1}{12}(\Delta\bar{u})^2\big].\end{aligned} \tag{3.49}$$

It should be noted that, due to assumptions and approximations, kinetic energy and fluid dissipation are proportional. Once again, the kinetic energy results mainly from the average velocity of the flow except for the non-flowing channels.

The comparison of the two terms corresponding in the balance (Eq. 3.46) is established as:

$$\frac{\text{dissipation}}{\text{kinetic energy}} = \tfrac{2}{3} C_{\mathrm{f}}^2 \frac{\nu\tau}{h_0^2},$$

but this value is only valid for one channel. This result is the consequence of the simplistic choice of a POISEUILLE profile for the computation of the parietal stress and the dissipation, and of the $1D$ approximation for the computation of the kinetic energy whereas the flow is unsteady; this reductive characteristic of the model has been shown in section 3.2.1.3.4.

3.2.4.4 Equations

The energy balance of the PISE-2C installation is based on the reduced configuration as defined in the FIGURE 3.15.

3.2.4.5 Energy of assemblies

In the following, the potential energy of the structure is taken as a reference because, at the initial instant, it contains all the mechanical energy of the system.

$$\begin{aligned}
\mathbb{K}_{\mathrm{i}} &: 6(\eta h_0)^2 K\left[\tfrac{1}{2}\frac{m}{K\tau^2}\left(\frac{\mathrm{d}\widetilde{Z}_1}{\mathrm{d}\bar{t}}\right)^2 + \tfrac{1}{2}\widetilde{Z}_1^2\right] && : \text{internal crown},\\
\mathbb{K}_{\mathrm{e}}^{\mathrm{s}} &: +6(\eta h_0)^2 K\left[\tfrac{1}{2}\frac{m}{K\tau^2}\left(\frac{\mathrm{d}\widetilde{Z}_7}{\mathrm{d}\bar{t}}\right)^2 + \tfrac{1}{2}\widetilde{Z}_7^2\right] && : \text{external crown (summits)},\\
\mathbb{K}_{\mathrm{e}}^{\mathrm{m}} &: +6(\eta h_0)^2 K\left[\tfrac{1}{2}\frac{m}{K\tau^2}\left(\frac{\mathrm{d}\widetilde{Z}_8}{\mathrm{d}\bar{t}}\right)^2 + \tfrac{1}{2}\widetilde{Z}_8^2\right] && : \text{external crown (medians)}.
\end{aligned}$$

3.2.4.6 Kinetic energy of fluid

The kinetic energy of the non-flowing channels involves only the difference in velocities at the ends of each channel.

$$\begin{aligned}
\mathbb{C}_{\mathrm{i}}^{\mathrm{n}} &: 6\rho U^2 b h_0\left[\tfrac{1}{12}(\Delta\bar{u}_6)^2\right] && : \text{non-flowing internal circumferential channels},\\
\mathbb{R}_{\mathrm{i}} &: +6\rho U^2 b h_0\left[\bar{u}_{\mathrm{m},7}^2 + \tfrac{1}{12}(\Delta\bar{u}_7)^2\right] && : \text{internal radial channels},\\
\mathbb{C}_{\mathrm{e}}^{\mathrm{d}} &: +12\rho U^2 b h_0\left[\bar{u}_{\mathrm{m},13}^2 + \tfrac{1}{12}(\Delta\bar{u}_{13})^2\right] && : \text{flowing external circumferential channels},\\
\mathbb{C}_{\mathrm{e}}^{\mathrm{n}} &: +6\rho U^2 b h_0\left[\tfrac{1}{12}(\Delta\bar{u}_{30})^2\right] && : \text{non-flowing external circumferential channels},\\
\mathbb{R}_{\mathrm{e}} &: +12\rho U^2 b h_0\left[\bar{u}_{\mathrm{m},31}^2 + \tfrac{1}{12}(\Delta\bar{u}_{31})^2\right] && : \text{external radial channels}.
\end{aligned}$$

The definitions of average velocity and the variations can be found in section 3.2.3.7.3.

3.2.4.7 Dissipation of the structure

As stated above, all the assemblies have the same properties:

$$\begin{aligned}
\mathbb{K}_{\mathrm{i}} &: 6D\frac{(\eta h_0)^2}{\tau^2}\left(\frac{\mathrm{d}\widetilde{Z}_1}{\mathrm{d}\bar{t}}\right)^2 && : \text{internal crown},\\
\mathbb{K}_{\mathrm{e}}^{\mathrm{s}} &: +6D\frac{(\eta h_0)^2}{\tau^2}\left(\frac{\mathrm{d}\widetilde{Z}_7}{\mathrm{d}\bar{t}}\right)^2 && : \text{external crown (summits)},\\
\mathbb{K}_{\mathrm{e}}^{\mathrm{m}} &: +6D\frac{(\eta h_0)^2}{\tau^2}\left(\frac{\mathrm{d}\widetilde{Z}_8}{\mathrm{d}\bar{t}}\right)^2 && : \text{external crown (medians)}.
\end{aligned}$$

3.2.4.8 Dissipation of fluid

It should be distinguished between the flowing channel and the non-flowing channel ($\bar{u}_{\mathrm{m}} = 0$).

$$\mathbb{C}_{\mathrm{i}}^{\mathrm{n}} \quad : \quad 4\mu U^2 \frac{C_{\mathrm{f}}^2}{\varepsilon}\left[\tfrac{1}{12}(\Delta\bar{u}_6)^2\right] \quad : \text{non-flowing internal circumferential channels,}$$

$$\mathbb{R}_{\mathrm{i}} \quad : \quad +4\mu U^2 \frac{C_{\mathrm{f}}^2}{\varepsilon}\left[\bar{u}_{\mathrm{m},7}^2 + \tfrac{1}{12}(\Delta\bar{u}_7)^2\right] \quad : \text{internal radial channels,}$$

$$\mathbb{C}_{\mathrm{e}}^{\mathrm{d}} \quad : \quad +8\mu U^2 \frac{C_{\mathrm{f}}^2}{\varepsilon}\left[\bar{u}_{\mathrm{m},13}^2 + \tfrac{1}{12}(\Delta\bar{u}_{13})^2\right] \quad : \text{flowing external circumferential channels,}$$

$$\mathbb{C}_{\mathrm{e}}^{\mathrm{n}} \quad : \quad +4\mu U^2 \frac{C_{\mathrm{f}}^2}{\varepsilon}\left[\tfrac{1}{12}(\Delta\bar{u}_{30})^2\right] \quad : \text{non-flowing external circumferential channels,}$$

$$\mathbb{R}_{\mathrm{e}} \quad : \quad +8\mu U^2 \frac{C_{\mathrm{f}}^2}{\varepsilon}\left[\bar{u}_{\mathrm{m},31}^2 + \tfrac{1}{12}(\Delta\bar{u}_{31})^2\right] \quad : \text{external radial channels.}$$

3.2.4.9 Flux at outlets

Due to the boundary conditions, it is reduced to a kinetic energy flux:

$$h_0\rho U^3 \sum_{i\in\mathbb{N}_{\mathrm{e}}^{\mathrm{e}}} \bar{u}_i^2\Big\{\bar{u}_i - \tfrac{1}{2}\varepsilon\eta\,\mathsf{St}\Big[\frac{\mathrm{d}\widetilde{Z}_{j(i)}}{\mathrm{d}\bar{t}} + \frac{\mathrm{d}\widetilde{Z}_{j(i)+1}}{\mathrm{d}\bar{t}}\Big]\Big\},$$

Where $j(i)$ is given by TABLE 3.6. If the velocity at outlets is independent of the index «i» and take for the value u_{26} (value of the local velocity at node 26), we need to distinguish the velocities of assemblies. Regrouping the elements and summing on $\mathbb{N}_{\mathrm{e}}^{\mathrm{e}}$, it becomes:

$$12\rho U^3 h_0\Big\{\bar{u}_{26}^2\Big[\bar{u}_{26} - \tfrac{1}{2}\varepsilon\eta\,\mathsf{St}\Big(\frac{\mathrm{d}\widetilde{Z}_7}{\mathrm{d}\bar{t}} + \frac{\mathrm{d}\widetilde{Z}_8}{\mathrm{d}\bar{t}}\Big)\Big]\Big\}.$$

Since $\eta\mathsf{St} = 1$, the flow resulting from the displacement of the outlet is of order $\varepsilon \ll 1$; we must see this as a manifestation of small-displacement hypothesis. Finally, examination of the figures and tables shows that the node 26 corresponds to the exit section of the channel 31, so that:

$$\bar{u}_{26} = \bar{u}_{\mathrm{m},31} + \tfrac{1}{2}\Delta\bar{u}_{31}.$$

In the case from release to fluctuations, the energy flow, integrated over the duration $\tau \to \infty$, represents the energy loss from the expulsion of a certain mass of fluid at a non-zero velocity.

3.2.4.10 Phenomenological analysis

From a numerical point of view, it is more practical to evaluate this balance by an integration from the initial time to the instant t. By bringing the total balance to the scale of the potential

energy of the structure, we will have the following groupings of scales:

$$\begin{aligned}
\frac{m}{K\tau^2} &: \text{kinetic energy of structure,}\\
1 &: \text{potential energy of structure,}\\
\frac{\rho U^2 b h_0}{(\eta h_0)^2 K} &: \text{kinetic energy of fluid,}\\
\frac{D(\eta h_0)^2}{(\eta h_0)^2 K\tau} &: \text{dissipation of structure (integrated),}\\
\frac{\mu U^2 C_{\mathrm{f}}^2 \tau}{\varepsilon(\eta h_0)^2 K} &: \text{dissipation of fluid (integrated),}\\
\frac{\rho U^3 h_0 \tau}{(\eta h_0)^2 K} &: \text{flux (integrated),}
\end{aligned}$$

after simplifications (see Eq.3.22 and section 3.2.3.1) and showing the groupings of scales of the problem:

$$m^*\ ,\ 1\ ,\ \frac{\gamma m^*}{\varepsilon}\ ;\ D^*\ ,\ \frac{\gamma m^* C_{\mathrm{f}}^{*2}\mathsf{Re}}{\mathsf{St}}\ ,\ \frac{\gamma m^*}{\varepsilon\mathsf{St}}.$$

Rather than REYNOLDS number which is not very suggestive, it is more explicit to introduce the characteristic time $\tau_\nu = h_0^2/\nu$ which evaluates the time required for diffusion to contaminate the entire width of a channel; similarly, the STROUHAL number is expressed with the transit time $\tau_U = b/U$ which evaluates the time required for a fluid particle to traverse a channel of length b at the velocity U. The above list can therefore be reformulated only with characteristic time ratios:

$$\frac{\tau_K^2}{\tau^2}\ ,\ 1\ ,\ \frac{\gamma}{\varepsilon}\frac{\tau_K^2}{\tau^2}\ ;\ \frac{\tau_D}{\tau}\ ,\ \frac{\gamma C_{\mathrm{f}}^2}{\varepsilon}\frac{\tau_K^2}{\tau^2}\frac{\tau}{\tau_\nu}\ ,\ \frac{\gamma}{\varepsilon}\frac{\tau_K^2}{\tau^2}\frac{\tau}{\tau_U}.$$

It represents the different terms of an integrated energy balance on the duration τ. In applications, the terms of the second member are generally small comparing to the second member and only act sensibly after several periods. Knowing that this is a problem of releasing in which, at the initial moment, all the energy is that of the structure, the following relation comes from the first member:

$$1 = (\tau_K/\tau_A)^2 \sup\{1\ ,\ \gamma/\varepsilon\} \quad\Longrightarrow\quad \tau_A = \tau_K\sqrt{\sup\{1\ ,\ \gamma/\varepsilon\}}, \tag{3.50}$$

which shows that the parameter which compares the kinetic energies of the structure and the fluid depends only on the respective inertias of the two media:

$$\tau_A = \tau_K\sqrt{\gamma/\varepsilon} > \tau_K,$$

This will conduct to the following:

$$\frac{\varepsilon}{\gamma}\ ,\ 1\ ,\ 1\ ;\ \frac{\tau_D}{\tau_K}\sqrt{\frac{\varepsilon}{\gamma}}\ ,\ C_{\mathrm{f}}^2\frac{\tau_K}{\tau_\nu}\sqrt{\frac{\gamma}{\varepsilon}}\ ,\ \frac{\tau_K}{\tau_U}\sqrt{\frac{\gamma}{\varepsilon}}.$$

From the point of view of the dissipative terms, the comparison is made with respect to the flux:

$$\frac{\tau_D}{\tau_K}\sqrt{\frac{\varepsilon}{\gamma}} \times \frac{\tau_U}{\tau_K}\sqrt{\frac{\varepsilon}{\gamma}} = \frac{\varepsilon}{\gamma}\frac{\tau_U\tau_D}{\tau_K^2} \quad\text{and}\quad C_{\mathrm{f}}^2\frac{\tau_K}{\tau_\nu}\sqrt{\frac{\gamma}{\varepsilon}} \times \frac{\tau_U}{\tau_K}\sqrt{\frac{\varepsilon}{\gamma}} = C_{\mathrm{f}}^2\frac{\tau_U}{\tau_\nu} = \frac{C_{\mathrm{f}}^2}{\varepsilon\mathsf{Re}}.$$

The comparison of the two terms that depends only on the flow (second expression). It does not involve τ_K nor γ, contrary to that which mixes fluid and solid (first expression). In short, to remain small with respect to energies, dissipative terms must verify the inequality:

$$\sqrt{\frac{\gamma}{\varepsilon}}\sup\{\frac{\varepsilon}{\gamma}\frac{\tau_D}{\tau_K}\ ,\ C_{\mathrm{f}}^2\frac{\tau_K}{\tau_\nu}\ ,\ \frac{\tau_K}{\tau_U}\}\lesssim 1.$$

However, it is important to remember that this inequality only holds for the first periods because it is inevitable that the dissipative terms convert all the mechanical energy initially present in the system into internal energy.

It is natural to wonder why the characteristic time τ_A does not emerge from the phenomenological analysis of the dynamic problem (see section 3.2.2.3). This is due to the fact that the configuration pointed to by the energy analysis is not specifically envisaged. Returning to the dynamic equations, it occurs when the terms are framed in the expression below:

$$\underbrace{\boxed{1}=\sup\{\frac{m}{K\tau^2}\ ,\ \frac{D}{K\tau}\ ,\ \boxed{\frac{(\delta p)}{\varepsilon\eta K}}\}}_{\text{structure}}\quad\text{where}\quad\underbrace{\boxed{\frac{(\delta p)}{\rho U^2}}=\sup\{\boxed{\mathsf{St}}\ ,\ \frac{C_{\mathrm{f}}}{\varepsilon\mathsf{Re}}\}}_{\text{flow}}\ .$$

Taking into account $\eta\mathsf{St}=1$, the resolution of this system effectively leads to: $\tau=\tau_A$. This point is taken numerically in section **??**.

3.2.5 Conclusions

This study constitutes a very simplified attempt to calculate the experimental installation of PISE-2C. Most of the objectives are met.

The description of the flow is reduced to the strict minimum:

- $2D$ flow, strongly confined, allowing the thin-layer approximation;
- vibrations of low amplitude and high frequency to apply boundary conditions on fixed walls (flattening) and linearising equations ;
- reduction of the thin-flayer approximation to $1D$ approximation at the price of the introduction of an empirical friction law; only one free parameters C_f is implemented to adjust the friction law.

The phenomenological analysis of the physical problem leads to the definition of a framework for the parameters guaranteeing the appropriateness of the approximations. Several classic results emerge naturally:

- the usual notions of frequency and damping are found ;
- the pressure force exerted by the fluid distributes into an in-phase contribution and a quadrature contribution ;
- although negligible in the balance of the forces acting on an assembly, the viscous frictions are susceptible to act indirectly, by modifying the pressure field.

With the aim to reducing the size of the problem, the method applied here exploits to the maximum the symmetries of the mock-up (so-called «flowering», the movements of seismic origin, devoid of symmetry, are not examined). Starting with an installation comprising 19 assemblies, it is thus possible to reduce the study to 3 assemblies. This alleviation allows to analytically highlight several properties:

- because of the symmetries, it suffices to take an interest in one-sixth of the heart, reducing the number of unknowns accordingly; these symmetries result in the existence of privileged flow paths, independent of one another ;
- the problem is thus reduced to a homogeneous system of three differential equations of the second order with constant and coupled coefficients.

Finally, we must not overlook the fact that this model is entirely linear, which masks the effects associated with large amplitudes.

The real weakness of the model appears when examining the energy balance. The calculation of friction force and viscous dissipation is based on a Poiseuille flow which, under the conditions observed in PISE-2C, is probably far from the reality. This results in an underestimation of the dissipation which must be compensated by an empirical increase in the coefficient of friction. However, balancing the energy balance does not guarantee an improvement in the dynamics. In any case, the characteristics of the energy balance are as follows:

- energy of the structure largely dominates over the kinetic energy;
- viscous dissipation largely dominates over the structural damping ;
- flux of kinetic energy at outlets is negligible.

This model is based on an example of small size (core with two crowns) chosen because it corresponds to the experimental facility PISE-2C currently under investigation. However, it is possible to generalise this approach to larger dimensions, the only obstacle being the size of the final differential system (in fact, the number of unknowns increases with the number of crowns).

3.3 Free-vibration experiments on PISE-2C

There were four groups of free-vibration experiments with different physical conditions and varying modes of vibration:

- Experiments in air with sole active assembly
- Experiments in water with sole active assembly
- Experiments in water with crown grouped assemblies activated (partial flowering)
- Experiments in water with whole mock-up active (total flowering)

As introduced in Chapter 3, big initial displacement as 3 mm will introduce unwanted affect from initial shock of release. Therefore, an initial displacement around 1 mm will be imposed at the beginning of each test both for experiments with sole assembly and multi assemblies. This initial displacement is at 1/3 of the inter-assembly channel width, therefore, non-linearity effects are expected to happen especially during the first several periods. The crab will pull the chosen assembly or assemblies along the outward radial direction and then release it or them in order to start the vibration.

For experiments in water, the container will be filled with water at a height above the assembly around 200 mm to assure that the whole mockup is immersed in water.

To facilitate the experiments, calibration factor of strain-gauge, structural stiffness and damping of each assembly have been calibrated (see FIGURE 3.4, 3.5). These calibrations were performed on the base of PISE-1A, difference of calibration factor for the assemblies installed on PISE-2C base may exist.

3.4 Methodologies of analysis on global behaviour of PISE-2C

To carry out the analysis on global behaviour of PISE-2C during the free-vibration movements, several global indicators have to be introduced.

3.4.1 Displacement

Displacements have been measured for each assembly by strain gauge. Since there are different delay time for the crab to release all the assemblies, the signals of displacements have been cut at the beginning in order to only take the duration when all the assemblies are in movement. Same as signal processing of PISE-1A, displacement signal of PISE-2C experiments have also been assessed with filtering to remove the unwanted high-frequency noise.

3.4.2 Velocity of assembly

Velocity of each assembly was deducted from the time evolution of displacement with 2nd-order time scheme.

$$\dot{x}_n(i) = \frac{3x_{n+1}(i) - 4x_n(i) + x_{n-1}(i)}{2\Delta t} \quad [\mathrm{m/s}], \tag{3.51}$$

where $\dot{x}_n$ and x_n are the velocity and displacement of Assembly No.i at t_n respectively.

3.4.3 Indicators of symmetry

The symmetry of PISE-2C installation is an important indicator of the complexity of PISE-2C (the level of order in oscillations of the assemblies) which justifies if the deterministic approach is acceptable in analysis.

To get an idea of the level of order in the experiments, several indicators of symmetry have been examined. In addition, this is also necessary for establishing the pertinence of the reticulate model.

We can divide the whole plan into 6 sections (see FIGURE 3.27)

- ▷ Section 1 :
  - Assemblies : 4, 12, 13, 14 ;
  - Complete channels : 3-4, 14-15, 15-16, 16-17, 15-38, 16-41 ;
  - Half channels : 3-14, 4-17 .
- ▷ Section 2 :
  - Assemblies : 3, 10, 11, 12 ;
  - Complete channels : 2-3, 11-12, 12-13, 13-14, 12-33, 13-36 ;
  - Half channels : 2-11, 3-14 .
- ▷ Section 3 :
  - Assemblies : 2, 8, 9, 10 ;
  - Complete channels : 1-2, 8-9, 9-10, 10-11, 9-28, 10-31 ;
  - Half channels : 1-8, 2-11 .
- ▷ Section 4 :

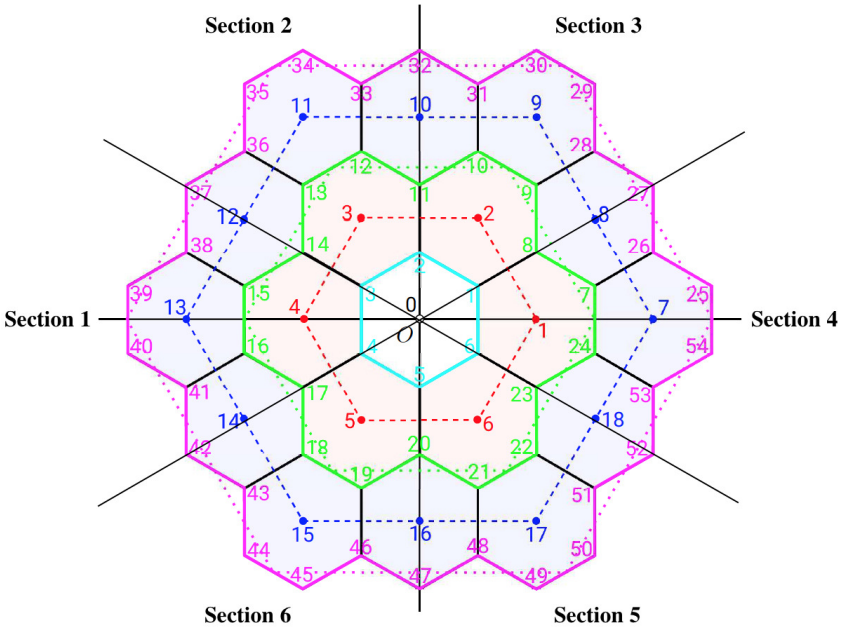

FIGURE 3.18: Sections of PISE-2C

- Assemblies : 1, 18, 7, 8 ;
- Complete channels : 6-1, 23-24, 24-7, 7-8, 24-53, 7-26 ;
- Half channels : 6-23, 1-8 .

▷ Section 5 :

- Assemblies : 6, 16, 17, 18 ;
- Complete channels : 5-6, 20-21, 21-22, 22-23, 21-48, 22-51 ;
- Half channels : 5-20, 6-23 .

▷ Section 6 :

- Assemblies : 5, 14, 15, 16 ;
- Complete channels : 4-5, 17-18, 18-19, 19-20, 18-43, 19-46 ;
- Half channels : 4-17, 5-20 .

In each sections, there are 4 assemblies allocated with 2 completely included in the section as well as the other two included both for the certain section and the adjacent section. Also, 6 complete channels are contained in one certain section, while 2 «half channels» located at the boundary of neighbouring sections.

To justify the symmetry of PISE-2C, time evolution of liquid volume contained in each section will be taken as an indicator. For Section i, the liquid volume:

$$V_i(t) = H * S^i(t)\ [\mathrm{m}^3], \quad \text{where,} \quad S_i(t) = S_c^i(t) + \frac{1}{2} S_h^i(t)\ [\mathrm{m}^2]. \tag{3.52}$$

Here, $S_i(t)$ is cross-section surface of Section i, $S_c^i(t)$ is the summed horizontal surface of all the complete channels contained in Section i, $S_h^i(t)$ is the summed horizontal surface of all the half channels.

3.4.4 Energy of assembly

Time evolutions of potential energy, kinetic energy and total energy of each assembly can be calculated from velocity and displacement. Therefore, we can obtain time evolutions of energies for different group of assemblies including the whole mock-up, different crowns and different sectors.

$$\begin{aligned}
&e_k(j,t) = \frac{1}{2} m_0 \dot{x}(j,t)^2; \qquad e_p(j,t) = \frac{1}{2} k x^2(j,t); \quad e_t(j,t) = e_k(j,t) + e_p(j,t);\\
&e_{ki}(t) = \sum_{j=1}^{6} e_k(j,t); \qquad e_{pi}(t) = \sum_{j=1}^{6} e_p(j,t); \; e_{ti} = \sum_{j=1}^{6} e_t(j,t);\\
&e_{ke}(t) = \sum_{j=7}^{18} e_k(j,t); \qquad e_{pe}(t) = \sum_{j=7}^{18} e_p(j,t); \; e_{te} = \sum_{j=7}^{18} e_t(j,t);\\
&e_{kt}(t) = \sum_{j=2}^{19} e_k(j,t); \qquad e_{pt}(t) = \sum_{j=2}^{19} e_p(j,t); \; e_{tt}(t) = \sum_{j=2}^{19} e_t(j,t).
\end{aligned} \tag{3.53}$$

Here, $e_k(j,t)$, $e_p(j,t)$ and $e_t(j,t)$ [J] are kinetic energy, potential energy and total energy of Assembly No.j at time point t respectively. $e_{ki}(t)$, $e_{pi}(t)$ and $e_{ti}(t)$ [J] are kinetic energy, potential energy and total energy of assemblies on internal crown at time point t. $e_{ke}(t)$, $e_{pe}(t)$ and $e_{te}(t)$ [J] are kinetic energy, potential energy and total energy of assemblies on external crown at time point t. $e_{kt}(t)$, $e_{pt}(t)$ and $e_{tt}(t)$ [J] are kinetic energy, potential energy and total energy of whole mockup at time point t.

3.4.5 Volume of liquid contained in the mockup

Volume of liquid in the mockup can be calculated as the multiplication results of horizontal cross-section surface and height of the mockup. Horizontal cross-section surface can be calculated by the sum of horizontal surface area of all the internal channels.

$$V(t) = H * S_{cross}(t) \quad [\mathrm{m}^3]. \tag{3.54}$$

$V(t)$ is the volume of liquid contained in the mockup, H is the height of the assembly, $S_{cross}(t)$ is the area of the horizontal cross-section surface.

3.4.6 Average outflow velocity

A virtual average outflow velocity $v(t)$ is introduced to characterise the average movement of the whole mockup. It will be the result of total liquid volume contained in the mock-up divided by the area of all the outflow surface. The outflow surface includes the top and bottom cross-section surface with the vertical gap surface $S_{side}(t)$ between the assemblies in outer crown.

$$v(t) = V(t)/(2 * S_{cross}(t) + S_{side}(t)) \quad [\mathrm{m/s}]. \tag{3.55}$$

As seen in free-vibration experiments of PISE-1A by PIV [26] and also the $3D$ NAVIER-STOKES simulation of PISE-1A, there are three flow regions existed: 2 recirculation regions

and 1 $2D$ region. It means that the outflow and inflow at the edge don't affect the flow in the $2D$ region. This observation can be extrapolated to PISE-2C. Since the volume variations in recirculation regions at upper and lower edges are small with regard to that in $2D$ region, the velocities coming from the upper and lower surface of PISE-2C are negligible comparing to the velocities coming from the vertical external faces. Therefore, the average flow velocity is mainly in representation of the horizontal velocity coming from the vertical external sides.

3.4.7 Surface confined by assemblies' center of external crown

To describe the global behaviour of the PISE-2C, another global quantity is introduced here as the surface area defined by the center of the assemblies on the external crown ([m^2]). As shown section 3.2.2.4.1, it is the area defined by blue dash line.

3.5 Total flowering

To analyse the dynamic behaviour of PISE-2C as an ensemble facility, an experiment with all the assemblies in the mockup activated (total flowering) was performed with five repeated tests. All the assemblies were pulled to a position where the initial displacement is 1 mm outward radially by the crab. They were released at approximately the same time to start the vibrations.

3.5.1 Displacements

Taking assembly 1, 7, 8 as the representatives, compare experimental results with numerical results obtained from reticulate model (section 3.2):

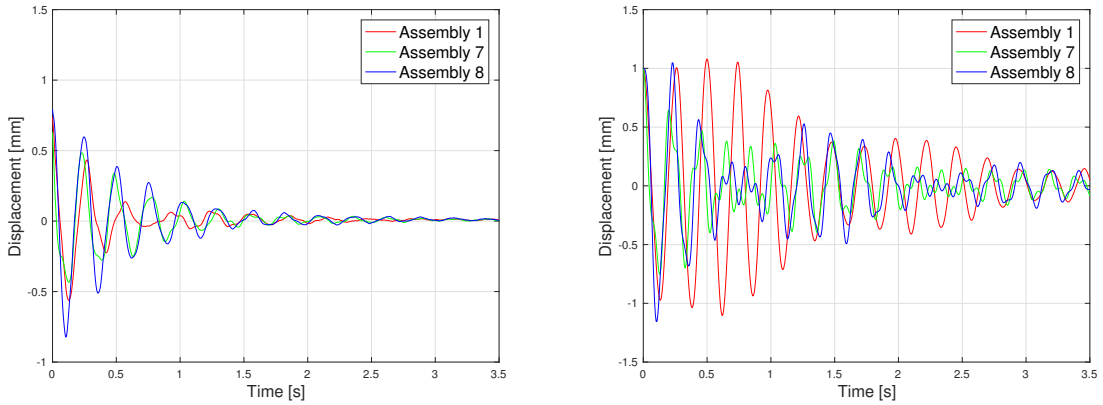

(a) Experiments (b) Analytical

FIGURE 3.19: Time evolution of displacement (Total Flowering)

Assembly 1 is on internal crown while assembly 7 and 8 are on external crown. For both experiments and analytical solution, the movement of assembly 1 and the movement of 7 and 8 are slightly out of phase. However, with time goes by, the movements tend to be realigned to same phase inasmuch that the two crowns are pushing each other during the oscillation.

The movements of assemblies predicted by the analytical model show much more intense harmonics than that in the experiments.

The displacements of all three assemblies, regardless which crowns it is on, decreases quicker than that of analytical solution.

3.5.2 Velocity

FIGURE 3.20 displays the comparison of velocity evolution between experiments and analytical solution for assembly 1, 7 and 8:

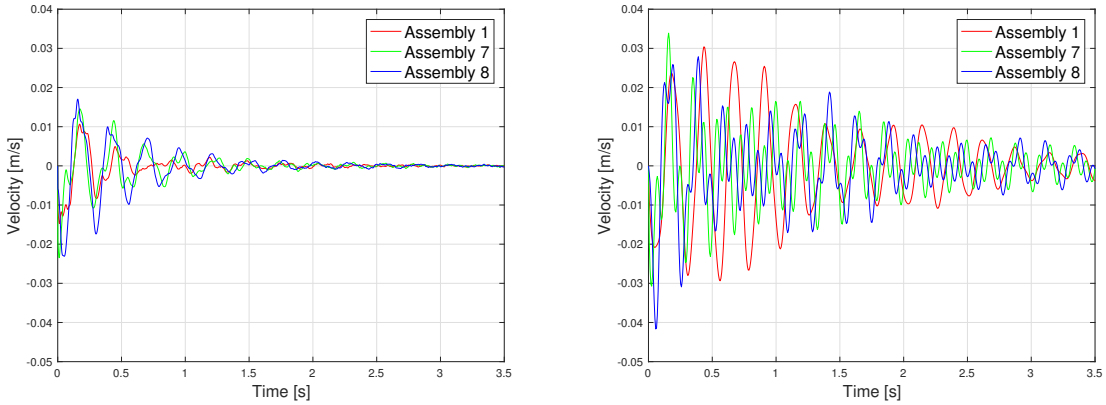

(a) Experiments (b) Analytical

FIGURE 3.20: Time evolution of velocity (Total Flowering)

Deducted from displacement, velocity evolution shows same behaviour as displacement evolution.

3.5.3 Energies of assembly

FIGURE 3.21 displays the comparison of energies (including potential energy, kinetic energy and total energy) for whole mock-up, internal crown and external crown.

In the experiments, potential energies dominate over kinetic energy that total energies are almost fully consisted of potential energies. Total energy of external crown is about 2 times than that of internal crown due to double assemblies located in external crown. Also, during the oscillation, there are some time instants when almost all the energies of structure are deposited in fluid. Supposing similar scenario in Phénix, large amount of mechanical energy from the structure transfers to the liquid sodium. This may highly increase the instability and possibility of sudden vaporisation for the liquid sodium. Energy of internal crown gets dissipated much more faster than that of external crown because of stronger confinement for assemblies on internal crown.

In comparison between the experiments and analytical solution, the mechanical energy of structure is much more quickly dissipated in the experiments than that of analytical solution.

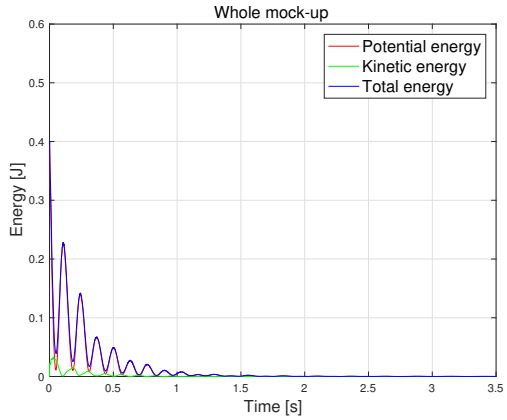

(a) Experiments

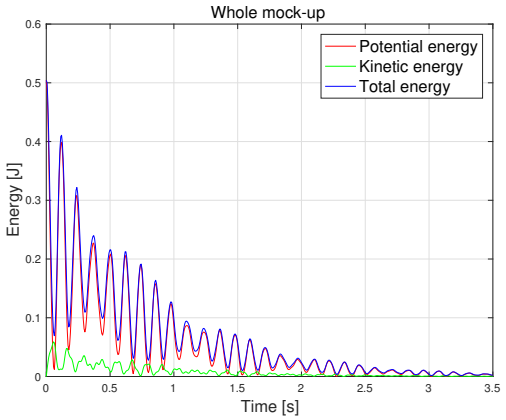

(b) Analytical

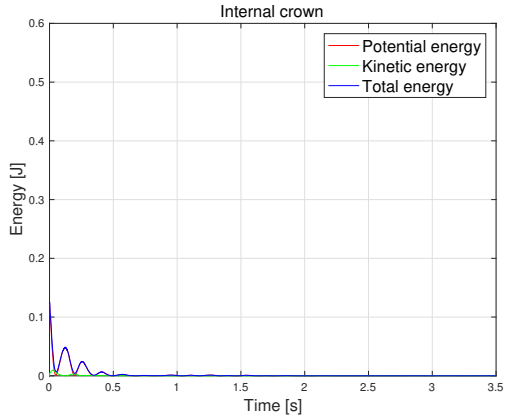

(c) Experiments

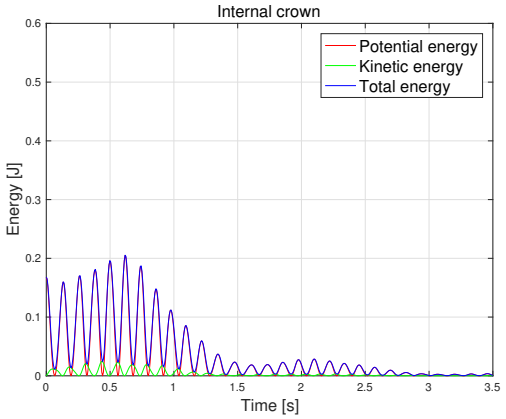

(d) Analytical

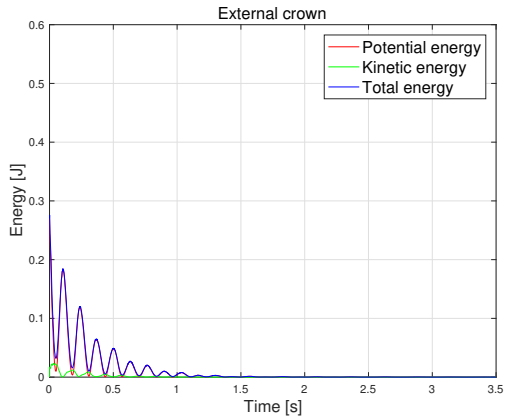

(e) Experiments

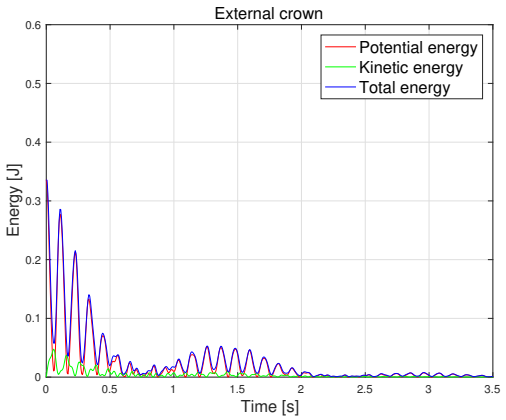

(f) Analytical

FIGURE 3.21: Time evolution of energies (Total flowering)

3.5.4 Volume contained in whole mockup

In experiments, confinement parameter $\eta = 0.1693$, different from that in the analytical solution where $\eta = 0.1$. FIGURE 3.22 displays the relative volume variations $\frac{V(t)-V_r}{V_r}$ with

time.

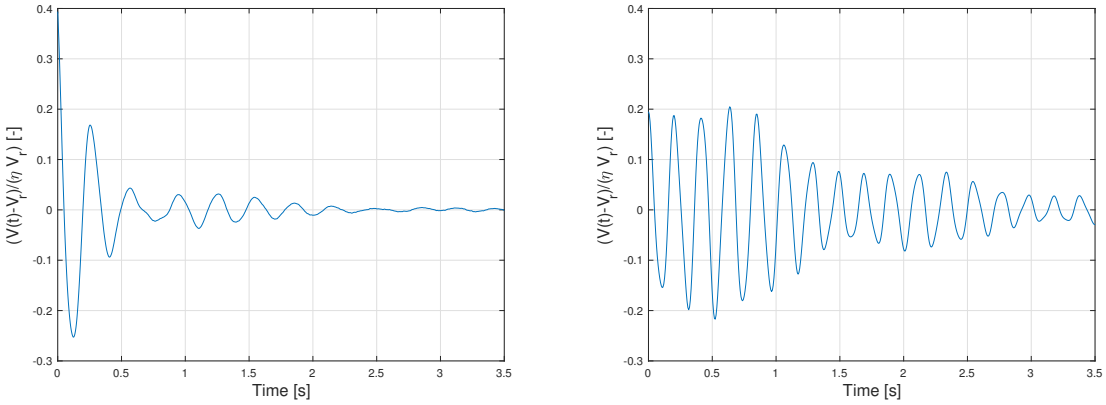

(a) Experiments (b) Analytical

FIGURE 3.22: $\frac{V(t)-V_r}{\eta V_r}$ (Total Flowering)

A maximum variation relative to volume at rest of 40% occurs at the beginning of the oscillation. This is already far from the assumption of linear model.

3.5.5 Average outflow velocity

FIGURE 3.23 shows the average outflow velocity of experiments calculated from volume variations as stated in above section.

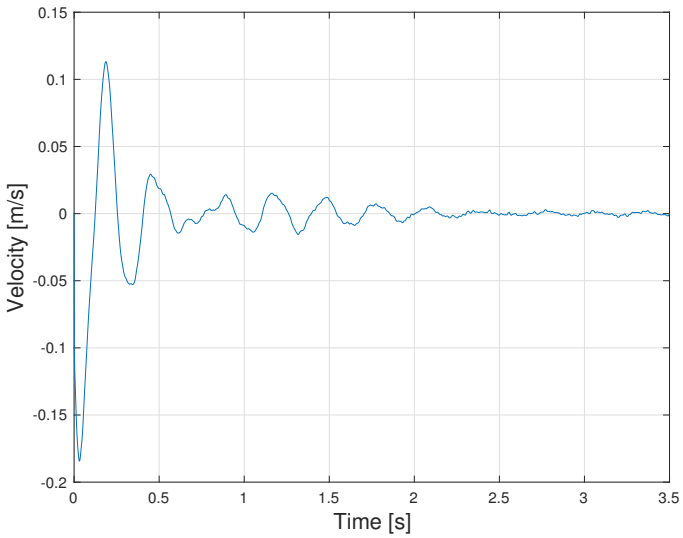

FIGURE 3.23: Average outflow velocity (Total flowering)

From around 0.6 to 0.7 s, the average outflow velocity is at a low level. This pause of respiration in PISE-2C may come from the realigning of oscillations.

3.5.6 Surface confined by centres on external crown

FIGURE 3.24 shows the time evolution of surface area difference $A(t) - A_r$ confined by the centres of assemblies on external crown.

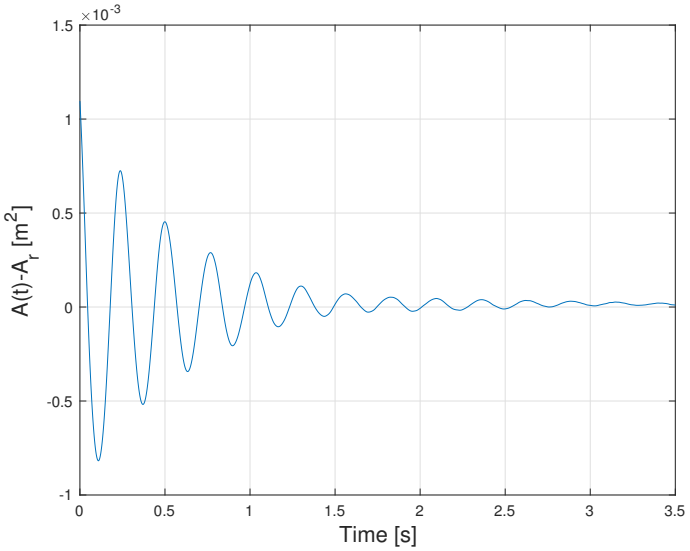

FIGURE 3.24: Surface area difference (Total flowering)

Surface area has a much more regular evolution behaviour than that of displacement because of averaging.

3.5.7 Indicators of symmetry

On internal crown, all the assemblies are supposed to be in radial symmetry. On external crown, 2 groups of assemblies in radial symmetry existed for assemblies with 3 external faces (e.g. assembly 7) and assemblies with 2 external faces (e.g. assembly 8). For assembly 7, assembly 13 is also the assembly in axial symmetry and for assembly 8, assembly 14 is the one in axial symmetry. FIGURE 3.25 plots the displacements of assemblies in symmetry.

For assembly 1, the displacements of assembly 2 and 6 are plotted. Assembly 9 and 13 are in comparison with assembly 7 while assembly 10 and 14 for assembly 8.

Although the assemblies displayed in the same figure are supposed to be in geometry, some disorders are observed among the displacements. In FIGURE 3.25(a), there is phase lag between the three assemblies on internal crown as well as different behaviour of harmonics as well as realignment of phase with time. Little differences in phase also exist for the assemblies on external crown in FIGURE 3.25(b,c).

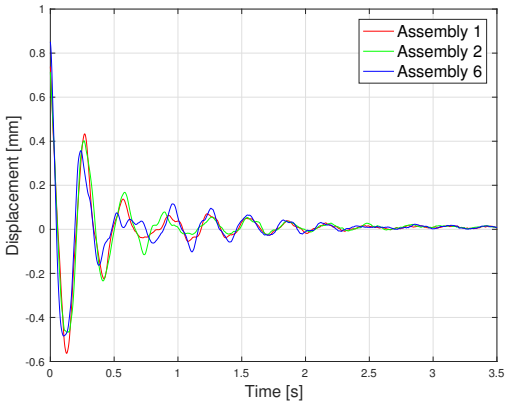

(a) Assembly 1

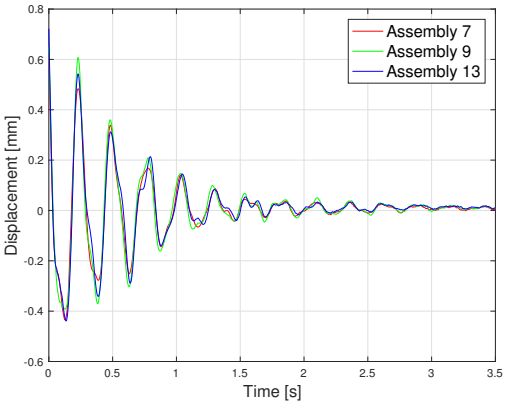

(b) Assembly 7

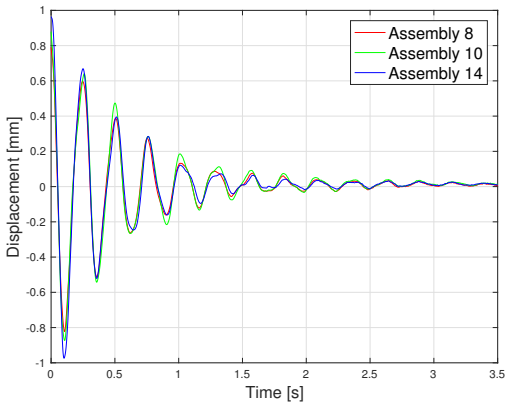

(c) Assembly 8

FIGURE 3.25: Time evolution of displacements in symmetry (Total flowering)

FIGURE 3.26 is the frequency response of displacements for assemblies supposed in symmetry. As observed with displacement curves in FIGURE 3.25, more discrepancies exist for assembly on internal crown. Also, peaks located closely in FIGURE 3.26 are consistent with the intense harmonics in FIGURE 3.25(a).

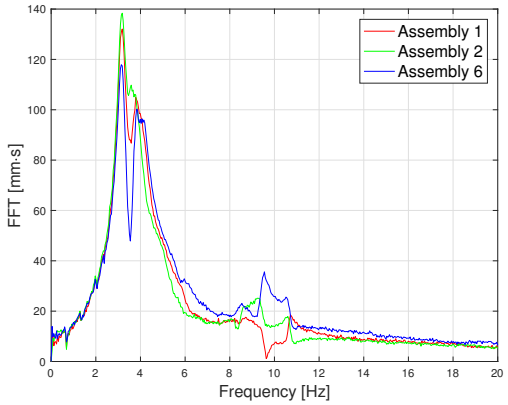

(a) Assembly 1

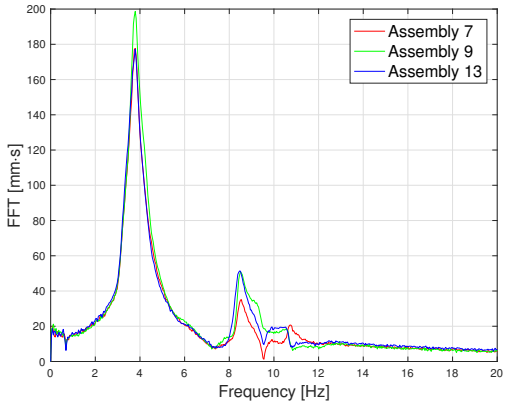

(b) Assembly 7

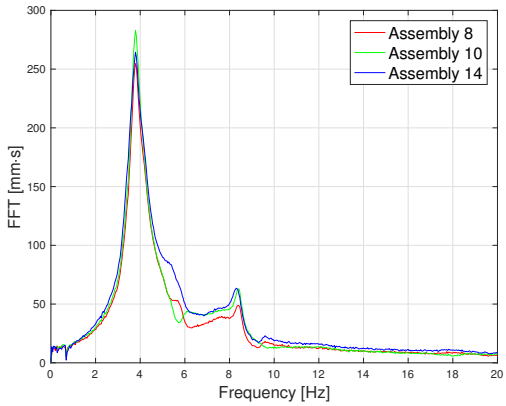

(c) Assembly 8

FIGURE 3.26: Frequency response of displacements in symmetry (Total flowering)

FIGURE 3.27 shows the volume evolutions of all six sections.

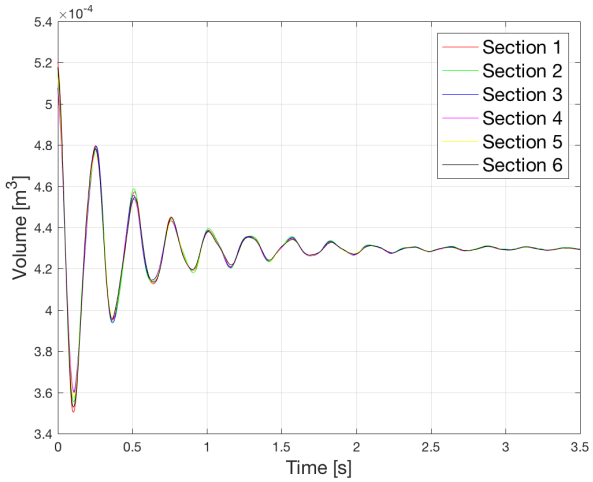

FIGURE 3.27: Volume of sections (Total flowering)

With shared half-channels, the disorder behaviours as seen in displacements have been averaged. Therefore, the six sections show similar behaviour in time evolutions of volumes contained.

3.6 Partial flowering : Internal crown

Experiments of partial flowering with internal crown excited have been performed.

3.6.1 Displacements

FIGREU 3.28 shows the comparison between experiment and analytical solution of displacements for assembly 1, 7 and 8.

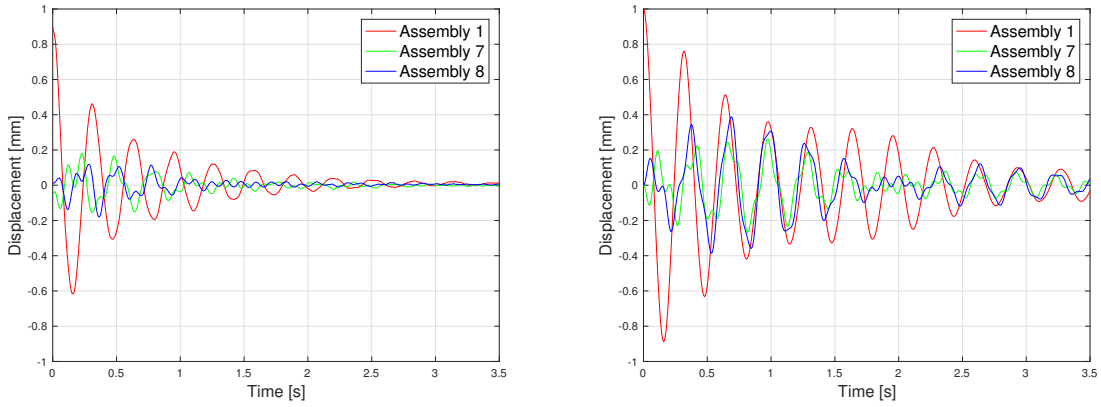

(a) Experiments (b) Analytical

FIGURE 3.28: Time evolution of displacement (Partial flowering: Internal crown)

In the experiments, unlike the displacement behaviour during total flowering, when the internal crown is in excitation as the driving crown, there is no longer realigning of phases after certain periods oscillation between the assemblies on internal crown (assembly 1) and external crown (assembly 7 & 8), instead, they are always out of phase between each other. Strong harmonics exist for the assemblies on external crown which prevents the propagation of oscillation for the two crowns to oscillate together as that in the case of total flowering. It also refrains the vibrating amplitudes of the these assemblies in a low level. Different behaviours of harmonics can be seen for assembly 7 and 8 due to different conditions of confinement. In contrast, not as much harmonics are figured in analytical solution. The damping rate of displacement in analytical solution is lower than that in experiments.

3.6.2 Velocity

FIGURE 3.29 is time evolution of velocity for assembly 1, 7 and 8. Phase difference between the assemblies and harmonics of the assemblies on the external crown can be observed more clearly with the derived velocities.

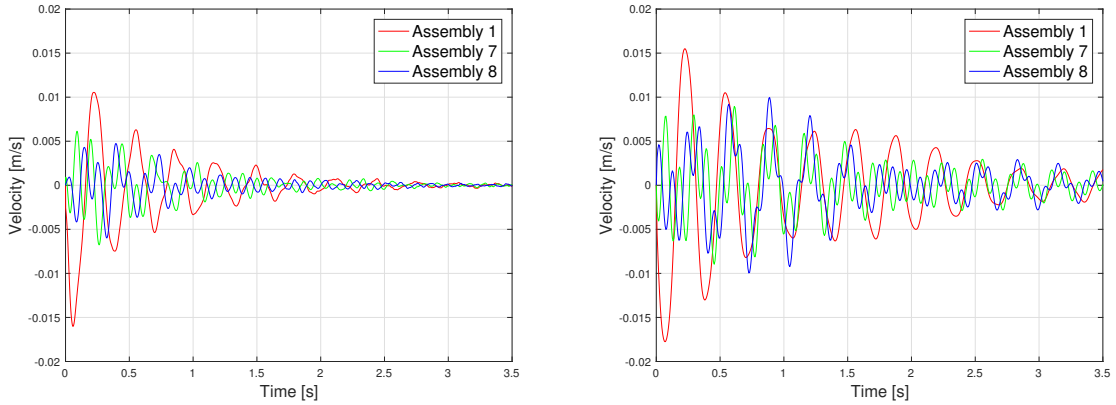

(a) Experiments (b) Analytical

FIGURE 3.29: Time evolution of velocity (Partial flowering: Internal crown)

3.6.3 Energies of assembly

FIGURE 3.30 shows the time evolution of energies in the case of partial flowering when internal crown is the driving crown.

Same as that during total flowering, potential energy of both crowns dominates. Kinetic energy is negligible comparing to potential energy. Inasmuch the excitation in internal crown, the energy of internal crown is the main contribution to total energy. Only a small portion of energy (less than 10%) has been transferred from the internal crown to the external crown. This energy transfer is dissipative. There is higher rate of energy dissipation in the experiments than in analytical solution.

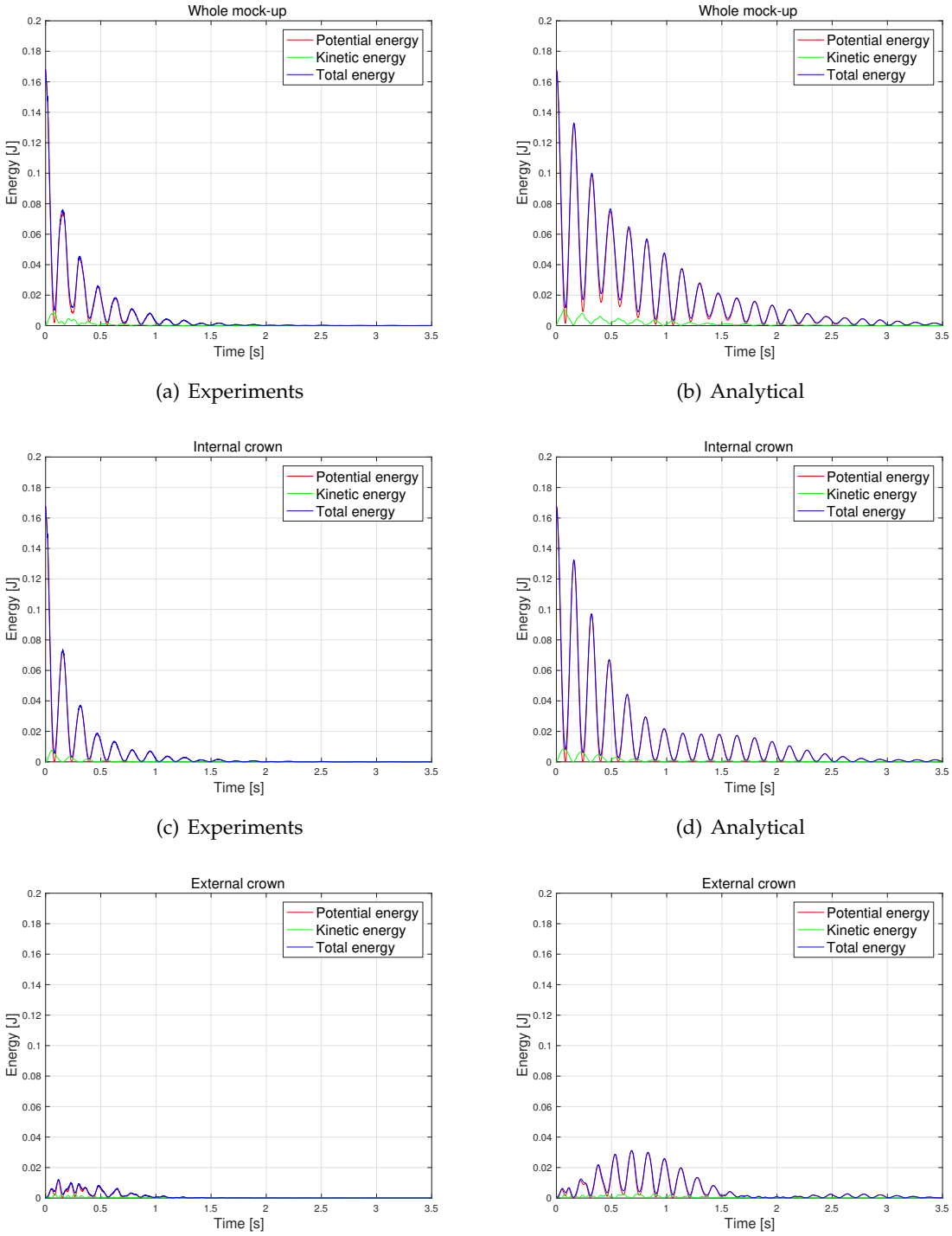

(a) Experiments (b) Analytical

(c) Experiments (d) Analytical

(e) Experiments (f) Analytical

FIGURE 3.30: Time evolution of energies (Partial flowering: Internal crown)

3.6.4 Volume contained in whole mockup

In experiments, $\eta = 0.1659$, different from that in analytical mode where $\eta = 0.1$. FIGURE 3.31 shows the time evolution of relative volume variations.

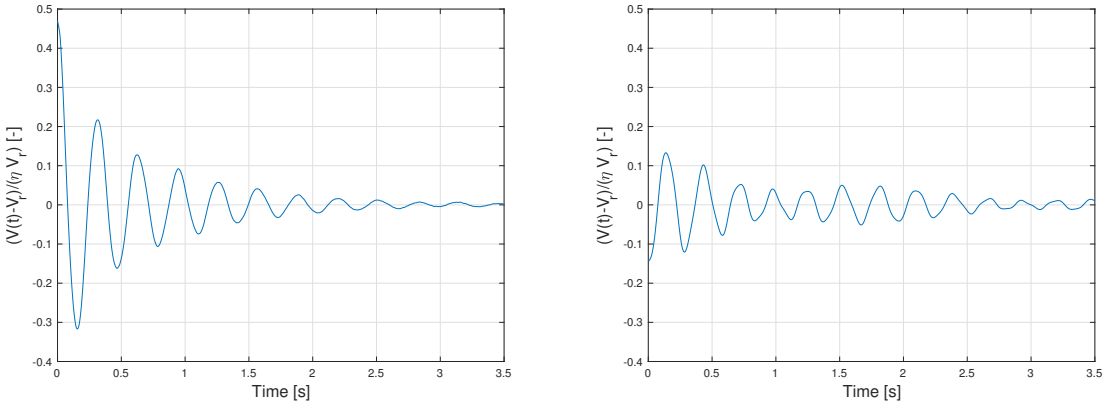

(a) Experiments (b) Analytical

FIGURE 3.31: $\frac{V(t)-V_r}{\eta V_r}$ (Partial flowering: Internal crown)

Different from the case of total flowering, the relative volume evolution is very regular. The volume variation is at very high level around 50% which is far from the assumption of linear model. It is higher than that in experiments of total flowering suggesting lower level of disorder in the case of partial flowering (internal crown) for the reason that disorder will compensate the differences among the assemblies leading to a lower global volume variations.

3.6.5 Average outflow velocity

FIGURE 3.32 displays the average outflow velocity calculated from volume variations in the case of partial flowering when internal crown is in excitation.

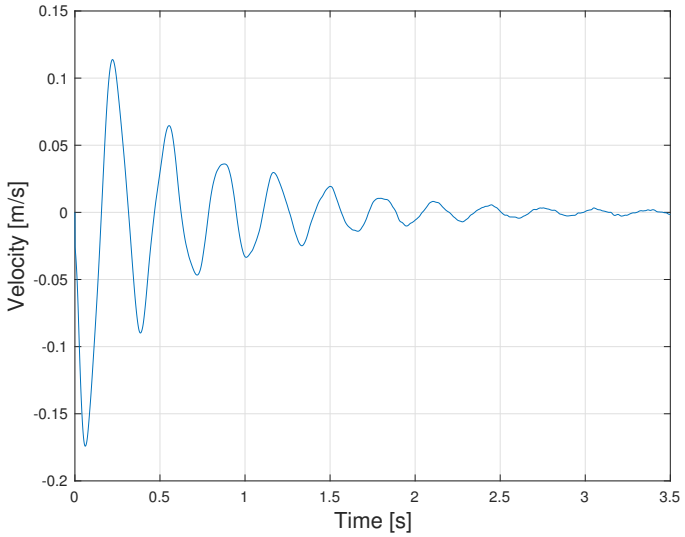

FIGURE 3.32: Average outflow velocity (Partial flowering: Internal crown)

Time evolution of the average outflow velocity is in regular oscillation without pause of respiration, as that during total flowering, due to lack of phase-realignment between two crowns.

3.6.6 Surface confined by centres on external crown

FIGURE 3.33 shows the time evolution of surface area difference $A(t) - A_r$ confined by the centres of assemblies on external crown in the case of partial flowering (Internal crown).

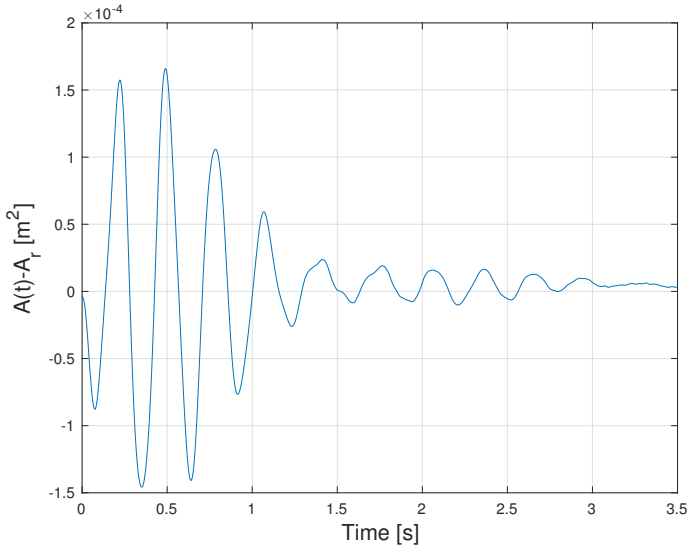

FIGURE 3.33: Surface area difference (Partial flowering: Internal crown)

Since the excitation is only in internal crown, the iregular oscillation of this surface difference starts from 0. The amplitude of surface area difference $A(t) - A_r$ is at a lower order than that in the case of total flowering.

3.6.7 Indicators of symmetry

FIGURE 3.34 shows the displacements for assemblies supposed to be in symmetry. For assemblies on internal crown (assembly 1, 2 & 6, see FIGURE 3.34(a)), there is slight difference in phase. Also, slight difference in harmonics is found among the displacements of assemblies on external crown (see FIGURE 3.34(b,c)). Comparing with the case of total flowering, the disorder has been reduced to a much lower level. This is consistent with the observation of volume variations.

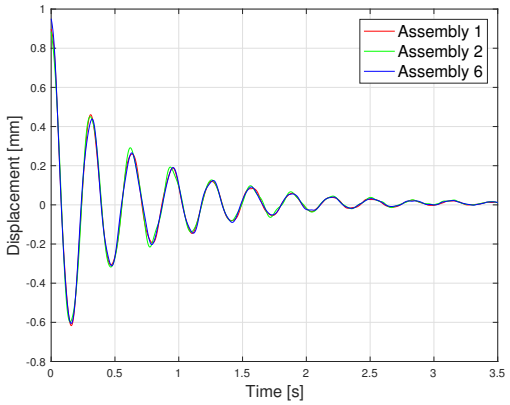

(a) Assembly 1

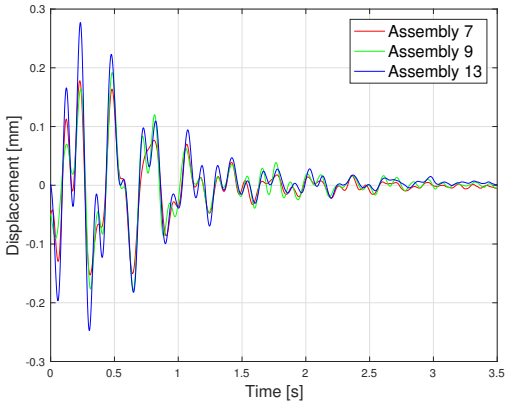

(b) Assembly 7

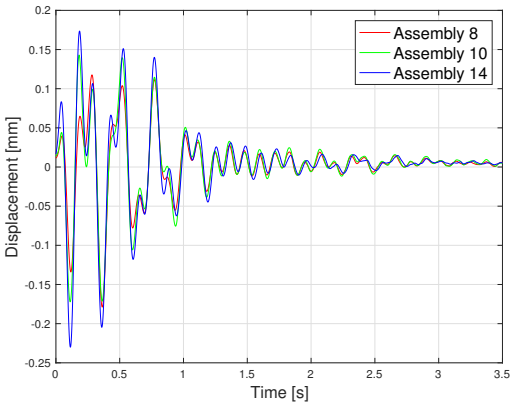

(c) Assembly 8

FIGURE 3.34: Time evolution of displacements in symmetry (Partial flowering: Internal crown)

FIGURE 3.35 is the frequency response of displacements for assemblies supposed in symmetry. Only slight discrepancies are observed in this case suggesting lower level of disorder.

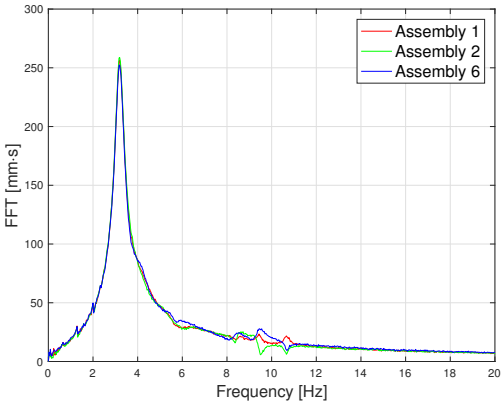

(a) Assembly 1

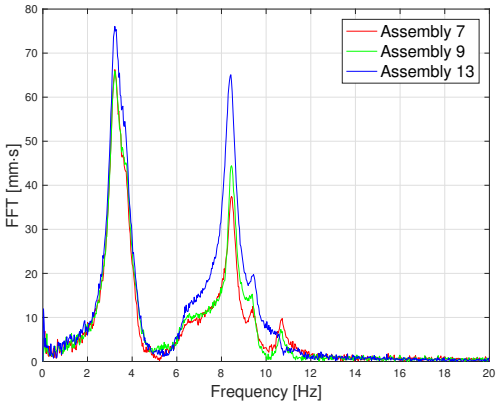

(b) Assembly 7

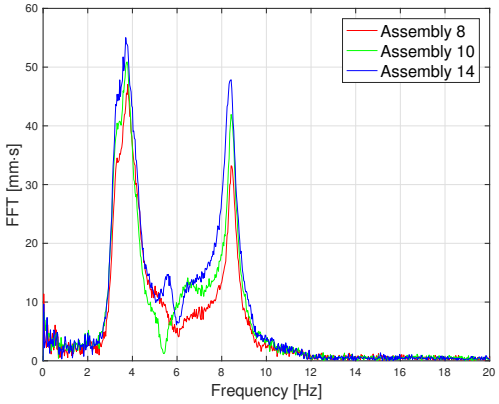

(c) Assembly 8

FIGURE 3.35: Frequency response of displacements in symmetry (Partial flowering: Internal crown)

FIGURE 3.36 shows the volume evolutions of all six sections. There are slight discrepancies among the six sections.

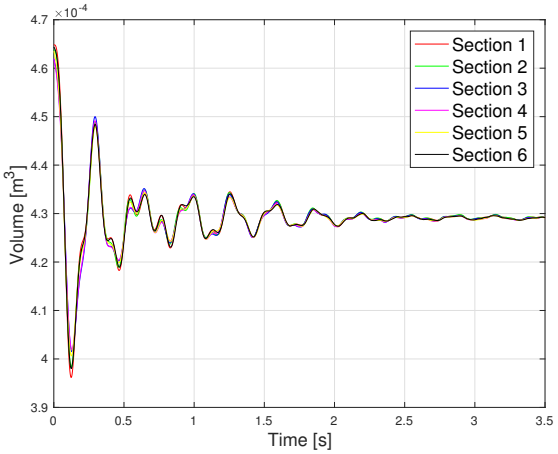

FIGURE 3.36: Volume of sections (Partial flowering: Internal crown)

3.7 Partial flowering : External crown

Experiments with only external crown excited have been conducted.

3.7.1 Displacements

FIGURE 3.37 shows the displacements of assembly 1 (internal crown), 7 & 8 (external crown). The displacements starts external crown then propagate to internal crown.

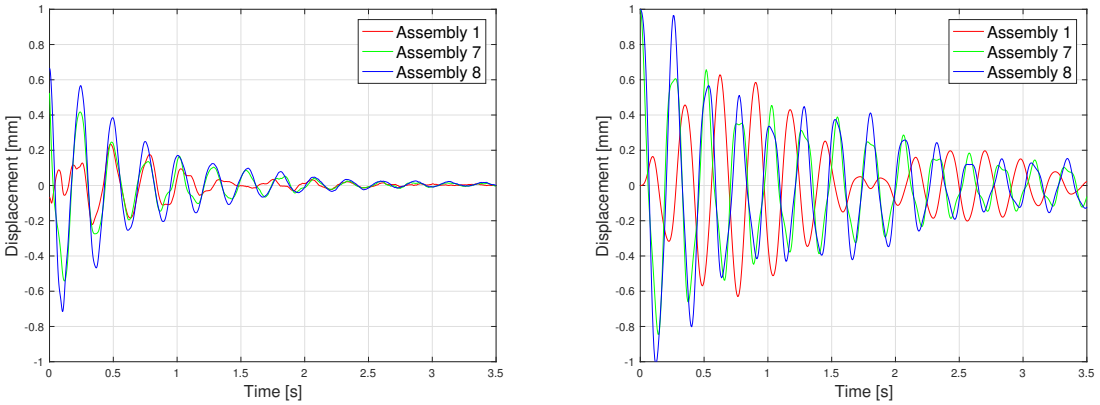

(a) Experiments (b) Analytical

FIGURE 3.37: Time evolution of displacement (Partial flowering: External crown)

Similar to the case of total flowering, realigning in phase of the displacements of the assemblies on two crowns happens after certain periods of oscillations. The assemblies on external crown are in regular oscillations while the assembly on internal crown is in harmonics. The analytical solution shows different behaviours: no realignment exists with assembly 1 is always in opposite phase with the other two. Same with the other two cases, experiments have higher damping than analytical solution.

3.7.2 Velocity

FIGURE 3.38 shows the velocity of assembly 1, 7 and 8. Consistent behaviours can be seen more clearly with the velocities as the derivative of displacements.

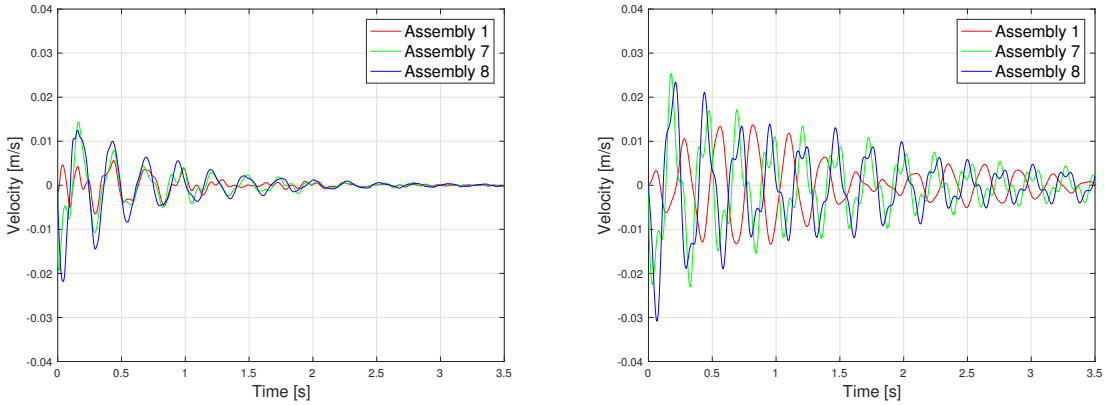

(a) Experiments (b) Analytical

FIGURE 3.38: Time evolution of velocity (Partial flowering: External crown)

3.7.3 Energies of assembly

FIGURE 3.39 displays the time evolutions of energies for whole mock-up and the two crowns in the case of partial flowering when external crown is excited.

Same with the cases of total flowering and partial flowering (internal crown), potential energy dominates over kinetic energy. Since the displacements start from the external crown, the main contribution to total energy of the whole mock-up comes from external crown. A very small portion of energy is transferred to internal crown. This energy transfer is dissipative. Also similar to the other two cases, at certain time instants, almost whole portion of energy of structure has been transferred to fluid. Also, there are higher rate of energy dissipations in experiments than that in analytical solutions.

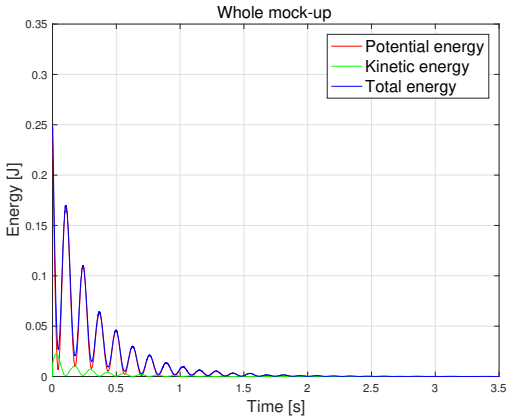

(a) Experiments

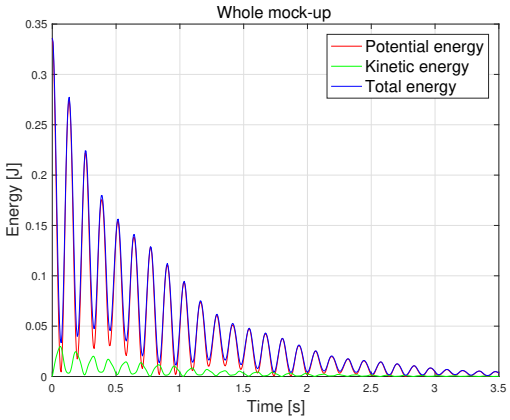

(b) Analytical

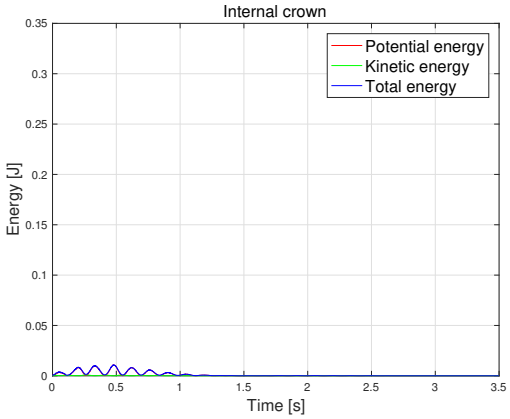

(c) Experiments

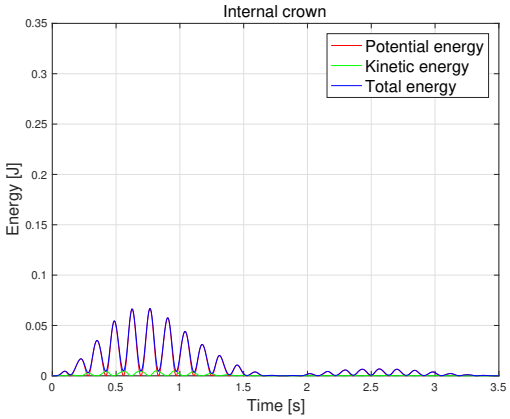

(d) Analytical

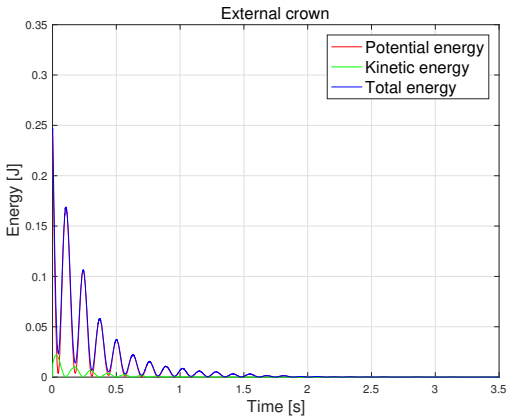

(e) Experiments

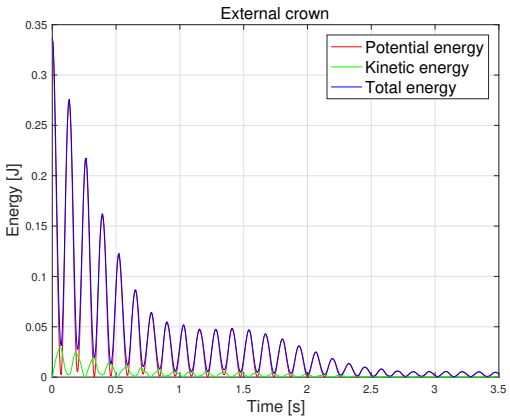

(f) Analytical

FIGURE 3.39: Time evolution of whole mockup's energy (Partial flowering: External crown)

3.7.4 Volume contained in whole mockup

In experiments, $\eta = 0.1694$. FIGURE 3.40 shows the relative volume variations.

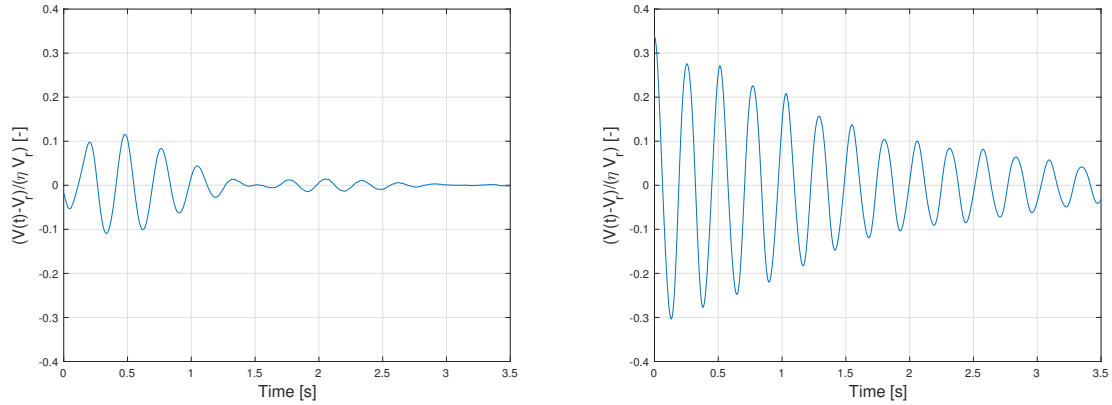

(a) Experiments (b) Analytical

FIGURE 3.40: $\frac{V(t)-V_r}{\eta V_r}$ (Partial flowering: External crown)

The highest level of relative volume variation is at around 0.1, lower than both the cases above. This suggests a higher level of disorder in this scenario of partial flowering when the external crown is in excitation. There is pause of respiration from around 1.4 to 1.6 s possibly resulting from phase realignment of assemblies in two crowns. Very different from the experiments, the volume variation of analytical solution is in regular oscillation with a higher amplitude.

3.7.5 Average outflow velocity

FIGURE 3.41 displays the average outflow velocity calculated from volume variations in the case of partial flowering when external crown is in excitation.

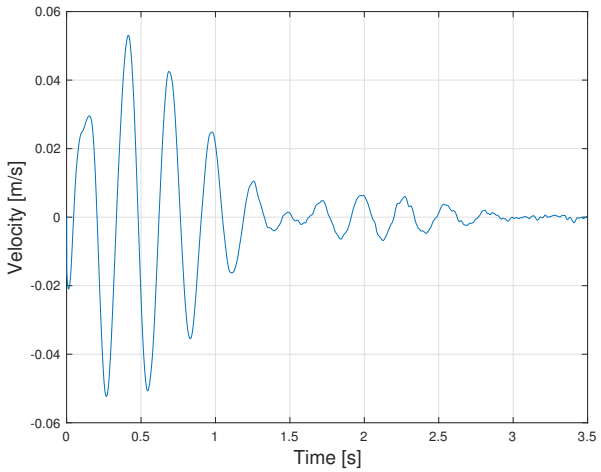

FIGURE 3.41: Average outflow velocity (Partial flowering: External crown)

3.7.6 Surface confined by centres on external crown

FIGURE 3.42 shows the time evolution of surface area difference $A(t) - A_r$ confined by the centres of assemblies on external crown in the case of partial flowering (External crown).

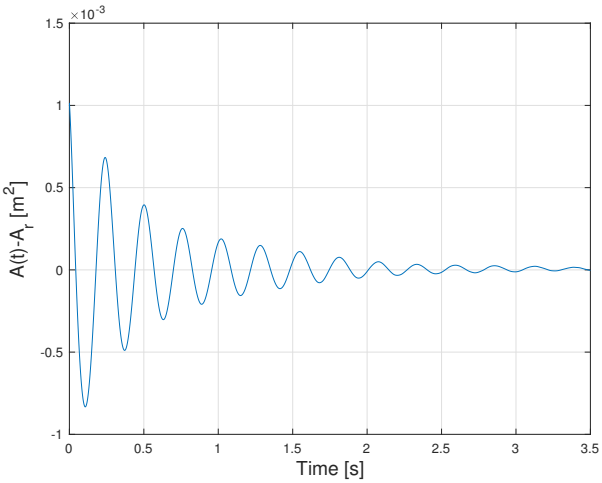

FIGURE 3.42: Surface area difference (Partial flowering: External crown)

The displacements start from the external crown. The time evolutions of surface area difference is in regular oscillation.

3.7.7 Indicators of symmetry

FIGURE 3.43(a) shows the displacements of assemblies on internal crown. Disorders can be observed among the three assemblies, especially during the first period of oscillation. Also there is difference in behaviour of harmonics. This disorder is consistent with the observation in volume variations.

For assemblies on external crown (see FIGURE 3.43(b,c)), there are less discrepancies than that on internal crown, but there are still slight discrepancies of phases among the assemblies in symmetry.

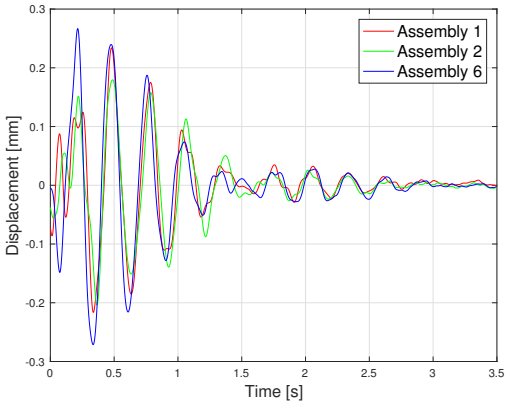

(a) Assembly 1

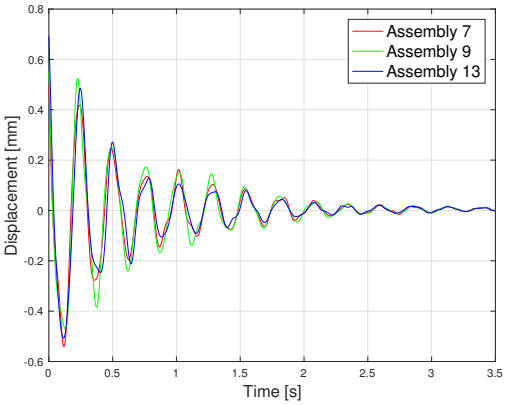

(b) Assembly 7

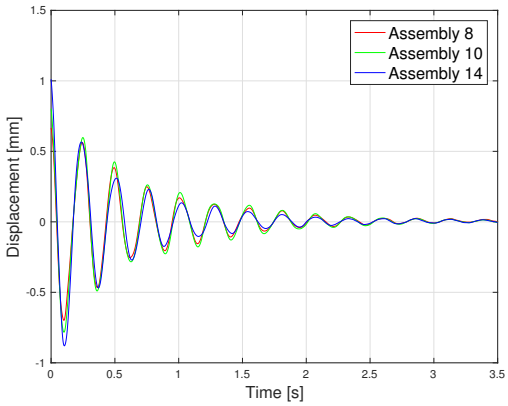

(c) Assembly 8

FIGURE 3.43: Time evolution of displacements in symmetry (Partial flowering: External crown)

FIGURE 3.44 is the frequency response of displacements for assemblies supposed in symmetry. Consistent with the observations in displacements, discrepancies exist for assemblies on internal crown while the assemblies on external crown are in consistency. In FIGRE 3.44, two peaks at frequencies in vicinity can be found for assembly 1 and 6 corresponding to the intense harmonics observed with the displacement curves in FIGURE 3.43(a), while only single value of frequency for assembly 2.

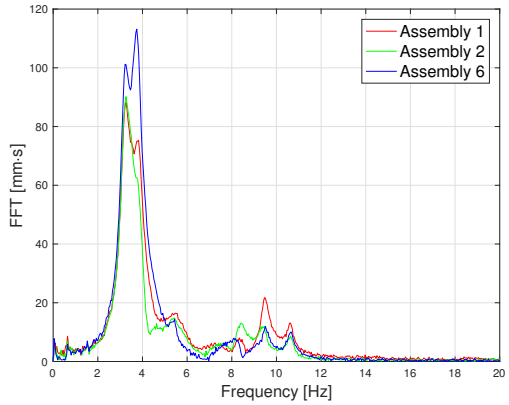

(a) Assembly 1

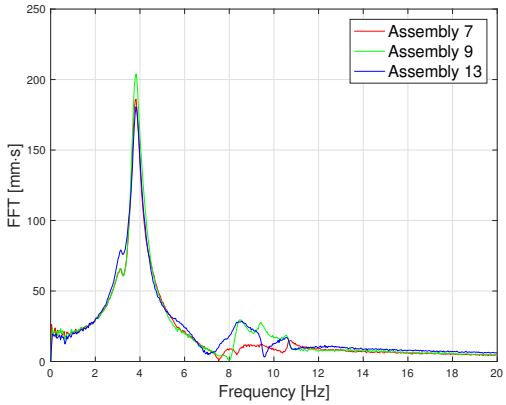

(b) Assembly 7

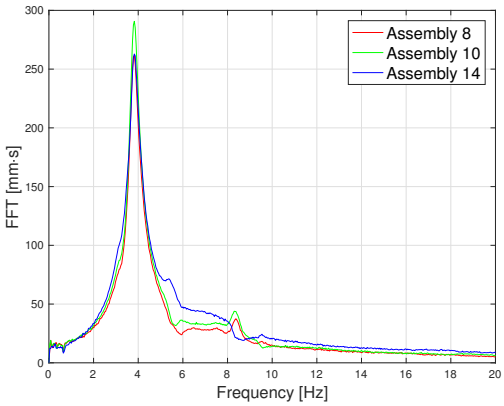

(c) Assembly 8

FIGURE 3.44: Frequency response of displacements in symmetry (Partial flowering: External crown)

FIGURE 3.45 shows the volume evolutions of all six sections. There are slight discrepancies among the six sections.

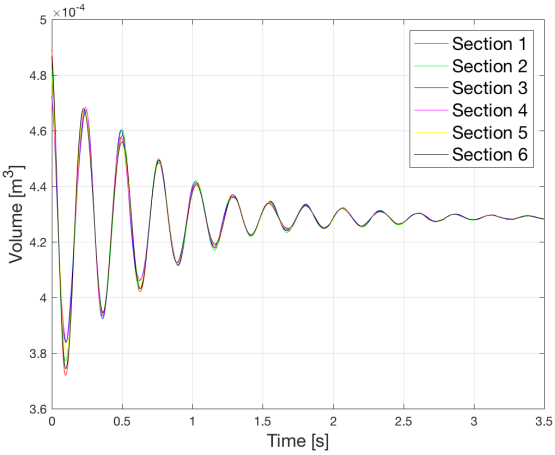

FIGURE 3.45: Volume of sections (Partial flowering: External crown)

3.8 Conclusions

In this chapter, free-vibration experiments on multi-assembly experimental facility PISE-2C in three different scenarios, including total flowering, partial flowering with internal crown excited and partial flowering with external crown excited, have been discussed. A reticulate model with homogenised linear hypothesis has been developed and verified with the experimental results.

During the computation of analytical model, the frequency has been adjusted (St^*) while the amplitudes of both linear quantities (displacement, velocity, pressure and volume) and quadratic quantities (energy) should be checked cautiously for the reason that the scales of the computation (confinement parameter η) are chosen differently from that in the experiments. Since there is only one parameter C_f^* in the friction model of the analytical analysis, it's not possible to adjust the dissipation ratio.

In the observation of displacements for assemblies on internal crown and assemblies on external crown in different scenarios, we can reach following conclusions:

- Realignment of phase for assemblies located on different crowns can be found in the case of total flowering and partial flowering (external crown) but not in partial flowering (internal crown) during the experiments; in the analytical solution, this behaviour can be seen for total flowering, but in the case of partial flowering (external crown), assembly on internal crown is always oscillating in opposite phase with the ones on external crown;
- The analytical model shows much more intense harmonics in the case of total flowering than the experiments;
- In the case of partial flowering (internal crown), strong harmonics exist for the assemblies on external crown (assembly 7&8) which refrain the movement of the assemblies to a low amplitude;
- Except in the scenario of partial flowering (internal crown), the assemblies on respective crowns tends to vibrate together after certain periods while the harmonics of external crown during partial flowering (internal crown) are preventing the propagation;
- The displacement curves suggest that the response of the system depend on the mode of initial excitation, some modes will lead to more complex scenario than others;
- There are always higher damping in the experiments than that in the analytical solutions.

Potential energies, kinetic energies and total mechanical energies of structure have been computed for the whole mock-up and respective crowns:

- The ratios between the energies are consistent for all three scenarios: potential energies are the main contributions to total mechanical energies while the kinetic energies are negligible;
- During all three different cases, there are time instants when almost the whole portion of structural mechanical energies are transferred to the fluid; similar behaviour may happen in Phénix reactor core, increasing the possibility of sudden vaporisation of liquid sodium;

- Dissipation time is always longer in the analytical model than that in the experiments suggesting lacks of dissipation modes in the linear model, second friction parameters, besides C_f^*, should be added to cover non-linearities; this will increase the computational power, but the size of the problem will stay the same.
- In the case when single crown gets excited, the motion of the other crown is dissipative. The magnitude of driven crown's energy is at a lower order than that of driving crown.

Relative volume variations and average outflow velocity calculated from volume variations, which mainly indicates the horizontal outflow velocity, have been applied as a global indicator of disorders in the mock-up during movements, while surface area confined by the assemblies' center on external crown is introduced as an indicator of synchronicity on external crown:

- The maximum amplitude of relative volume variations can be as high as 40% and 50% during total flowering and partial flowering (internal crown) respectively; this is far from the hypothesis of linear model;
- Highest amplitude of relative volume variations is found in the case of partial flowering (internal crown) suggesting least disorders in this scenario;
- Pause of respiration due to realignment of phase have been seen in total flowering and partial flowering (external crown).
- External crown is in better synchronicity when it is excited initially (total flowering and partial flowering (external crown)) according to more regular oscillations of surface area.

Besides, symmetries of the mock-up have been checked with displacements of assemblies supposed to be in symmetry and the volume contained in sections:

- Less differences of displacements and spectra among assemblies supposed to be in symmetry are found in the case of partial flowering (internal crown), which is consistent with the observation of relative volume variations;
- Relative lower level of synchronicity can be seen in external crown during partial flowering (internal crown), consistent with that of surface area confined by the assemblies' center on external crown.
- Concerning the spectra, the fundamental is quite clear. However, the frequencies generated are approximately at the order of the first harmonic but are much less centred.
- The case of partial flowering (internal crown) is the one that generates the most complex spectral content.

All in all, the analysis on PISE-2C experiments suggests that:

- The good symmetry observed in the experiments suggests that the deterministic tool is acceptable in analysis;
- Coupling with base affect the calibration of mechanical parameters for the assemblies on PISE-2C;

- Affect coming from coupling with container during the experiments cannot be assessed quantitively;
- Differences of mechanical parameters among assemblies propagate in the system, therefore, stochastic analysis should help in the analysis of such a dispersion;
- Linear model gives longer dissipation time than the experiments, when applied in safety design, higher standards will be set according to the dissipation time, which is preferred for redundancy reason.

Chapter 4

Conclusions

In the objective to assess the dissipative effects in dynamic behaviours of SFR core during core flowering and seismic events, numerical, experimental and analytical approaches have been paid based on the two test facilities: mono-assembly test facility PISE-1A and multi-assembly test facility PISE-2C.

PISE-1A

To improve the understanding of fluid-structure interaction phenomena with respect of added mass and different physical properties (including densities and viscosities), two series of free-vibration experiments have been performed on PISE-1A. The first is in water with different water heights and the second is in water-glycerol mixture with different mass fractions of glycerol, thus different densities and viscosities. Corresponding numerical interpretations have been conducted with $3D$ NAVIER-STOKES model coupled with $1D$ damped spring-mass equation implemented in CAST3M code.

To characterise the structural parameters, free-vibration experiments in air have been carried out. Several different signal processing techniques and data analysis methodologies have been discussed. After comparison, ERA method was chosen as the reference data analysis methodology.

For the first series of experiments with varying water height, damping coefficient increases with increasing added mass as the water height increases. Comparing the case when water height at the top of the assembly with a thin foil cover and that when at full water height with upper water tank filled, edge effect of the recirculation from the top shows little influence on damping coefficient and vibrating frequency.

For the experiments with different mass fractions of glycerol in the water-glycerol mixture, damping coefficient increases and energy dissipation accelerates with increasing mass fractions due to increasing fluid force.

Moreover, sources of uncertainties have been discussed:

- Uncertainties coming from non-linearities and initial shock results in uncertainties when determining damping and frequency. This will not only affect the numerical simulation inasmuch that it is highly sensitive to structural parameters calculated from free-vibration experiments in air, but also affect the accuracy when characterising damping coefficients and frequencies calibrated from the experiments. Also, coupling of the assembly with the base during movements in air will also affect the characterising of structural parameter (see Appendix C) ;

- As introduced parameters based on ideal damper system to describe the movement of the assembly, frequency and damping coefficient are supposed to be constant all along

the vibrating duration which is not the case in reality (see FIGURE 2.20). Therefore, the assumption of weakly damped oscillator is not met in the experiments, the value of the damping coefficients and frequencies will not be as meaningful as its varying trends, indeed they can be taken as indicators of the dissipative effects in the system;

- Boundary transfer is not considered in the numerical simulation. Since the initial displacement is as big as 1/7 of the channel width, it may have influences on the dynamic behaviour during the movements. Corresponding analytical analysis shall be helpful to understand this phenomena better;

- In numerical simulation, as discussed in Appendix B, coupling of the assembly with the container during experiments in liquids have not been taken into account. This effect will explain the lower damping coefficients of the experiments comparing the numerical simulations. However, lower frequencies resulted from numerical computations are not expected by this simplified model. More elaborated model shall be need for better understanding.

PISE-2C

Free-vibration experiments on multi-assembly experimental facility PISE-2C in three different scenarios, including total flowering, partial flowering with internal crown excited and partial flowering with external crown excited, have been discussed. A reticulate model with homogenised linear hypothesis has been developed and verified with the experimental results.

Displacements of all 18 assemblies measured by strain gauge in the experiments have been processed. Velocities were derived from the displacement signals after removing high-frequency noises. Potential, kinetic and total mechanical energies have been calculated for each assembly, each crown and the whole mock-up. Global parameters including volume contained in the mock-up and average outflow velocity have been introduced to describe the global behaviour of the hole mock-up. The complexity and synchronicity was checked with several indicators of symmetry.

The analysis on PISE-2C experiments and reticulate model draws to following conclusions:

- The good symmetry observed in the experiments suggests that the deterministic tool is acceptable in analysis;

- Coupling with base affect the calibration of mechanical parameters for the assemblies on PISE-2C;

- Influence coming from coupling with container during the experiments cannot be assessed quantitively;

- Linear model gives longer dissipation time than the experiments, which will be preferred in safety design for redundancy reason.

Perspectives

To continue the research on fluid-structure interaction phenomena in dynamic behaviours in SFR core, there are a lot works can be followed in the recent future:

- As observed in the comparison of solutions from reticulate model and experiments, improvement of the reduced linear model, including a more sophisticated friction model in second order to capture the non-linearities, shall be made;
- As already designed and planned, injection experiments on PISE-2C experimental facility will improve our knowledge in fluid-structure interaction under injection scenario;
- $3D$ numerical interpretations for PISE-2C experiments will help to understand the phenomena in a clearer way.

Appendix A

Analytical Analysis Based on Added Mass and Damping

Analytical analysis based on a 2D geometry with an oscillating inner cylinder and a fixed outer cylinder will be introduced. Two hypothesis, strong confinement and small amplitudes are implemented. Both dynamic and energy analysis will be discussed to examine if added mass and added damping are apllicable for both real fluid and perfect fluid with regard to two different motion scenario, including imposed movement and free movement.

A.1 Position of the problem

In this chapter, two hypothesis will be implemented in the discussion:

H1 - Strong confinement (approximation of tangent plane and linearisation),

H2 - Small amplitudes (transfer of boundary condition),

Approximation of perfect fluid and real fluid with two problem scenarios, including imposed movement and free movement will be examined.

A.1.1 Geometry

2D geometry with two cylinders will be discussed in this chapter (FIGURE A.1).

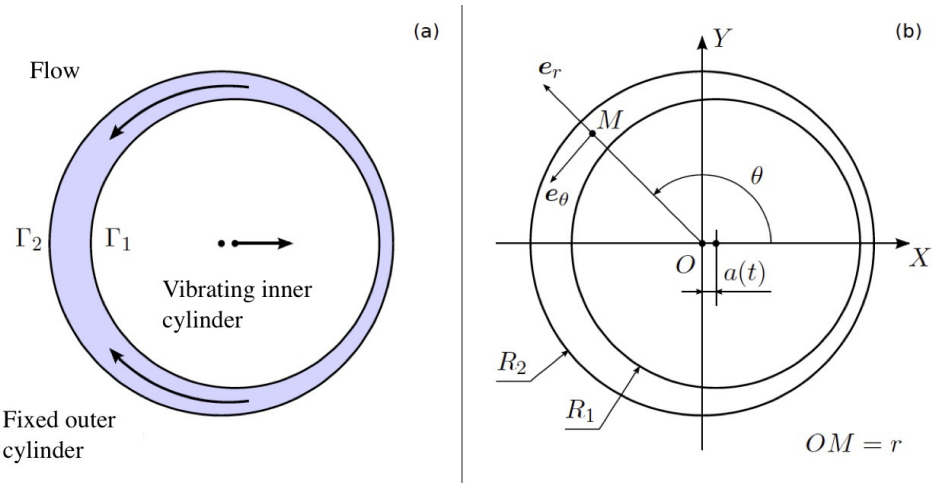

FIGURE A.1: Geometry

The geometry is constituted by two cylinders, Γ_1 as vibrating inner cylinder and Γ_2 as fixed outer cylinder. The radius of the two cylinders are R_1 and R_2 respectively. $R_2 - R_1 = b > 0$. Since the twin-blade support has already limited the motion of the assembly to one dimension, we can suppose that the vibration of the internal cylinder, which is in representation of the assembly, is along the axis X with displacement $a(t) = a_0 \cos(2\pi\, t/\tau)$. Here, $a_0 < b$ is the amplitude, τ is the period and t is the time. The geometry can be characterised by two parameters:

$$\eta = b/R_2 \quad \text{and} \quad \varepsilon = a_0/b. \tag{A.1}$$

In this term, the hypothesis H1 and H2 can be written as $\eta \ll 1$ and $\varepsilon \ll 1$ respectively.

A.1.2 Solid

The solid domain is constituted by a mobile cylindrical body $\mathcal{C}_1$ of radius R_1, with homogeneous mass of M and a surface $\partial\mathcal{C}_1 = \Gamma_1$. There are two kinds of external force acting on $\mathcal{C}_1$:

- restoring force : $-K\,\boldsymbol{a}$,
- friction force : $-D\,\dot{\boldsymbol{a}}$,
- external force : $\boldsymbol{F}_\mathrm{e}$.

A.1.3 Fluid

The channel between the two cylinders is filled with a viscous incompressible fluid of density ρ and dynamic viscosity μ (kinetic viscosity $\nu = \mu/\rho$). For this 2D problem, the gravity will not play any roles and the thermal effect are negligible (isothermal flow).

A.1.4 Equations and boundary conditions

The movement of solid is governed by the equation following in the form of spring-mass system:

$$M\,\ddot{\boldsymbol{a}} + D\,\dot{\boldsymbol{a}} + K\,\boldsymbol{a} = \boldsymbol{F}(t) = \boldsymbol{F}_\mathrm{e} - \int_{\Gamma_1} \boldsymbol{\sigma}\cdot\boldsymbol{n}\,\mathrm{d}s, \tag{A.2}$$

Where $\boldsymbol{\sigma} = -p\,\mathbf{I} + 2\mu\mathbf{D}$ is the stress tensor of the fluid and $\boldsymbol{n}$ is the external normal vector to the fluid domain.

The movement of fluid satisfies the conservation equations:

$$\operatorname{div}\boldsymbol{v} = 0 \quad \text{and} \quad \partial\boldsymbol{v}/\partial t + \boldsymbol{\nabla v}\cdot\boldsymbol{v} = -(1/\rho)\,\boldsymbol{\nabla}p + \nu\Delta\boldsymbol{v}.$$

Regardless of the approximation (perfect fluid or real fluid), non-penetration condition will be true on both cylinders Γ_1 and Γ_2:

$$\Gamma_1 \ : \quad \boldsymbol{v}\cdot\boldsymbol{n} = \dot{\boldsymbol{a}}\cdot\boldsymbol{n} \quad \text{and} \quad \Gamma_2 \ : \quad \boldsymbol{v}\cdot\boldsymbol{n} = 0.$$

This condition is sufficient in the case of perfect fluid, while in the case of real fluid, non-slip condition should be added:

$$\Gamma_1 \ : \quad \boldsymbol{v} - (\boldsymbol{v}\cdot\boldsymbol{n})\boldsymbol{n} = \dot{\boldsymbol{a}} - (\dot{\boldsymbol{a}}\cdot\boldsymbol{n})\boldsymbol{n} \quad \text{and} \quad \Gamma_2 \ : \quad \boldsymbol{v} - (\boldsymbol{v}\cdot\boldsymbol{n})\boldsymbol{n} = 0.$$

A.2 General properties

The system of solid vibrating in fluid with one-dimensional movement can be described as a mass-spring system with fluid force $\boldsymbol{F}(t)$ and external force $\boldsymbol{F}_{\mathrm{e}}(t)$:

$$M\,\ddot{\boldsymbol{a}} + D\,\dot{\boldsymbol{a}} + K\,\boldsymbol{a} = \boldsymbol{F}(t) + \boldsymbol{F}_{\mathrm{e}}(t) \quad \mapsto \quad (M + M')\,\ddot{\boldsymbol{a}} + (D + D')\,\dot{\boldsymbol{a}} + K\,\boldsymbol{a} = \boldsymbol{F}_{\mathrm{e}}(t), \tag{A.3}$$

Here, M' and D' are specific constant added mass and added damping. The main objective of this chapter will be to examine whether the fluid force can be decomposed into two composites in phase with $\ddot{\boldsymbol{a}}$ et $\dot{\boldsymbol{a}}$ repectively:

$$\boldsymbol{F} = -M'\,\ddot{\boldsymbol{a}} - D'\,\dot{\boldsymbol{a}}. \tag{A.4}$$

The concept "Added mass" can also be applied to energy terms.

$$E_{\mathcal{S}} + E_{\mathrm{f}} = \tfrac{1}{2}M\,\dot{\boldsymbol{a}}^2 + \int_{\mathcal{A}} \tfrac{1}{2}\rho \boldsymbol{v}^2\,\mathrm{d}A \quad \mapsto \quad E_{\mathrm{c}} = E_{\mathcal{S}} + E_{\mathrm{f}} = \tfrac{1}{2}(M + M'')\,\dot{\boldsymbol{a}}^2 \tag{A.5}$$

$E_{\mathcal{S}}$ are E_{f} are the kinetic energy of the solid and fluid. M'' is the added mass which is supposed to be constant.

Define the mechanical energy of the system as $E_{\mathrm{m}} = E_{\mathcal{S}} + E_{\mathrm{f}} + \frac{1}{2}K\boldsymbol{a}^2$:

$$\frac{\mathrm{d}E_{\mathrm{m}}}{\mathrm{d}t} = \dot{\boldsymbol{a}} \cdot \boldsymbol{F}_{\mathrm{e}} - (D + D'')\,\dot{\boldsymbol{a}}^2. \tag{A.6}$$

A.2.1 Dynamic approaches

Imposing $M_* = M + M'$ and $D_* = D + D'$ in Eq. A.3(2):

$$M_*\,\ddot{a} + D_*\,\dot{a} + K\,a = F_e. \tag{A.7}$$

A.2.1.1 Imposed movement

Suppose a case with harmonic movement with a period τ:

$$a = a_0\cos(2\pi\,t/\tau), \quad \dot{a} = -2\pi\frac{a_0}{\tau}\sin(2\pi\,t/\tau), \quad \text{and} \quad \ddot{a} = -4\pi^2\frac{a_0}{\tau^2}\cos(2\pi\,t/\tau).$$

The force $F_{\mathrm{e}}(t)$ is unknown. Therefore, Eq. A.7 will be transformed as:

$$\left(1 - 4\pi^2\frac{M_*}{K\tau^2}\right)\cos(2\pi\,t/\tau) - 2\pi\frac{D_*}{K\tau}\sin(2\pi\,t/\tau) = \frac{F_e(t)}{Ka_0}. \tag{A.8}$$

From the first term, we can define a critical value for the period:

$$\tau_{\mathrm{c}} = 2\pi\sqrt{\frac{M_*}{K}} \quad \Longleftrightarrow \quad \frac{M'}{M} = \frac{1}{4\pi^2}\frac{K\tau_{\mathrm{c}}^2}{M} - 1. \tag{A.9}$$

This critical value corresponds to the resonance of the mass-spring system. The frequency $f_c = 1/\tau_c$ is therefore the fundamental frequency of the system. This will allow the evaluation of added mass M'.

A.2.1.2 Free movement

In this case, $F_{\mathrm{e}}(t) = 0$ and the displacement $a(t)$ is unknown. The solution to Eq. A.7 will be:

$$a(t) = a_0 \exp(p\,t)\big[\cos(q\,t) - (p/q)\sin(q\,t)\big] \quad \text{where} \quad p = -\frac{D_*}{2M_*} \quad \text{and} \quad q = \frac{\sqrt{4KM_* - D_*^2}}{2M_*}. \tag{A.10}$$

A.2.1.3 Fluid force

The fluid resisting the movement of the solid will results in a fluid force acting on the solid body:

$$\boldsymbol{F}(t) = -\int_{\Gamma_1} \boldsymbol{\sigma}\cdot\boldsymbol{n}\,\mathrm{d}s. \tag{A.11}$$

With momentum equation and Leibniz rule, the equation can be reformed into:

$$\boldsymbol{F}(t) = -\frac{\mathrm{d}}{\mathrm{d}t}\int_{\mathcal{A}} \rho\boldsymbol{v}\,\mathrm{d}V + \int_{\Gamma_2} \boldsymbol{\sigma}\cdot\boldsymbol{n}\,\mathrm{d}A.$$

A.2.2 Energy approach

The varying rate of kinetic energy of both solid and fluid are:

▷ *solid domain* $\mathcal{C}_1$: $\quad \dfrac{\mathrm{d}E_{\mathcal{S}}}{\mathrm{d}t} = M\,\dot{\boldsymbol{a}}\cdot\ddot{\boldsymbol{a}}$

▷ *fluid domain* $\mathcal{A}$: $\quad \dfrac{\mathrm{d}E_{\mathrm{f}}}{\mathrm{d}t} = -\displaystyle\int_{\partial\mathcal{A}} \big[\tfrac{1}{2}\rho\boldsymbol{v}^2(\boldsymbol{v}-\boldsymbol{w}) - \boldsymbol{v}\cdot\boldsymbol{\sigma}\big]\cdot\boldsymbol{n}\,\mathrm{d}s - \int_{\mathcal{A}} \boldsymbol{\sigma} : \mathbf{D}\,\mathrm{d}A,$

Here, on Γ_1, $\boldsymbol{w} = \dot{\boldsymbol{a}}$, while on Γ_2, $\boldsymbol{w} = 0$. After taking into account the non-penetration condition and adherent condition, it will become:

$$\frac{\mathrm{d}E_{\mathrm{f}}}{\mathrm{d}t} = \int_{\Gamma_1} \boldsymbol{\sigma} : \boldsymbol{n}\dot{\boldsymbol{a}}\,\mathrm{d}s - 2\mu\int_{\mathcal{A}} \mathbf{D} : \mathbf{D}\,\mathrm{d}A.$$

Therefore, the varying rate of the sum of both solid's and fluid's kinetic energy will be:

$$\begin{aligned}\frac{\mathrm{d}}{\mathrm{d}t}\big(E_{\mathcal{S}} + E_{\mathrm{f}}\big) &= \dot{\boldsymbol{a}}\cdot\big(\boldsymbol{F} + \boldsymbol{F}_{\mathrm{e}} - D\dot{\boldsymbol{a}} - K\boldsymbol{a}\big) + \int_{\Gamma_1} \boldsymbol{\sigma} : \boldsymbol{n}\dot{\boldsymbol{a}}\,\mathrm{d}s - 2\mu\int_{\mathcal{A}} \mathbf{D} : \mathbf{D}\,\mathrm{d}A,\\ &= \dot{\boldsymbol{a}}\cdot\boldsymbol{F}_{\mathrm{e}} - D\,\dot{\boldsymbol{a}}^2 - \tfrac{1}{2}K\frac{\mathrm{d}\boldsymbol{a}^2}{\mathrm{d}t} - 2\mu\int_{\mathcal{A}} \mathbf{D} : \mathbf{D}\,\mathrm{d}A.\end{aligned} \tag{A.12}$$

Therefore, for the mechanical energy of the system:

$$\frac{\mathrm{d}E_{\mathrm{m}}}{\mathrm{d}t} = \dot{\boldsymbol{a}}\cdot\boldsymbol{F}_{\mathrm{e}} - D\dot{\boldsymbol{a}}^2 - 2\mu\int_{\mathcal{A}} \mathbf{D} : \mathbf{D}\,\mathrm{d}A. \tag{A.13}$$

With Eq. A.5, it will then be transformed into:

$$\tfrac{1}{2}\frac{\mathrm{d}}{\mathrm{d}t}\big[(M+M'')\dot{\boldsymbol{a}}^2 + K\,\boldsymbol{a}^2\big] = \dot{\boldsymbol{a}}\cdot\boldsymbol{F}_{\mathrm{e}} - (D+D')\,\dot{\boldsymbol{a}}^2 \quad \text{where} \quad D''\dot{\boldsymbol{a}}^2 = 2\mu\int_{\mathcal{A}} \mathbf{D} : \mathbf{D}\,\mathrm{d}A, \tag{A.14}$$

If the structural damping and the external force are known, the energy approach will have M'' and D'' independent of each other.

A.2.2.1 Imposed movement

With imposed displacement $a(t) = a_0 \cos(2\pi t/\tau)$, the mechanical energy balance can be written as:

$$\left(1 - 4\pi^2 \frac{M + M''}{K\tau^2}\right) \cos\left(2\pi \frac{t}{\tau}\right) - 2\pi \frac{D + D''}{K\tau} \sin\left(2\pi \frac{t}{\tau}\right) = \frac{F_e(t)}{K a_0}, \tag{A.15}$$

Comparing with Eq. A.8. $M' = M''$ and $D' = D''$.

A.2.2.2 Free movement

The study of free movement from Eq. A.14 will give solution provided in previous section A.2.1.2.

A.3 Linearisation

The following approach will elaborate four analytical solutions in the limit of the two hypothesis H1 and H2:

- ▷ *Perfect-fluid approximation* :
  - imposed movement ;
  - free movement ;
- ▷ *Real fluid* :
  - imposed movement ;
  - free movement ;

A.3.1 Fluid flow

The problem is stated in the limit of hypothesis H1 and H2. The equations of movement will be reduced to mass conservation equation and linearised Navier-Stokes equations. Non-penetration condition will take the same form regardless of other approximations. In the case of real fluid, the adherent condition should be added to constitute the complete boundary conditions.

A.3.1.1 Scaling

The variables can be scaled as:

$$\begin{aligned} &x = R_2\,\bar{x}, \quad y = b\,\bar{y}, \quad t = \tau\,\bar{t} \\ &u(x,y,t) = U\,\bar{u}(\bar{x},\bar{y},\bar{t}), \quad v(x,y,t) = V\,\bar{v}(\bar{x},\bar{y},\bar{t}), \quad p(x,y,t) = p_0 + (\delta p)\,\tilde{p}(\bar{x},\bar{y},\bar{t}) \\ &a = a_0\,\bar{a}(\bar{t}), \end{aligned}$$

Here, depending on the fluid, the unknown scalings are:

- ▷ *imposed movement* : U, V et (δp).

▷ *free movement* : U, V, (δp) et τ.

Non-Dimensional parameters following will be introduced to describe the fluid flow:

$$\begin{aligned}
\eta = b/R_2 \ll 1 &\quad : \text{parameter of confinement,}\\
\varepsilon = a_0/b \ll 1 &\quad : \text{parameter of amplitudes,}\\
\mathsf{Re} = Ub/\nu &\quad : \text{REYNOLDS number,}\\
\mathsf{St} = R_2/(U\tau) &\quad : \text{STROUHAL number,}\\
\mathsf{Eu} = (\delta p)/(\rho U^2) &\quad : \text{EULER number.}
\end{aligned}$$

A.3.1.2 Equations

The equation of fluid will be:

$$\frac{\partial \bar{u}}{\partial \bar{x}} + \frac{\partial \bar{v}}{\partial \bar{y}} = 0.$$

$$\mathsf{St}\,\frac{\partial \bar{u}}{\partial \bar{t}} + \bar{u}\,\frac{\partial \bar{u}}{\partial \bar{x}} + \bar{v}\,\frac{\partial \bar{u}}{\partial \bar{y}} = -\frac{(\delta p)}{\rho U^2}\,\frac{\partial \tilde{p}}{\partial \bar{x}} + \frac{1}{\eta\,\mathsf{Re}}\,\frac{\partial^2 \bar{u}}{\partial \bar{y}^2},$$

$$V = \eta U.$$

Here,

$$\frac{(\delta p)}{\rho U^2} = \sup\Big\{\mathsf{St},\, 1,\, \frac{1}{\eta\,\mathsf{Re}}\Big\} \quad \text{and} \quad 0 = -\frac{\partial \tilde{p}}{\partial \bar{y}}. \tag{A.16}$$

A.3.1.3 Boundary conditions

A.3.1.3.1 Transfer of boundary conditions

In first approximation, the equation of the moving cylinder $\Gamma_1(t)$ is independent of time: $\bar{y} = 1$. We can refer to this boundary condition as $\Gamma_{1|a=0}$. This transfer, also known as flattening of boundary conditions, is due to the fact that Γ_1 is displacing in very small displacement where the flow grows: $\varepsilon \ll 1 \;\Leftrightarrow\; a_0 \ll b$.

A.3.1.3.2 Non-penetration condition

This condition has the same form in two fluid types and in first approximation:

$$\bullet \text{ on } \Gamma_1 \;:\quad \bar{v} = -\varepsilon\,\mathsf{St}\,\dot{\bar{a}}\cos\bar{x}, \qquad \bullet \text{ on } \Gamma_2 \;:\quad \bar{v} = 0.$$

We can decide the scales;

$$\epsilon\mathsf{St} = 1.$$

A.3.1.3.3 Non-slip condition

The non-dimensional condition of adhesion will be:

$$\bullet \text{ on } \Gamma_1 \text{ and } \Gamma_2 \;:\quad \bar{u} = 0.$$

A.3.2 Interaction force

With the definition of fluid force from Eq. A.11 where $\boldsymbol{\sigma} = -p\,\mathbf{I} + 2\mu\mathbf{D}$. In first approximation, we can establish two results as below:

$$\mathbf{D} \simeq \frac{U}{b}\begin{pmatrix} \eta\dfrac{\partial \bar{v}}{\partial \bar{y}} & \frac{1}{2}\dfrac{\partial \bar{u}}{\partial \bar{y}} \\ \frac{1}{2}\dfrac{\partial \bar{u}}{\partial \bar{y}} & \eta\dfrac{\partial \bar{u}}{\partial \bar{x}} \end{pmatrix} \quad \text{and} \quad \boldsymbol{n} \simeq \begin{pmatrix} -\varepsilon\eta\,\bar{a}\sin\bar{x} \\ 1 \end{pmatrix}.$$

As the integral of constant pressure on a closed boundary is zero, p_0 will be eliminated and we will get:

$$\boldsymbol{\sigma}\cdot\boldsymbol{n} \simeq \rho U^2 \begin{pmatrix} \dfrac{1}{\mathsf{Re}}\dfrac{\partial \bar{u}}{\partial \bar{y}} \\ -\dfrac{(\delta p)}{\rho U^2}\,\tilde{p}. \end{pmatrix}.$$

When projected to $\boldsymbol{e}_X$, the effective contribution of fluid force on the direction in which the inner cylinder moves is:

$$\boldsymbol{F}\cdot\boldsymbol{e}_X = F(t) = -R_2(\delta p)\int_0^{2\pi} \tilde{p}(\bar{x},1,\bar{t})\cos\bar{x}\,\mathrm{d}\bar{x}.$$

A.3.3 Kinetic energy

The kinetic energy of the fluid domain can be expressed as:

$$E_\mathrm{f} \simeq \tfrac{1}{2}\rho b R_2 U^2 \int_0^{2\pi}\mathrm{d}\bar{x}\int_0^1 \bar{u}^2\,\mathrm{d}\bar{y} = \tfrac{1}{2}\varepsilon^2\eta\,\frac{\rho R_2^4}{\tau^2}\int_0^{2\pi}\mathrm{d}\bar{x}\int_0^1 \bar{u}^2\,\mathrm{d}\bar{y}. \tag{A.17}$$

A.3.4 Viscous dissipation

By definition : $\phi = 2\mu\mathbf{D} : \mathbf{D}$, established in first approximation:

$$\phi \simeq \mu\frac{U^2}{b^2}\Big(\frac{\partial \bar{u}}{\partial \bar{y}}\Big)^2 \quad\Longrightarrow\quad \Phi = \frac{\mu U^2}{\eta}\int_0^{2\pi}\mathrm{d}\bar{x}\int_0^1\Big(\frac{\partial \bar{u}}{\partial \bar{y}}\Big)^2\mathrm{d}\bar{y}.$$

A.4 Resolution

A.4.1 Perfect fluid

For perfect fluid, $(\delta p) = \mathsf{St}\rho U^2$, we will search for general solution of the following problem:
▷ *Equations* :

$$\frac{\partial \bar{u}}{\partial \bar{x}} + \frac{\partial \bar{v}}{\partial \bar{y}} = 0, \quad \frac{\partial \bar{u}}{\partial \bar{t}} = -\frac{\partial \tilde{p}}{\partial \bar{x}} \quad \text{et} \quad 0 = -\frac{\partial \tilde{p}}{\partial \bar{y}}. \tag{A.18}$$

▷ *Boundary conditions* :

$$\bullet\ \text{on } \Gamma_1 \ :\quad \bar{v} = -\dot{\bar{a}}(\bar{t})\,\cos\bar{x}, \qquad \bullet\ \text{on } \Gamma_2 \ :\quad \bar{v} = 0. \tag{A.19}$$

The solution of this problem can be obtained without definition of $a(t)$:

$$\bar{u} = \dot{\bar{a}}\,\sin\bar{x}, \quad \bar{v} = -\dot{\bar{a}}\,\bar{y}\,\sin\bar{x} \quad \text{and} \quad \tilde{p} = \ddot{\bar{a}}\,\cos\bar{x}. \tag{A.20}$$

The kinetic energy of the fluid domain will be:

$$E_{\mathrm{f}} = \frac{\pi}{2}\,\varepsilon^2\eta\,\frac{\rho R_2^4}{\tau^2}\,\dot{\bar{a}}^2. \tag{A.21}$$

Apply the PFD on $\mathcal{C}_1$ to give the following form:

$$M\frac{a_0}{\tau^2}\,\ddot{\bar{a}} + D\frac{a_0}{\tau}\,\dot{\bar{a}} + Ka_0\,\bar{a} = -(\delta p)R_2\,\pi\ddot{\bar{a}}.$$

Normalise the equation with the restoring force and define:

$$\tau_M = \sqrt{\frac{M}{K}}, \quad \tau_D = \frac{D}{K} \quad \text{and} \quad \tau_F = \sqrt{\frac{\rho R_2^2}{\eta K}},$$

Then the equation will be written as:

$$\left(\frac{\tau_M^2}{\tau^2} + \pi\frac{\tau_F^2}{\tau^2}\right)\ddot{\bar{a}} + \frac{\tau_D}{\tau}\,\dot{\bar{a}} + \bar{a} = 0. \tag{A.22}$$

We can define the time scale τ:

$$\tau \sim \sqrt{\tau_M^2 + \pi\tau_F^2}.$$

The energetic approach will give:

$$E_{\mathrm{f}} = \int_{\mathcal{A}} \tfrac{1}{2}\rho\boldsymbol{v}^2\,\mathrm{d}A = \tfrac{1}{2}M''\dot{\boldsymbol{a}}^2 \quad \Longleftrightarrow \quad \tfrac{1}{2}\rho U^2 R_2 b\int_0^{2\pi}\mathrm{d}\bar{x}\int_0^1 \dot{\bar{a}}^2\,\sin^2\bar{x}\,\mathrm{d}\bar{y} = \tfrac{1}{2}M''\frac{a_0^2}{\tau^2}\,\dot{\bar{a}}^2.$$

After all calculation, we will find: $M' = M''$.

A.4.2 Real fluid

For the case of real fluid, we will be searching for general solution of the following problem:
▷ *Equations* :

$$\begin{cases} \dfrac{\partial\bar{u}}{\partial\bar{x}} + \dfrac{\partial\bar{v}}{\partial\bar{y}} = 0, \quad \dfrac{\partial\bar{u}}{\partial\bar{t}} = -\dfrac{\partial\tilde{p}}{\partial\bar{x}} + \dfrac{1}{\sigma}\dfrac{\partial^2\bar{u}}{\partial\bar{y}^2} \quad \text{and} \quad 0 = -\dfrac{\partial\tilde{p}}{\partial\bar{y}} \quad \text{where} \quad \sigma = \dfrac{b^2}{\nu\tau} \sim 1. & \text{(A.23a)} \\ \dfrac{\tau_M^2}{\tau^2}\,\ddot{\bar{a}} + \dfrac{\tau_D}{\tau}\,\dot{\bar{a}} + \bar{a} = \overline{F}_{\mathrm{e}} - \dfrac{\tau_F^2}{\tau^2}\displaystyle\int_0^{2\pi}\tilde{p}(\bar{x},\bar{t})\cos\bar{x}\,\mathrm{d}\bar{x} \quad \text{where} \quad F_{\mathrm{e}} = Ka_0\,\overline{F}_{\mathrm{e}}. & \text{(A.23b)} \end{cases}$$

▷ *Boundary conditions* :

$$\begin{aligned} &\bullet \text{ on } \Gamma_1 \ : \quad \bar{u} = 0, \quad \bar{v} = -\dot{\bar{a}}\cos\bar{x} \\ &\bullet \text{ on } \Gamma_2 \ : \quad \bar{u} = \bar{v} = 0. \end{aligned} \tag{A.24}$$

A.4.2.1 Imposed movement

In the case of an imposed movement $\bar{a} = \exp(2\mathrm{i}\pi\,\bar{t})$, the problem is linear. We will be looking for a periodic solution:

$$\bar{u} = \bar{\boldsymbol{U}}(\bar{x},\bar{y})\,\mathrm{e}^{\,2\mathrm{i}\pi\,\bar{t}}, \quad \bar{v} = \overline{V}(\bar{x},\bar{y})\,\mathrm{e}^{\,2\mathrm{i}\pi\,\bar{t}}, \quad \tilde{p} = \widetilde{\boldsymbol{P}}(\bar{x})\,\mathrm{e}^{\,2\mathrm{i}\pi\,\bar{t}} \quad \text{and} \quad \overline{F}_{\mathrm{e}} = \widetilde{F}_{\mathrm{e}}\,\mathrm{e}^{\,2\mathrm{i}\pi\,\bar{t}}\,.$$

The equation will be written as:

$$\frac{\partial \bar{\boldsymbol{U}}}{\partial \bar{x}} + \frac{\partial \overline{V}}{\partial \bar{y}} = 0, \quad 2\mathrm{i}\pi\ \bar{\boldsymbol{U}} = -\widetilde{\boldsymbol{P}}' + \frac{1}{\sigma}\frac{\partial^2 \bar{\boldsymbol{U}}}{\partial \bar{y}^2} \quad \text{where} \quad \widetilde{\boldsymbol{P}}' = \frac{\mathrm{d}\widetilde{\boldsymbol{P}}}{\mathrm{d}\bar{x}},$$

Boundary condition will be:

$$\begin{aligned} &\bullet \text{ on } \Gamma_1 \ : \quad \bar{\boldsymbol{U}} = 0, \quad \overline{V} = -2\mathrm{i}\pi\ \cos\bar{x} \\ &\bullet \text{ on } \Gamma_2 \ : \quad \bar{\boldsymbol{U}} = \overline{V} = 0. \end{aligned}$$

Impose $\overline{W}(\bar{x},\bar{y}) = \bar{\boldsymbol{U}}(\bar{x},\bar{y}) - (\mathrm{i}/2\pi)\,\widetilde{\boldsymbol{P}}'(\bar{x})$, the equation will now be written as:

$$\frac{\partial^2 \overline{W}}{\partial \bar{y}^2} - 2\mathrm{i}\pi\sigma\ \overline{W} = 0 \quad \Longrightarrow \quad \overline{W} = A(\bar{x})\ \mathrm{e}^{\alpha\bar{y}} + B(\bar{x})\ \mathrm{e}^{-\alpha\bar{y}} \quad \text{where} \quad \alpha = (1+\mathrm{i})\sqrt{\pi\sigma}.$$

Therefore,

$$\bar{\boldsymbol{U}} = A(\bar{x})\ \mathrm{e}^{\alpha\bar{y}} + B(\bar{x})\ \mathrm{e}^{-\alpha\bar{y}} + (\mathrm{i}/2\pi)\,\widetilde{\boldsymbol{P}}'. \tag{A.25}$$

The boundary conditions will be transformed as:

$$\begin{cases} \bullet \text{ on } \Gamma_1 \ : \quad A\ \mathrm{e}^{\alpha} + B\ \mathrm{e}^{-\alpha} + \dfrac{\mathrm{i}\widetilde{\boldsymbol{P}}'}{2\pi} = 0, \\ \bullet \text{ on } \Gamma_2 \ : \quad A + B + \dfrac{\mathrm{i}\widetilde{\boldsymbol{P}}'}{2\pi} = 0. \end{cases} \quad \Longrightarrow \quad \begin{cases} A = -\dfrac{1-\mathrm{e}^{-\alpha}}{\mathrm{e}^{\alpha}-\mathrm{e}^{-\alpha}}\,\dfrac{\mathrm{i}\widetilde{\boldsymbol{P}}'}{2\pi}, \\ B = -\dfrac{\mathrm{e}^{\alpha}-1}{\mathrm{e}^{\alpha}-\mathrm{e}^{-\alpha}}\,\dfrac{\mathrm{i}\widetilde{\boldsymbol{P}}'}{2\pi}. \end{cases}$$

We can deduct $\overline{V}$ from mass conservation:

$$\begin{aligned} \overline{V}(\bar{x},\bar{y}) &= \overline{V}(\bar{x},0) - \frac{\partial}{\partial \bar{x}}\int_0^{\bar{y}} \bar{\boldsymbol{U}}(\bar{x},\bar{y}')\,\mathrm{d}\bar{y}' \\ &= \overline{V}(\bar{x},0) - \frac{1}{\alpha}\big[A'\big(\mathrm{e}^{\alpha\bar{y}}-1\big) + B'\big(1-\mathrm{e}^{-\alpha\bar{y}}\big)\big] - \frac{\mathrm{i}\,\widetilde{\boldsymbol{P}}''}{2\pi}\bar{y}, \end{aligned}$$

Then the boundary conditions will be:

$$\begin{cases} \bullet \text{ on } \Gamma_1 \ : \quad \overline{V}(\bar{x},0) - \dfrac{1}{\alpha}\big[A'\big(\mathrm{e}^{\alpha}-1\big) + B'\big(1-\mathrm{e}^{-\alpha}\big)\big] - \dfrac{\mathrm{i}\,\widetilde{\boldsymbol{P}}''}{2\pi} = -2\mathrm{i}\pi\ \cos\bar{x}, \\ \bullet \text{ on } \Gamma_2 \ : \quad \overline{V}(\bar{x},0) = 0. \end{cases}$$

After calculation, we will get:

$$\widetilde{\boldsymbol{P}} = \frac{4\pi^2\alpha\ \cos\bar{x}}{2\,\mathrm{th}(\alpha/2)-\alpha}, \quad A = \frac{\mathrm{e}^{\alpha}-1}{\mathrm{e}^{2\alpha}-1}\frac{4\mathrm{i}\pi^2\,\alpha\ \cos\bar{x}}{\alpha-2\,\mathrm{th}(\alpha/2)} \quad \text{and} \quad B = \frac{1-\mathrm{e}^{-\alpha}}{1-\mathrm{e}^{-2\alpha}}\frac{4\mathrm{i}\pi^2\,\alpha\ \cos\bar{x}}{\alpha-2\,\mathrm{th}(\alpha/2)},$$

which will determine the solution.

Impose $\xi = \sqrt{\pi\sigma}$ and $\theta = \mathrm{th}\,\xi$, we will obtain the pressure as:

$$\tilde{p}(\bar{x},\bar{y},\bar{t}) = 4\pi^2\Re\big[\mathrm{e}^{\varphi}\,\mathrm{e}^{\mathrm{i}\,(2\pi\bar{t}+\psi)}\big]\ \cos\bar{x} = 4\pi^2\,\mathrm{e}^{\varphi(\sigma)}\cos\big[2\pi\,\bar{t}+\psi(\sigma)\big]\ \cos\bar{x}. \tag{A.26}$$

Therefore the fluid force acting on Γ_1 will be:

$$\begin{aligned} F = \boldsymbol{F}\cdot\boldsymbol{e}_X &= -4\pi^3 R_2(\delta p)\,\mathrm{e}^{\varphi(\sigma)}\cos\big[2\pi\,\bar{t}+\psi(\sigma)\big] \\ &= -4\pi^3 R_2(\delta p)\,\mathrm{e}^{\varphi(\sigma)}\big[\cos\psi(\sigma)\cos(2\pi\,\bar{t}) - \sin\psi(\sigma)\sin(2\pi\,\bar{t})\big]. \end{aligned} \tag{A.27}$$

In first approximation, effective kinetic energy coming from the azimuthal component of the velocity will be:

$$\begin{aligned} E_\mathrm{f} &= \tfrac{1}{2}\varepsilon^2\eta\,\frac{\rho R_2^4}{\tau^2}\int_0^{2\pi}\mathrm{d}\bar{x}\int_0^1 \bar{u}^2\,\mathrm{d}\bar{y} \\ &= \frac{\pi}{2}\varepsilon^2\eta\,\frac{\rho R_2^4}{\tau^2}\int_0^1\left[\Re\left\{\left(A_*\,\mathrm{e}^{\,\alpha\bar{y}}+B_*\,\mathrm{e}^{\,-\alpha\bar{y}}-\frac{\mathrm{i}\,\widetilde{\boldsymbol{P}}_*}{2\pi}\right)\mathrm{e}^{\,2\mathrm{i}\pi\,\bar{t}}\right\}\right]^2\mathrm{d}\bar{y}. \end{aligned} \tag{A.28}$$

Analytical solution leads to an explicit expression of kinetic energy, it is preferable to proceed numerically for verifying the added mass and damping.

A.4.2.2 Free movement

The equations are the same as the periodic case but it has to be proceeded by LAPLACE transform. We need to replace $\hat{p}$ by $\sigma\,\hat{p}$.

The LAPLACE transform of Eq. A.23a for initial velocity at zero will be written as:

$$\frac{1}{\sigma}\frac{\partial^2\hat{u}}{\partial\bar{y}^2}-s\hat{u}=\frac{\partial\hat{p}}{\partial\bar{x}},$$

Therefore, we will have the LAPLACE transform of the pressure:

$$\hat{p}=\frac{\sqrt{\sigma s}\,\mathrm{sh}\,\sqrt{\sigma s}}{2(1-\mathrm{ch}\,\sqrt{\sigma s})+\sqrt{\sigma s}\,\mathrm{sh}\,\sqrt{\sigma s}}\,s(s\hat{a}-1)\cos\bar{x}.$$

Considering now the LAPLACE transform of Eq. A.23b :

$$\frac{\tau_M^2}{\tau^2}\,s(s\hat{a}-1)+\frac{\tau_D}{\tau}\,(s\hat{a}-1)+\hat{a}=-\frac{\tau_F^2}{\tau^2}\int_0^{2\pi}\hat{p}(\bar{x},\bar{t})\cos\bar{x}\,\mathrm{d}\bar{x},$$

Where we can precise the form of second member:

$$\begin{aligned} \frac{\tau_M^2}{\tau^2}\,s(s\hat{a}-1)+\frac{\tau_D}{\tau}\,(s\hat{a}-1)+\hat{a} &= -\pi\frac{\tau_F^2}{\tau^2}\frac{\sqrt{\sigma s}\,\mathrm{sh}\,\sqrt{\sigma s}}{2(1-\mathrm{ch}\,\sqrt{\sigma s})+\sqrt{\sigma s}\,\mathrm{sh}\,\sqrt{\sigma s}}\,s(s\hat{a}-1) \\ &= -\pi\frac{\tau_F^2}{\tau^2}\left(1-\frac{\mathrm{th}\,\frac{1}{2}\sqrt{\sigma s}}{\frac{1}{2}\sqrt{\sigma s}}\right)^{-1}s(s\hat{a}-1), \end{aligned} \tag{A.29}$$

We will be still needing for distributing the terms on the right on the terms on the left for identifying the added mass and added damping.

By conclusion, the LAPLACE transform of the displacement will be:

$$\hat{a}=\frac{1}{s}-\frac{1}{s}\left[\left(\frac{\tau_M^2}{\tau^2}+\pi\frac{\tau_F^2}{\tau^2}\frac{\frac{1}{2}\sqrt{\sigma s}}{\frac{1}{2}\sqrt{\sigma s}-\mathrm{th}\,\frac{1}{2}\sqrt{\sigma s}}\right)s^2+\frac{\tau_D}{\tau}\,s+1\right]^{-1}. \tag{A.30}$$

A.5 Conclusion

In principal, the dynamic approach and the energy approach are equivalent since the the latter is obtained by integration of the former. All the questions lies in the existence and identification of the parameters.

In fact, there is no evidence that such a decomposition of Eq. A.4 and Eq. A.6 is possible in general. However, it is possible in particular case such as during imposed movement. The results obtained from the two approaches are identical for all the hypothesis.

More general results are achieved in the frame of linearisation. In the case of perfect fluid, we prove the existence of added mass and added damping, regardless of the movement, imposed or free. The two approaches are equivalent.

The case of real fluid leads to less complete results. In the case of imposed movement, it is possible to prove the deformation of $\boldsymbol{F}$ according to the form Eq. A.4. But, it is not possible to reach the same result with the energy approach due to the complexity of calculation. Numerical verification will be valued in this case.

For the case of free movement, there is nothing allowing us to generalise the value. The complexity of the analytical solution constitutes an obstacle for the dynamic approach. On the other hand, the energy approach remains exploitable, at least numerically.

Appendix B

Oscillations of two cylinders coupled by fluid

In the comparison of experimental results and numerical calculation, discrepancies between the damping coefficient and frequency calibrated from the experiments and calculated from simulation have been observed. In this appendix, to suggest a reasonable explanation to these discrepancies, we will try to find a solution to the problem with a simplified model of two coupled oscillating cylinders.

B.1 Introduction

In experiments, coupled oscillation of hexagonal assembly and outer hexagonal channel is involved. For purpose of simplification, the geometry has been reduced to two cylinders representing the assembly and container respectively (FIGURE B.1).

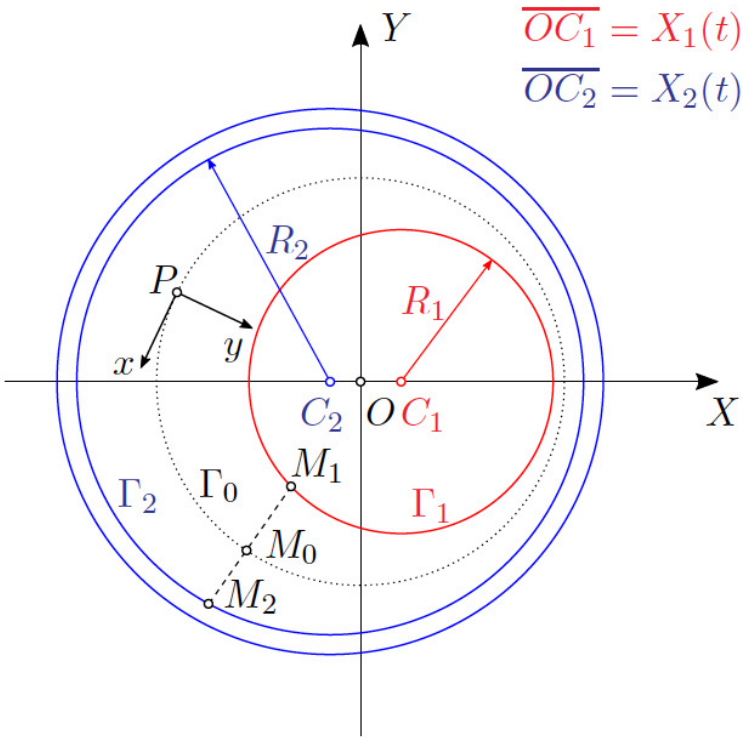

FIGURE B.1: Geometry of two coupled cylinders

Two cylinders Γ_1 and Γ_2 represents the wall of the inner hexagonal assembly and inner wall of the container respectively. The radius of the two cylinders are R_1 and R_2 ($R_2 > R_1$). The coordinate system is defined as shown in the figure by $\{O; X, Y\}$. C_1 and C_2 are the center of Γ_1 and Γ_2 respectively. Since the movement of the assembly has been constrained to one-dimensional movement by the twin-blade support, the movement of Γ_1 and Γ_2 can be supposed to happen on the only axis of X. Therefore, the displacement of C_1 and C_2 can be expressed as $\overline{OC_1} = X_1(t)$ and $\overline{OC_2} = X_2(t)$. The movement of the fluid is described with a local coordinate $\{P; x, y\}$ at a fixed circle Γ_0 with $R_0 = \frac{1}{2}(R_1 + R_2)$.

The system should be treated as a damped spring-mass problem. The movement of Γ_1, Γ_2 and also the fluid are in interest of study, especially the influence of Γ_2's oscillation on global damping of the system. At initial time, the assembly Γ_1 is displaced at $X_1(0) = a$ with initial velocity $\dot{X}_1 = 0$ while the container Γ_2 has displacement $X_2(0) = 0$ and initial velocity $\dot{X}_2 = 0$.

B.2 Position of problem

B.2.1 Geometry

The displacement can be described by two parameters:

$$\begin{aligned} &\alpha = a/b \leq 1 && \text{:parameter of amplitude} \\ &\epsilon = b/R_0 = (R_2 - R_1)/R_0 \ll 1 && \text{:parameter of confinement} \end{aligned} \tag{B.1}$$

Here, a is the initial displacement of Γ_1 and b is the average width of the channel. The position of a point M in the fluid domain can be represented by local coordinate:

$$\overrightarrow{OM} = \overrightarrow{OP} + \overrightarrow{PM} = (R_0 - y)\mathbf{e_r}, \;\; y = R_0 - r, x = R_0\theta. \tag{B.2}$$

Here, θ is the polar angle from the origin in respective of axis OX and r is the module of the radial vector.

The equation of the two circles in local variables provided by trigonometry can be expressed as:

$$F_k(x, y, t) = (1 - \frac{y}{R_0} - \frac{X_k}{R_0}\cos\frac{x}{R_0})^2 + \frac{X_k^2}{R_0^2}\sin^2\frac{x}{R_0} - \frac{R_k^2}{R_0^2} = 0, \;\; k = 1, 2. \tag{B.3}$$

The external normal vector of the fluid domain are:

$$\mathbf{n_k} = \frac{\pm 1}{\|\nabla F_k\|}\big[\big(1 - \frac{y}{R_0} - \frac{X_k}{R_0}cos\frac{X}{R_0}\big)\mathbf{e_y} - \frac{X_k}{R_0}(1 - \frac{y}{R_0})sin\frac{x}{R_0}\mathbf{e_x}\big]. \tag{B.4}$$

Where the positive and negative signal corresponds with Γ_1 and Γ_2 respectively. Therefore,

$$\|F_k\|^2 = \big[\frac{X_k^2}{R_0^2}\big(1 - \frac{y}{R_0}\big)^2 sin^2\theta + \big(1 - \frac{y}{R_0} - \frac{X_k}{R_0}cos\theta\big)^2\big]. \tag{B.5}$$

The width of the local channel from M_1 on Γ_1 to M_2 on Γ_2 with M_0 on Γ_0 can be expressed as:

$$h(x,t) = M_1M_2 = R_2\left(\sqrt{1-\frac{X_2^2}{R_2^2}sin^2\frac{x}{R_0}}+\frac{X_2}{R_2}cos\frac{x}{R_0}\right)-R_1\left(\sqrt{1-\frac{X_1^2}{R_1^2}sin^2\frac{x}{R_0}}+\frac{X_1}{R_1}cos\frac{x}{R_0}\right). \tag{B.6}$$

B.2.2 Fluid

The fluid is viscous and incompressible.

B.2.2.0.1 Equations

The local velocity in polar coordinate $\mathbf{v} = v_r\mathbf{e_r} + v_\theta\mathbf{e}_\theta$ also can be expressed in cartesian system $\mathbf{v} = u\mathbf{e_x} + v\mathbf{e_y}$. Here, $v_r = -v$ and $v_\theta = u$.

Therefore, the Navier-Stokes equations describing the fluid behaviour are transformed as following:

$$\begin{cases} \dfrac{R_0}{R_0-y}\dfrac{\partial u}{\partial x}+\dfrac{1}{R_0-y}\dfrac{\partial}{\partial y}[(R_0-y)v]=0, \\ \dfrac{\partial u}{\partial t}+\dfrac{R_0u}{R_0-y}\dfrac{\partial u}{\partial x}+v\dfrac{\partial u}{\partial y}-\dfrac{uv}{R_0-y}=-\dfrac{R_0}{\rho(R_0-y)}\dfrac{\partial p}{\partial x}+\nu\left(\dfrac{\partial}{\partial y}\left\{\dfrac{1}{R_0-y}\dfrac{\partial}{\partial y}[(R_0-y)u]\right\}\right. \\ \qquad\qquad\qquad\qquad\left.+\dfrac{R_0^2}{(R_0-y)^2}\dfrac{\partial^2u}{\partial x^2}-\dfrac{2R_0}{(R_0-y)^2}\dfrac{\partial v}{\partial x}\right), \\ \dfrac{\partial v}{\partial t}+\dfrac{R_0u}{R_0-y}\dfrac{\partial v}{\partial x}+v\dfrac{\partial v}{\partial y}+\dfrac{u^2}{R_0-y}=-\dfrac{1}{\rho}\dfrac{\partial p}{\partial y}+\nu\left(\dfrac{\partial}{\partial y}\left\{\dfrac{1}{R_0-y}\dfrac{\partial}{\partial y}[(R_0-y)v]\right\}\right. \\ \qquad\qquad\qquad\qquad\left.+\dfrac{R_0^2}{(R_0-y)^2}\dfrac{\partial^2v}{\partial x^2}+\dfrac{2R_0}{(R_0-y)^2}\dfrac{\partial u}{\partial x}\right). \end{cases} \tag{B.7}$$

B.2.2.0.2 Stress tensor

The stress tensor:

$$\sigma = -p\mathbf{I}+\tau, \text{where } \tau = 2\mu\mathbf{D}. \tag{B.8}$$

In local coordinate, it becomes:

$$D_{xx} = \frac{R_0}{R_0-y}\frac{\partial u}{\partial x}-\frac{v}{R_0-y},\ D_{yy} = \frac{\partial v}{\partial y},\ D_{xy} = D_{yx} = \frac{1}{2}\left[(R_0-y)\frac{\partial}{\partial y}\left(\frac{u}{R_0-y}\right)+\frac{R_0}{R_0-y}\frac{\partial v}{\partial x}\right]. \tag{B.9}$$

B.2.3 Solid

The movements of the two cylinders are described with one-dimensional damped spring-mass equation as following:

$$M_k\ddot{X}_k + D_k\dot{X}_k + K_kX_k = -\mathbf{e_X}\cdot\int_{\Gamma_k}\sigma\cdot\mathbf{n_k}d\ell,\ \ k=1,2. \tag{B.10}$$

Here, M_k is the mass, D_k is the damping ratio, K_k is the stiffness.

B.2.4 Boundary conditions

There are two types of boundary conditions according to approximation for the fluid flow: non-penetration condition and adherent condition.

B.2.4.1 Non-penetration condition

On the surface, the fluid flow satisfies the equation $F(x, y, t) = 0$. This condition can be translated into $\mathrm{d}F/\mathrm{d}t = 0$, therefore, $\partial F/\partial t + \nabla F \cdot \mathbf{v} = 0$. With the equation above, this equation can be transformed into:

$$\begin{aligned}&\left[\left(1 - \frac{y_{|k}}{R_0}\right) cos\frac{x}{R_0} - \frac{X_k}{R_0}\right]\dot{X}_k \\ &- \frac{X_k}{R_0}\left(1 - \frac{y_{|k}}{R_0}\right) sin\frac{x}{R_0} u_{|\Gamma_k} + \left(1 - \frac{y_{|k}}{R_0} - \frac{X_k}{R_0} cos\frac{x}{R_0}\right) v_{|k} = 0,\ k = 1, 2.\end{aligned} \tag{B.11}$$

Where $y_{|k} = \pm\frac{1}{2}h(x, t)$.

B.2.4.2 No-slip condition

Considering viscous fluid to the wall, the equation will be:

$$u_{|k}\mathbf{e_x} + v_{|k}\mathbf{e_y} = \dot{X}_k\mathbf{e_X},\ \ k = 1, 2. \tag{B.12}$$

B.3 Scaling

B.3.1 Geometry

Two scaling parameters have already been defined as Eq. B.1. The scaling of geometry for x and y can be defined as:

$$x = R_0\overline{x},\ y = b\overline{y}. \tag{B.13}$$

The movement of Γ_1 and Γ_2 can be defined as:

$$X_1 = a\overline{X_1},\ X_2 = \eta a\overline{X_2},\ \text{here } \eta \leq 1. \tag{B.14}$$

Therefore, the equation of the local channel width $h(x, t)$ can be transformed into following non-dimensional form:

$$\begin{aligned}&(1 - \epsilon\overline{y} - \eta^{k-1}\alpha\epsilon\overline{X_k}cos\theta)^2 + \eta^{2(k-1)}\alpha^2\epsilon^2\overline{X_k}^2 sin^2\theta - (1 \mp \frac{1}{2}\epsilon)^2 = 0, \\ &b + (\delta h)\tilde{h} = a(\eta\overline{X}_2 - \overline{X}_1)cos\theta + R_0(1 + \frac{1}{2}\epsilon)\sqrt{1 - \eta^2\frac{a^2}{R_2^2}\overline{X}_2^2 sin^2\theta} - R_0(1 - \frac{1}{2}\epsilon)\sqrt{1 - \frac{a^2}{R_1^2}\overline{X}_1^2 sin^2\theta}.\end{aligned} \tag{B.15}$$

In first approximation, taking into account $\overline{x} = \theta$:

$$\begin{aligned} &\overline{y} = \pm\frac{1}{2} - \eta^{k-1}\alpha\overline{X}_k cos\overline{x}, \\ &\frac{(\delta h)}{R_0}\tilde{h} = -\alpha\epsilon(\overline{X}_1 - \eta\overline{X}_2)[cos\overline{x} - \frac{1}{2}\alpha\epsilon(\overline{X}_1 + \eta\overline{X}_2)sin^2\overline{x}]. \end{aligned} \tag{B.16}$$

Except when $\overline{x} = \pm\pi$ where $|cos\overline{x}| \ll 1$, we can obtain the value of (δh) and $\tilde{h}(\overline{x}, \overline{t})$:

$$(\delta h) = \alpha\epsilon R_0,\ \tilde{h}(\overline{x}, \overline{t}) = -(\overline{X}_1 - \eta\overline{X}_2)cos\overline{x}. \tag{B.17}$$

The component of the normal vectors can be expressed as:

$$n_{k,x} = \mp\eta^{k-1}\alpha\epsilon\overline{X}_k sin\overline{x},\ n_{k,y} = \pm 1,\ \text{with}\ \|F_k\| \simeq 1, k = 1, 2. \tag{B.18}$$

B.3.2 Fluid

B.3.2.1 Equations

The parameters of the fluid can be non-dimensionalized as:

$$t = \tau\bar{t},\ u = U\overline{u},\ v = V\overline{v},\ p = p_0 + (\delta p)\tilde{p},\ \mathsf{St} = \frac{R_0}{U\tau},\ \mathsf{Re} = \frac{Ub}{\nu}. \tag{B.19}$$

Here, $p_0 = p(t = 0)$, $V = \epsilon U$ can be deducted from mass conservation.

Therefore, the equation in first approximation can be transformed as:

$$\begin{cases} \dfrac{\partial\overline{u}}{\partial\overline{x}} + \dfrac{\partial\overline{v}}{\partial\overline{y}} = 0, \\ \mathsf{St}\dfrac{\partial\overline{u}}{\partial\overline{t}} + \overline{u}\dfrac{\partial\overline{u}}{\partial\overline{x}} + \overline{v}\dfrac{\partial\overline{u}}{\partial\overline{y}} = -\dfrac{(\delta p)}{\rho U^2}\dfrac{\partial\tilde{p}}{\partial\overline{x}} + \dfrac{1}{\epsilon\mathsf{Re}}\dfrac{\partial^2\overline{u}}{\partial\overline{y}^2}, \\ 0 = -\dfrac{\partial\tilde{p}}{\partial\overline{y}}, \\ \dfrac{(\delta p)}{\rho U^2} = \sup\Big\{\mathsf{St}, 1, \dfrac{1}{\epsilon\mathsf{Re}}\Big\}. \end{cases} \tag{B.20}$$

This equation is characterised with approximation of small movement. The first term of correction can be the centrifuge acceleration.

B.3.2.2 Stress tensor

The strain can be translated as:

$$D_{xx} = \frac{U}{R_0}\frac{\partial\bar{u}}{\partial\bar{x}}, \quad D_{yy} = \frac{U}{R_0}\frac{\partial\bar{v}}{\partial\bar{y}} \quad \text{et} \quad D_{xy} = D_{yx} = \tfrac{1}{2}\frac{U}{\varepsilon R_0}\frac{\partial\bar{u}}{\partial\bar{y}}. \tag{B.21}$$

B.3.2.3 Pressure force

The pressure force acting on the wall can be calculated as: Here, in the case of incompressible fluid, it is possible to suppose $p_0 = 0$, therefore, for Γ_k, in first approximation:

$$F_{k,X} = \mp\rho U^2 R_0 \int_0^{2\pi} \Big[\frac{(\delta p)}{\rho U^2}\,\tilde{p}\cos\bar{x}\Big]\,\mathrm{d}\bar{x}. \tag{B.22}$$

Although the friction is negligible in first approximation, the contribution of friction can not be eliminated for the dispositive phenomenon. It should be still taken into account in the momentum balance of fluid.

B.3.3 Solid

Eq. B.10 can be written in non-dimensioqnalized form as:

$$\frac{M_1}{K_1\tau^2}\,\ddot{\bar{X}}_1 + \frac{D_1}{K_1\tau}\,\dot{\bar{X}}_1 + \bar{X}_1 = -\frac{(\delta p)}{\alpha\varepsilon K_1}\int_0^{2\pi} \tilde{p}\cos\bar{x}\,\mathrm{d}\bar{x}, \tag{B.23a}$$

$$\frac{M_2}{K_2\tau^2}\,\ddot{\bar{X}}_2 + \frac{D_2}{K_2\tau}\,\dot{\bar{X}}_2 + \bar{X}_2 = \frac{(\delta p)}{\eta\alpha\varepsilon K_2}\int_0^{2\pi} \tilde{p}\cos\bar{x}\,\mathrm{d}\bar{x}. \tag{B.23b}$$

Implicitly, the scaling of this equation suggests that the stiffness is the main driving factor of the motion.

B.3.4 Boundary conditions

B.3.4.1 Non-penetration condition

In the first approximation, Eq. B.11 can be expressed as:

$$\bar{v}_{|k} = -\eta^{k-1}\alpha\big(\mathsf{St}\dot{\bar{X}}_k\cos\bar{x} - \bar{X}_k\bar{u}_{|k}\sin\bar{x}\big). \tag{B.24}$$

A possible degeneracy will only depend on STROUHAL number.

B.3.4.2 No-slip condition

Eq. B.12 will be transformed into:

$$\begin{cases} \bar{u}_{|k} + \eta^{k-1}\alpha\varepsilon\mathsf{St}\,\dot{\bar{X}}_k\sin\bar{x} = 0, \\ \bar{v}_{|k} + \eta^{k-1}\alpha\mathsf{St}\,\dot{\bar{X}}_k\cos\bar{x} = 0. \end{cases} \tag{B.25}$$

B.4 Phenomenological analysis

B.4.1 Hypothesis

Damping is the source of the friction force in the fluid. To achieve an easier resolution, Eq. B.7 should be linearised. The two properties will be satisfied when:

$$\frac{(\delta p)}{\rho U^2} = \mathsf{St} = \frac{1}{\varepsilon\mathsf{Re}} \gg 1 \quad\Longrightarrow\quad U = \varepsilon\frac{(\delta p)\,b}{\mu} \quad \text{et} \quad b^2 = \nu\tau. \tag{B.26}$$

The scales of the pressure and time are still unknown. It is still not possible to confirm this configuration by one condition for the data. The last relation simply translate the fact that the characteristic time of oscillation should be in the order of diffusion time.

Other hypothesis are suggested by Eq. B.23. The experimental results of PISE-1A give a single characteristic frequency. In the reason of mass, it is suggested that the frequency depends on the mass-spring system constituted by the inner cylinder Γ_1 and the inertial

force acting on Γ_2 is negligible:

$$\tau = \tau_1 = \sqrt{\frac{M_1}{K_1}}, \quad \text{et} \quad \frac{M_2}{K_2\tau_1^2} = \frac{M_2}{M_1}\frac{K_1}{K_2} \ll 1 \quad \Longrightarrow \quad b^2 = \nu\sqrt{\frac{M_1}{K_1}}. \tag{B.27}$$

Moreover, dissipative phenomenon of structure are supposed to be marginal:

$$\frac{D_1}{K_1\tau_1} \lesssim 1 \quad \Longleftrightarrow \quad \frac{D_1}{\sqrt{M_1K_1}} \lesssim 1.$$

B.4.2 Dynamics of the assemblies

The equation of the balance of the two assemblies can be written as:

$$\begin{aligned}
\ddot{\bar{X}}_1 + \frac{D_1}{\sqrt{M_1K_1}}\dot{\bar{X}}_1 + \bar{X}_1 &= -\frac{(\delta p)}{\alpha\varepsilon K_1}\int_0^{2\pi}\tilde{p}\cos\bar{x}\,\mathrm{d}\bar{x},\\
\frac{D_2}{K_2}\sqrt{\frac{K_1}{M_1}}\dot{\bar{X}}_2 + \bar{X}_2 &= \frac{(\delta p)}{\eta\alpha\varepsilon K_2}\int_0^{2\pi}\tilde{p}\cos\bar{x}\,\mathrm{d}\bar{x}.
\end{aligned}$$

Since the movement of the inner cylinder is the source of all the movements of the system, the scale of pressure can be deducted as:

$$(\delta p) = \alpha\varepsilon K_1 \quad \Longrightarrow \quad U = \alpha\varepsilon^2\frac{(M_1K_1^3)^{1/4}}{\rho\nu^{1/2}}, \quad \eta = \frac{K_1}{K_2}.$$

B.4.3 Boundary conditions

The condition $\mathsf{St} \gg 1$ allows to precise the first approximation of no-slip condition:

$$\alpha = 1/\mathsf{St} \ll 1 \quad \Longrightarrow \quad \bar{u}_{|k} = 0 \quad \text{et} \quad \bar{v}_{|k} = -\eta^{k-1}\dot{\bar{X}}_k\cos\bar{x}. \tag{B.28}$$

This equation impose the limitation of initial displacement of Γ_1. In consequence, Eq.B.16 can be reduced to $\bar{y}_{|k} = \pm 1$ and it is possible to transfer the boundary condition on a non-displaced position.

B.5 Resolution

The dissipation of the structure can be negligible, therefore, the equation of the system will be:

$$\frac{\partial\bar{u}}{\partial\bar{x}} + \frac{\partial\bar{v}}{\partial\bar{y}} = 0, \quad \frac{\partial\bar{u}}{\partial\bar{t}} = -\frac{\partial\tilde{p}}{\partial\bar{x}} + \frac{1}{\sigma}\frac{\partial^2\bar{u}}{\partial\bar{y}^2}, \tag{B.29a}$$

$$k = 1, 2 : \quad \bar{y}_{|k} = \pm\tfrac{1}{2}, \quad \bar{u}_{|k} = 0, \quad \bar{v}_{|k} = -\eta^{k-1}\dot{\bar{X}}_k\cos\bar{x}, \tag{B.29b}$$

$$\ddot{\bar{X}}_1 + \bar{X}_1 = -\int_0^{2\pi}\tilde{p}\cos\bar{x}\,\mathrm{d}\bar{x}, \quad \bar{X}_2 = \int_0^{2\pi}\tilde{p}\cos\bar{x}\,\mathrm{d}\bar{x}. \tag{B.29c}$$

$$\bar{t} = 0 : \quad \bar{u} = \bar{v} = \tilde{p} = 0, \quad \bar{X}_1 = 1, \quad \bar{X}_2 = 0. \tag{B.29d}$$

B.5.1 Integration

Apply LAPLACE transform on Eq. B.29, the adherent condition Eq. B.29b lead to:

$$\hat{u} = \frac{1}{s}\Big[\frac{\mathrm{ch}(\sqrt{\sigma s}\,\bar{y})}{\mathrm{ch}(\frac{1}{2}\sqrt{\sigma s})} - 1\Big]\frac{\mathrm{d}\hat{p}}{\mathrm{d}\bar{x}}. \tag{B.30}$$

$$\hat{p} = s\,\frac{s(\widehat{X}_1 - \eta\widehat{X}_2) - 1}{1 - \mathrm{th}(\frac{1}{2}\sqrt{\sigma s})/(\frac{1}{2}\sqrt{\sigma s})}\cos\bar{x}, \tag{B.31}$$

$$\widehat{X}_1 = \frac{\pi\, s + s\big[\pi\eta\, s^2 + 1 - \mathrm{th}(\frac{1}{2}\sqrt{\sigma s})/(\frac{1}{2}\sqrt{\sigma s})\big]}{\pi\, s^2 + (s^2+1)\big[\pi\eta\, s^2 + 1 - \mathrm{th}(\frac{1}{2}\sqrt{\sigma s})/(\frac{1}{2}\sqrt{\sigma s})\big]}, \tag{B.32a}$$

$$\widehat{X}_2 = \frac{-\pi s}{\pi\, s^2 + (s^2+1)\big[\pi\eta\, s^2 + 1 - \mathrm{th}(\frac{1}{2}\sqrt{\sigma s})/(\frac{1}{2}\sqrt{\sigma s})\big]}, \tag{B.32b}$$

B.6 External fixed cylinder

For comparison, it is interesting to develop the same calculation in the case when the outer cylinder is fixed. The equations of this problem will be:

$$\frac{\partial\bar{u}}{\partial\bar{x}} + \frac{\partial\bar{v}}{\partial\bar{y}} = 0, \quad \frac{\partial\bar{u}}{\partial\bar{t}} = -\frac{\partial\tilde{p}}{\partial\bar{x}} + \frac{1}{\sigma}\frac{\partial^2\bar{u}}{\partial\bar{y}^2}, \tag{B.33a}$$

$$k=1: \quad \bar{y}_{|1} = +\tfrac{1}{2}, \quad \bar{u}_{|1} = 0, \quad \bar{v}_{|1} = -\dot{\bar{X}}_1\cos\bar{x}, \tag{B.33b}$$

$$k=2: \quad \bar{y}_{|2} = -\tfrac{1}{2}, \quad \bar{u}_{|2} = 0, \quad \bar{v}_{|2} = 0, \tag{B.33c}$$

$$\ddot{\bar{X}}_1 + \bar{X}_1 = -\int_0^{2\pi}\tilde{p}\cos\bar{x}\,\mathrm{d}\bar{x}, \tag{B.33d}$$

$$\bar{t}=0: \quad \bar{u} = \bar{v} = \tilde{p} = 0, \quad \bar{X}_1 = 1. \tag{B.33e}$$

The pressure and displacement obtained through LAPLACE will be:

$$\hat{p} = \frac{s(s\widehat{X}_1 - 1)}{1 - \mathrm{th}(\frac{1}{2}\sqrt{\sigma s})/(\frac{1}{2}\sqrt{\sigma s})}\cos\bar{x}, \tag{B.34}$$

$$\widehat{X}_1 = \frac{\pi s + s\big[1 - \mathrm{th}(\frac{1}{2}\sqrt{\sigma s})/(\frac{1}{2}\sqrt{\sigma s})\big]}{\pi s^2 + (s^2+1)\big[1 - \mathrm{th}(\frac{1}{2}\sqrt{\sigma s})/(\frac{1}{2}\sqrt{\sigma s})\big]}. \tag{B.35}$$

B.7 Spectra

Transfer LAPLACE $\widehat{G}(s)$ transform to FOURIER $\widetilde{G}(\bar{f})$, we will have:

$$\left.\begin{aligned}\widetilde{X}_1 &= \;\; 4\pi\sqrt{\pi\bar{f}}\,(1 - 16\pi^4\bar{f}^4)\,\frac{Q}{D}\\ \widetilde{X}_2 &= -4\pi\sqrt{\pi\bar{f}}\,(1 - 4\pi^2\bar{f}^2)\,\frac{Q}{D}\end{aligned}\right\} \quad \text{where} \quad Q = \frac{\mathrm{sh}\,\sqrt{\pi\bar{f}} - \sin\sqrt{\pi\bar{f}}}{\mathrm{ch}\,\sqrt{\pi\bar{f}} + \cos\sqrt{\pi\bar{f}}}.$$

The spectra will be:

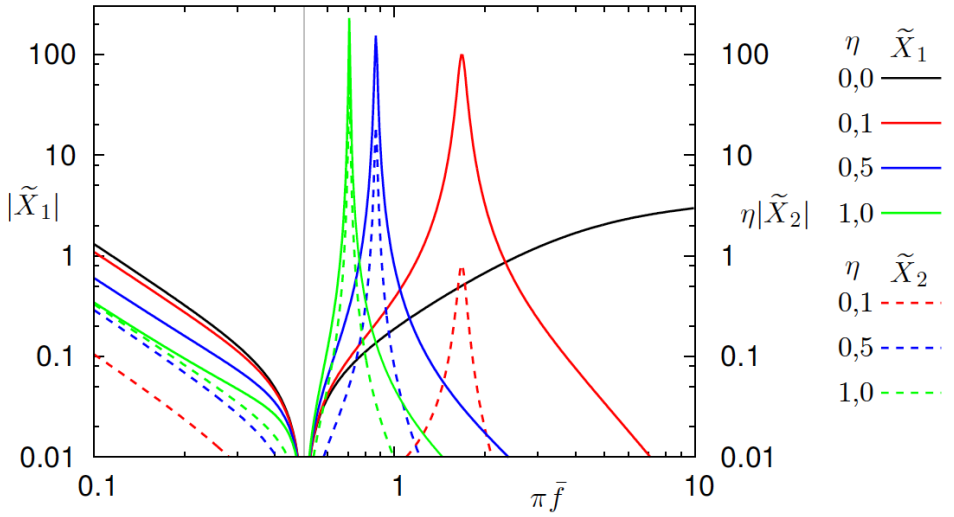

FIGURE B.2: Spectra

The FOURIER should be interpreted as a transfer function in polar representation as $\widetilde{X} = |\widetilde{X}|\exp(-\mathrm{j}\phi)$. In this case, since the phase only depend on the sign, the spectra are either on phase or in the opposite.

One of the inconvenience of the frequency analysis is that it will not indicate the effective frequency of the oscillations. But, the phenomenological analysis has suggested that $f_c = (1/2\pi)\sqrt{K_1/M_1}$ and the frequency of movement are close to this value.

When η increases, the stiffness of the outer cylinder decreases. Therefore, this figure gives following information:

- ▷ the increase of maxima indicates a variation variation of the amplitudes in the same direction
- ▷ the decrease of the peak width suggests a reduction of damping
- ▷ the shift of the maxima to the left indicates an interaction with the increasingly plausible natural frequency

B.8 Conclusion

In general, the evolution of the two families of spectra with the stiffness parameter η is consistent with what is expected.

With respect to the objective, the results are positive. More precisely, taking into account the movement of the outer cylinder has effect of reducing damping.

Because of the simplicity of the model, these results are indicative and should be taken up by a more comprehensive model, with the damping of the structure and the hexagonal shape of the cylinders taken into consideration.

This coupling effect is not included in $3D$ NAVIER-STOKES model. It can explain the fact that the numerical simulation tend to give higher damping than the experiments since the coupling of assembly and container tends to decrease the damping coefficient. However, in order to explain why the frequency computed from numerical simulation is always lower than that of the experiments, further study should be made.

Appendix C

System of DOF at 2

The free-vibration experiments in air of PISE-1A suggest that there may be coupling between the movements assembly and the base. Since there is no strong interaction between the base and the air as that in the free-vibration experiments in fluid, it is possible to study this coupling with a mass-spring system with two degrees of freedom.

C.1 Position of the problem

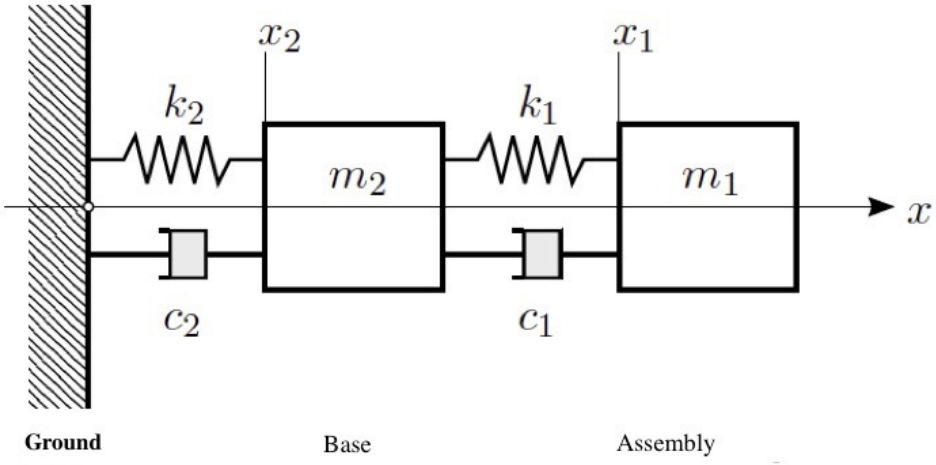

FIGURE C.1: System of two degrees of freedom

As shown in FIGURE C.1, the system is represented by a mass-spring system with damping. Index 1 is applied to the assembly while index 2 is for the base. The position of the assembly and the base are x_1 and x_2 respectively as marked by the x-coordinate with origin on the fixed surface of the ground. x_{n0} are the position when the two springs is at rest.

The assembly will be displaced to a given position $x_1(0)$ by a external force F with unknown modules. At the beginning , the force F will be removed to start the vibration.

C.2 Initial equilibrium

At the beginning, the system is at equilibrium and the balance of the system can be described by the following equations:

$$F = -k_1\big\{[x_1(0) - x_{10}] - [x_2(0) - x_{20}]\big\}, \tag{C.1a}$$
$$0 = +k_1\big\{[x_1(0) - x_{10}] - [x_2(0) - x_{20}]\big\} - k_2[x_2(0) - x_{20}], \tag{C.1b}$$

The solution to the above equations will be:

$$x_2(0) = x_{20} + \frac{k_1}{k_1 + k_2}[x_1(0) - x_{10}] \quad \text{and} \quad F = -\frac{k_1 k_2}{k_1 + k_2}[x_1(0) - x_{10}]. \tag{C.2}$$

C.3 Transient equations

C.3.1 Time domain

If we take the displacement of the masses from the position at rest:

$$X_1(t) = x_1(t) - x_{10} \quad \text{et} \quad X_2(t) = x_2(t) - x_{20}. \tag{C.3}$$

We will have:

$$m_1\ddot{X}_1 + c_1(\dot{X}_1 - \dot{X}_2) + k_1(X_1 - X_2) = 0, \tag{C.4a}$$
$$m_2\ddot{X}_2 - c_1(\dot{X}_1 - \dot{X}_2) + c_2\dot{X}_2 - k_1(X_1 - X_2) + k_2X_2 = 0, \tag{C.4b}$$

In matrix form:

$$\begin{pmatrix} m_1 & 0 \\ 0 & m_2 \end{pmatrix} \cdot \ddot{\boldsymbol{X}} + \begin{pmatrix} c_1 & -c_1 \\ -c_1 & c_1 + c_2 \end{pmatrix} \cdot \dot{\boldsymbol{X}} + \begin{pmatrix} k_1 & -k_1 \\ -k_1 & k_1 + k_2 \end{pmatrix} \cdot \boldsymbol{X} = 0. \tag{C.5}$$

The analytical solution to this problem will not be available since the hypothesis of proportional damping is too complicated for application.

C.3.2 Frequency domain

Eq. C.4 can also be approached by LAPLACE transform. After resolving the linear system, imposing $c_0 = c_1 + c_2$ et $k_0 = k_1 + k_2$, it will become:

$$\begin{aligned}
D(s) &= \Big(s^2 + \frac{c_1}{m_1}\,s + \frac{k_1}{m_1}\Big)\Big(s^2 + \frac{c_0}{m_2}\,s + \frac{k_0}{m_2}\Big) - \Big(\frac{c_1}{m_2}\,s + \frac{k_1}{m_2}\Big)^2; \\
N_1(s) &= \Big(s^2 + \frac{c_0}{m_2}\,s + \frac{k_0}{m_2}\Big)\Big\{X_1(0)\,s + \frac{c_1}{m_1}\big[X_1(0) - X_2(0)\big]\Big\} \\
&\quad + \Big(\frac{c_1}{m_1}\,s + \frac{k_1}{m_1}\Big)\Big[X_2(0)\,s - \frac{c_1}{m_2}\,X_1(0) + \frac{c_0}{m_2}\,X_{2(0)}\Big]; \\
N_2(s) &= \Big(s^2 + \frac{c_1}{m_1}\,s + \frac{k_1}{m_1}\Big)\Big[X_2(0)\,s - \frac{c_1}{m_2}\,X_1(0) + \frac{c_0}{m_2}\,X_2(0)\Big] \\
&\quad + \Big(\frac{c_1}{m_2}\,s + \frac{k_1}{m_2}\Big)\Big\{X_1(0)\,s + \frac{c_1}{m_1}\big[X_1(0) - X_{2(0)}\big]\Big\};
\end{aligned} \tag{C.6}$$

Therefore,

$$\widehat{X}_1(s) = N_1(s)/D(s) \quad \text{and} \quad \widehat{X}_2(s) = N_2(s)/D(s). \tag{C.7}$$

FOURIER transform will be given by the following expression:

$$\widetilde{X}_1(f) = \widehat{X}_1(2\pi \mathrm{j} f) + \widehat{X}_1(-2\pi \mathrm{j} f) \quad \text{and} \quad \widetilde{X}_2(f) = \widehat{X}_2(2\pi \mathrm{j} f) + \widehat{X}_2(-2\pi \mathrm{j} f). \tag{C.8}$$

The numerical results are shown in FIGURE C.2:

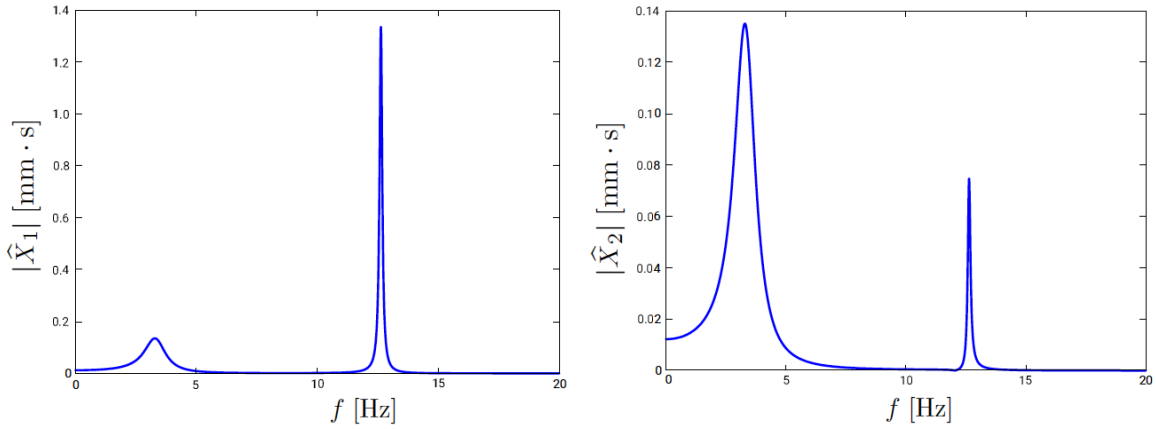

(a) Assembly (b) Base

FIGURE C.2: Spectra of the displacements

As expected, the spectra exhibits two different modes, the first, $f_1 \simeq 12{,}5\,\mathrm{Hz}$, is associated with the assembly, while the second, $f_2 \simeq 3\,\mathrm{Hz}$, is associated the base. The level of the response has a different by factor 10. Note that the theoretical facility has no spurious frequency.

C.4 Energies

C.4.1 Kinetic energy

Kinetic energy for the two masses will be:

$$\mathrm{e}_{cn} = \tfrac{1}{2} m_n \dot{X}_n^2. \tag{C.9}$$

C.4.2 Potential energy

The potential energies stored in the spring by the deformation are:

$$\mathrm{e}_{\mathrm{p}1} = \tfrac{1}{2} k_1 (\dot{X}_1 - \dot{X}_2)^2 \quad \text{and} \quad \mathrm{e}_{\mathrm{p}2} = \tfrac{1}{2} k_2 \dot{X}_2^2. \tag{C.10}$$

C.4.3 Total energy

The total energy of each mass is defined as following:

$$\begin{aligned} \mathrm{e}_{\mathrm{t}1} &= \mathrm{e}_{\mathrm{c}1} + \mathrm{e}_{\mathrm{p}1} \quad &&: \text{assembly}\,; \\ \mathrm{e}_{\mathrm{t}2} &= \mathrm{e}_{\mathrm{c}2} + \mathrm{e}_{\mathrm{p}2} \quad &&: \text{base}. \end{aligned} \tag{C.11}$$

The total energy of the whole system will be:

$$\mathrm{e_t} = \mathrm{e_{t1}} + \mathrm{e_{t2}}. \tag{C.12}$$

C.4.4 Energy balance

The equations obtained is shown as below:

$$\begin{aligned} \tfrac{1}{2}\frac{\mathrm{d}}{\mathrm{d}t}(m_1\dot{X}_1^2) + k_1\dot{X}_1(X_1 - X_2) &= -c_1\dot{X}_1(\dot{X}_1 - \dot{X}_2), \\ \tfrac{1}{2}\frac{\mathrm{d}}{\mathrm{d}t}(m_2\dot{X}_2^2) - k_1\dot{X}_2(X_1 - X_2) + \tfrac{1}{2}\frac{\mathrm{d}}{\mathrm{d}t}(k_2X_2^2) &= \quad c_1\dot{X}_2(\dot{X}_1 - \dot{X}_2) - c_2\dot{X}_2^2. \end{aligned}$$

After summation, the equation becomes:

$$\tfrac{1}{2}\frac{\mathrm{d}}{\mathrm{d}t}\left[m_1\dot{X}_1^2 + m_2\dot{X}_2^2 + k_1(X_1 - X_2)^2 + k_2X_2^2\right] = -\left[c_1(\dot{X}_1 - \dot{X}_2)^2 + c_2\dot{X}_2^2\right]. \tag{C.13}$$

The second term represents the dissipation. The total energy of the system will remain constant if the dissipation of the system is zero ($c_1 = c_2 = 0$).

After integration from 0 to infinity, taking into account the zero initial velocity, it will be transformed into:

$$\underbrace{\tfrac{1}{2}\left\{k_1[X_1(0) - X_2(0)]^2 + k_2X_2^2(0)\right\}}_{\text{initial energy}} = \underbrace{\int_0^\infty \left[c_1(\dot{X}_1 - \dot{X}_2)^2 + c_2\dot{X}_2^2\right]\mathrm{d}t}_{\text{total dissipation}}. \tag{C.14}$$

C.5 Resolution

Analytical solution will not be exploitable. Therefore, in this part, we will go for numerical integration. The method used here is provided by the GSL library. It is a 8th order RUNGE-KUTTA,amended by PRINCE-DORMANT (rk8pd).

TABLE C.1 shows the structural parameters and initial displacements implemented for the calculations.

TABLE C.1: Structural parameters and initial displacements

	Mass [kg]	Stiffness [kg/s^2]	Damping [kg/s]	$x_n(0) - x_{n0}$ [mm]
Assembly	8.905	56019	7.378	1
Base	300	80000	2000	0.41

FIGRE C.3 are the results for the two masses:

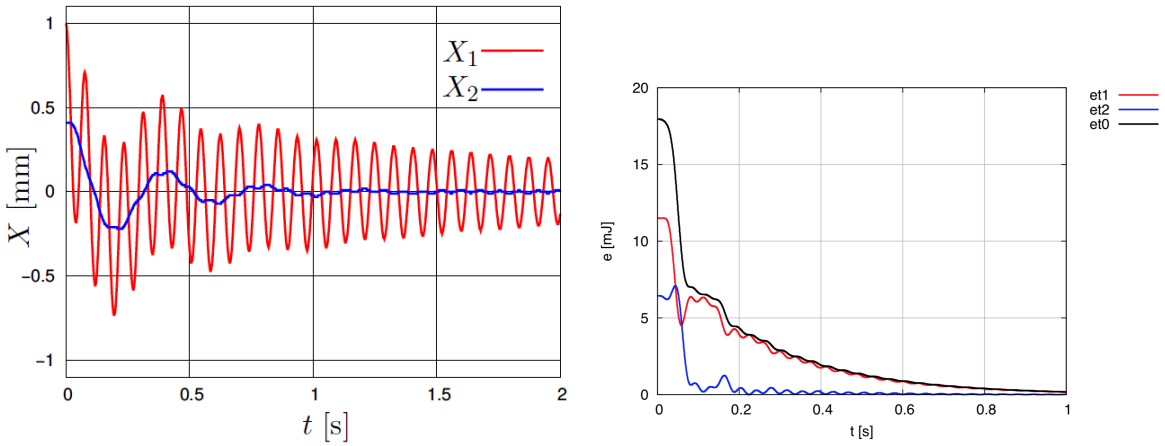

(a) Displacement (b) Energy

FIGURE C.3: Spectra of the displacements

The very different values of the physical parameters justify the very contrasting results. The values used were obtained by trials with comparison to the experimental results. It appears that the assembly can be considered as an isolated system after the movements of the base have ceased around 1 s.

C.6 Conclusion

The results obtained will suggest an explication to the experimental results. The movements of the base cannot be ignored, although we have no direct methods to determine its physical characteristics and follow its displacements. However, assembling PISE-1A as a linear system at 2 degrees of freedom is certainly an approximation worth of discussion.

Appendix D

3D Effects: Recirculation Flow

In this chapter, we will discuss fluid flow confined between two cylinders of limited length, with the 3D recirculation in the longitudinal direction taken into consideration. For the first approach, the movement of the inner cylinder will be imposed so that to focus on the behaviour of the fluid flow in the channel.

We will discuss on the case when the inner cylinder is in motion while the outer cylinder is fixed. Translation scenario will be considered: the moving inner cylinder displace in parallel with the fixed outer cylinder.

The principal objects of this appendix is to to evaluate the extent of the edge effects.

In reason of multitudes of small parameters presented in this problem, an asymptotic approach will be proceeded.

D.1 Geometry and kinematics

We introduce two basic coordinate systems, Cartesian and cylindrical coordinates, as well as the local coordinates attached to the fixed cylinder. Two kinds of boundary conditions apply to the fluid flow: non-penetration condition and adherent condition.

D.1.1 Geometry

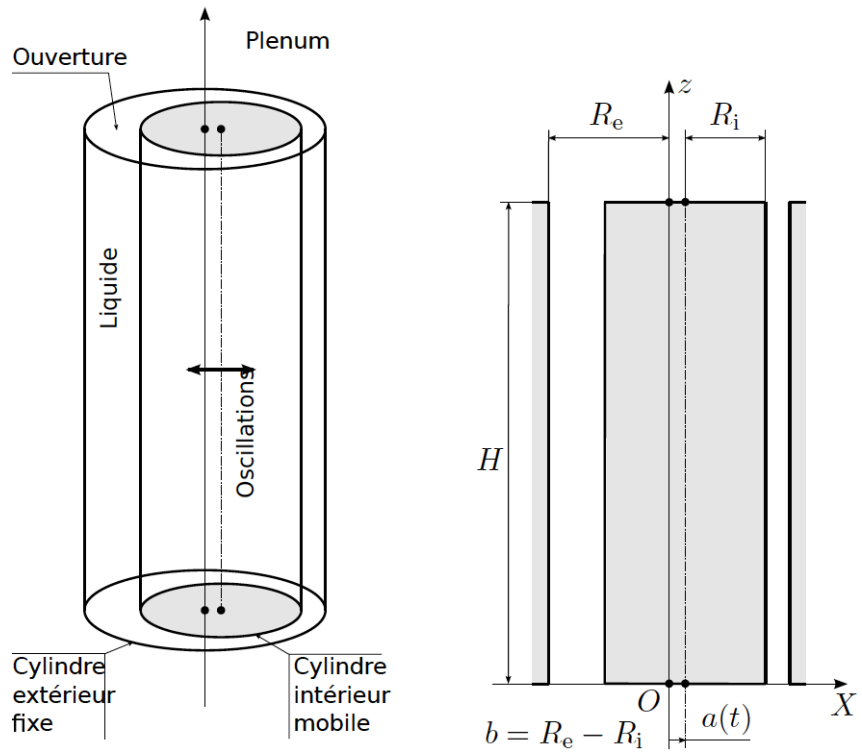

(a) 3D view (b) 2D view

FIGURE D.1: Rigid displacement

The general disposition is shown in FIGURE D.1. The fluid domain $\mathcal{D}$ is confined between the two rigid cylinders of radius $R_e > R_i$ with :

$$b \triangleq R_e - R_i, \tag{D.1}$$

and of height H.

For a global description, we will develop a cartesian coordinate system with origin O as stated in FIGURE D.1. Also we can refer to cylindrical coordinate system $\{r, \theta, z\}$.

The outer cylinder is fixed while the inner cylinder is moving in translation with its axis staying in the plan $\{O\,; X, z\}$ and parallel to the axis Oz. At time t, the distance between the axis of the two cylinders are imposed and have the value of:

$$a(t) \triangleq a_0 \cos \omega t. \tag{D.2}$$

The description of flow will be more naturally represented in the system of normal coordinates $\{P\,; x, y, z\}$ which is attached to the outer cylindrical wall:

$$x \triangleq R_e\,\theta \quad \text{et} \quad y \triangleq R_e - r. \tag{D.3}$$

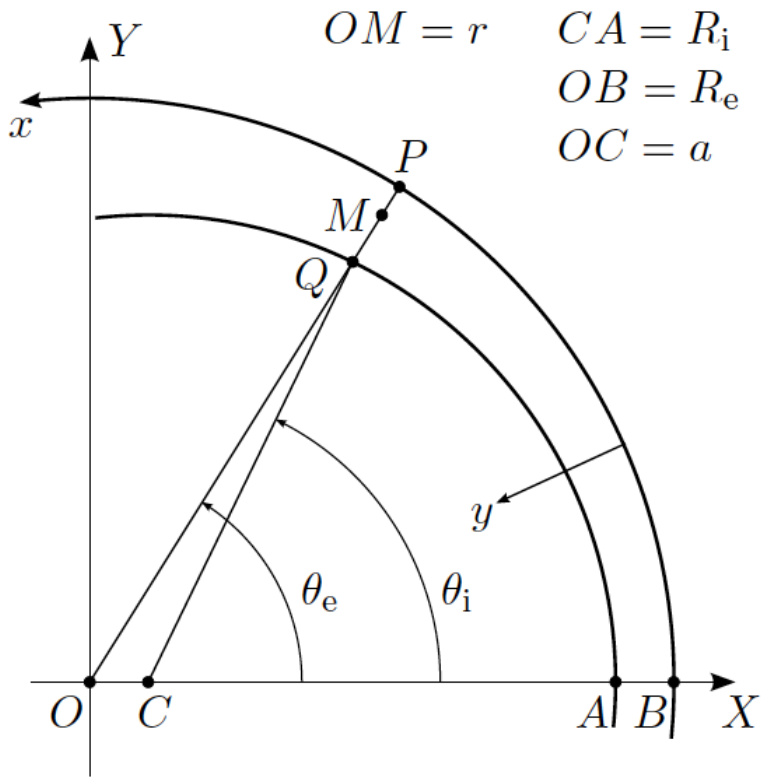

FIGURE D.2: Notations

Shown by one point P of outer cylinder (angle θ_e, centred at O), one point Q of inner cylinder (angle θ_i, centred at C) stayed on the radius OP and by a point M located between between the P and Q:

$$\begin{cases} X_P \triangleq R_\mathrm{e}\,\cos\theta_\mathrm{e}, & x_P = R_\mathrm{e}\,\theta_\mathrm{e}, \\ Y_P \triangleq R_\mathrm{e}\,\sin\theta_\mathrm{e}, & y_P = 0. \end{cases} \tag{D.4}$$

$$\begin{cases} X_Q \triangleq a + R_\mathrm{i}\cos\theta_\mathrm{i}, \\ Y_Q \triangleq R_\mathrm{i}\sin\theta_\mathrm{i}, \\ x_Q = R_\mathrm{e}\,\theta_\mathrm{e}, \\ y_Q = R_\mathrm{e} - a\cos\theta_\mathrm{e} - \sqrt{R_\mathrm{i}^2 - a^2\sin^2\theta_\mathrm{e}}. \end{cases} \tag{D.5}$$

$$\begin{cases} X_M \triangleq r_M\,\cos\theta_\mathrm{e} = (R_\mathrm{e} - y_M)\cos\theta_\mathrm{e}, \\ Y_M \triangleq r_M\,\sin\theta_\mathrm{e} = (R_\mathrm{e} - y_M)\sin\theta_\mathrm{e}, \\ x_M = R_\mathrm{e}\,\theta_\mathrm{e}, \quad y_M \triangleq R_\mathrm{e} - r_M, \end{cases} \tag{D.6}$$

Here θ_i should be considered as a function of θ_e and a. Q is displacing at $\theta_\mathrm{i} = \mathrm{cste}$. We can deduct θ_i:

$$a\cos\theta_\mathrm{e} + \sqrt{R_\mathrm{i}^2 - a^2\sin^2\theta_\mathrm{e}} = \sqrt{R_\mathrm{i}^2 + 2aR_\mathrm{i}\cos\theta_\mathrm{i} + a^2}. \tag{D.7}$$

D.1.1.1 Boundary condition

To give the conditions, we require to evaluate the velocity of the wall at point P and Q. There two types of conditions:

- *conservation* : non-penetration condition (Slipping)
- *experimental origin* : condition of adhesion.

The first should be valid in all the case while the second will only work in the case where the viscous friction plays an important role.

D.1.1.1.1 Outer cylinder

Normal: $\boldsymbol{n} \triangleq -(\boldsymbol{e}_X \cos\theta_\mathrm{e} + \boldsymbol{e}_Y \sin\theta_\mathrm{e})$. Velocity: $\boldsymbol{v}_P = 0$.

$$\begin{array}{ll} \text{Normal velocity:} & \boldsymbol{v}_P \cdot \boldsymbol{n} = 0, \\ \text{Tangential velocity:} & \boldsymbol{v}_P - (\boldsymbol{v}_P \cdot \boldsymbol{n})\boldsymbol{n} = 0. \end{array} \tag{D.8}$$

D.1.1.1.2 Inner cylinder

Normal: $\boldsymbol{n} = \cos\theta_\mathrm{i}\, \boldsymbol{e}_X + \sin\theta_\mathrm{i}\, \boldsymbol{e}_Y$. Velocity: $\boldsymbol{v}_Q = \dot{a}\, \boldsymbol{e}_X$.

$$\begin{array}{ll} \text{Vitesse normale :} & \boldsymbol{v}_Q \cdot \boldsymbol{n} = \dot{a}\, \cos\theta_\mathrm{i}, \\ \text{Vitesse tangentielle :} & \boldsymbol{v}_Q - (\boldsymbol{v}_Q \cdot \boldsymbol{n})\boldsymbol{n} = \dot{a} \sin\theta_\mathrm{i}\, (\sin\theta_\mathrm{i}\, \boldsymbol{e}_X - \cos\theta_\mathrm{i}\, \boldsymbol{e}_Y). \end{array} \tag{D.9}$$

D.2 Fluid and flow

The fluid is incompressible and viscous. The kinematic source of the fluid flow is the motion of the inner cylinder.

D.2.1 Equations

The problem can be described by the following equations:

$$\begin{cases} X = r\cos\theta, \\ Y = r\sin\theta, \\ z = z. \end{cases} \qquad \begin{cases} r = R_\mathrm{e} - y, \\ \theta = x/R_\mathrm{e}, \\ z = z. \end{cases} \tag{D.10}$$

$$\frac{1}{r}\frac{\partial}{\partial r}(r v_r) + \frac{1}{r}\frac{\partial v_\theta}{\partial \theta} + \frac{\partial v_z}{\partial z} = 0. \tag{D.11}$$

$$\begin{cases} \rho\Big(\dfrac{\partial v_r}{\partial t} + v_r\dfrac{\partial v_r}{\partial r} + \dfrac{v_\theta}{r}\dfrac{\partial v_r}{\partial \theta} - \dfrac{v_\theta^2}{r} + v_z\dfrac{\partial v_r}{\partial z}\Big) \\ \qquad = -\dfrac{\partial p}{\partial r} + \mu\Big\{\dfrac{\partial}{\partial r}\Big[\dfrac{1}{r}\dfrac{\partial}{\partial r}(r v_r)\Big] + \dfrac{1}{r^2}\dfrac{\partial^2 v_r}{\partial \theta^2} - \dfrac{2}{r^2}\dfrac{\partial v_\theta}{\partial \theta} + \dfrac{\partial^2 v_r}{\partial z^2}\Big\}, \\ \rho\Big(\dfrac{\partial v_\theta}{\partial t} + v_r\dfrac{\partial v_\theta}{\partial r} + \dfrac{v_\theta}{r}\dfrac{\partial v_\theta}{\partial \theta} + \dfrac{v_r v_\theta}{r} + v_z\dfrac{\partial v_\theta}{\partial z}\Big) \\ \qquad = -\dfrac{1}{r}\dfrac{\partial p}{\partial \theta} + \mu\Big\{\dfrac{\partial}{\partial r}\Big[\dfrac{1}{r}\dfrac{\partial}{\partial r}(r v_\theta)\Big] + \dfrac{1}{r^2}\dfrac{\partial^2 v_\theta}{\partial \theta^2} + \dfrac{2}{r^2}\dfrac{\partial v_r}{\partial \theta} + \dfrac{\partial^2 v_\theta}{\partial z^2}\Big\}, \\ \rho\Big(\dfrac{\partial v_z}{\partial t} + v_r\dfrac{\partial v_z}{\partial r} + \dfrac{v_\theta}{r}\dfrac{\partial v_z}{\partial \theta} + v_z\dfrac{\partial v_z}{\partial z}\Big) \\ \qquad = -\dfrac{\partial p}{\partial z} + \mu\Big[\dfrac{1}{r}\dfrac{\partial}{\partial r}\Big(r\dfrac{\partial v_z}{\partial r}\Big) + \dfrac{1}{r^2}\dfrac{\partial^2 v_z}{\partial \theta^2} + \dfrac{\partial^2 v_z}{\partial z^2}\Big]. \end{cases} \tag{D.12}$$

$$\begin{cases} \boldsymbol{e}_r = -\boldsymbol{e}_y = \quad \boldsymbol{e}_X \cos\theta + \boldsymbol{e}_Y \sin\theta, \\ \boldsymbol{e}_\theta = \quad \boldsymbol{e}_x = -\boldsymbol{e}_X \sin\theta + \boldsymbol{e}_Y \cos\theta. \end{cases} \qquad \begin{cases} \boldsymbol{e}_X = \boldsymbol{e}_r \cos\theta - \boldsymbol{e}_\theta \sin\theta, \\ \boldsymbol{e}_Y = \boldsymbol{e}_r \sin\theta + \boldsymbol{e}_\theta \cos\theta. \end{cases} \tag{D.13}$$

$$\begin{cases} v_r \triangleq -v = \quad v_X \cos\theta + v_Y \sin\theta, \\ v_\theta \triangleq \quad u = -v_X \sin\theta + v_Y \cos\theta, \\ v_z \triangleq \quad w, \end{cases} \qquad \begin{cases} v_X = -u\sin\theta - v\cos\theta, \\ v_Y = \quad u\cos\theta - v\sin\theta, \\ v_z = \quad w. \end{cases} \tag{D.14}$$

where $\boldsymbol{v} = v_X\,\boldsymbol{e}_X + v_Y\,\boldsymbol{e}_Y + v_z\,\boldsymbol{e}_z = v_r\,\boldsymbol{e}_r + v_\theta\,\boldsymbol{e}_\theta + v_z\,\boldsymbol{e}_z = u\,\boldsymbol{e}_x + v\,\boldsymbol{e}_y + w\,\boldsymbol{e}_z$.

D.2.2 Boundary conditions

Outer cylinder

▷ *Cartesian coordinates* :

- Slipping: $\boldsymbol{v}\cdot\boldsymbol{n} = 0 \iff v_X\cos\theta + v_Y\sin\theta = 0.$
- Adhesion: $\boldsymbol{v} - (\boldsymbol{v}\cdot\boldsymbol{n})\boldsymbol{n} = 0 \iff \begin{cases} v_X\sin\theta - v_Y\cos\theta = 0, \\ v_Y\cos\theta - v_X\sin\theta = 0, \\ v_Z = 0. \end{cases}$ (D.15)

▷ *Local coordinates* :

- Slipping: $v = 0.$
- Adhesion: $u = 0, \quad w = 0.$ (D.16)

Inner cylinder Equation: $F_\mathrm{i}(X, Y, t) = (X-a)^2 + Y^2 - R_\mathrm{i}^2 = 0.$

▷ *Cartesian coordinates* :

- Slipping:
$$\frac{\partial F_\mathrm{i}}{\partial t} + \boldsymbol{\nabla} F_\mathrm{i}\cdot\boldsymbol{v} = 0 \iff (v_X - \dot{a})\cos\theta_\mathrm{i} + v_Y\sin\theta_\mathrm{i} = 0.$$
- Adhesion:
$$\boldsymbol{v} - (\boldsymbol{v}\cdot\boldsymbol{n})\boldsymbol{n} = \boldsymbol{v}_Q - (\boldsymbol{v}_Q\cdot\boldsymbol{n})\boldsymbol{n} \iff \begin{cases} (v_X-\dot{a})\sin\theta_\mathrm{i} - v_Y\cos\theta_\mathrm{i} = 0, \\ v_Y\cos\theta_\mathrm{i} - (v_X-\dot{a})\sin\theta_\mathrm{i} = 0, \\ v_Z = 0. \end{cases}$$ (D.17)

▷ *Local coordinates* :

- Slipping: $v\,\cos(\theta_\mathrm{i}-\theta) - u\,\sin(\theta_\mathrm{i}-\theta) = -\dot{a}\,\cos\theta_\mathrm{i}.$
- Adhesion: $u\,\cos(\theta_\mathrm{i}-\theta) + v\,\sin(\theta_\mathrm{i}-\theta) = -\dot{a}\,\sin\theta_\mathrm{i}, \quad w = 0.$ (D.18)

Regroupe the two last conditions, it will become a simple results as:

$$u = -\dot{a}\sin\theta \quad \text{et} \quad v = -\dot{a}\cos\theta. \tag{D.19}$$

Extreme sections

$$z = 0 \quad \text{et} \quad z = H, \qquad p = p_\mathrm{a}. \tag{D.20}$$

D.2.3 Scaling

D.2.3.1 Independent variables

- cartesian coordinates : $X \triangleq R_e \bar{X}$, $Y \triangleq R_e \bar{Y}$, $z \triangleq H \bar{z}$,
- cylindrical coordinates : $\theta = \theta$, $r \triangleq R_e \bar{r}$, $z = H \bar{z}$, (D.21)
- local coordinates : $x \triangleq R_e \bar{x}$, $y \triangleq b \bar{y}$, $z = H \bar{z}$.

$$t \triangleq \omega^{-1} \bar{t}. \tag{D.22}$$

$$\theta = \bar{x} \quad \text{et} \quad \bar{r} = 1 - \varepsilon \bar{y}. \tag{D.23}$$

$$a \triangleq \alpha \varepsilon R_e \bar{a}, \quad R_i \triangleq (1-\varepsilon) R_e \qquad \text{où} \quad \eta = R_e/H, \quad \alpha \triangleq a_0/b, \quad \text{et} \quad \varepsilon = b/R_e. \tag{D.24}$$

D.2.4 Velocity and pressure

For velocity:

$$u \triangleq U \bar{u}, \quad v \triangleq V \bar{v} \quad \text{et} \quad w \triangleq W \bar{w}. \tag{D.25}$$

For pressure:

$$p \triangleq p_a + (\delta p) \bar{p}, \tag{D.26}$$

where p_a is a reference pressure.

D.2.5 Non-dimensionalised formulation

D.2.5.1 Mass conservation

$$\frac{1}{\varepsilon}\frac{V}{U}\frac{1}{1-\varepsilon\bar{y}}\frac{\partial}{\partial \bar{y}}[(1-\varepsilon\bar{y})\bar{v}] + \frac{1}{1-\varepsilon\bar{y}}\frac{\partial \bar{u}}{\partial \bar{x}} + \eta\frac{W}{U}\frac{\partial \bar{w}}{\partial \bar{z}} = 0. \tag{D.27}$$

The degeneracy of the balance impose the definitions following:

$$V \triangleq \varepsilon U \quad \text{et} \quad W \triangleq U/\eta. \tag{D.28}$$

D.2.5.2 Momentum conservation

$$
\begin{cases}
\mathsf{St}\dfrac{\partial \bar{u}}{\partial \bar{t}} + \bar{v}\dfrac{\partial \bar{u}}{\partial \bar{y}} + \dfrac{1}{1-\varepsilon\bar{y}}\bar{u}\dfrac{\partial \bar{u}}{\partial \bar{x}} - \dfrac{\varepsilon\,\bar{u}\bar{v}}{1-\varepsilon\bar{y}} + \bar{w}\dfrac{\partial \bar{u}}{\partial \bar{z}} = -\dfrac{1}{1-\varepsilon\bar{y}}\dfrac{(\delta p)}{\rho U^2}\dfrac{\partial \bar{p}}{\partial \bar{x}} \\
\quad + \dfrac{1}{\varepsilon^2\mathsf{Re}}\left(\dfrac{\partial}{\partial \bar{y}}\left\{\dfrac{1}{1-\varepsilon\bar{y}}\dfrac{\partial}{\partial \bar{y}}[(1-\varepsilon\bar{y})\bar{u}]\right\}\right. \\
\qquad\qquad \left. + \dfrac{\varepsilon^2}{(1-\varepsilon\bar{y})^2}\dfrac{\partial^2 \bar{u}}{\partial \bar{x}^2} - \dfrac{2\varepsilon^3}{(1-\varepsilon\bar{y})^2}\dfrac{\partial \bar{v}}{\partial \bar{x}} + \varepsilon^2\eta^2\dfrac{\partial^2 u}{\partial z^2}\right), \\
\mathsf{St}\dfrac{\partial \bar{v}}{\partial \bar{t}} + \bar{v}\dfrac{\partial \bar{v}}{\partial \bar{y}} + \dfrac{1}{1-\varepsilon\bar{y}}\bar{u}\dfrac{\partial \bar{v}}{\partial \bar{x}} + \dfrac{1}{\varepsilon}\dfrac{\bar{u}^2}{1-\varepsilon\bar{y}} + \bar{w}\dfrac{\partial \bar{v}}{\partial \bar{z}} = -\dfrac{1}{\varepsilon^2}\dfrac{(\delta p)}{\rho U^2}\dfrac{\partial \bar{p}}{\partial \bar{y}} \\
\quad + \dfrac{1}{\varepsilon^2\mathsf{Re}}\left(\dfrac{\partial}{\partial \bar{y}}\left\{\dfrac{1}{1-\varepsilon\bar{y}}\dfrac{\partial}{\partial \bar{y}}[(1-\varepsilon\bar{y})\bar{v}]\right\}\right. \\
\qquad\qquad \left. + \dfrac{\varepsilon^2}{(1-\varepsilon\bar{y})^2}\dfrac{\partial^2 \bar{v}}{\partial \bar{x}^2} + \dfrac{2\varepsilon}{(1-\varepsilon\bar{y})^2}\dfrac{\partial \bar{u}}{\partial \bar{x}} + \varepsilon^2\eta^2\dfrac{\partial^2 \bar{v}}{\partial \bar{z}^2}\right), \\
\mathsf{St}\dfrac{\partial \bar{w}}{\partial \bar{t}} + \bar{v}\dfrac{\partial \bar{w}}{\partial \bar{y}} + \dfrac{1}{1-\varepsilon\bar{y}}\bar{u}\dfrac{\partial \bar{w}}{\partial \bar{x}} + \bar{w}\dfrac{\partial \bar{w}}{\partial \bar{z}} \\
\quad = -\eta^2\dfrac{(\delta p)}{\rho U^2}\dfrac{\partial \bar{p}}{\partial \bar{z}} + \dfrac{1}{\varepsilon^2\mathsf{Re}}\left\{\dfrac{1}{1-\varepsilon\bar{y}}\dfrac{\partial}{\partial \bar{y}}\left[(1-\varepsilon\bar{y})\dfrac{\partial \bar{w}}{\partial \bar{y}}\right] + \dfrac{\varepsilon^2}{(1-\varepsilon\bar{y})^2}\dfrac{\partial^2 \bar{w}}{\partial \bar{x}^2} + \varepsilon^2\eta^2\dfrac{\partial^2 \bar{w}}{\partial \bar{z}^2}\right\},
\end{cases}
\tag{D.29}
$$

where:

$$
\begin{aligned}
\mathsf{Re} &\triangleq UR_e/\nu = \varepsilon^{-1}Ub/\nu \quad &&: \text{REYNOLDS number,} \\
\mathsf{St} &\triangleq \omega R_e/U = \varepsilon^{-1}\omega b/U \quad &&: \text{STROUHAL number.}
\end{aligned}
\tag{D.30}
$$

D.2.5.3 Boundary conditions

$$
(1-\varepsilon)\cos\theta_i = \cos\theta\sqrt{1-2\varepsilon+\varepsilon^2(1-\alpha^2\bar{a}^2\sin^2\theta)} - \varepsilon\,\alpha\bar{a}\,\sin^2\theta. \tag{D.31}
$$

Outer cylinder $\bar{y} = 0$. See Eq. D.16.

$$
\begin{aligned}
&\circ \text{ Slipping:} \quad && \bar{v} = 0, \\
&\circ \text{ Adhesion:} \quad && \bar{u} = 0, \quad \bar{w} = 0.
\end{aligned}
\tag{D.32}
$$

Outer cylinder $\varepsilon\bar{y}_i = 1 - \sqrt{1-2\varepsilon+\varepsilon^2(1-\alpha^2\bar{a}^2\sin^2\theta)} - \varepsilon\,\alpha\bar{a}\,\cos\theta$. See Eq. D.18.

$$
\begin{aligned}
&\circ \text{ Slipping:} && \varepsilon\,\bar{v}\cos(\theta_i-\theta) - \bar{u}\sin(\theta_i-\theta) = -\varepsilon\mathsf{St}\,\alpha\dot{\bar{a}}\cos\theta_i. \\
&\circ \text{ Adhesion:} && \begin{cases} \bar{u}\cos(\theta_i-\theta) + \varepsilon\,\bar{v}\sin(\theta_i-\theta) = -\varepsilon\mathsf{St}\,\alpha\dot{\bar{a}}\sin\theta_i, \\ \bar{w} = 0. \end{cases}
\end{aligned}
\tag{D.33}
$$

Extreme sections

$$
\bar{z} = 0 \quad \text{and} \quad \bar{z} = 1, \qquad \bar{p} = 0. \tag{D.34}
$$

Periodicity

$$
\forall \bar{x} \in [0,\, 2\pi], \quad f(\bar{x},\bar{y},\bar{z},\bar{t}) \equiv f(\bar{x}+2\pi,\bar{y},\bar{z},\bar{t}), \tag{D.35}
$$

D.2.5.4 Geometrical developments

Some quantities are purely geometric and can be developed independently of the flow dynamics. This is the case with θ_i. Its expression involves the confinement parameter, $\varepsilon = b/R_\mathrm{e} \ll 1$, and the parameter of amplitude, $\alpha = a_0/b \leq 1$:

$$\begin{cases} \cos\theta_\mathrm{i} = \cos\bar{x} - \varepsilon\,\alpha\bar{a}\sin^2\bar{x} - \varepsilon^2\alpha\bar{a}(1+\tfrac{1}{2}\alpha\bar{a}\cos\bar{x})\sin^2\bar{x} + O\left\{\varepsilon^3\right\} \\ \theta_\mathrm{i} = \bar{x} + \varepsilon(1+\varepsilon)\,\alpha\bar{a}\sin\bar{x} + O\left\{\varepsilon^3\right\}. \end{cases} \tag{D.36}$$

We can develop the equation for inner cylinder in local variables with the same manner:

$$\bar{y}_\mathrm{i} = 1 - \alpha\bar{a}\cos\bar{x} + \tfrac{1}{2}\varepsilon(1+\varepsilon)\,\alpha^2\bar{a}^2\sin^2\bar{x} + O\left\{\varepsilon^3\right\}. \tag{D.37}$$

D.3 Perfect fluid

D.3.1 Statement of problem

D.3.1.1 Equations

$$\frac{\partial\bar{u}}{\partial\bar{x}} + \frac{\partial}{\partial\bar{y}}[(1-\varepsilon\,\bar{y})\,\bar{v}] + (1-\varepsilon\,\bar{y})\frac{\partial\bar{w}}{\partial\bar{z}} = 0. \tag{D.38}$$

$$\begin{aligned} (1-\varepsilon\,\bar{y})\Big(\mathsf{St}\,\frac{\partial\bar{u}}{\partial\bar{t}} + \bar{v}\frac{\partial\bar{u}}{\partial\bar{y}} + \bar{w}\frac{\partial\bar{u}}{\partial\bar{z}}\Big) + \bar{u}\frac{\partial\bar{u}}{\partial\bar{x}} - \varepsilon\,\bar{u}\bar{v} &= -\frac{(\delta p)}{\rho U^2}\frac{\partial\bar{p}}{\partial\bar{x}}, \\ (1-\varepsilon\,\bar{y})\Big(\mathsf{St}\,\frac{\partial\bar{v}}{\partial\bar{t}} + \bar{v}\frac{\partial\bar{v}}{\partial\bar{y}} + \bar{w}\frac{\partial\bar{v}}{\partial\bar{z}}\Big) + \bar{u}\frac{\partial\bar{v}}{\partial\bar{x}} + \frac{\bar{u}^2}{\varepsilon} &= -\frac{1-\varepsilon\,\bar{y}}{\varepsilon^2}\frac{(\delta p)}{\rho U^2}\frac{\partial\bar{p}}{\partial\bar{y}}, \\ (1-\varepsilon\,\bar{y})\Big(\mathsf{St}\,\frac{\partial\bar{w}}{\partial\bar{t}} + \bar{v}\frac{\partial\bar{w}}{\partial\bar{y}} + \bar{w}\frac{\partial\bar{w}}{\partial\bar{z}}\Big) + \bar{u}\frac{\partial\bar{w}}{\partial\bar{x}} &= -\eta^2(1-\varepsilon\,\bar{y})\frac{(\delta p)}{\rho U^2}\frac{\partial\bar{p}}{\partial\bar{z}}. \end{aligned} \tag{D.39}$$

The conditions on wall limited with slipping, see Eq. D.32$_1$ and Eq. D.33$_1$; on the extreme sections, see Eq. D.34.

D.3.1.2 Slipping condition

Big amplitude $\alpha \sim 1$

$$\begin{aligned} \bar{v}_\mathrm{i} + \tfrac{1}{2}\varepsilon\,\alpha^2\bar{a}^2\left(\frac{\partial\bar{v}}{\partial\bar{y}}\right)_\mathrm{i}\sin^2\bar{x} = (1+\varepsilon)\,\alpha\bar{a}\,\bar{u}_\mathrm{i}\sin\bar{x} + \tfrac{1}{2}\varepsilon\,\alpha^3\bar{a}^3\left(\frac{\partial\bar{u}}{\partial\bar{y}}\right)_\mathrm{i}\sin^3\bar{x} \\ - \mathsf{St}\,\alpha\dot{\bar{a}}(\cos\bar{x} - \varepsilon\,\alpha\bar{a}\,\sin^2\bar{x}) + O\left\{\varepsilon^2\right\}. \end{aligned} \tag{D.40}$$

To equilibrate the first and the last term of Eq. D.40 :

$$\mathsf{St} = 1/\alpha \geq 1. \tag{D.41}$$

Small amplitude $\alpha \ll 1$

$$\bar{v}_\mathrm{i} - \alpha\bar{a}\cos\bar{x}\left(\frac{\partial\bar{v}}{\partial\bar{y}}\right)_\mathrm{i} = (1+\varepsilon)\,\alpha\bar{a}\,\bar{u}_\mathrm{i}\sin\bar{x} - \dot{\bar{a}}(\cos\bar{x} - \varepsilon\,\alpha\bar{a}\,\sin^2\bar{x}) + O\left\{\alpha^2\right\}. \tag{D.42}$$

D.3.1.3 Scaling of pressure

$$u = U\,\bar{u}, \quad v = \varepsilon U\,\bar{v} \quad \text{and} \quad (\delta p)/(\rho U^2) = p_{\mathrm{a}} + \mathsf{St}\,\bar{p}.$$
$$\begin{cases} \bar{u}(\bar{x},\,\bar{y},\,\bar{z},\,\bar{t}) \triangleq \bar{u}^{(0)}(\bar{x},\,\bar{y},\,\bar{t}) & +\varphi_1(\varepsilon,\eta)\bar{u}^{(1)}(\bar{x},\,\bar{y},\,\bar{z},\,\bar{t}) + \dots \\ \bar{v}(\bar{x},\,\bar{y},\,\bar{z},\,\bar{t}) \triangleq \bar{v}^{(0)}(\bar{x},\,\bar{y},\,\bar{t}) & +\psi_1(\varepsilon,\eta)\bar{v}^{(1)}(\bar{x},\,\bar{y},\,\bar{z},\,\bar{t}) + \dots \\ \bar{w}(\bar{x},\,\bar{y},\,\bar{z},\,\bar{t}) \triangleq & \zeta_1(\varepsilon,\eta)\bar{w}^{(1)}(\bar{x},\,\bar{y},\,\bar{z},\,\bar{t}) + \dots \\ \bar{p}(\bar{x},\,\bar{y},\,\bar{z},\,\bar{t}) \triangleq \bar{p}^{(0)}(\bar{x},\,\bar{t}) & +\varpi_1(\varepsilon,\eta)\,\bar{p}^{(1)}(\bar{x},\,\bar{y},\,\bar{z},\,\bar{t}) + \dots \end{cases} \tag{D.43}$$

D.3.2 External scaling, first approximation

This scaling covers the entire assembly. It is expected to observe the approximation of the tangent plane in the radial direction and a singularity at each end.

D.3.2.0.1 Big amplitude, $\alpha \sim 1$

The upper indices for the first approximation are not reproduced. We have:

$$\alpha\,\mathsf{St} = 1 \quad \text{et} \quad \alpha\,(\delta p)/(\rho U^2) = 1, \tag{D.44}$$

and it will become as following in first approximation:

$$\frac{\partial \bar{u}}{\partial \bar{x}} + \frac{\partial \bar{v}}{\partial \bar{y}} = 0, \quad \frac{\partial \bar{u}}{\partial \bar{t}} + \alpha\Big(\bar{u}\frac{\partial \bar{u}}{\partial \bar{x}} + \bar{v}\frac{\partial \bar{u}}{\partial \bar{y}}\Big) = -\frac{\partial \bar{p}}{\partial \bar{x}} \quad \text{et} \quad 0 = -\frac{\partial \bar{p}}{\partial \bar{y}}. \tag{D.45}$$

These equations are accompanied by a slipping condition on each cylinder:

$$\begin{array}{ll} \bar{y} = 0, & \bar{v} = 0. \\ \bar{y} = \bar{y}_{\mathrm{i}} \triangleq 1 - \alpha\,\bar{a}\cos\bar{x}, & \bar{v} = \alpha\bar{a}\,\bar{u}\sin\bar{x} - \dot{\bar{a}}\cos\bar{x}. \qquad [\text{condition Eq.}D.40] \end{array} \tag{D.46}$$

The singular character of this approximation comes from the impossibility of connecting the variable pressure $\bar{p}(\bar{x},\,\bar{t})$ to the pressures imposed on the extremities, since by definition $\bar{p}^{(0)}$ is independent of $\bar{z}$. The dependence of the pressure on the $\bar{z}$ coordinate can only arise from the higher orders and the connection with the extreme regions.

D.3.2.1 Small amplitude, $\alpha \ll 1$

By derivation of Eq. D.45$_2$ and Eq. D.45$_1$, it will become in following form when integrate from $\bar{y} = 0$ to $\bar{y} = 1$:

$$\frac{\partial^2 \bar{p}}{\partial \bar{x}^2} = -\ddot{\bar{a}}\cos\bar{x} \quad \Longrightarrow \quad \bar{p}(\bar{x},\bar{t}) = \ddot{\bar{a}}\cos\bar{x} + C(\bar{t}), \tag{D.47}$$

where $C(\bar{t})$ is a constant of integration, periodic function of time, uniform in the space, which is not corresponded to the phsysics.

$$\bar{u}^{(0)}(\bar{x},\bar{y},\bar{t}) = \dot{\bar{a}}\sin\bar{x}, \quad \bar{v}^{(0)}(\bar{x},\bar{y},\bar{t}) = -\dot{\bar{a}}\bar{y}\cos\bar{x} \quad \text{et} \quad \bar{p}^{(0)}(\bar{x},\bar{t}) = \ddot{\bar{a}}\cos\bar{x}. \tag{D.48}$$

The azimuthal component of velocity and pressure are independent of $\bar{y}$ while the radio component is a linear function.

D.3.3 Internal scaling

The pressure is imposed and constant at $z = 0$ and $z = H$. It cannot be corresponded to the value generated by the oscillations of the inner cylinders. It is therefore necessary to establish an approximation adapted to the edge effects.

D.3.3.1 First approximation

Scales In the vicinity of edges, $z = z_0$ where $z_0 = 0$ or H. We can define $\tilde{z}$:

$$\bar{z} \stackrel{\triangle}{=} \bar{z}_0 + \lambda\,\tilde{z} \quad \text{où} \quad \bar{z}_0 \stackrel{\triangle}{=} z_0/H \quad \text{et} \quad \lambda \stackrel{\triangle}{=} h/H \ll 1. \tag{D.49}$$

The scale h is that we can searching for in the internal domain. The scales of u, v and p will be the same as in external scaling. Moreover, the component w in first approximation should also be nondimensionalised:

$$w \stackrel{\triangle}{=} W_h\,\widetilde{w}.$$

Equations The mass conservation Eq. D.38 is:

$$\frac{\partial\tilde{u}}{\partial\bar{x}} + \frac{\partial}{\partial\bar{y}}[(1-\varepsilon\,\bar{y})\,\tilde{v}] + \frac{\eta}{\lambda}\frac{W_h}{U}\,(1-\varepsilon\,\bar{y})\frac{\partial\widetilde{w}}{\partial\tilde{z}} = 0.$$

Therefore we can deduct:

$$W_h \stackrel{\triangle}{=} (\lambda/\eta)\,U = (h/R_\mathrm{e})\,U.$$

The scale of w takes a value bigger than that given by the definition Eq. $D.28_2$.

The movement conservation Eq. D.39 will be:

$$\begin{aligned}
(1-\varepsilon\,\bar{y})\Big(\mathsf{St}\,\frac{\partial\tilde{u}}{\partial\bar{t}} + \tilde{v}\frac{\partial\tilde{u}}{\partial\bar{y}} + \widetilde{w}\frac{\partial\tilde{u}}{\partial\tilde{z}}\Big) + \tilde{u}\frac{\partial\tilde{u}}{\partial\bar{x}} - \varepsilon\,\tilde{u}\tilde{v} &= -\frac{(\delta p)}{\rho U^2}\,\frac{\partial\tilde{p}}{\partial\bar{x}},\\
(1-\varepsilon\,\bar{y})\Big(\mathsf{St}\,\frac{\partial\tilde{v}}{\partial\bar{t}} + \tilde{v}\frac{\partial\tilde{v}}{\partial\bar{y}} + \widetilde{w}\frac{\partial\tilde{v}}{\partial\tilde{z}}\Big) + \tilde{u}\frac{\partial\tilde{v}}{\partial\bar{x}} + \frac{\tilde{u}^2}{\varepsilon} &= -\frac{1-\varepsilon\,\bar{y}}{\varepsilon^2}\,\frac{(\delta p)}{\rho U^2}\,\frac{\partial\tilde{p}}{\partial\bar{y}},\\
(1-\varepsilon\,\bar{y})\Big(\mathsf{St}\,\frac{\partial\widetilde{w}}{\partial\bar{t}} + \tilde{v}\frac{\partial\widetilde{w}}{\partial\bar{y}} + \widetilde{w}\frac{\partial\widetilde{w}}{\partial\tilde{z}}\Big) + \tilde{u}\frac{\partial\widetilde{w}}{\partial\bar{x}} &= -\frac{\eta^2}{\lambda^2}(1-\varepsilon\,\bar{y})\frac{(\delta p)}{\rho U^2}\,\frac{\partial\tilde{p}}{\partial\tilde{z}}.
\end{aligned}$$

where $(\delta p)/(\rho U^2) = \mathsf{St} = 1/\alpha \geq 1$.

Boundary conditions The boundary conditions are not affected. However, it is necessary to add the corresponding condition to external solution.

$$\underset{\tilde{z}\to\pm\infty,}{\text{dév}}\,\{\tilde{u},\,\tilde{v},\,\widetilde{w},\,\tilde{p}\} \simeq \underset{\bar{z}\to 0|1,}{\text{dév}}\,\{\bar{u},\,\bar{v},\,0,\,\bar{p}\}.$$

Large amplitude

• *Equations* :

$$\begin{aligned}
&\frac{\partial \tilde{u}}{\partial \bar{x}} + \frac{\partial \tilde{v}}{\partial \bar{y}} + \frac{\partial \widetilde{w}}{\partial \tilde{z}} = 0.\\
&\frac{\partial \tilde{u}}{\partial \bar{t}} + \alpha\Big(\tilde{u}\frac{\partial \tilde{u}}{\partial \bar{x}} + \tilde{v}\frac{\partial \tilde{u}}{\partial \bar{y}} + \widetilde{w}\frac{\partial \tilde{u}}{\partial \tilde{z}}\Big) = -\frac{\partial \tilde{p}}{\partial \bar{x}},\\
&0 = -\frac{\partial \tilde{p}}{\partial \bar{y}},\\
&\frac{\partial \widetilde{w}}{\partial \bar{t}} + \alpha\Big(\tilde{u}\frac{\partial \widetilde{w}}{\partial \bar{x}} + \tilde{v}\frac{\partial \widetilde{w}}{\partial \bar{y}} + \widetilde{w}\frac{\partial \widetilde{w}}{\partial \tilde{z}}\Big) = -\frac{\partial \tilde{p}}{\partial \tilde{z}}.
\end{aligned}$$

• *Boundary conditions* :

$$\begin{aligned}
&\bar{y} = 0, && \tilde{v} = 0,\\
&\bar{y} = 1 - \alpha\bar{a}\,\cos\bar{x}, && \tilde{v} = \alpha\bar{a}\,\tilde{u}\sin\bar{x} - \dot{\bar{a}}\cos\bar{x},\\
&\tilde{z} = 0|1, && \tilde{p} = 0,\\
&\underset{\tilde{z}\to\pm\infty}{\text{dév}}\,\{\tilde{u},\,\tilde{v},\,\widetilde{w},\,\tilde{p}\} \equiv \underset{\tilde{z}\to 0|1}{\text{dév}}\,\{\bar{u},\,\bar{v},\,0,\,\bar{p}\}.
\end{aligned}$$

Small amplitude

$$\frac{\partial \tilde{u}}{\partial \bar{x}} + \frac{\partial \tilde{v}}{\partial \bar{y}} + \frac{\partial \widetilde{w}}{\partial \tilde{z}} = 0. \tag{D.50}$$

$$\frac{\partial \tilde{u}}{\partial \bar{t}} = -\frac{\partial \tilde{p}}{\partial \bar{x}}, \quad 0 = -\frac{\partial \tilde{p}}{\partial \bar{y}}, \quad \frac{\partial \widetilde{w}}{\partial \bar{t}} = -\frac{\partial \tilde{p}}{\partial \tilde{z}}. \tag{D.51}$$

$$\begin{aligned}
&\bar{y} = 0, && \tilde{v} = 0,\\
&\bar{y} = 1, && \tilde{v} = -\dot{\bar{a}}\cos\bar{x},\\
&\tilde{z} = 0|1, && \tilde{p} = 0,\\
&\underset{\tilde{z}\to\pm\infty}{\text{dév}}\,\{\tilde{u},\,\tilde{v},\,\widetilde{w},\,\tilde{p}\} \equiv \underset{\tilde{z}\to 0|1}{\text{dév}}\,\{\bar{u},\,\bar{v},\,0,\,\bar{p}\}.
\end{aligned} \tag{D.52}$$

The external approximation is singular at $\bar{z} = 0$ or $\bar{z} = 1$. For easier understanding, we will focus in the region $\bar{z} = 0$. The combination of Eq. D.51 and Eq. D.50 with integration will conduct to the equation of pressure:

$$\Delta_{\|}\tilde{p} = -\ddot{\bar{a}}\cos\bar{x} \quad \text{where} \quad \Delta_{\|} \equiv \partial^2/\partial\bar{x}^2 + \partial^2/\partial\tilde{z}^2.$$

This problem dispose a particular evident solution:

$$\tilde{p}^{(0)} = \ddot{\bar{a}}(1 - \mathrm{e}^{-\tilde{z}})\cos\bar{x}. \tag{D.53}$$

Therefore we can deduct:

$$\begin{cases}
\tilde{u}^{(0)}(\bar{x},\bar{y},\tilde{z},\bar{t}) = \quad \dot{\bar{a}}(1 - \mathrm{e}^{-\tilde{z}})\sin\bar{x},\\
\tilde{v}^{(0)}(\bar{x},\bar{y},\tilde{z},\bar{t}) = -\dot{\bar{a}}\bar{y}\cos\bar{x},\\
\widetilde{w}^{(0)}(\bar{x},\bar{y},\tilde{z},\bar{t}) = -\dot{\bar{a}}\,\mathrm{e}^{-\tilde{z}}\cos\bar{x},
\end{cases} \tag{D.54}$$

Here the elimination of integration constant results from the coupling condition and periodicity. The ejection-aspiration of fluid happens at $\bar{x} = 0$ and $\bar{x} = \pi$ as we expected. The radial component is not changed, the correction of pressure comes from the modification of

axial and azimuthal components. There is a exponentially decrease of the axial component, which confirms that this component plays only an extremely weak role on the external scale. We also verify that the constant $C(t)$ of the expression Eq. D.47$_2$ is null.

D.4 Conclusions

Recirculation flow with cylindrical geometry has been discussed in translation scenario. In PISE-1A experiments, as can be observed both in the experiments and numerical simulation, recirculation flow from the top and bottom won't play an important role in dynamic behaviour of the system.

Appendix E

Analytical and Numerical Analysis on Two-dimensional Fluid Channel Model with Oscillating Wall and Continuous Injection

In this chapter, the problem scenario with a simplified two-dimensional channel of incompressible viscous fluid with continuous injection and oscillating plate modelled by Navier-Stokes will be presented for better understanding the dynamic behaviour with continuous injection and better characterisation of the dissipation involved in this scenario.

A decomposed non-dimensionlisation system at second order will be introduced for establishment of asymptotic analysis. Thin-layer approximation will be applied to all the orders of the analysis. For reference solution and perturbation, local analysis will be established for mass conservation and momentum conservation while global kinetic theorem will be discussed with asymptotic analysis.

Moreover, corresponding numerical simulation with 2D Navier-Stokes model implemented in Cast3M will be presented.

E.1 Phenomenological analysis

E.1.1 Two-dimensional geometry and basic conditions

The horizontal hexagonal ring type cross-section of the fluid domain surrounding the assembly is spreaded into a two-dimensional fluid channel, shown as FIGURE E.1.

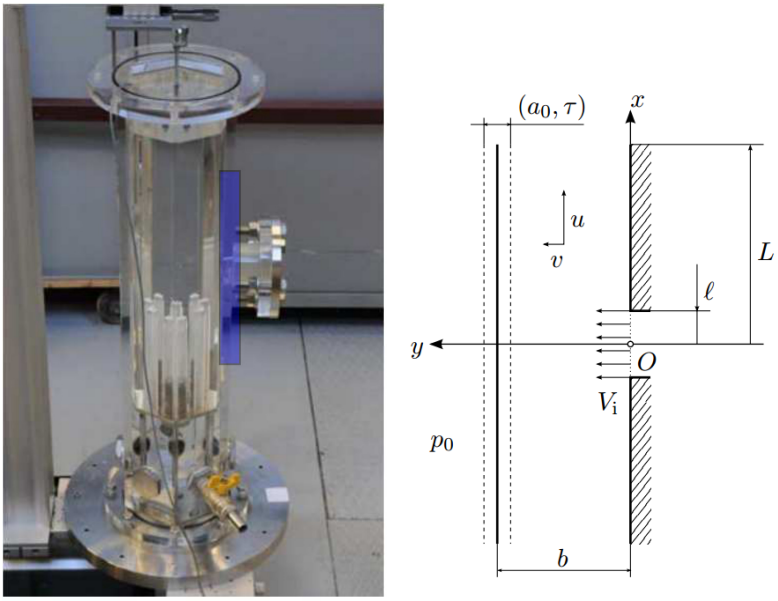

FIGURE E.1: Plan of the 2-D fluid field

In this problem, an incompressible viscous fluid with a density ρ and viscosity ν will be considered in the fluid domain as shown in FIGURE E.1. As can be seen in the figure, the fluid domain is limited by a non-moving wall and an oscillating plate with a half-height of L. The inlet is located in the center of the wall with a half-height of ℓ.
According to the coordinate in FIGURE E.1, the position of the oscillating plate can be described as:

$$y_p(t) = b + a(t) \tag{E.1}$$

where, $a(t)$ is a sin function to the time with an amplitude of a_0 and a period of τ. This function is imposed by the case. For better characterization of the oscillating amplitude, a non-dimensional parameter α can be defined as:

$$\alpha = a_0/b \tag{E.2}$$

The fluid injected through the inlet is characterized by a constant plain velocity profile along the inlet with the velocity $V_i\mathbf{e_y}$.

In this report, for convenience, an aspect ratio $\epsilon = b/L$ is introduced. Another non-dimensional geometry ratio η is defined as $\eta = \ell/L$, here $\eta \sim \epsilon$, can also be expressed as $\eta = \eta_*\epsilon,\ \eta_* \sim 1$.

It is assumed that both η and ϵ are small comparing to the unity, therefore the influence of the settlement area is limited in the vicinity of the inlet so that the flow will be almost one-dimensional in the region away from the inlet. The analytical model here will only discuss the area when the flow is nearly one-dimensional while the numerical model will treat the whole fluid domain. The fluid domain treated by analytical analysis will be demonstrated as the shaded area in FIGURE E.2, while that treated by numerical analysis is the whole domain with the light blue background.

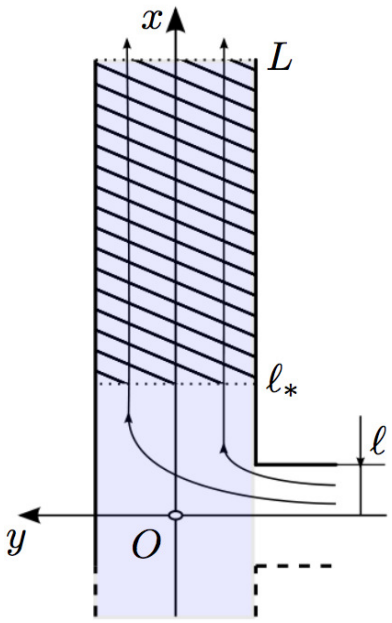

FIGURE E.2: Fluid domain solved by analytical analysis

The flow field is symmetrical along the plane $x = 0$.

The velocity field $v = u(x, y, t)\mathbf{e_x} + v(x, y, t)\mathbf{e_y}$ must meet the non-penetration condition along the two walls, as:

$$\ell \leqslant |x| \leqslant L, v(x, 0, t) = 0 \;\&\; |x| \leqslant L, v[x, b + a(t), t] = da/dt \tag{E.3}$$

Finally, the fluid flow is immersed into an atmosphere where there is an uniform and constant pressure p_0. The gravity pressure is not considered in this issue. Note here, the weight of plate does not affect due to imposed motion. The pressure can be defined with static pressure and gravity:

$$p_g = p_{st} + \rho g y. \tag{E.4}$$

E.1.2 Dimensioned equations

Mass conservation:

$$\frac{\partial u}{\partial x} + \frac{\partial v}{\partial y} = 0. \tag{E.5}$$

Momentum conservation:

$$\frac{\partial u}{\partial t} + u\frac{\partial u}{\partial x} + v\frac{\partial u}{\partial y} = -\frac{1}{\rho}\frac{\partial p}{\partial x} + \nu\left(\frac{\partial^2 u}{\partial x^2} + \frac{\partial^2 u}{\partial y^2}\right); \tag{E.6a}$$

$$\frac{\partial v}{\partial t} + u\frac{\partial v}{\partial x} + v\frac{\partial v}{\partial y} = -\frac{1}{\rho}\frac{\partial p}{\partial y} + \nu\left(\frac{\partial^2 v}{\partial x^2} + \frac{\partial^2 v}{\partial y^2}\right). \tag{E.6b}$$

Boundary conditions:

$$y = 0, \begin{cases} |x| \leqslant \ell \;:\; u = 0,\; v = V_i; \\ \ell \leqslant |x| \leqslant L \;:\; u = 0,\; v = 0. \end{cases} \tag{E.7}$$

$$y = b + a(t), |x| \leqslant L \ : u = 0, \ v = \dot{a}. \tag{E.8}$$

$$x = \pm L, 0 \leqslant y \leqslant b \ : \ p = p_0. \tag{E.9}$$

Note that this condition is arbitrary, the condition at the outlet is not known exactly. It results from the quasi one-dimensional nature of the flow field. When thin-layer approximation is applied, this condition will not be important any more. The elliptic equations will become parabolic. Therefore, the solution on x direction only depends on the condition upstream without the affect from the outlet condition. Although the non-slip condition may impose discussion of boundary layer, the asymptotic analysis will only be taken for the main flow not on boundary layer.

E.1.3 Decomposition

This problem is treated as a perturbation problem. The prior definition of a reference solution is required for the conventional approach. Then a small-amplitude perturbation term should be superimposed so as to linearize the inertial convective force.

Since the reference solution is obtained at the position $a(t) = 0$, the pressure of the reference solution $p_s(x, y)$ will be a steady solution, can be written as:

$$p(x, y, t) = p_s(x, y) + p'(x, y, t); \tag{E.10}$$

Here, the terms with subscription 's' are the variables of the reference solutions and the terms with prime are the variables of the perturbations.

Note that, the definition domain of y for $p_s(x, y)$ and $p'(x, y, t)$ are different. However, with the small perturbation hypothesis ($\alpha = a_0/b \ll 1$), the changing domain can be approximately transformed into domain without displacement, therefore the varying definition domains $p'(x, y, t)$ can be projected on the fixed domain of $p'(x, y, t)$. This effect will also affect the linearization of the momentum equations.

As a result, we will see two kinds of effects:

- Displacement effect (α): result from the fact that the boundary conditions at time t is not exactly written on the real border and lead to the transfer of the boundary conditions;
- Movement effect (αSt): result from the movement of the wall and the perturbation of the reference solution and lead to the linearization of the equations.

E.1.4 Scaling

The non-dimensional of the variables can be written as following Eq. E.11:

$$\begin{cases} x = L\bar{x}; y = b\bar{y}; t = \tau\bar{t}; a = a_0\tilde{a}; \\ u = u + u' = U\,\hat{u} = U(\bar{u} + \varphi_1\,\tilde{u}_1 + \varphi_2\,\tilde{u}_2 + \ldots)\,; \\ v = v + v' = V\,\hat{v} = V(\bar{v} + \psi_1\,\tilde{v}_1 + \psi_2\,\tilde{v}_2 + \ldots)\,; \\ p = p + p' = p_0 + (\delta p)\,\hat{p} = p_0 + (\delta p)(\bar{p} + \varpi_1\,\tilde{p}_1 + \varpi_2\,\tilde{p}_2 + \ldots). \end{cases} \tag{E.11}$$

Here, U, V, δp are dimensioned scaling parameters and φ, ψ, ω are the non-dimensioned scaling parameters which are going to be determined in the following sections.

Several non-dimensional parameters are introduced as below:

$$\epsilon = b/L,\ \eta = \ell/L,\ \mathsf{Eu} = (\delta p)/(\rho U^2),\ \mathsf{Re} = Ub/\nu, \mathsf{St} = L/U\tau.$$

Here, ϵ is the parameter defining the aspect ratio as introduced previously, η is the parameter defining the ratio between the inlet length and the height, Eu is the EULER number, Re is the REYNOLDS number, St is the STROUHAL number.

E.1.5 Non-dimensioned equations

With the scaling introduced previously, the dimensioned governing equations can be non-dimensionalized into following form:

▷ *Mass conservation* :

$$\varphi\frac{\partial \hat{u}}{\partial \bar{x}} + \psi\frac{\partial \hat{v}}{\partial \bar{y}} = 0. \tag{E.12}$$

▷ *Momentum conservation*:

$$\begin{aligned}
\mathsf{St}\frac{\partial \hat{u}}{\partial \bar{t}} + \hat{u}\,\frac{\partial \hat{u}}{\partial \bar{x}} + \hat{v}\,\frac{\partial \hat{u}}{\partial \bar{y}} &= -\mathsf{Eu}\,\frac{\partial \hat{p}}{\partial \bar{x}} + \frac{1}{\varepsilon\mathsf{Re}}\left(\epsilon^2\frac{\partial^2 \hat{u}}{\partial \bar{x}^2} + \frac{\partial^2 \hat{u}}{\partial \bar{y}^2}\right);\\
\mathsf{St}\frac{\partial \hat{v}}{\partial \bar{t}} + \hat{u}\,\frac{\partial \hat{v}}{\partial \bar{x}} + \hat{v}\,\frac{\partial \hat{v}}{\partial \bar{y}} &= -\frac{\mathsf{Eu}}{\epsilon^2}\,\frac{\partial \hat{p}}{\partial \bar{y}} + \frac{1}{\varepsilon\mathsf{Re}}\left(\epsilon^2\frac{\partial^2 \hat{v}}{\partial \bar{x}^2} + \frac{\partial^2 \hat{v}}{\partial \bar{y}^2}\right).
\end{aligned} \tag{E.13}$$

▷ *Boundary conditions*:

$$\begin{array}{lll}
|\bar{x}| \to 0, & \bar{y} \in [0,\ 1 + \alpha\,\tilde{a}(\bar{t})] & : \text{ matching given conditions};\\
|\bar{x}| \in [\eta,\ 1], & \bar{y} = 0 & : \hat{u} = 0,\ \hat{v} = 0;\\
|\bar{x}| \le 1, & \bar{y} = 1 + \alpha\,\tilde{a}(\bar{t}) & : \hat{u} = 0,\ \hat{v} = \dot{\tilde{a}};\\
|\bar{x}| = 1, & \bar{y} \in [0,\ 1 + \alpha\,\tilde{a}(\bar{t})] & : \hat{p} = 0.
\end{array}$$

E.1.6 Thin-layer approximation

Eq. E.5 can be transfered into following form:

$$\epsilon\frac{\partial \hat{u}}{\partial \bar{x}} + \frac{V}{U}\frac{\partial \hat{v}}{\partial \bar{y}} = 0. \tag{E.14}$$

Since simplifications depending on mass conservation will induce drastic change to the system solved due to freezing the shape of the velocity profile, the most conservative way to simplify the problem is to make the simplification depending on momentum conservation where accelerations and forces will be considered. Therefore, we can suppose:

$$V = \epsilon U, \tag{E.15}$$

so the mass balance becomes invariant regardless of the variants.

However, this definition does not fulfill this subject totally. In fact, if U is the right scale for u_s, it will not be the most practical choice. This can be seen on the global mass conservation:

$$\ell V_i = \int_0^b u_s(\cdot, y)dy = Ub\int_0^1 \hat{u}(\cdot, \overline{y})d\overline{y}. \tag{E.16}$$

Because of

$$\int_0^1 \hat{u}(\cdot, \overline{y}) d\overline{y} = 1, \tag{E.17}$$

therefore, we have:

$$U = \frac{\eta}{\epsilon} V_i. \tag{E.18}$$

Here, two unknown dimensioned scaling parameters U and V are determined by Eq. E.18 and Eq. E.15.

Considering the area near the inlet, $\overline{v} = V_i/V = 1$, we can get $V_i = V = \epsilon U$. Comparing this with Eq. E.15, it can be found that $\eta = 1$ is implied here, which is contradict to the given condition. This proves that Eq. E.15 does not work in the area near the inlet where thin-layer approximation is not fulfilled.

Therefore, as mentioned before, the fluid domain solved by the analytical analysis are reduced regions shown as FIGURE E.2.

Thin-layer approximation ($\epsilon \ll 1$) will be applied to the problem solved here and will be valid on all the orders.

Standing on the physical point of view, the pressure forces are the main driving forces for the fluid flow, while inertial forces and frictions are acting opposite to the pressure forces. Considering the momentum conservation equations, we will have:

$$\textbf{Pressure forces} = sup\{\textbf{Unsteady acceleration}, \textbf{Inertial forces}, \textbf{Frictions}\}.$$

Therefore, when comparing the magnitudes of the pressure terms in Eq. E.13, inertial terms and friction terms, we can get:

$$\mathsf{Eu} = sup\left\{\mathsf{St}, 1, 1 : \frac{1}{\epsilon \mathsf{Re}} : \epsilon^2 \left\{1, 1 : \frac{1}{\epsilon \mathsf{Re}}\right\}\right\}, \tag{E.19}$$

so the scaling parameter δp will be decided:

$$\delta p = \rho U^2 \mathsf{Eu} = \rho U^2 sup\left\{\mathsf{St}, 1, \frac{1}{\epsilon \mathsf{Re}}\right\} \text{ [Pa]}. \tag{E.20}$$

Define $C_f = \frac{1}{\epsilon \mathsf{Re}}$, therefore:

$$\delta p = \rho U^2 \mathsf{Eu} = \rho U^2 sup\left\{\mathsf{St}, 1, C_f\right\} \text{ [Pa]}. \tag{E.21}$$

With this relationship, the value of Eu can be fixed by the highest value from comparison of St, 1 and C_f. It will be decided later.

Considering the quasi one-dimensional flow field, the terms of $\hat{v}$ in the momentum conservation equation on y direction be negligible. Therefore the non-dimensionalized equations will be simplified into following equations, with laplacian term in momentum equations becoming parabolic:

▷ *Mass conservation* :

$$\varphi \frac{\partial \hat{u}}{\partial \bar{x}} + \psi \frac{\partial \hat{v}}{\partial \bar{y}} = 0. \tag{E.22}$$

▷ *Momentum conservation*:

$$\begin{aligned} \mathsf{St}\frac{\partial \hat{u}}{\partial \bar{t}} + \hat{u}\,\frac{\partial \hat{u}}{\partial \bar{x}} + \hat{v}\,\frac{\partial \hat{u}}{\partial \bar{y}} &= -\mathsf{Eu}\,\frac{\partial \hat{p}}{\partial \bar{x}} + C_f \frac{\partial^2 \hat{u}}{\partial \bar{y}^2}\,; \\ 0 &= -\frac{\partial \hat{p}}{\partial \bar{y}}. \end{aligned} \tag{E.23}$$

▷ *Boundary conditions*:

$$\begin{array}{lll} |\bar{x}| \to 0, & \bar{y} \in [0,\, 1+\alpha\,\tilde{a}(\bar{t})] & : \text{ matching given conditions}\,; \\ |\bar{x}| \in [\eta,\, 1], & \bar{y} = 0 & : \ \hat{u} = 0,\ \hat{v} = 0\,; \\ |\bar{x}| \le 1, & \bar{y} = 1+\alpha\,\tilde{a}(\bar{t}) & : \ \hat{u} = 0,\ \hat{v} = \dot{\tilde{a}}\,; \\ |\bar{x}| = 1, & \bar{y} \in [0,\, 1+\alpha\,\tilde{a}(\bar{t})] & : \ \hat{p} = 0. \end{array}$$

E.1.7 Reference solution

The reference solution is only correspondent to the inlet flow, thus in this case, the reference solution is stationary ($\mathsf{St} \to 0, \alpha \to 0$).

E.1.7.1 Mass conservation

Mass conservation equation of the reference solution will be shown as following:

$$\frac{\partial \bar{u}}{\partial \bar{x}} + \frac{\partial \bar{v}}{\partial \bar{y}} = 0. \tag{E.24}$$

E.1.7.2 Momentum conservation

According to Eq. E.47, the non-dimensioned momentum conservation equation can be written as:

$$\bar{u}\frac{\partial \bar{u}}{\partial \bar{x}} + \bar{v}\frac{\partial \bar{u}}{\partial \bar{y}} = -\mathsf{Eu}\frac{\partial \bar{p}}{\partial \bar{x}} + C_f \frac{\partial^2 \bar{u}}{\partial \bar{y}^2}; \tag{E.25a}$$

$$0 = -\frac{\partial \bar{p}}{\partial \bar{y}}. \tag{E.25b}$$

In this case,

$$\textbf{Pressure forces} = sup\{\textbf{Inertial forces},\ \textbf{Frictions}\}.$$

Therefore, when comparing the magnitudes of the pressure terms in Eq. E.25, inertial terms and friction terms, we can get:

$$\delta p = \rho U^2 \mathsf{Eu} = \rho U^2 sup\left\{1, C_f\right\}. \tag{E.26}$$

The $\mathsf{Eu} - \text{vs} - \frac{1}{C_f}$ curve can be shown as FIGURE E.3:

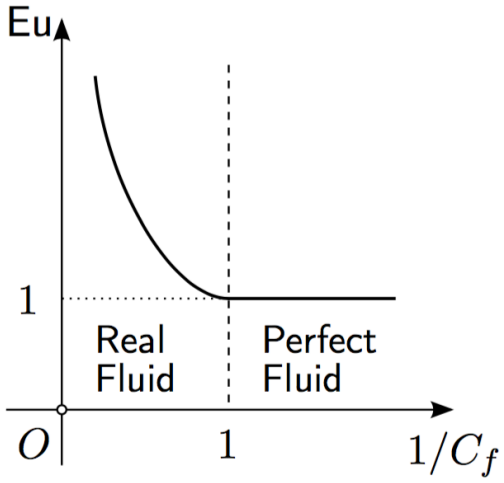

FIGURE E.3: $\mathsf{Eu} - vs - \epsilon\mathsf{Re}$ curve

Depending on the values, it leads to three kinds of solutions:

- Approximation of perfect fluid with boundary layers: $\frac{1}{C_f} \gg 1 \Rightarrow \mathsf{Eu} = 1$;
- Stokes approximation: $\frac{1}{C_f} \ll 1 \Rightarrow \mathsf{Eu} = C_f$;
- Approximation of thin layer (Prandtl approximation): $\mathsf{Eu} = 1 = \frac{1}{C_f}$.

E.1.7.3 Boundary conditions

The boundary conditions of the reference solution will be transformed into the form below:

$$\begin{array}{llll} |\bar{x}| \to 0, & \bar{y} \in [0,\,1] & : & \text{matching given conditions}\,; \\ |\bar{x}| \in [\eta,\,1], & \bar{y} = 0 & : & \bar{u} = 0,\ \bar{v} = 0\,; \\ |\bar{x}| \leq 1, & \bar{y} = 1 & : & \bar{u} = 0,\ \bar{v} = 0\,; \\ |\bar{x}| = 1, & \bar{y} \in [0,\,1] & : & \bar{p} = 0. \end{array} \tag{E.27}$$

E.1.8 Perturbation

This section is devoted to linear or quasi-linear first approximation. Therefore, it can not provide results for mean values which are all zero due to the periodicity.

E.1.8.1 Mass conservation

After eliminating the reference term, the mass conservation equation of the perturbation will be like:

$$\varphi\frac{\partial\tilde{u}}{\partial\overline{x}} + \psi\frac{\partial\tilde{v}}{\partial\overline{y}} = 0. \tag{E.28}$$

Here, φ and ψ is the first-order scaling parameter φ_1 and ψ_1.

Similar to the discussion for mass conservation of the reference solution, we can suppose $\varphi = \psi$, therefore:

$$\frac{\partial\tilde{u}}{\partial\overline{x}} + \frac{\partial\tilde{v}}{\partial\overline{y}} = 0. \tag{E.29}$$

E.1.8.2 Momentum conservation

The momentum equations are shown as following:

$$\mathsf{St}\frac{\partial \tilde{u}}{\partial \bar{t}} + \bar{u}\frac{\partial \tilde{u}}{\partial \bar{x}} + \tilde{u}\frac{\partial}{\partial \bar{x}}(\bar{u} + \cancel{\varphi \tilde{u}}) + \bar{v}\frac{\partial \tilde{u}}{\partial \bar{y}} + \tilde{v}\frac{\partial}{\partial \bar{y}}(\bar{u} + \cancel{\varphi \tilde{u}}) = -\mathsf{Eu}\frac{\varpi}{\varphi}\frac{\partial \tilde{p}}{\partial \bar{x}} + C_f\frac{\partial^2 \tilde{u}}{\partial \bar{y}^2}; \tag{E.30a}$$

$$0 = -\frac{\partial \tilde{p}}{\partial \bar{y}}; \tag{E.30b}$$

here due to the assumption that $\varphi \ll 1$, the terms with canceling lines can be negligible.

E.1.8.3 Boundary conditions

According to the discussion in section E.1.3, we can transfer the boundary condition for $\bar{y} = 1$ like following:

$$\begin{aligned} &\bar{y} = 0, \quad \eta < |\bar{x}| \leq 1 \quad : \quad \tilde{u} = 0, \qquad \tilde{v} = 0\,; \\ &\bar{y} = 1, \quad |\bar{x}| \leq 1 \quad : \quad \varphi\,\tilde{u} = -\alpha\,\tilde{a}\,\frac{\partial \bar{u}}{\partial \bar{y}}, \qquad \varphi\,\tilde{v} = \alpha\Big(\mathsf{St}\,\dot{\tilde{a}} - \tilde{a}\,\frac{\partial \bar{v}}{\partial \bar{y}}\Big). \end{aligned} \tag{E.31}$$

For the boundary condition on the moving plate (the second line of Eq. E.31), the first condition represents the displacement effect while the second condition represents the movement effect of the moving plate.

E.1.8.4 First approximation

The cause of the fluctuation is the movement of the plate, it is necessary to preserve the condition of Eq. E.31 by setting:

$$\varphi = \alpha\, sup\{\mathsf{St},\, 1\}.$$

Here perfect fluid hypothesis is taken account which is not considered in the analysis below.

The scaling parameter φ of perturbation is determined here combining the amplitudes (α) and the time scale (St) of the perturbation.

In the requirements of the transfer of the boundary conditions and the linearization of the equations, we will get:

$$\alpha \ll 1 \quad \text{and} \quad \varphi = \alpha\, sup\{\mathsf{St},\, 1\} \ll 1. \tag{E.32}$$

The discussion will focus on the value of Strouhal number, Reynolds number and their implications on the value ϖ. Compare the magnitudes of the different terms in Eq. E.30, the value of ϖ (the scaling for the pressure induced by perturbation) can be decided as following:

$$\varpi_* = \mathsf{Eu}\varpi = \alpha \mathsf{St} sup\Big\{\mathsf{St}, 1, C_f\Big\}. \tag{E.33}$$

The solution is demonstrated in FIGURE E.4:

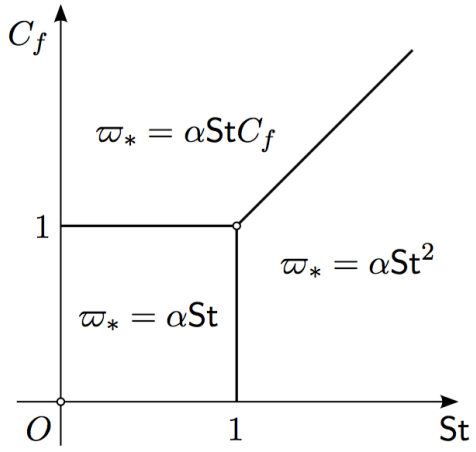

FIGURE E.4: The values of ϖ_*

Whatever the value is, the scaling ϖ_* of the pressure fluctuation leads to the balance of the longitudinal momentum while the transversal balance will have $\frac{\partial \tilde{p}}{\partial \overline{y}} = 0$. This concequented in the characterization of the thin layer approximation.

Regarding Eq. E.32 and the thin-layer approximation, the problem is fulfilled for the first approximation:

$$\frac{\partial \tilde{u}}{\partial \overline{x}} + \frac{\partial \tilde{v}}{\partial \overline{y}} = 0. \tag{E.34}$$

$$\mathrm{St}\frac{\partial \tilde{u}}{\partial \overline{t}} + \boxed{\overline{u}\frac{\partial \tilde{u}}{\partial \overline{x}} + \tilde{u}\frac{\partial \overline{u}}{\partial \overline{x}} + \overline{v}\frac{\partial \tilde{u}}{\partial \overline{y}} + \tilde{v}\frac{\partial \overline{u}}{\partial \overline{y}}} = -\frac{\varpi_*}{\alpha \mathrm{St}}\frac{\partial \tilde{p}}{\partial \overline{x}} + C_f \frac{\partial^2 \tilde{u}}{\partial \overline{y}^2}; \qquad \frac{\partial \tilde{p}}{\partial \overline{y}} = 0. \tag{E.35}$$

$$\begin{aligned} &\overline{y} = 0, \quad |\overline{x}| \leq 1 \quad : \ \tilde{u} = 0, \qquad \tilde{v} = 0\,; \\ &\overline{y} = 1, \quad |\overline{x}| \leq 1 \quad : \ \tilde{u} = -\frac{1}{\mathrm{St}}\,\tilde{a}\frac{\partial \overline{u}}{\partial \overline{y}}, \qquad \tilde{v} = \dot{\tilde{a}}. \end{aligned} \tag{E.36}$$

On the moving plate, since $\overline{u} = 0$, $\frac{\partial \overline{v}}{\partial \overline{y}} = -\frac{\partial \overline{u}}{\partial \overline{x}} = 0$, the boundary condition on the moving plate is transformed into Eq. E.36.

The framed terms in Eq. E.35 shows the coupling between the reference solution and the perturbation.

When the geometry of the domain is fixed, the different combinations of the scaling's values of St and C_f will constitute a flow map determined by St and C_f which will determine the scaling of the pressure as shown in FIGURE E.4. This coupling can only take place when the other terms in Eq. E.35 are in order 1. These combinations will be listed in TABLE E.1 and FIGURE E.5.

TABLE E.1: Flow map regions

Region	Scaling	Region	Scaling	Region	Scaling
a	$1 \gg \mathrm{St} \gg C_f$	d	$C_f \gg \mathrm{St} \gg 1$	b	$\mathrm{St} \gg 1 \gg C_f$
f	$1 \gg C_f \gg \mathrm{St}$	e	$C_f \gg 1 \gg \mathrm{St}$	c	$\mathrm{St} \gg C_f \gg 1$
a ∪ f	$\varpi_* = \alpha \mathrm{St}$	d ∪ e	$\varpi_* = \alpha \mathrm{St} C_f$	b ∪ c	$\varpi_* = \alpha \mathrm{St}^2$

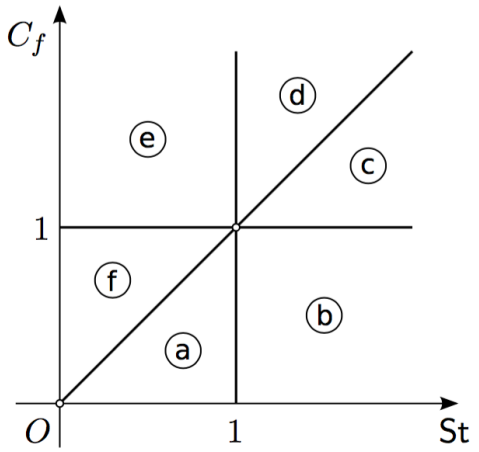

FIGURE E.5: Flow map

In regions a and b, the frictional forces are negligible; in regions c and d the inertial forces are negligible and the momentum balance is linearized; regions e and f are correspondent to quasi-static approximation. So the flow-map can be regrouped and simplified like following FIGURE E.6:

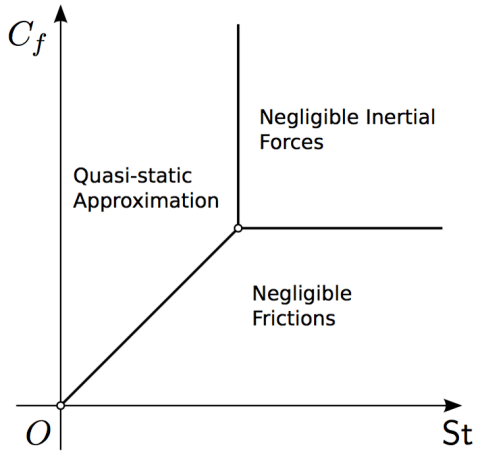

FIGURE E.6: Simplified flow map

E.1.9 Kinetic energy theorem

For better understanding of the dissipation and pressure work in the global vision of the phenomenon, kinetic energy theorem will be discussed here in this section.

Based on kinetic energy theorem, a comprehensive approach is established to specify the phenomenon in the view of energy sources and fluxes. Define $\mathcal{V}(t)$ is the global volume of the whole fluid domain at time t and $\partial\mathcal{V}$ is the surface of the domain. Since $\mathcal{V}(t)$ is not fixed domain and the fluid is incompressible and viscous, the theorem will be written as:

$$\frac{\mathrm{d}}{\mathrm{d}t}\int_{\mathcal{V}} \tfrac{1}{2}\rho\boldsymbol{v}^2\,\mathrm{d}V + \int_{\partial\mathcal{V}} \tfrac{1}{2}\rho\boldsymbol{v}^2(\boldsymbol{v}-\boldsymbol{w})\cdot\boldsymbol{n}\,\mathrm{d}A + \int_{\partial\mathcal{V}} p(\boldsymbol{v}\cdot\boldsymbol{n})\,\mathrm{d}A = \int_{\partial\mathcal{V}} \boldsymbol{v}\cdot\mathbf{T}\cdot\boldsymbol{n}\,\mathrm{d}A - \int_{\mathcal{V}} \mathbf{T}:\mathbf{D}\,\mathrm{d}V,$$

where, $\boldsymbol{w}\cdot\boldsymbol{n}$ is the normal velocity of the displacement of $\partial\mathcal{V}$ and $\mathbf{T} = 2\mu\mathbf{D}$ is the viscous component of the stress tensor.

Introduce $f(x,y,t) = y - b - a(t) = 0$ as the equation of the moving wall, the non-penetration condition can be written as:

$$\frac{\mathrm{d}f}{\mathrm{d}t} = -\frac{\partial f}{\partial t}/\|\boldsymbol{\nabla} f\| = -\dot{a} + v = 0 \quad \text{with} \quad \boldsymbol{w}\cdot\boldsymbol{n} = \dot{a} \quad \& \quad \boldsymbol{v}\cdot\boldsymbol{n} = v.$$

Therefore, the surface integrals can be transformed into following:

$$\int_{\partial\mathcal{V}} \tfrac{1}{2}\rho\boldsymbol{v}^2(\boldsymbol{v}-\boldsymbol{w})\cdot\boldsymbol{n}\,\mathrm{d}A = -\tfrac{1}{2}\rho V_i^3\ell + \int_0^y \tfrac{1}{2}\rho\boldsymbol{v}^2 u\,\mathrm{d}y\,;$$

$$\int_{\partial\mathcal{V}} p(\boldsymbol{v}\cdot\boldsymbol{n})\,\mathrm{d}A = -\int_0^\ell pV_i\,\mathrm{d}x + \dot{a}\int_0^L p\,\mathrm{d}x + p_0\int_0^y u\,\mathrm{d}y\,;$$

$$\int_{\partial\mathcal{V}} \boldsymbol{v}\cdot\mathbf{T}\cdot\boldsymbol{n}\,\mathrm{d}A = \int_0^\ell V_i T_{yy}\,\mathrm{d}x + \int_0^y (uT_{xx} + vT_{xy})\,\mathrm{d}y + \dot{a}\int_0^L T_{yy}\,\mathrm{d}x\,;$$

To complete the system of the theorem, mass conservation equation is introduced here:

$$\frac{\mathrm{d}}{\mathrm{d}t}\int_{\mathcal{V}} \rho\,\mathrm{d}V + \int_{\partial\mathcal{V}} \rho(\boldsymbol{v}-\boldsymbol{w})\cdot\boldsymbol{n}\,\mathrm{d}A = 0.$$

Because of incompressibility, the integral of the volume can be calculated as:

$$\int_{\mathcal{V}} \mathrm{d}V = Ly(t) \quad \Longrightarrow \quad \frac{\mathrm{d}}{\mathrm{d}t}\int_{\mathcal{V}} \rho\,\mathrm{d}V = \rho L\dot{a}.$$

So,

$$\int_{\partial\mathcal{V}} \rho(\boldsymbol{v}-\boldsymbol{w})\cdot\boldsymbol{n}\,\mathrm{d}A = -\rho V_i\ell + \rho\int_0^y u\,\mathrm{d}y \quad \Longrightarrow \quad \int_0^y u\,\mathrm{d}y = V_i\ell - L\dot{a}.$$

Consequently,

$$\underbrace{\frac{\mathrm{d}}{\mathrm{d}t}\int_{\mathcal{V}} \tfrac{1}{2}\rho\boldsymbol{v}^2\,\mathrm{d}V}_{\substack{\text{varying rate of}\\ \text{kinetic energy}}} = \underbrace{\int_0^\ell (p - p_0 + \tfrac{1}{2}\rho V_i^2)V_i\,\mathrm{d}x}_{\substack{\text{inlet mechanic}\\ \text{energy}}} - \underbrace{\int_0^y \tfrac{1}{2}\rho\boldsymbol{v}^2 u\,\mathrm{d}y}_{\substack{\text{outlet mechanic}\\ \text{energy}}} - \underbrace{\dot{a}\int_0^L (p-p_0)\,\mathrm{d}x}_{\text{work of pressure}} - \underbrace{\int_{\mathcal{V}} \mathbf{T}:\mathbf{D}\,\mathrm{d}V}_{\substack{\text{viscous}\\ \text{dissipation}}}$$
$$+ \underbrace{\int_0^\ell V_i T_{yy}\,\mathrm{d}x + \int_0^{y_\mathrm{P}} (uT_{xx} + vT_{xy})\,\mathrm{d}y + \dot{a}\int_0^L T_{yy}\,\mathrm{d}x}_{\substack{\text{work of}\\ \text{friction force}}}. \tag{E.37}$$

However, it is found that the transfer of the boundary conditions will affect some of the integrals and also the integrated volume of the fluid domain is not fixed. To overcome the difficulties, the first term of the Eq. E.37 will be expanded according to Leibniz method:

$$\frac{\mathrm{d}}{\mathrm{d}t}\int_{\mathcal{V}(t)} \tfrac{1}{2}\rho\boldsymbol{v}^2\,\mathrm{d}V = \int_{\mathcal{V}(t)} \frac{\partial}{\partial t}\left(\tfrac{1}{2}\rho\boldsymbol{v}^2\right)\mathrm{d}V + \int_{\partial\mathcal{V}(t)} \tfrac{1}{2}\rho\boldsymbol{v}^2(\boldsymbol{w}\cdot\boldsymbol{n})\,\mathrm{d}A.$$

With the thin-layer approximation valid at all the orders, Eq. E.37 can be transformed into following form:

$$\begin{aligned}
&\tfrac{1}{2}\mathsf{St}\,\frac{\mathrm{d}}{\mathrm{d}\bar{t}}\int_{\mathcal{V}}\hat{u}^2\,\mathrm{d}V=\tfrac{1}{2}\mathsf{St}\int_{\mathcal{V}}\frac{\partial\hat{u}^2}{\partial\bar{t}}\,\mathrm{d}V+\tfrac{1}{2}\alpha\mathsf{St}\,\dot{\tilde{a}}\int_0^1\hat{u}^2\,\mathrm{d}\bar{x}\\
&=\int_0^1\Big(\mathsf{Eu}\,\hat{p}+\frac{1}{2\eta_*^2}\Big)\,\mathrm{d}\bar{x}-\tfrac{1}{2}\int_0^{1+\alpha\,\tilde{a}}\hat{u}^3\,\mathrm{d}\bar{y}-\alpha\mathsf{St}\,\mathsf{Eu}\,\dot{\tilde{a}}\int_0^1\hat{p}\,\mathrm{d}\bar{x}-C_f\int_{\mathcal{V}}\Big(\frac{\partial\hat{u}}{\partial\bar{y}}\Big)^2\,\mathrm{d}V\\
&\quad+2\varepsilon^2C_f\int_0^1\frac{\partial\hat{v}}{\partial\bar{y}}\,\mathrm{d}\bar{x}+\varepsilon^2C_f\int_0^{1+\alpha\,\tilde{a}}\Big(2\hat{u}\frac{\partial\hat{u}}{\partial\bar{x}}+\hat{v}\frac{\partial\hat{u}}{\partial\bar{y}}\Big)\,\mathrm{d}\bar{y}+2\alpha\mathsf{St}\varepsilon^2C_f\,\dot{\tilde{a}}\int_0^1\frac{\partial\hat{v}}{\partial\bar{y}}\,\mathrm{d}\bar{x}.
\end{aligned}\tag{E.38}$$

Eq. E.38 is the starting point of the following asymptotic analysis with all the physics of the problem included. The square of the velocity here leads to second-order analysis. Also, the integral limits are time-varying, therefore Leibniz rule has to be applied.

E.1.9.1 Stationary solution

With first approximation $\alpha\to 0$, the solution will be shifted into stationary solution like following:

$$0=\int_0^1\Big(\mathsf{Eu}\,\bar{p}+\frac{1}{2\eta_*^2}\Big)\,\mathrm{d}\bar{x}-\tfrac{1}{2}\int_0^1\bar{u}^3\,\mathrm{d}\bar{y}-C_f\int_{\mathcal{V}}\Big(\frac{\partial\bar{u}}{\partial\bar{y}}\Big)^2\,\mathrm{d}V+2\varepsilon^2C_f\int_0^1\frac{\partial\bar{v}}{\partial\bar{y}}\,\mathrm{d}\bar{x}+\varepsilon^2C_f\int_0^1\Big(2\bar{u}\frac{\partial\bar{u}}{\partial\bar{x}}+\bar{v}\frac{\partial\bar{u}}{\partial\bar{y}}\Big)\,\mathrm{d}\bar{y}.$$

The last two terms are negligible when comparing with the third term, so the equation for first approximation can be written as:

$$0=\underbrace{\int_0^1\Big(\mathsf{Eu}\,\bar{p}+\frac{1}{2\eta_*^2}\Big)\,\mathrm{d}\bar{x}-\tfrac{1}{2}\int_0^1\bar{u}^3\,\mathrm{d}\bar{y}}_{\text{flux of mechanic energy}}\underbrace{-C_f\int_{\mathcal{V}}\Big(\frac{\partial\bar{u}}{\partial\bar{y}}\Big)^2\,\mathrm{d}V}_{\substack{\text{viscous}\\ \text{dissipation}}}.$$

In the case of $\mathsf{Eu}=sup\{1,\,C_f\},C_f\ll 1$, the viscous dissipation is negligible so the outlet energy flux of the fluid domain is almost equal to the inlet. While for the case of $1/C_f\lesssim 1$ and $\mathsf{Eu}=C_f$, the inlet energy will be nearly fully consumed by viscous dissipation.

E.1.9.2 Perturbation

With the second-order variables, the problem will be transmitted into following form:
▷ *Equations* :

$$\begin{cases}
\dfrac{\partial}{\partial\bar{x}}(\bar{u}+\varphi_1\,\tilde{u}_1+\varphi_2\,\tilde{u}_2+\ldots)+\dfrac{\partial}{\partial\bar{y}}(\bar{v}+\psi_1\,\tilde{v}_1+\psi_2\,\tilde{v}_2+\ldots)=0\,;\\
\mathsf{St}\dfrac{\partial}{\partial\bar{t}}(\varphi_1\,\tilde{u}_1+\varphi_2\,\tilde{u}_2+\ldots)+(\bar{u}+\varphi_1\,\tilde{u}_1+\varphi_2\,\tilde{u}_2+\ldots)\dfrac{\partial}{\partial\bar{x}}(\bar{u}+\varphi_1\,\tilde{u}_1+\varphi_2\,\tilde{u}_2+\ldots)\\
+(\bar{v}+\psi_1\,\tilde{v}_1+\psi_2\,\tilde{v}_2+\ldots)\dfrac{\partial}{\partial\bar{y}}(\bar{u}+\varphi_1\,\tilde{u}_1+\varphi_2\,\tilde{u}_2+\ldots)=-\mathsf{Eu}\dfrac{\partial}{\partial\bar{x}}(\bar{p}+\varpi_1\,\tilde{p}_1+\varpi_2\,\tilde{p}_2+\ldots)\\
+C_f\Big[\varepsilon^2\dfrac{\partial^2}{\partial\bar{x}^2}(\bar{u}+\varphi_1\,\tilde{u}_1+\varphi_2\,\tilde{u}_2+\ldots)+\dfrac{\partial^2}{\partial\bar{y}^2}(\bar{u}+\varphi_1\,\tilde{u}_1+\varphi_2\,\tilde{u}_2+\ldots)\Big]\,;\\
0=-\dfrac{\partial}{\partial\bar{y}}(\bar{p}+\varpi_1\,\tilde{p}_1+\varpi_2\,\tilde{p}_2+\ldots).
\end{cases}$$

▷ *Boundary conditions* :

$$\begin{cases} \bar{u}(\bar{x},0)+\varphi_1\,\tilde{u}_1(\bar{x},0,\bar{t})+\varphi_2\,\tilde{u}_2(\bar{x},0,\bar{t})+\ldots=0,\\ \bar{v}(\bar{x},0)+\psi_1\,\tilde{v}_1(\bar{x},0,\bar{t})+\psi_2\,\tilde{v}_2(\bar{x},0,\bar{t})+\ldots=0\\ \bar{u}(\bar{x},1)+\alpha\,\tilde{a}(\bar{t})\dfrac{\partial\bar{u}}{\partial\bar{y}}(\bar{x},1)+\frac{1}{2}\alpha^2\tilde{a}^2(\bar{t})\dfrac{\partial^2\bar{u}}{\partial\bar{y}^2}(\bar{x},1)+\ldots\\ \qquad\qquad+\varphi_1\,\tilde{u}_1(\bar{x},1,\bar{t})+\varphi_1\,\alpha\tilde{a}(\bar{t})\dfrac{\partial\tilde{u}_1}{\partial\bar{y}}(\bar{x},1,\bar{t})+\varphi_2\,\tilde{u}_2(\bar{x},1,\bar{t})+\ldots=0,\\ \bar{v}(\bar{x},1)+\psi_1\,\tilde{v}_1(\bar{x},1,\bar{t})+\psi_1\,\alpha\,\tilde{a}\dfrac{\partial\tilde{v}_1}{\partial\bar{y}}(\bar{x},1,\bar{t})+\psi_2\,\tilde{v}_2(\bar{x},1,\bar{t})+\ldots=\alpha\mathsf{St}\,\dot{\tilde{a}}. \end{cases}$$

Assuming that the thin-layer approximation is always true and eliminating the stationary terms, we will get the equations shown below:

▷ *Equations* :

$$\begin{cases} \dfrac{\partial}{\partial\bar{x}}(\varphi_1\,\tilde{u}_1+\varphi_2\,\tilde{u}_2)+\dfrac{\partial}{\partial\bar{y}}(\psi_1\,\tilde{v}_1+\psi_2\,\tilde{v}_2)=0\,;\\ \mathsf{St}\dfrac{\partial}{\partial\bar{t}}(\varphi_1\,\tilde{u}_1+\varphi_2\,\tilde{u}_2)+\bar{u}\dfrac{\partial}{\partial\bar{x}}(\varphi_1\,\tilde{u}_1+\varphi_2\,\tilde{u}_2)+\varphi_1\,\tilde{u}_1\dfrac{\partial}{\partial\bar{x}}(\bar{u}+\varphi_1\,\tilde{u}_1)+\varphi_2\,\tilde{u}_2\dfrac{\partial\bar{u}}{\partial\bar{x}}\\ \qquad\qquad+\bar{v}\dfrac{\partial}{\partial\bar{y}}(\varphi_1\,\tilde{u}_1+\varphi_2\,\tilde{u}_2)+\psi_1\,\tilde{v}_1\dfrac{\partial}{\partial\bar{y}}(\bar{u}+\varphi_1\,\tilde{u}_1)+\psi_2\,\tilde{v}_2\dfrac{\partial\bar{u}}{\partial\bar{y}}\\ \qquad\qquad=-\mathsf{Eu}\dfrac{\partial}{\partial\bar{x}}(\varpi_1\,\tilde{p}_1+\varpi_2\,\tilde{p}_2)+C_f\dfrac{\partial^2}{\partial\bar{y}^2}(\varphi_1\,\tilde{u}_1+\varphi_2\,\tilde{u}_2)\,;\\ 0=-\dfrac{\partial}{\partial\bar{y}}(\varpi_1\,\tilde{p}_1+\varpi_2\,\tilde{p}_2). \end{cases}$$

▷ *Boundary conditions* :

$$\begin{cases} \varphi_1\,\tilde{u}_1(\bar{x},0,\bar{t})+\varphi_2\,\tilde{u}_2(\bar{x},0,\bar{t})+\ldots=0,\\ \psi_1\,\tilde{v}_1(\bar{x},0,\bar{t})+\psi_2\,\tilde{v}_2(\bar{x},0,\bar{t})+\ldots=0\\ \alpha\,\tilde{a}(\bar{t})\dfrac{\partial\bar{u}}{\partial\bar{y}}(\bar{x},1)+\frac{1}{2}\alpha^2\tilde{a}^2(\bar{t})\dfrac{\partial^2\bar{u}}{\partial\bar{y}^2}(\bar{x},1)+\varphi_1\,\tilde{u}_1(\bar{x},1,\bar{t})+\varphi_1\alpha\tilde{a}\Big(\dfrac{\partial\tilde{u}_1}{\partial\bar{y}}\Big)(\bar{x},1,\bar{t})+\varphi_2\,\tilde{u}_2(\bar{x},1,\bar{t})+\ldots=0,\\ \psi_1\,\tilde{v}_1(\bar{x},1,\bar{t})+\psi_1\,\alpha\,\tilde{a}\dfrac{\partial\tilde{v}_1}{\partial\bar{y}}(\bar{x},1,\bar{t})+\psi_2\,\tilde{v}_2(\bar{x},1,\bar{t})+\ldots=\alpha\mathsf{St}\,\dot{\tilde{a}}. \end{cases}$$

After eliminating the fist-order terms, we will get the equations for second order:

▷ *Equations* :

$$\begin{cases} \varphi_2\dfrac{\partial\tilde{u}_2}{\partial\bar{x}}+\psi_2\dfrac{\partial\tilde{v}_2}{\partial\bar{y}}=0\,;\\ \varphi_2\mathsf{St}\dfrac{\partial\tilde{u}_2}{\partial\bar{t}}+\varphi_2\,\bar{u}\dfrac{\partial\tilde{u}_2}{\partial\bar{x}}+\boxed{\varphi_1^2\,\tilde{u}_1\dfrac{\partial\tilde{u}_1}{\partial\bar{x}}}+\varphi_2\,\tilde{u}_2\dfrac{\partial\bar{u}}{\partial\bar{x}}+\varphi_2\,\bar{v}\dfrac{\partial\tilde{u}_2}{\partial\bar{y}}+\boxed{\varphi_1\psi_1\,\tilde{v}_1\dfrac{\partial\tilde{u}_1}{\partial\bar{y}}}+\psi_2\,\tilde{v}_2\dfrac{\partial\bar{u}}{\partial\bar{y}}\\ \qquad\qquad=-\varpi_2\mathsf{Eu}\dfrac{\partial\tilde{p}_2}{\partial\bar{x}}+\dfrac{\varphi_2}{\varepsilon\mathsf{Re}}\dfrac{\partial^2\tilde{u}_2}{\partial\bar{y}^2}\,;\\ 0=-\dfrac{\partial\tilde{p}_2}{\partial\bar{y}}. \end{cases} \tag{E.39}$$

▷ *Boundary conditions* :

$$\begin{cases} \tilde{u}_2(\bar{x},0,\bar{t}) = 0, \quad \tilde{v}_2(\bar{x},0,\bar{t}) = 0 \\ \boxed{\frac{1}{2}\alpha^2\tilde{a}^2(\bar{t})\frac{\partial^2\bar{u}}{\partial\bar{y}^2}(\bar{x},1) + \varphi_1\alpha\,\tilde{a}\Big(\frac{\partial\tilde{u}_1}{\partial\bar{y}}\Big)(\bar{x},1,\bar{t})} + \varphi_2\,\tilde{u}_2(\bar{x},1,\bar{t}) = 0, \\ \boxed{\psi_1\,\alpha\,\tilde{a}\frac{\partial\tilde{v}_1}{\partial\bar{y}}(\bar{x},1,\bar{t})} + \psi_2\,\tilde{v}_2(\bar{x},1,\bar{t}) = 0. \end{cases} \tag{E.40}$$

E.1.9.2.1 Scaling

We can keep the scaling of first order for $\varphi_1 = \psi_1 = \alpha\mathsf{St}$. Also because of the reason mentioned in section E.1.8.1, we can take $\psi_2 = \varphi_2$. ϖ should be the value which will lead a second-order solution different from zero. In order to preserve the diving term with pressure gradient, comparing the magnitudes of the different terms, we can get:

$$\varpi_2\mathsf{Eu} = sup\{\varphi_2\mathsf{St},\ \varphi_2,\ \alpha^2\mathsf{St}^2,\ \varphi_2/(\varepsilon\mathsf{Re})\} = sup\{\varphi_2\mathsf{St},\ \alpha^2\mathsf{St}^2,\ \varphi_2/(\varepsilon\mathsf{Re})\}.$$

$\mathsf{St} \geqslant 1$ is supposed here.
To preserve the dominant term (the framed terms) in Eq. E.39, we should have:

$$\alpha^2\mathsf{St}^2 = \varphi_2\,sup\{\mathsf{St},\ 1,\ 1/(\varepsilon\mathsf{Re})\} = \varphi_2\,\mathsf{St} \quad \Longleftrightarrow \quad \varphi_2 = \alpha^2\mathsf{St}.$$

Also, we need to preserve the dominant terms in Eq. E.40. The scaling for the second order can be written as:

$$\varphi_2 = \alpha^2\mathsf{St} \quad \Longrightarrow \quad \varpi_2\mathsf{Eu} = \alpha^2\mathsf{St}\,sup\{\mathsf{St},\ C_f\} = \alpha^2\mathsf{St}^2 \gtrsim \alpha^2. \tag{E.41}$$

The scaling parameters for pressure and determined here combining the amplitudes and the time scales of the oscillation.

E.1.9.2.2 Kinetic energy theorem

The terms in Eq. E.37 can be transformed into second-order form like following:

$$\frac{\mathrm{d}}{\mathrm{d}t}\int_{\mathcal{V}}\tfrac{1}{2}\rho\boldsymbol{v}^2\,\mathrm{d}V \Rightarrow \tfrac{1}{2}\mathsf{St}\int_0^1\mathrm{d}\bar{x}\Big\{2\alpha\mathsf{St}\int_0^1\bar{u}\frac{\partial\tilde{u}_1}{\partial\bar{t}}\,\mathrm{d}\bar{y} + \alpha^2\mathsf{St}\Big[\int_0^1\Big(2\bar{u}\frac{\partial\tilde{u}_2}{\partial\bar{t}} + \mathsf{St}\frac{\partial\tilde{u}_1^2}{\partial\bar{t}}\Big)\mathrm{d}\bar{y} + 2\tilde{a}\bar{u}(1)\frac{\partial\tilde{u}_1}{\partial\bar{t}}(1)\Big]\Big\}$$
$$+ \tfrac{1}{2}\alpha\mathsf{St}\,\dot{\tilde{a}}\Big[\int_0^1\bar{u}^2\,\mathrm{d}\bar{x} + 2\alpha\mathsf{St}\int_0^1\bar{u}\tilde{u}_1\,\mathrm{d}\bar{x} + \alpha^2\mathsf{St}\int_0^1\big(2\bar{u}\tilde{u}_2 + \mathsf{St}\tilde{u}_1^2\big)\,\mathrm{d}\bar{x}\Big];$$

$$\int_0^\ell(p - p_0 + \tfrac{1}{2}\rho V_i^2)V_i\,\mathrm{d}x \Rightarrow \int_0^1\Big[\mathsf{Eu}\big(\bar{p} + \varpi_1\tilde{p}_1 + \varpi_2\tilde{p}_2\big) + \frac{1}{2\eta_*^2}\Big]\,\mathrm{d}\bar{x};$$

$$\int_0^y\tfrac{1}{2}\rho\boldsymbol{v}^2u\,\mathrm{d}y \Rightarrow \frac{1}{2}\Big\{\int_0^1\bar{u}^3\,\mathrm{d}\bar{y} + \alpha\Big[3\mathsf{St}\int_0^1\bar{u}^2\tilde{u}_1\,\mathrm{d}\bar{y} + \tilde{a}\bar{u}^3(1)\Big]$$
$$+ \alpha^2\Big[3\mathsf{St}\int_0^1\big(\bar{u}^2\tilde{u}_2 + \mathsf{St}\,\bar{u}\tilde{u}_1^2\big)\,\mathrm{d}\bar{y} + 3\mathsf{St}\,\tilde{a}\bar{u}^2(1)\tilde{u}_1(1) + \tfrac{3}{2}\tilde{a}^2\bar{u}^2(1)\frac{\partial\bar{u}}{\partial\bar{y}}(1)\Big]\Big\};$$

$$\dot{a}\int_0^L(p - p_0)\,\mathrm{d}x \Rightarrow \alpha\mathsf{St}\,\mathsf{Eu}\,\dot{\tilde{a}}\int_0^1\big(\bar{p} + \varpi_1\tilde{p}_1 + \varpi_2\tilde{p}_2\big)\,\mathrm{d}\bar{x};$$

$$\int_{\mathcal{V}} \mathbf{T} : \mathbf{D}\,\mathrm{d}V \Rightarrow C_f \int_0^1 \mathrm{d}\bar{x}\left[\int_0^1 \Big(\frac{\partial \bar{u}}{\partial \bar{y}}\Big)^2 \mathrm{d}\bar{y} + \alpha\Big\{2\mathsf{St}\int_0^1 \frac{\partial \bar{u}}{\partial \bar{y}}\frac{\partial \tilde{u}_1}{\partial \bar{y}}\,\mathrm{d}\bar{y} + \tilde{a}\Big(\frac{\partial \bar{u}}{\partial \bar{y}}\Big)^2(1)\Big\}\right];$$

$$\int_0^\ell V_i T_{yy}\,\mathrm{d}x + \int_0^y (uT_{xx} + vT_{xy})\,\mathrm{d}y + \dot{a}\int_0^L T_{yy}\,\mathrm{d}x \Rightarrow C_f \int_0^1 \mathrm{d}\bar{x}\left[\alpha^2\Big\{\int_0^1 \mathsf{St}\Big[2\frac{\partial \bar{u}}{\partial \bar{y}}\frac{\partial \tilde{u}_2}{\partial \bar{y}} + \mathsf{St}\Big(\frac{\partial \tilde{u}_1}{\partial \bar{y}}\Big)^2\Big]\,\mathrm{d}\bar{y} + 2\mathsf{St}\,\tilde{a}\frac{\partial \bar{u}}{\partial \bar{y}}(1)\frac{\partial \tilde{u}_1}{\partial \bar{y}}(1) + \tfrac{1}{2}\tilde{a}^2\Big[\frac{\partial}{\partial \bar{y}}\Big(\frac{\partial \bar{u}}{\partial \bar{y}}\Big)^2\Big](1)\Big\}\right].$$

The complete equation can be written as:

$$\begin{aligned}
&\tfrac{1}{2}\mathsf{St}\int_0^1 \mathrm{d}\bar{x}\Big\{2\alpha\mathsf{St}\int_0^1 \bar{u}\frac{\partial \tilde{u}_1}{\partial \bar{t}}\,\mathrm{d}\bar{y} + \alpha^2\mathsf{St}\Big[\int_0^1 \Big(2\bar{u}\frac{\partial \tilde{u}_2}{\partial \bar{t}} + \mathsf{St}\frac{\partial \tilde{u}_1^2}{\partial \bar{t}}\Big)\,\mathrm{d}\bar{y} + 2\tilde{a}\bar{u}(1)\frac{\partial \tilde{u}_1}{\partial \bar{t}}(1)\Big]\Big\}\\
&\quad + \tfrac{1}{2}\alpha\mathsf{St}\,\dot{\tilde{a}}\Big[\int_0^1 \bar{u}^2\,\mathrm{d}\bar{x} + 2\alpha\mathsf{St}\int_0^1 \bar{u}\tilde{u}_1\,\mathrm{d}\bar{x} + \alpha^2\mathsf{St}\int_0^1 \big(2\bar{u}\tilde{u}_2 + \mathsf{St}\tilde{u}_1^2\big)\,\mathrm{d}\bar{x}\Big]\\
&= \int_0^1 \Big[\mathsf{Eu}\big(\bar{p} + \varpi_1\tilde{p}_1 + \varpi_2\tilde{p}_2\big) + \frac{1}{2\eta_*^2}\Big]\,\mathrm{d}\bar{x}\\
&\quad - \frac{1}{2}\Big\{\int_0^1 \bar{u}^3\,\mathrm{d}\bar{y} + \alpha\Big[3\mathsf{St}\int_0^1 \bar{u}^2\tilde{u}_1\,\mathrm{d}\bar{y} + \tilde{a}\bar{u}^3(1)\Big]\\
&\qquad\quad + \alpha^2\Big[3\mathsf{St}\int_0^1 \big(\bar{u}^2\tilde{u}_2 + \mathsf{St}\,\bar{u}\tilde{u}_1^2\big)\,\mathrm{d}\bar{y} + 3\mathsf{St}\,\tilde{a}\bar{u}^2(1)\tilde{u}_1(1) + \tfrac{3}{2}\tilde{a}^2\bar{u}^2(1)\frac{\partial \bar{u}}{\partial \bar{y}}(1)\Big]\Big\}\\
&\quad - \alpha\mathsf{St}\,\mathsf{Eu}\,\dot{\tilde{a}}\int_0^1 \big(\bar{p} + \varpi_1\tilde{p}_1 + \varpi_2\tilde{p}_2\big)\,\mathrm{d}\bar{x}\\
&\quad - C_f\int_0^1 \mathrm{d}\bar{x}\left[\int_0^1 \Big(\frac{\partial \bar{u}}{\partial \bar{y}}\Big)^2\mathrm{d}\bar{y} + \alpha\Big\{2\mathsf{St}\int_0^1 \frac{\partial \bar{u}}{\partial \bar{y}}\frac{\partial \tilde{u}_1}{\partial \bar{y}}\,\mathrm{d}\bar{y} + \tilde{a}\Big(\frac{\partial \bar{u}}{\partial \bar{y}}\Big)^2(1)\Big\}\right.\\
&\quad \left. + \alpha^2\Big\{\int_0^1 \mathsf{St}\Big[2\frac{\partial \bar{u}}{\partial \bar{y}}\frac{\partial \tilde{u}_2}{\partial \bar{y}} + \mathsf{St}\Big(\frac{\partial \tilde{u}_1}{\partial \bar{y}}\Big)^2\Big]\,\mathrm{d}\bar{y} + 2\mathsf{St}\,\tilde{a}\frac{\partial \bar{u}}{\partial \bar{y}}(1)\frac{\partial \tilde{u}_1}{\partial \bar{y}}(1) + \tfrac{1}{2}\tilde{a}^2\Big[\frac{\partial}{\partial \bar{y}}\Big(\frac{\partial \bar{u}}{\partial \bar{y}}\Big)^2\Big](1)\Big\}\right].
\end{aligned}$$

The terms here are correspondent to varying rate of kinetic energy, inlet mechanic energy, outlet mechanic energy, work of pressure, viscous dissipation and work of friction force respectively from left to right.
We can seperate the equation according to the different orders of the scaling:

$$\mathsf{Eu} = sup\{1\,;\,C_f\},\quad \varpi_1\mathsf{Eu} = \alpha\mathsf{St}^2,\quad \text{et}\quad \varpi_2\mathsf{Eu} = \alpha^2\mathsf{St}^2.$$

The equations seperated are shown below:
▷ *Order 1* :

$$0 = \int_0^1 \Big(\mathsf{Eu}\,\bar{p} + \frac{1}{2\eta_*^2}\Big)\,\mathrm{d}\bar{x} - \tfrac{1}{2}\int_0^1 \bar{u}^3\,\mathrm{d}\bar{y} - C_f\int_0^1 \Big(\frac{\partial \bar{u}}{\partial \bar{y}}\Big)^2\mathrm{d}\bar{y}. \tag{E.42}$$

The problem on Order 1 has already been treated in section E.1.9.1.
▷ *Order* α :

$$\begin{aligned}
&\mathsf{St}^2\int_0^1 \mathrm{d}\bar{x}\int_0^1 \bar{u}\frac{\partial \tilde{u}_1}{\partial \bar{t}}\,\mathrm{d}\bar{y} + \tfrac{1}{2}\mathsf{St}\,\dot{\tilde{a}}\int_0^1 \bar{u}^2\,\mathrm{d}\bar{y}\\
&= \mathsf{St}^2\int_0^1 \tilde{p}_1\,\mathrm{d}\bar{x} - \tfrac{1}{2}\Big[3\mathsf{St}\int_0^1 \bar{u}^2\tilde{u}_1\,\mathrm{d}\bar{y} + \tilde{a}\bar{u}^3(1)\Big] - \mathsf{St}\,\mathsf{Eu}\,\dot{\tilde{a}}\int_0^1 \bar{p}\,\mathrm{d}\bar{x}\\
&\quad - C_f\int_0^1 \mathrm{d}\bar{x}\Big[2\mathsf{St}\int_0^1 \frac{\partial \bar{u}}{\partial \bar{y}}\frac{\partial \tilde{u}_1}{\partial \bar{y}}\,\mathrm{d}\bar{y} + \tilde{a}\Big(\frac{\partial \bar{u}}{\partial \bar{y}}\Big)^2(1)\Big].
\end{aligned} \tag{E.43}$$

Due to linearity of the problem, the time average of all terms are zero, so we are able to study on instant energy balances.

The contribution of the dissipation induced by perturbation will not affect the positive sign of the total dissipation, in other words, the contribution of the dissipation caused by the stationary reference flow is still dominant.

When St has a large value, the equation will be simplified to the balance of the time dereviative of the kinetic energy of the perturbation in the flow domain (the first term in the equation on the left) and the pressure work done by the perturbation (the first term on the right of the equation).

▷ *Order* α^2 :

$$\begin{aligned}
&\tfrac{1}{2}\mathsf{St}^2\int_0^1 \mathrm{d}\bar{x}\left[\int_0^1\left(2\bar{u}\frac{\partial\tilde{u}_2}{\partial\bar{t}}+\mathsf{St}\frac{\partial\tilde{u}_1^2}{\partial\bar{t}}\right)\mathrm{d}\bar{y}+2\tilde{a}\bar{u}(1)\frac{\partial\tilde{u}_1}{\partial\bar{t}}(1)\right]+\mathsf{St}^2\,\dot{\tilde{a}}\int_0^1\bar{u}\tilde{u}_1\,\mathrm{d}\bar{x}\\
&=\mathsf{St}^2\int_0^1\tilde{p}_2\,\mathrm{d}\bar{x}-\tfrac{1}{2}\left[3\mathsf{St}\int_0^1\left(\bar{u}^2\tilde{u}_2+\mathsf{St}\,\bar{u}\tilde{u}_1^2\right)\mathrm{d}\bar{y}+3\mathsf{St}\,\tilde{a}\bar{u}^2(1)\tilde{u}_1(1)+\tfrac{3}{2}\tilde{a}^2\bar{u}^2(1)\frac{\partial\bar{u}}{\partial\bar{y}}(1)\right]\\
&\quad-\mathsf{St}^3\,\dot{\tilde{a}}\int_0^1\tilde{p}_1\,\mathrm{d}\bar{x}-C_f\int_0^1\mathrm{d}\bar{x}\left(\int_0^1\left\{\mathsf{St}\left[2\frac{\partial\bar{u}}{\partial\bar{y}}\frac{\partial\tilde{u}_2}{\partial\bar{y}}+\mathsf{St}\left(\frac{\partial\tilde{u}_1}{\partial\bar{y}}\right)^2\right]\right\}\mathrm{d}\bar{y}\right.\\
&\qquad\left.+2\mathsf{St}\,\tilde{a}\frac{\partial\bar{u}}{\partial\bar{y}}(1)\frac{\partial\tilde{u}_1}{\partial\bar{y}}(1)+\tfrac{1}{2}\tilde{a}^2\left[\frac{\partial}{\partial\bar{y}}\left(\frac{\partial\bar{u}}{\partial\bar{y}}\right)^2\right](1)\right).
\end{aligned}\tag{E.44}$$

Considering the term with an order of St^3 which is resulted from averaging process, with $\mathsf{St}\sim 1$, the magnitude of this term will not cause a big problem, but with $\mathsf{St}\gg 1$, the term will strongly affect the balance. It will not only work on reducing the influence of the unsteady term by its higher order of St but also act on the general equilibrium.

Therefore, we can translate Eq. E.44 into the form shown below:

$$\begin{aligned}
\tfrac{1}{2}\int_0^1\mathrm{d}\bar{x}\int_0^1\frac{\partial\tilde{u}_1^2}{\partial\bar{t}}\,\mathrm{d}\bar{y}+\dot{\tilde{a}}\int_0^1\tilde{p}_1\,\mathrm{d}\bar{x}=&\mathsf{St}^{-1}\left[\int_0^1\tilde{p}_1\,\mathrm{d}\bar{x}-C_f\int_0^1\mathrm{d}\bar{x}\int_0^1\left(\frac{\partial\tilde{u}_1}{\partial\bar{y}}\right)^2\mathrm{d}\bar{y}\right.\\
&\left.-\int_0^1\mathrm{d}\bar{x}\left(\int_0^1\bar{u}\frac{\partial\tilde{u}_2}{\partial\bar{t}}\,\mathrm{d}\bar{y}+2\tilde{a}\tilde{u}(1)\frac{\tilde{u}_1}{\partial\bar{t}}(1)\right)\right].
\end{aligned}$$

The sum of the two terms in Eq. E.44 on order St^3 will be on St^2 order, compensated by the sum of the other terms on lower order. It shows that the dissipation will be small while the terms on the left have large fluctuations.

E.1.10 Conclusions

The problem scenario was established in this chapter and decomposed into two parts: a stationary reference solution and a superimposed small-amplitude perturbation term. Scaling system for non-dimensionalization was introduced. Local analysis for mass conservation, momentum conservation and boundary condition and global analysis for kinetic theorem were established. A flow map characterized by C_f and St was built to describe the perturbation flow condition.

E.2 Numerical analysis

Numerical results resolved by Cast3M will be presented in this chapter [**?**]. Simulation conditions will be demonstrated with the equations solved in Cast3M. Analysis of average pressure on the moving plate, average inlet pressure and rates between global pressure work and dissipation will be shown in this chapter.

E.2.1 Conditions of the Simulations

E.2.1.1 Simulation conditions

As shown in FIGURE E.1, the basic geometry parameters will be demonstrated in the following TABLE E.2:

TABLE E.2: Basic parameters of the geometry

L [m]	ℓ [m]	b [m]	a_0 [m]	ϵ [$-$]	η [$-$]	α [$-$]	V_i [m/s]
3.5	0.05	0.1	0.001	0.0286	0.0143	0.01	5

The period of the oscillating plate τ and the viscosity ν were varied in order to reach different values of St and Re. All of the other parameters of the flow field, such as geometry and inlet velocity, were fixed for all the simulations.
The oscillation of the plate can be described by a $sine$ function as shown in Eq. E.45.

$$a = a_0 \sin(\frac{2\pi}{\tau}t). \tag{E.45}$$

The mesh (shown as FIGURE E.7) with a total size of 8e4 elements was generated directly by Cast3M. The mesh size was optimized in order to reach an optimized numerical result with coarser mesh in the longitudinal center and finer mesh near the walls and near the inlet. A stable mesh with an velocity profile deducted from Eq. E.45 implemented on the oscillating plate was used for simulations. In Cast3M, dimensioned quantities are used for calculation. Therefore, non-dimensionalization will be carried on during post-processing. As discussed in previous chapter, the fluid domain solved numerically is the complete domain with the vicinity of inlet considered. 2-D Navier-Stokes equations for incompressible viscous fluid were applied in the model with small-motion approximation implemented. Non-slip and non-penetration condition were established for all the walls including the moving plate. Weak bounding condition for outlet pressure ($\oint p_0 dA = 0$) was imposed.

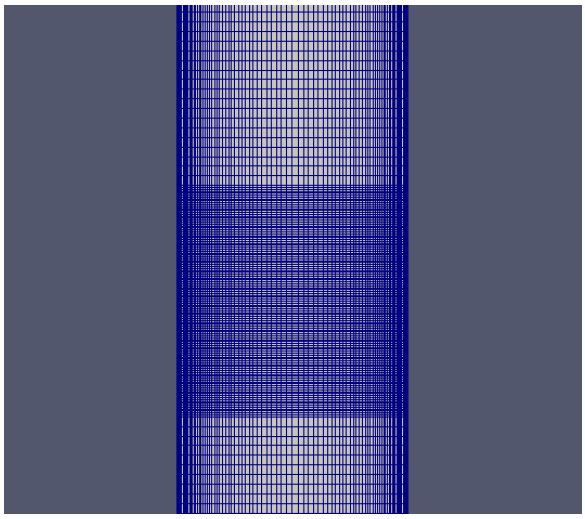

FIGURE E.7: Part of the mesh near the inlet

Second-order backward differentiation formula (BDF2) time scheme was implemented in the calculations for the reason of better behavior in energy balance than that of first-order time scheme.

E.2.1.2 Governing equations solved by Cast3M

The actual equation solved by Cast3M will be:
▷ *Mass conservation*:

$$\frac{\partial u}{\partial x}+\frac{\partial v}{\partial y}=0. \tag{E.46}$$

▷ *Momentum conservation*:

$$\frac{\partial u}{\partial t}+u\frac{\partial u}{\partial x}+v\frac{\partial u}{\partial y}=-\frac{1}{\rho}\frac{\partial p}{\partial x}+\nu\left(\frac{\partial^2 u}{\partial x^2}+\frac{\partial^2 u}{\partial y^2}\right); \tag{E.47a}$$

$$\frac{\partial v}{\partial t}+u\frac{\partial v}{\partial x}+v\frac{\partial v}{\partial y}=-\frac{1}{\rho}\frac{\partial p}{\partial y}+\nu\left(\frac{\partial^2 v}{\partial x^2}+\frac{\partial^2 v}{\partial y^2}\right). \tag{E.47b}$$

▷ *Boundary conditions*:

$$y=0,\begin{cases}|x|\leqslant \ell \ : \ u=0,\ v=V_i;\\ \ell\leqslant|x|\leqslant L \ : \ u=0,\ v=0.\end{cases} \tag{E.48}$$

$$y=b,|x|\leqslant L \ : u=0,\ v=\dot{a}. \tag{E.49}$$

$$x=\pm L,0\leqslant y\leqslant b \ : \ \oint pdA=0. \tag{E.50}$$

E.2.1.3 Non-dimensional parameters and scalings

With the dimensioned parameters used in Cast3M computation, the scaling parameters and non-dimensional parameters can be calculated using following equations as already be discussed in phenomenological analysis:

$$U = \frac{\eta}{\epsilon}V_i; \quad V = \epsilon U = \eta V_i; \quad \mathsf{Re} = Ub/\nu; \quad \mathsf{St} = L/U\tau;$$
$$C_f = \frac{1}{\epsilon \mathsf{Re}}; \quad \mathsf{Eu} = sup\{1, C_f\}; \quad \delta p = \rho U^2 \mathsf{Eu}; \quad \varpi = \frac{\alpha \mathsf{St}}{\mathsf{Eu}} sup\{\mathsf{St}, 1, C_f\} = \alpha \mathsf{Eu} \frac{sup\{\mathsf{St}, 1, C_f\}}{sup\{1, C_f\}}. \tag{E.51}$$

Two parameters St and C_f which will decide the positions of the cases in the flow map (FIGURE E.6) are demonstrated in TABLE E.3.

TABLE E.3: St and C_f of the simulated cases

St	0.35	0.7	1.4	2.8	4.67	7	9.33	14
Re	5,10,15,20,25,30,35,40,45,50							
C_f	7,3.5,2.333,1.75,1.4,1.17,1,0.875,0.778,0.7							

Note here, the values with high Sts used here in Cast3M exceed the limits of discussions in phenomenological analysis.
The locations of all the cases resolved in the flow map will be shown in following FIGURE E.8. Two series of cases with $\mathsf{St} = 0.35$ and $\mathsf{St} = 0.7$ are located in the region of quasi-static approximation. While the other 5 cases are located in the regions where friction is negligible and where inertia is negligible with cases of lower Re compatible with inertia negligible conditions and cases of higher Re situated in the region where friction is negligible.

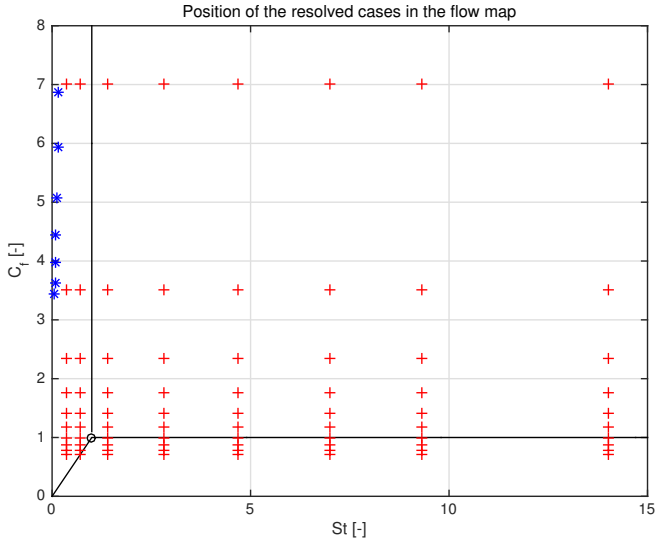

FIGURE E.8: Positions of the resolved cases in the flow map

Also experiments with continuous injections were conducted on PISE-1a, oscillations of the assembly were observed and calibrated during the experiments. These experiments will be documented in later reports. The blue asteroid points demonstrate the position of these

conducted experiments in the flow map. The experimental cases are located in the quasi-static region with low Sts which are included in the regions discussed by analytical and numerical analysis in this report.

E.2.2 Data analysis

E.2.2.1 Velocity and pressure profiles

Three cases with $\mathsf{St} = 0.35, C_f = 2.333$, $\mathsf{St} = 1.4, C_f = 2.333$ and $\mathsf{St} = 1.4, C_f = 0.7$ located in the regions quasi-static, inertia negligible and friction negligible respectively were chosen. Norm velocity profile and pressure profile for the time-point at the end of the simulation ($t = 10\tau$) will be demonstrated in the following FIGURE E.9.

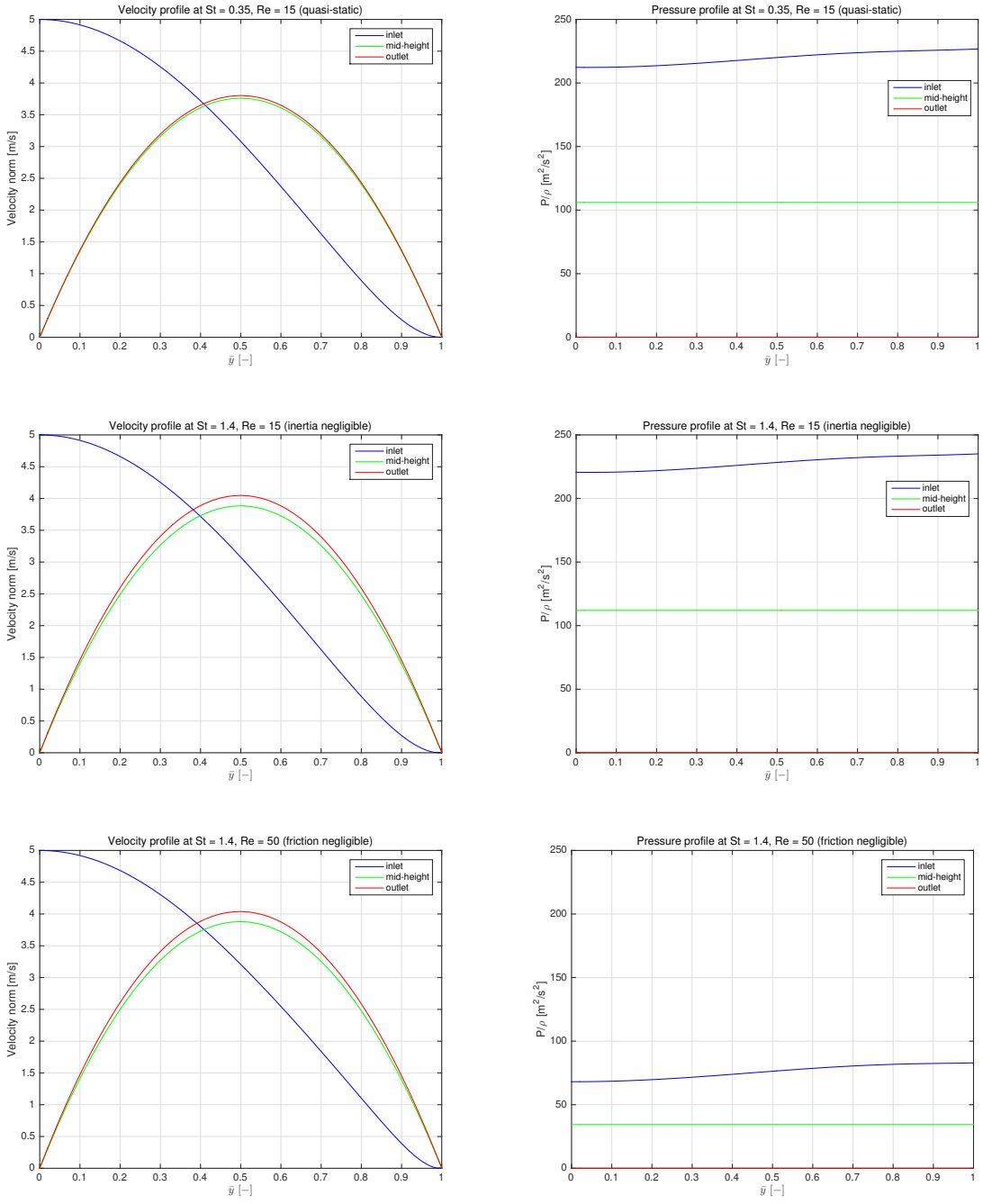

FIGURE E.9: Velocity profile and pressure profile

The velocity profile of the quasi-static case at the mid-height and outlet are very similar showing no velocity gradient along the y direction. Pressure profiles along y-direction is almost flat. For the case with negligible frictions, the pressure magnitude is much lower than that of the other two cases.

E.2.2.2 Time evolutions

Global dissipations, average pressure on the oscillating plate and average inlet pressure were coupled in Cast3M:

$$\begin{aligned}\textbf{Global Dissipation} &= \int_{\mathcal{V}} \nu \left|\nabla \mathbf{u}\right|^2 \mathrm{d}\mathcal{V} \\ &= \nu \int_{\mathcal{V}} \left[\left(\frac{\partial u}{\partial x}\right)^2 + \left(\frac{\partial u}{\partial y}\right)^2\right] \mathrm{d}\mathcal{V} + \nu \int_{\mathcal{V}} \left[\left(\frac{\partial v}{\partial x}\right)^2 + \left(\frac{\partial v}{\partial y}\right)^2\right] \mathrm{d}\mathcal{V};\end{aligned} \tag{E.52}$$

$$\begin{aligned}\textbf{Average Pressure on the Oscillating Plate} &= \frac{\textbf{Pressure Integral on the Oscillating Plate}}{\textbf{Surface of the Oscillating Plate}} \\ &= \frac{\int_{A_p} p \, \mathrm{d}A}{A_p}.\end{aligned} \tag{E.53}$$

$$\textbf{Average Inlet Pressure} = \frac{\textbf{Pressure Integral of Inlet}}{\textbf{Surface of the Inlet}} \tag{E.54}$$

$$= \frac{\int_{A_{in}} p \, \mathrm{d}A}{A_{in}}.$$

Here, $\mathcal{V}$ is the whole fluid domain, A_p is the surface domain of the oscillating plate and A_{in} is the surface domain of the inlet.
Take one simulation $\mathsf{St} = 1.4$ and $\mathsf{Re} = 5$ as example.The time evolutions of the global dissipation, average pressure on the oscillating plate and average inlet pressure will be shown in following FIGURE E.10.

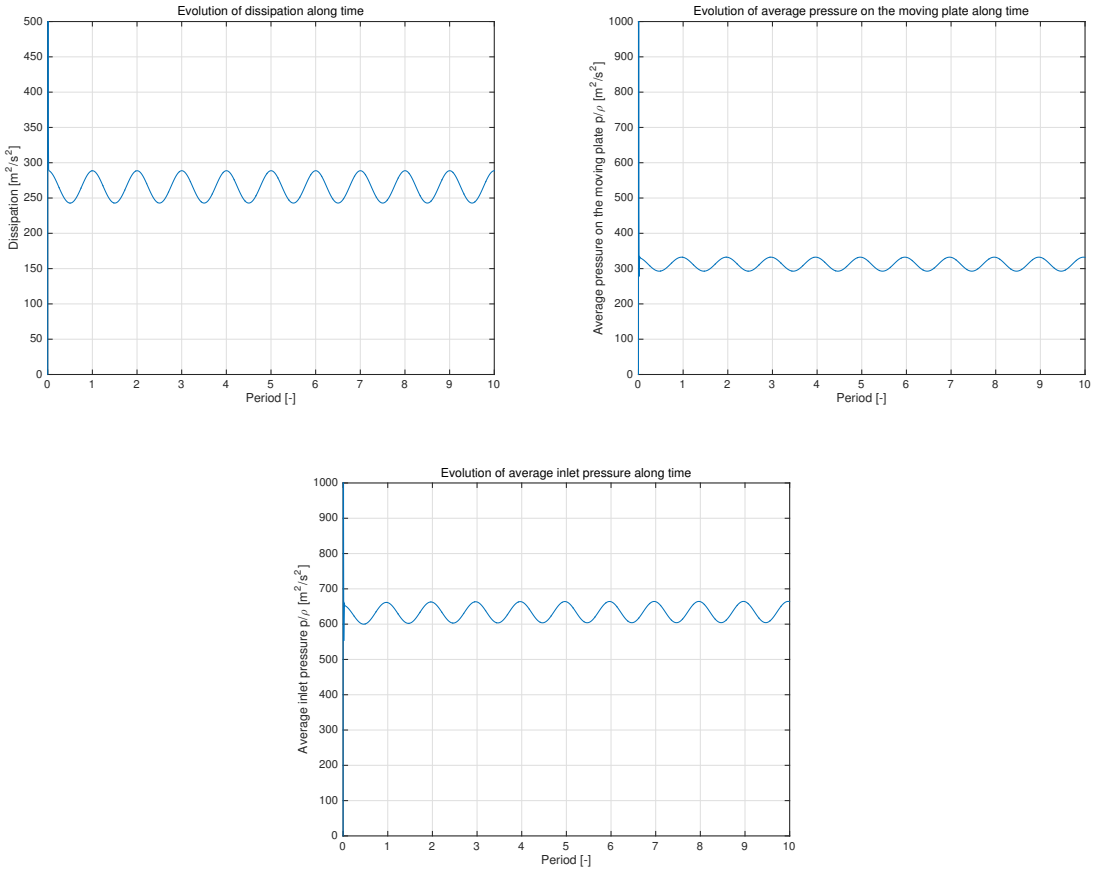

FIGURE E.10: Time evolutions of global dissipation, average pressure on the moving plate and average inlet pressure

To analyze the steady periodic behavior of the fluid flow, all the simulations were run for 10 periods in order to reach a steadily oscillating state. The norm of the time evolution function of dissipation, average pressure on the moving plate and average inlet pressure at the 7th, 8th, 9th and 10th period were calculated using the following form: $\|f\|^2 = \frac{1}{T}\int_0^T f^2(t)dt$.

The results will be shown in TABLE E.4:

TABLE E.4: Norm of the time evolutions

	7th+8th	**8th+9th**	**9th+10th**	**7th**	**8th**	**9th**	**10th**
Disspation	1.0048e5	1.0050e5	1.0052e5	1.0046e5	1.0049e5	1.0051e5	1.0053e5
Average pressure on the moving plate	5.5100e8	5.5100e8	5.5100e8	5.5100e8	5.5100e8	5.5100e8	5.5100e8
Average inlet pressure	44.9417	44.9501	44.9563	44.9368	44.9466	44.9536	44.9589

Comparing the norm for 2 periods and 1 period, the differences between are vey small indicating that the results are not sensitive to the number of periods taken for analysis. The differences of the results for neighboring periods are less than 0.05%. Therefore, we can suppose that the simulations have already reached a steadily oscillating state at the 9th

period. So the results at the 9th were taken for analysis following.
With least-squares method, the best fit function for the 9th period can be written as:
▷ *Dissipation*:

$$y = 23.1119 * \sin(\frac{2\pi}{1.0185}t - 1.3452 \pm 0.2500) + 265.8597 \pm 0.7600 \ \ [\mathrm{m}^2/\mathrm{s}^2];$$

▷ *Average pressure on the oscillating plate*:

$$y = 19.8367 * \sin(\frac{2\pi}{1.0010}t - 1.3983 \pm 0.2200) + 312.5846 \pm 0.7200 \ \ [\mathrm{m}^2/\mathrm{s}^2];$$

▷ *Average pressure on the inlet*:

$$y = 30.0972 * \sin(\frac{2\pi}{1.0012}t - 1.3977 \pm 0.2200) + 634.3593 \pm 0.7200 \ \ [\mathrm{m}^2/\mathrm{s}^2].$$

E.2.2.3 Average pressure on the oscillating plate

Average pressure on the oscillating plate were calculated as following:

$$\begin{aligned}\textbf{Average Pressure on the Oscillating Plate} &= \frac{\textbf{Pressure Integral on the Oscillating Plate}}{\textbf{Surface of the Oscillating Plate}} \\ &= \frac{\int_{A_p} p \, \mathrm{d}A}{A_p} \\ &= \frac{\int_{-1}^{1} \delta p(\bar{p} + \varpi\tilde{p}) \, \mathrm{d}\bar{x}}{\int_{-1}^{1} \mathrm{d}\bar{x}}.\end{aligned}$$

Mean values were taken for the analysis of the stationary parts and then the perturbation parts with mean values extracted were taken for the analysis of the perturbation parts. Non-dimensionalization were performed as discussed in the previous chapter for first-order stationary part and perturbation part.
The mean part can be expressed by:

$$\textbf{Stationary Part} = \frac{L\int_{-1}^{1} \overline{p} d\overline{x}}{2L} = \frac{\int_{-1}^{1} \overline{p} d\overline{x}}{2}.$$

The perturbation part can be expressed by:

$$\textbf{Perturbation Part} = \frac{\int_{-1}^{1} \tilde{p} d\overline{x}}{2}.$$

The evolution of non-dimensioned numerical results along C_f and the evolution along St are shown in FIGURE E.11 and FIGURE E.12 respectively.
Note here, QS is abbreviated for "quasi-static approximation", FN is abbreviated for "friction is negligible" while IN is abbreviated for "inertia is negligible".

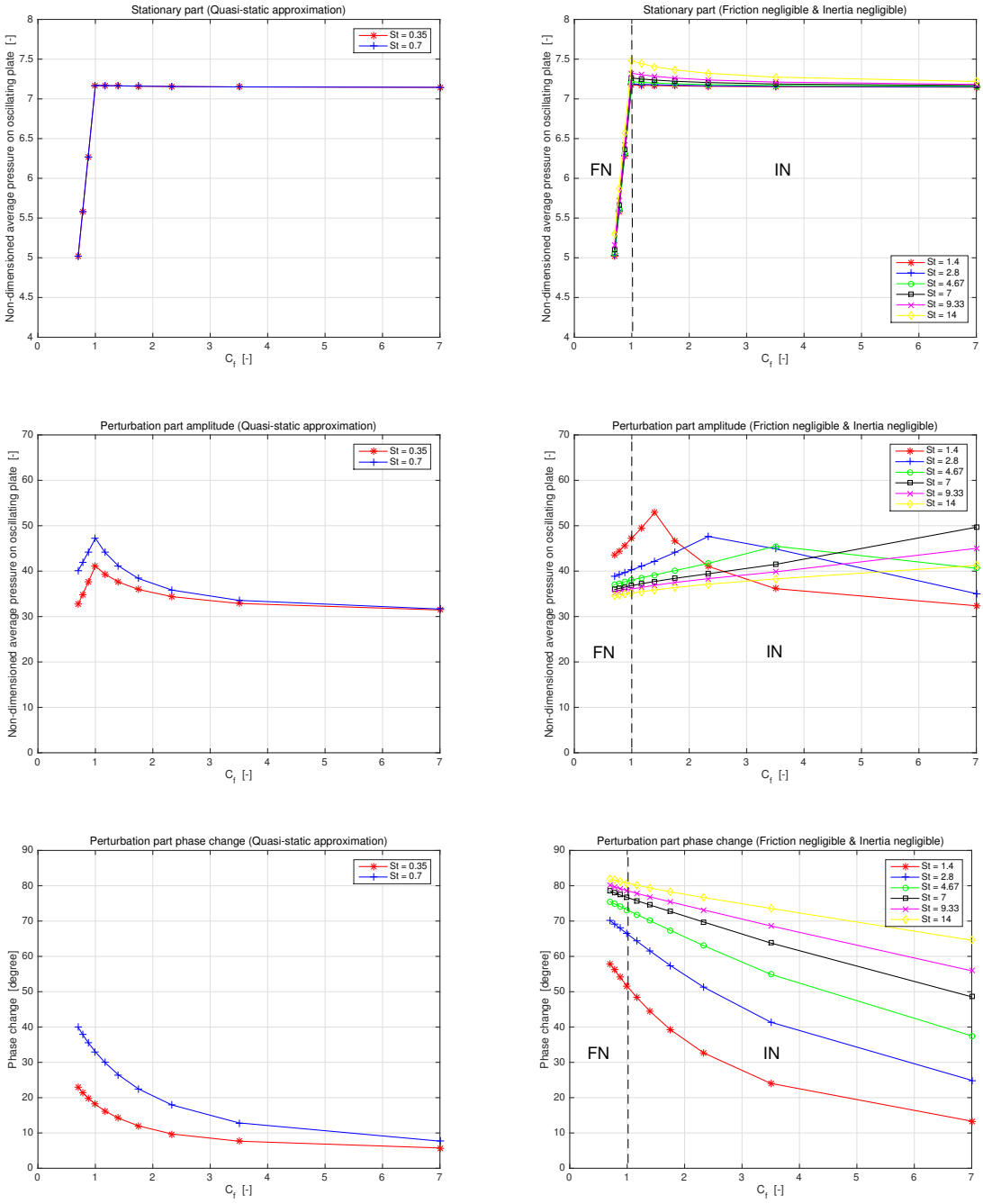

FIGURE E.11: Evolution of average pressure along C_f

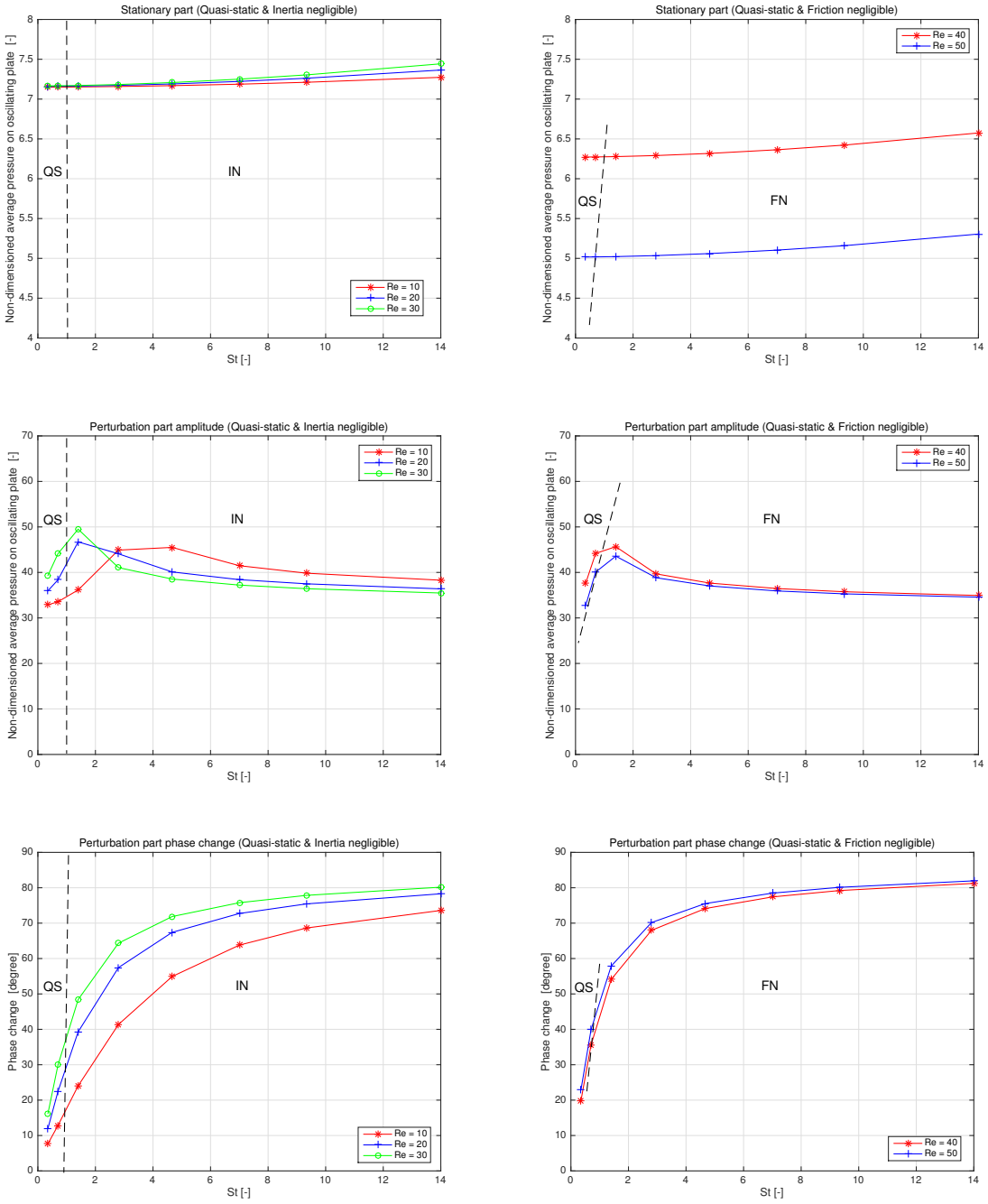

FIGURE E.12: Evolution of average pressure along St

E.2.2.3.1 Staionary part

For the stationary part, the change of the scaling is affecting the curves. For all the curves of different Sts, the non-dimensioned average pressures slightly decrease with the C_f increases and the decreasing speeds are becoming slower and slower. As can be seen in Eq. E.25, when $C_f < 1$, $\mathsf{Eu} = 1$, with C_f increases (Re decreases), the flow regime is transferring from friction negligible to inertia negligible, dissipation term will take a more and more important role which will lead to a decrease of the pressure term.

Also by comparing the values with the same C_f (same Re), we can see that when the St increases, the non-dimensioned average pressure increases. But the differences between different C_f at the same value of St reduces from low C_f to high C_f (from high Re to low Re). As described in phenomenological analysis, like in Eq. E.25, there is no role of St for the solution of the stationary parts which is different from what we observed here. This may result from the fact that, thin boundary layer approximation was used in the phenomenological analysis, the friction force is supposed to act on the entire width of the channel. Also when St number increases, the flow regime is changing with the boundary layer effect is getting more and more important. The mean values of the second-order terms are not zero and are influenced by Sts, this may be the reason why the stationary parts are affected by the values of Sts.

E.2.2.3.2 Amplitudes of perturbation part

Due to the reason that the choice of the scalings is not precise, the asymptotic analysis results may be far from order 1 like shown here. Comparing the amplitudes of the perturbation parts, for the cases affecting by the change of the scaling ϖ, the amplitudes of the perturbation parts first increase approximately linear to the value of C_f, then decreases with C_f increases after the changing point and the decreasing speed is reducing which is similar to that of the stationary part. But we can observe that, the influence of the decreased C_f for the amplitudes of the perturbation parts are higher than that for the stationary part. From the lowest value of C_f to the highest value of C_f, the amplitudes of the perturbation parts decreases more than 30%. As stated in the momentum conservation equation for perturbation in Eq. E.30, with C_f increases, the dissipation induced by the oscillation will become more and more important, so the perturbation pressure has decreased. While for the cases with $\mathsf{St} > C_f > 1$, the curves keep increasing with C_f increases.
From evolution curves of perturbation amplitudes along St, the perturbation amplitudes will decrease with St increases when $\mathsf{St} > sup\{1, C_f\}$ while it increases when $\mathsf{St} < sup\{1, C_f\}$.

E.2.2.3.3 Phase shift of perturbation part

Also from FIGURE E.11 and FIGURE E.12, observing the figures for phase change, we can find that with the C_f increases, all the curves of the phase change of the perturbation parts have similar decreasing trend and also for same C_f the phase change increases with the St increases. In Eq. E.25, the unsteady term will first introduce a phase change of $\frac{\pi}{2}$ to the perturbation pressure, then the amplitudes of the other terms will decide the amplitudes of the phase change. The changing trends of the phase changes copes with the phenomena described in Eq. E.25.

E.2.2.4 Average inlet pressure

Average inlet pressure were calculated using Eq. E.55:

$$\begin{aligned}\textbf{Average Inlet Pressure} &= \frac{\textbf{Pressure Integral of Inlet}}{\textbf{Surface of the Inlet}} \\ &= \frac{\int_{A_{in}} p \, \mathrm{d}A_{in}}{A_{in}} \\ &= \frac{\int_{-\frac{\ell}{L}}^{\frac{\ell}{L}} \delta p(\bar{p} + \varpi \tilde{p}) \, \mathrm{d}\bar{x}}{2\eta}.\end{aligned} \tag{E.55}$$

The stationary part can be expressed as:

$$\textbf{Stationary Part} = \frac{\int_{-\frac{\ell}{L}}^{\frac{\ell}{L}} \overline{p} \, \mathrm{d}\overline{x}}{2\eta}. \tag{E.56}$$

The perturbation part can be expressed as:

$$\textbf{Perturbation Part} = \frac{\int_{-\frac{\ell}{L}}^{\frac{\ell}{L}} \tilde{p} \, \mathrm{d}\overline{x}}{2\eta}. \tag{E.57}$$

The results of the average inlet pressure are shown in FIGURE E.13.

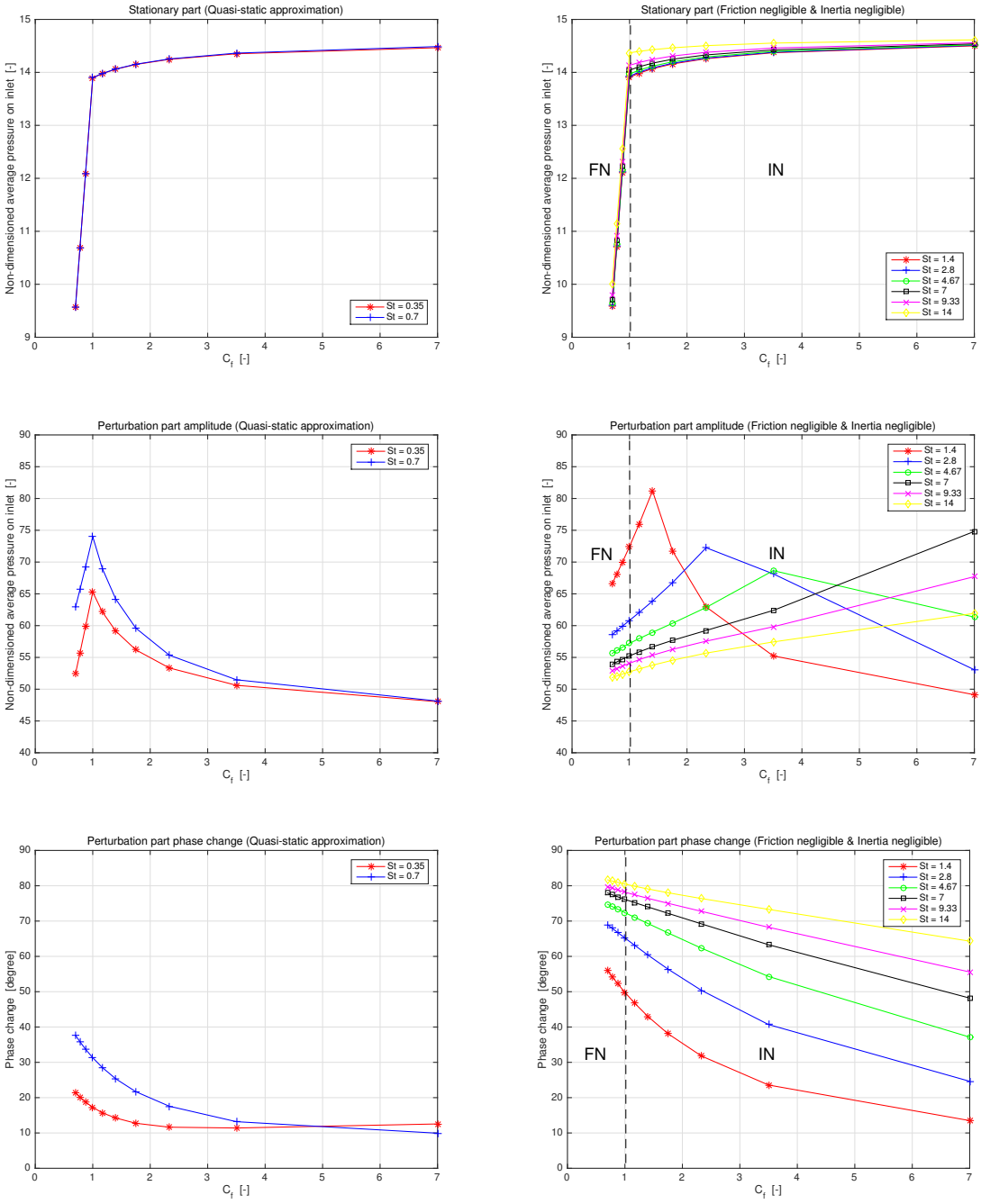

FIGURE E.13: Evolution of average inlet pressure along C_f

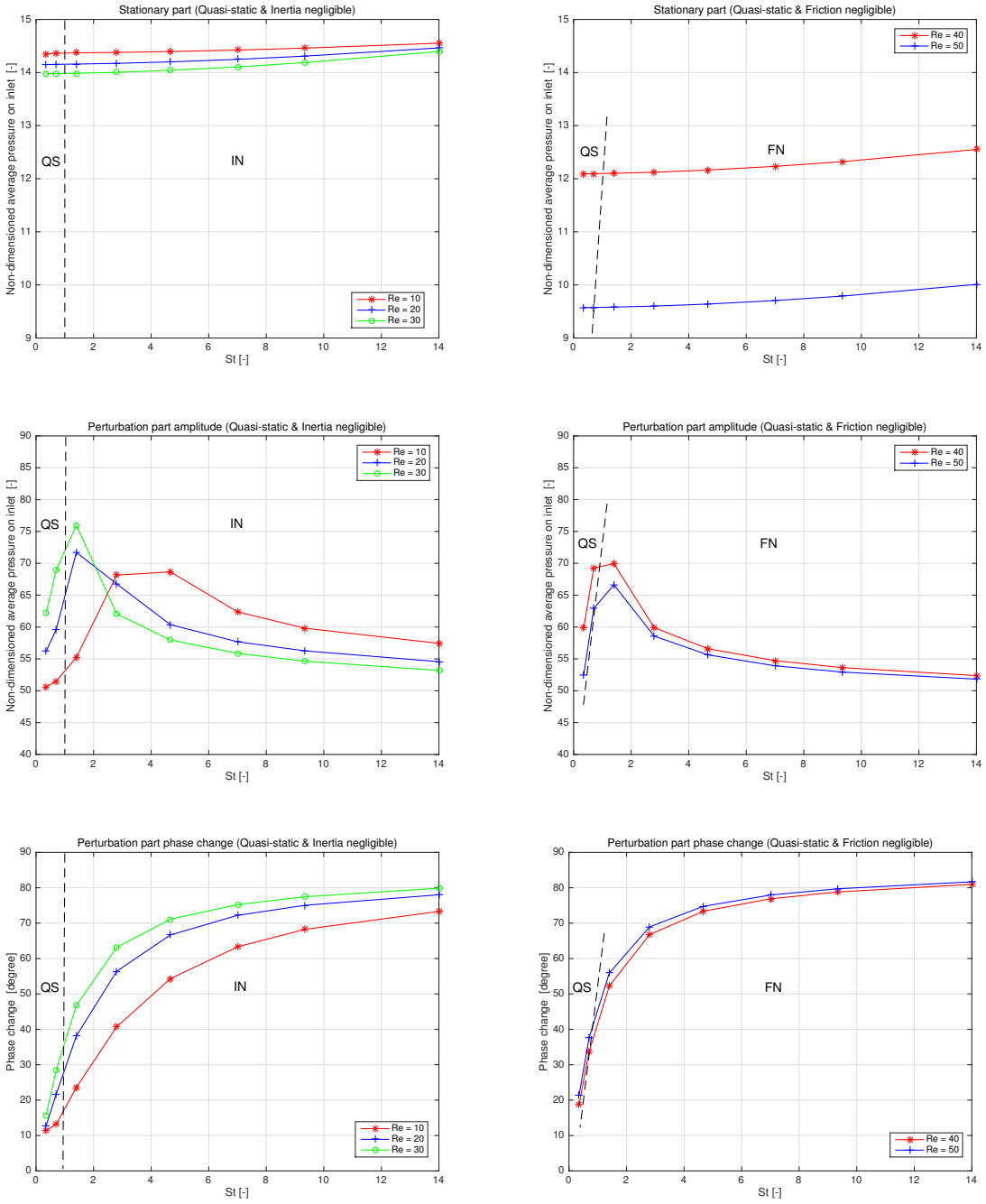

FIGURE E.14: Evolution of average inlet pressure along St

For the stationary part of the average inlet pressure, it is increasing with C_f increases for all St with a reducing speed after the change of scaling when $C_f > 1$. Comparing the amplitude of the average inlet pressure to that of the average pressure on the oscillating plate, it can be observed that the pressure at the inlet is at the same level with that on the oscillating plate. For same C_f, there is an increase of the values along St due to the increasing of the boundary layer effect and time averages of the second order terms.
For the amplitudes of the perturbation part, similar to that of average pressure on the oscillating plate, the amplitudes are decreasing along C_f for the case of St $> sup\{1, C_f\}$.

For the phase change of the perturbation part, for all St, the phase changes are reducing with C_f increases but for there are exceptions for $\mathsf{St} = 0.35$. The cases with $C_f = 7, 3.5$ are slightly increasing. The phase change is increasing along St similar to that of the average pressure on the oscillating plate.

E.2.2.5 Dissipation and pressure work

Global dissipation and pressure work were calculated during the post-processing.

$$\textbf{Pressure Work} = \int_{\partial\mathcal{V}} p\mathbf{u}\cdot\mathbf{n}\,\mathrm{d}\partial\mathcal{V}.$$

To compare dissipation and pressure work, rate of the two terms are introduced:

$$\textbf{Rate of Dissipation \& Pressure Work} = \frac{\textbf{Global Dissipation}}{\textbf{Pressure Work}} = \frac{\int_{\mathcal{V}}\mu\left|\nabla\mathbf{u}\right|^2\,\mathrm{d}\mathcal{V}}{\int_{\partial\mathcal{V}} p\mathbf{u}\cdot\mathbf{n}\,\mathrm{d}\partial\mathcal{V}}$$

Mean parts of the dissipation and pressure works were extracted and then the stationary parts of dissipation and pressure work were calculated by using the mean parts of the dissipation divided by the mean parts of pressure works. The amplitudes of the perturbation parts of the dissipation and pressure work were calculated and then the perturbation part the rate is achieved by the perturbation parts of the dissipation dividing by that of pressure work. Note here, the rate is the rate of the dimensional quantity.
The rates of dissipation and pressure work of all the cases will be shown in the following FIGURE E.15.

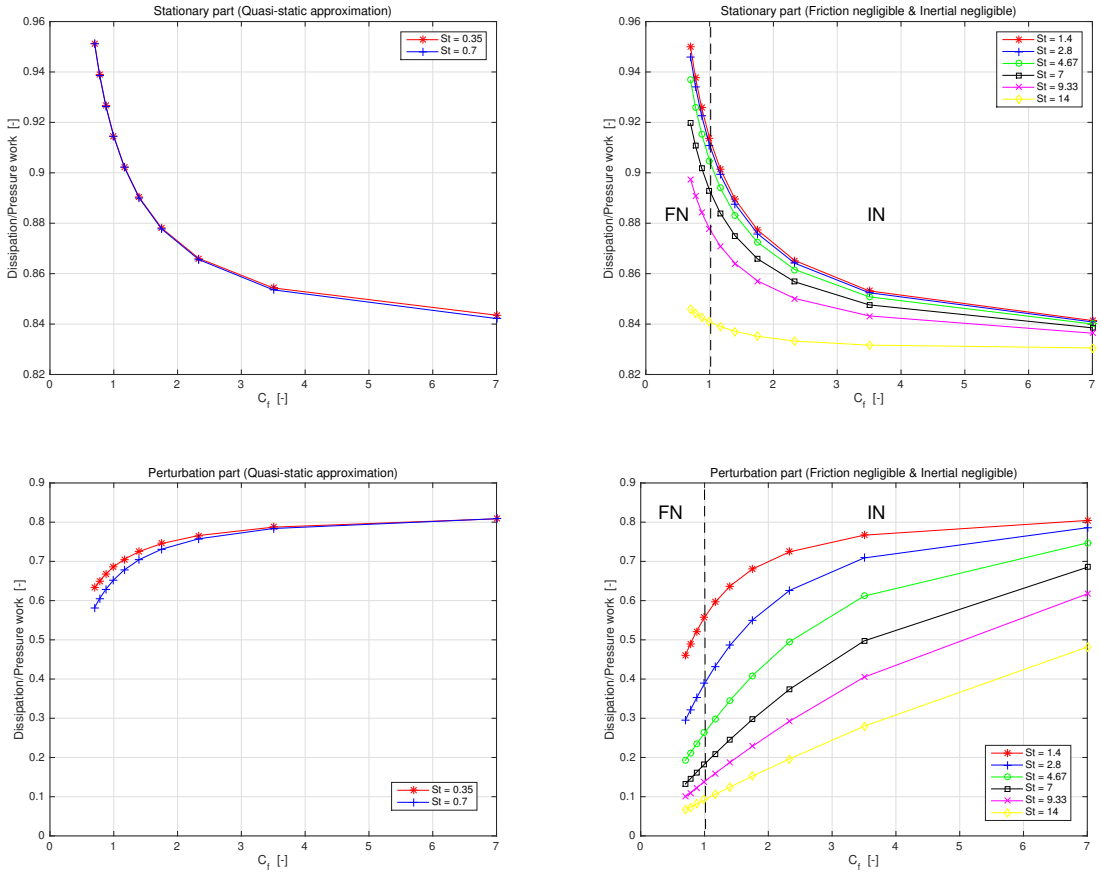

FIGURE E.15: Evolution of rates of dissipation and pressure work along C_f

In FIGURE E.15, comparing the curves for stationary part, it can be observed that with C_f increases, the rates of dissipation and pressure work are decreasing for all the curves with different Sts and the decreasing trend are becoming more and more flat. As shown as Eq. E.42, the rate calculated here demonstrates the rate between the third term and the first term in the equation. It is showing that with Re increases, the contribution of the kinetic energy flux to the energy balance is decreasing.
In this case, the order of the rate can be demonstrate as:

$$\frac{C_f}{\mathsf{Eu}} = \frac{C_f}{sup\{1, C_f\}} = \begin{cases} C_f, \text{when } C_f < 1 \\ 1, \quad \text{when } C_f > 1 \end{cases}$$

This can explain the reason why the value of the rates in FIGURE E.15 are ranging from 1 to 0.8, still on the same magnitude.
For the perturbation part, the rates of the amplitudes of dissipation and pressure work are demonstrated above in FIGURE E.15. Opposite to the stationary parts, the rates increase with C_f increases and the increasing rate is becoming smaller. For same value of C_f, the rates are decreasing while the St increase, but the difference is becoming smaller and smaller while C_f increases.
Considering Eq. E.43 and Eq. E.44, it is evident that the rate will decrease with the St increases.

E.2.3 Conclusions

In this chapter, numerical results resolved by Cast3M has been shown here. Average pressure on the oscillating plate, average inlet pressure and rates between global work and dissipation were analyzed with asymptotic method introduced in the previous chapter. Nonzero time averages of the second-order terms and the changing flow regime with boundary layer effects were demonstrated in the mean part of the average pressure (stationary part). Global dissipation is almost at the same order of pressure work while the rate is decreasing with C_f and St increases. The perturbation is not vary dissipative.

E.3 Conclusions

In this report, a two-dimensional incompressible viscous fluid channel model with an oscillating plate implemented and Navier-Stokes model were introduced for the simplification of the fluid domain around the assemblies in a SFR core.

Phenomenologically, the problem was decomposited into two parts: a stationary reference solution and a small-amplitude perturbation term which has been expanded into second order. A scaling system was introduced for non-dimensionalization of the governing equations, including mass conservation, momentum conservation, kinetic energy equation and boundary conditions, for both the reference solution and the perturbation solution. Two non-dimensioned parameters C_f and St were chosen for characterizing the flow condition, therefore a flow map with C_f on the y-axis and St on the x-axis were introduced. Also, the experiments conducted with continous injection are placed in the quasi-static region of the flow map which is included in the analytical and numerical discussion of this report.

Numerical solutions resolved by Cast3M were presented. Results of rate of dissipation and pressure work, average pressure on the oscillating plate and average inlet pressure were discussed according to the phenomenological analysis. Stationary parts were calculated with the mean value and perturbation parts were calculated with mean value extracted. As discussed in analytical analysis, there are means of second order variables involved in the stationary parts which is the reason that the stationary parts are varied with different St. Furthermore, by comparing the dissipation and the pressure work, the perturbation is not very dissipasitive.

To continue the work, more refined models will be studied with different numerical models, including Navier-Stokes, Euler and Euler linear model. Also improvement of the numerical models will be carried. More experiments with continous injections will be performed both on PISE-1A and PISE-2C.

Bibliography

[1] U. DoE *et al.*, "A technology roadmap for Generation IV nuclear energy systems," in *Nuclear Energy Research Advisory Committee and the Generation IV International Forum*, pp. 48–52, 2002.

[2] F. Gauche and J. Rouault, "French SFR R&D program and design activities for SFR prototype ASTRID," *Energy Procedia*, vol. 7, pp. 314–316, 2011.

[3] A. Vasile, "ASTRID: Advanced Sodium Technological Reactor for Industrial Demonstration," in *Forty-Eighth Meeting of The Technical Working Group on Fast Reactors*, pp. 25–29, 2015.

[4] P. Le Coz, J. Sauvage, and J. Serpantié, "Sodium-cooled fast reactors: the ASTRID plant project," in *Proceedings of ICAPP*, p. 2851, 2011.

[5] M. Schneider, "Fast breeder reactors in France," *Science and Global Security*, vol. 17, no. 1, pp. 36–53, 2009.

[6] Power Reactor Information System, "PHENIX." https://www.iaea.org/PRIS/CountryStatistics/ReactorDetails.aspx?current=162, 2017.

[7] P. Dumaz *et al.*, "Avancement des étude AURN," internal report, CEA, 2012.

[8] J. Cardolaccia, "Modèle 3D d'un coeur Phénix simplifié sous EUROPLEXUS : Simulation du phénomène de gerbage avec couplage fluide-structure," tech. rep., CEA-Saclay DEN/DANS/DM2S/SEMT/EMSI/11-023/A, 2012.

[9] J. Guidez *et al.*, "Scenario explicatif des quatre arrêts par réactivité négative (AURN) survenus à Phénix en 1989 et 1990," internal report, CEA/DEN/DSNI/DIR DO 225, 2008.

[10] F. Mellier and J. Bosq, "Phénix : Étude de l'impact des assemblages DAC sur les assemblages fertiles voisins," internal report, CEA/DEN/CAD/DER/SPRC/LEDC 01-411, 2001.

[11] M. Gentili, *Aspects neutroniques associés à des réseaux irréguliers d'assemblages dans un coeur de RNR-Na*. PhD thesis, Aix-Marseille, 2015.

[12] V. Pascal, B. Gastaldi, and M. Vanier, "Phénix-Essais fin de vie : calculs neutroniques en soutien à l'essai « Échauffement DAC-fertiles»," internal report, CEA Cadarache/DEN/CAD/DER/SPRC/LEDC 08-415, 2008.

[13] D. Broc, "Comportement dynamique des coeurs RNR-Na : Interprétation des essais SYMPHONY (séisme) et Rapsodie (injection)," internal report, CEA-Saclay/DEN/DANS/DM2S/SEMT/EMSI/11-008/A, 2012.

[14] M.-E. Pasquini, "Developement of physical model for vapour explosion in superheated sodium," Master's thesis, University of Pisa, Italy, 2011.

[15] E. Semeraro, *Experimental investigation on hydrodynamic phenomena associated with a sudden gas expansion in a narrow channel*. PhD thesis, Université Pierre et Marie Curie-Paris VI, 2014.

[16] J. F. Semblat and A. Pecker, "Waves and vibrations in soils: Earthquakes, Traffic, Shocks, Construction works," in *Waves and vibrations in soils: Earthquakes, Traffic, Shocks, Construction works*, p. 500 p, IUSS Press, Jan. 2009.

[17] E. Juhásová, *Seismic effects on structures*, vol. 67. Elsevier, 2013.

[18] S. Chen, M. t. Wambsganss, and J. Jendrzejczyk, "Added mass and damping of a vibrating rod in confined viscous fluids," *Journal of Applied Mechanics*, vol. 43, no. 2, pp. 325–329, 1976.

[19] J. Cardolaccia, *Manuel de l'utilisateur du code BASILIQ*. CEA/DEN/DANS/DM2S/SEMT/DYN/NT/A7-001/A.

[20] J. Cardolaccia, "Plan de développement BASILIQ," tech. rep., CEA-Saclay DEN/DANS/DM2S/SEMT/DIR/PD/007/B.

[21] D. Broc and J. F. Sigrist, "Fluid structure interactions for tube bundles: Physical meaning of a Rayleigh damping," in *ASME 2010 Pressure Vessels and Piping Division/K-PVP Conference*, pp. 51–59, American Society of Mechanical Engineers, 2010.

[22] J.-F. SIGRIST and D. BROC, "Méthodes numériques de calculs couplés fluide/structure méthode d'homogénéisation pour l'analyse vibratoire de faisceaux tubulaires," *Techniques de l'ingénieur Calcul et modélisation en mécanique*, vol. base documentaire : TIB178DUO., no. ref. article : bm5202, 2012. fre.

[23] Q. Desbonnets, *Méthode d'homogénéisation pour la vibration de faisceaux de tubes en présence de fluide*. PhD thesis, Paris 6, 2012.

[24] A. N. Gineau, *Modélisation multi-échelle de l'interaction fluide-structure dans les systèmes tubulaires*. PhD thesis, Paris 6, 2015.

[25] N. Al Sayed, "Benchmark IFS sur les méthodes numériques pour la simulation du phénomène de gerbage du coeur Phénix," in *LaMSID-UMR 8193 CNRS-EDF-CEA*, 2013.

[26] L. Sargentini, *Étude des mécanismes d'interaction fluide-structure d'un cœur RNR-Na lors de l'évacuation d'une poche de gaz*. PhD thesis, Université Pierre et Marie Curie-Paris VI, 2014.

[27] G. Artini, "Numerical and Experimental Analysis of a Fluid Structure Interacton Model for a FBR Core: Edge Effects," Master's thesis, University of Pisa, Italy, 2014.

[28] R. CAST3M, "Cast3m: Documentation," *EUROSIM/CEA SEMT*, 2004.

[29] B. Carriteau, "Résultats expérimentaux sur l'interaction fluide structure d'un cylindre hexagonal vibrant dans un espace confiné," tech. rep., CEA/DEN/DANS/DM2S/STMF/LIEFT, 2017.

[30] N. M. Newmark, "A method of computation for structural dynamics," *Journal of the engineering mechanics division*, vol. 85, no. 3, pp. 67–94, 1959.

[31] P. Verpeaux and T. Charras, "Dynamique du solide: modification du schema de Newmark aux cas nonlinéaires," *CSMA, Giens*, 2013.

[32] J. Kevorkian and J. D. Cole, *Perturbation methods in applied mathematics*, vol. 34. Springer Science & Business Media, 2013.

[33] J.-N. Juang and R. S. Pappa, "An eigensystem realization algorithm for modal parameter identification and model reduction," *Journal of Guidance*, vol. 8, no. 5, pp. 620–627, 1985.

[34] R. Gibert, *Vibration des structures*. Collection de la Direction des Études et Recherches d'Électricité de France, 1988.

[35] S. Butterworth, "On the theory of filter amplifiers," *Wireless Engineer*, vol. 7, no. 6, pp. 536–541, 1930.

[36] A. V. Oppenheim, *Discrete-time signal processing*. Pearson Education India, 1999.

[37] F. Gustafsson, "Determining the initial states in forward-backward filtering," *IEEE Transactions on Signal Processing*, vol. 44, no. 4, pp. 988–992, 1996.

[38] F. J. Harris, "On the use of windows for harmonic analysis with the discrete fourier transform," *Proceedings of the IEEE*, vol. 66, no. 1, pp. 51–83, 1978.

[39] M. Abramowitz and I. A. Stegun, *Handbook of mathematical functions: with formulas, graphs, and mathematical tables*, vol. 55. Courier Corporation, 1964.

[40] Y. Shinohara and T. Shimogo, "Vibrations of square and hexagonal cylinders in a liquid," *Journal of Pressure Vessel Technology*, vol. 103, no. 3, pp. 233–239, 1981.

[41] E. Jacquelin, D. Brochard, C. Trollat, and L. Jézéquel, "Homogenization of a non-linear array of confined beams," *Nuclear Engineering and Design*, vol. 165, no. 1-2, pp. 213–223, 1996.

[42] E. Jacquelin, J. Lainé, C. Trollat, and L. Jézéquel, "Modelling the behaviour of a PWR core by a homogenization technique," *Computer methods in applied mechanics and engineering*, vol. 155, no. 1-2, pp. 1–13, 1998.